

Azərbaycan Milli Elmlər Akademiyası
Fizika-Riyaziyyat və Texnika Elmləri Bölməsi
Fizika İnstitutu

4

Fizika

Cild

X

2004

Bakı ✱ Elm

GRUNEISEN PARAMETERS AND ISOTHERMAL COMPRESSIBILITY OF GaS SINGLE CRYSTALS

Z.A. ISKENDERZADE, V.D. FARADJEV, E.M. KURBANOV, E.K. KASUMOVA

*Azerbaijan Technical University,
Az. 1073, Baku, H. Javid ave., 25*

The temperature dependences of Gruneisen parameters and compressibilities of GaS in the temperature range 80-410K have been investigated. It is shown that the Gruneisen parameters decreases and the compressibilities increases with increasing temperature.

GaS crystallises in the layered structure with hexagonal spatial symmetry D_{6h}^4 and contains four molecular units in the unit cell; lattice parameters at 300 K are $a=0.358$ nm and $c=1.55$ nm. Each layer consists of four sublayers in the sequence S-Ga-Ga-S. The bonding between layers is mainly of Van der Waals type, while within layers there exists a strong covalent bond. The weakness of the interlayer bond compared to the intralayer one leads to interesting physical properties, owing to a strong structural anisotropy.

In order to determine Gruneisen parameters and compressibilities we learned elastic properties of GaS. The linear elastic properties may be described with elastic constants. The elastic constants of GaS were calculated from the longitudinal and transverse ultrasound velocities propagating along and perpendicular to the C-axis.

The GaS single crystals were grown by Bridgman technique. The samples were formed in rectangular shape by cleaving and mechanical polishing with dimensions varying 5 to 10 mm along the C-axis, and from 5 to 8 mm in the layer plane. The faces perpendicular to the crystallographic C-axis were easily cleaved reflecting of layered structure. The faces parallel to the C-axis were mechanically polished to make $90 \pm 0,5^\circ$ to the C-face.

The sound velocities were measured by pulse-phase method. From measured velocities and value of the mass density ($\rho=3750$ kg/m³) we obtain elastic constants of GaS. At room temperature $C_{11}=15,7$; $C_{13}=1,35$; $C_{33}=3,87$; $C_{44}=1,1$ and $C_{66}=6,15$ in units 10^{10} N/m². Taking into account the temperature dependence of density the temperature dependence of elastic constants were built [1].

The compressibilities along (B_{\parallel}) and perpendicular (B_{\perp}) to the C-axis can be expressed in terms of the elastic constants, yielding:

$$B_{\parallel} = \frac{C_{11} + C_{12} - 2C_{13}}{C_{33}(C_{11} + C_{12}) - 2C_{13}^2},$$

$$B_{\perp} = \frac{C_{33} - C_{13}}{C_{33}(C_{11} + C_{12}) - 2C_{13}^2},$$

$$B = B_{\parallel} + 2B_{\perp}.$$

Using the elastic constants, we obtain $B_{\parallel} \approx 0,23$; $B_{\perp} \approx 0,036$, $B \approx 0,302$ in units 10^{-10} Pa⁻¹. These values are in agreement with calorimetric measurements. Thus, the crystal is much more compressible along the C-axis than perpendicular to it.

The compressibility anisotropy is due to large difference of intra- and interlayer forces.

In the temperature region 80-410 K compressibility linear increase with increasing temperature and the slope of B_{\parallel} more than that of B_{\perp} . This fact indicates that along the C-axis contribution of thermal expansion to value of compressibility is much more than perpendicular to it.

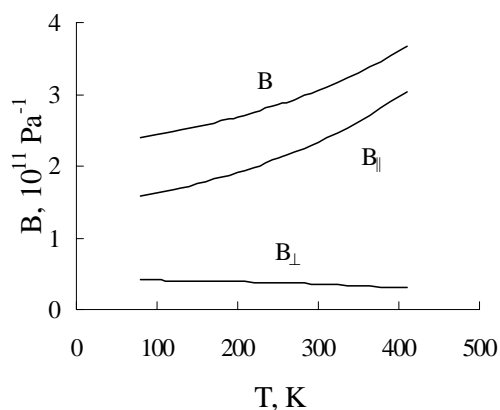


Fig.1. The temperature dependence of isothermal compressibility B of GaS single crystals: B_{\parallel} , B_{\perp} - compressibilities along and perpendicular to the C-axis, respectively.

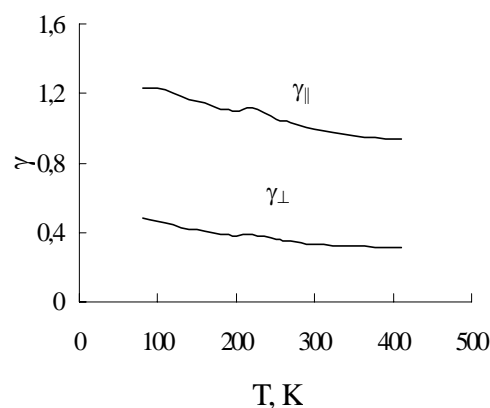


Fig.2. The temperature dependence of Gruneisen parameters of GaS single crystals: γ_{\parallel} , γ_{\perp} - Gruneisen parameters along and perpendicular to the layer plane.

The Gruneisen parameters also can be obtained from

elastic constants. In the case of hexagonal crystals, one can define two independent Gruneisen parameters: γ_{\parallel} and γ_{\perp} . They are related to the elastic constants by

$$\gamma_{\parallel} = \frac{V}{C_p} [(C_{11} + C_{12})\alpha_{\parallel} + C_{13}\alpha_{\perp}],$$

$$\gamma_{\perp} = \frac{V}{C_p} [C_{33}\alpha_{\perp} + 2C_{13}\alpha_{\parallel}],$$

where V – molar volume; C_p – molar heat capacity at stationary pressure; α_i – components of the thermal expansion.

In [2] the temperature dependence of Gruneisen

parameters was built without taking into account the temperature dependence of elastic constants. According to [2] γ_{\parallel} is negative in the narrow temperature interval 30-

50 K and this can be understood with a main role "bending" waves in thermal properties of layer crystal.

In view of temperature dependences of elastic constants [1], thermal expansion [3] and heat capacity [4] the temperature dependence of Gruneisen parameters were built in the temperature region 80-410 K. At $T=200$ K our values $\gamma_{\parallel}=1.073$, $\gamma_{\perp}=0.379$ are in a good agreement with data

[2]: $\gamma_{\parallel}=0.8$, $\gamma_{\perp}=0.35$. As it is shown, $\gamma_{\parallel} > \gamma_{\perp}$. Thus

anharmonicity of the interatomic forces is more in the strong bonding direction.

[1] V. Farajov, R. Akdeniz, E. Kasumova. International scientific conference UNITECH'03-Gabrovo proceedings. Technical University of Gabrovo, Bulgaria, 20-21 November 2003. University publishing house "V. Aprilov" – Gabrovo. 2003. V. II. P. 333-336.

[2] N. A. Abdullayev. Izvestiya NANA, seriya fiz.-mat. i tekhn. nauk, 2000, No. 2, p. 7-13.

[3] M. M. Kurbanov. Avtoreferat diss. Baku, 1973.

[4] K. K. Mamedov, I. Q. Kerimov, M. P. Mekhtiyeva, E. A. Masimov. Neorganicheskie materialy (Inorganic materials), 1972, v. 8, p. 2096-2098.

Z.Ə. İsgəndərzadə, V.C. Fərəcov, E.M. Qurbanov, E.K.Qasimova

GaS MONOKRİSTALLARININ QRUNAYZEN PARAMETRLƏRİ VƏ İZOTERMİKİ SİXİLMASI

80-410K temperatur intervalında GaS monokristallarının Qrunayzen parametrlərinin və izotermiki sıxılmasının temperatur asılılıqları tədqiq edilmişdir. Göstərilmişdir ki, temperaturun artması ilə Qrunayzen parametrləri azalır, izotermiki sıxılma isə artır.

З.А. Искендерзаде, В.Д. Фараджев, Е.М. Курбанов, Э.К. Касумова

ПАРАМЕТРЫ ГРЮНАЙЗЕНА И ИЗОТЕРМИЧЕСКАЯ СЖИМАЕМОСТЬ МОНОКРИСТАЛЛОВ GaS

Исследованы температурные зависимости параметров Грюнайзена и изотермической сжимаемости монокристаллов GaS в интервале температур 80-410K. Показано, что с увеличением температуры параметры Грюнайзена уменьшаются, а изотермическая сжимаемость увеличивается.

Received: 20.09.2004

THE LANTHANUM OXY-SULFIDES, ACTIVATED BY NEODYMIUM IONS ARE PERSPECTIVE CRYSTALS FOR THE MINIATURE LASERS

G.I. ABUTALIBOV, A.A. MAMEDOV

*Institute of Physics, Azerbaijan National Academy of Sciences,
Baku AZ-1143, H. Javid av.,33, interservis @azeri.com*

The decay kinetics of $^4F_{3/2}$ of level Nd^{3+} in the crystals La_2O_2S has been investigated. The dependence of threshold of generation on the nonresonance losses and the output power on the input one at the multimode regimes has been calculated.

In spite of the fact, that three-valence neodymium ions in the crystals La_2O_2S have intensive absorption bands and the big cross-section of the laser transition in the comparison with the corresponding parameters of three-valence neodymium ion in YAG, because of the bad optical quality, $La_2O_2S-Nd^{3+}$ hasn't been widely applied in laser technique. In the work [1], it is informed, that in $La_2O_2S-Nd^{3+}$ at the impulse pumping, the generation with the threshold lower, than YAG- Nd^{3+} has been obtained and is proposed, that the differential efficiency in 8-12 times bigger, than YAG- Nd^{3+} in the continuous mode can be achieved. In the difference from the lamp pumping, at the pumping by the semiconductor lasers or light emitting diode, the crystals with the bigger sizes don't need and that's why $La_2O_2S-Nd^{3+}$ can become the perspective materials for miniature lasers. The aim of the present work is the comparison of the dependence of threshold generation on the nonresonance losses, and also the dependence of output on the pumping power for $La_2O_2S-Nd^{3+}$ with the analogical dependence YAG- Nd^{3+} and the investigation of the concentration quenching of neodymium ions in La_2O_2S .

1. The concentration quenching of neodymium ions in La_2O_2S

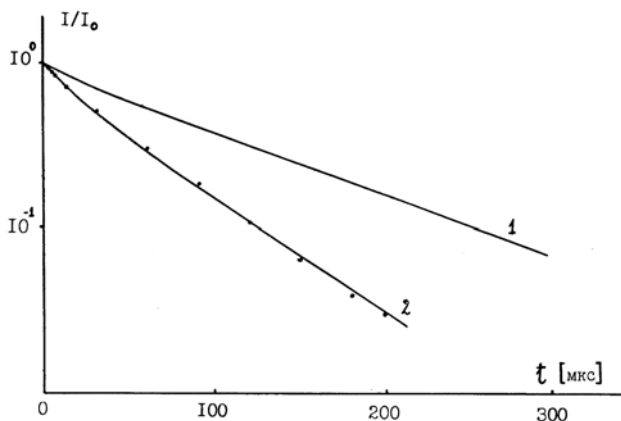


Fig. 1. The experimental (total lines) and calculated (dots) decay curves of the upper laser level of neodymium in the crystal La_2O_2S at the different neodymium concentrations and the excitation with $\lambda=0,53\text{mcm}$: 1-0,8%; 2-x=1,8%.

The curve 1 corresponds to the radiation decay.

The decay curves of $^4F_{3/2}$ of Nd^{3+} layer ions in La_2O_2S is presented on the fig.1. The decay curve is exponential with the constant time 100msec at the small ion concentration. This time is radiation time. At the big concentration the curve

becomes the nonexponential, however on the far stage the output on the exponential part takes place.

As it is known, the concentration quenching of neodymium ions goes in three stages, which reveal on decay curves.

The first stage is the statically ordered, the second stage of the statistically disordered decay connects with acceptor relative intensity y ($y = \frac{n_A}{n_0}$, n_0 – is the total number of lattice points in the volume unit, which can be full of acceptors) by the ratio [2]

$$W_{CT} = y C_{DA} \sum_i R_i^{-6} \quad (1)$$

where sum is taken by all points of acceptor sublattice (center in donor), but C_{DA} is microparameter, which characterizes the donor-acceptor interaction. For the definition of C_{DA} microparameter it is need to know the lattice sum $\sum_i R_i^{-6}$.

At the definition of lattice sum the structural data, taken from the work [3], according to which La_2O_2S has space group D_{3d}^3 were used. The point symmetry, filled by lanthanum (neodymium) is C_{3v} . The elementary cell of La_2O_2S is ortorombical with parameters: $a=4\text{\AA}$, $c=6,82\text{\AA}$, $c/a=1,7$. The lattice sum, calculated by us, is equal to $3,4 \cdot 10^{45} \text{ cm}^{-6}$, and minimal distance between neodymium ions $R_0=3,7\text{\AA}$. Knowing the lattice sum and velocity of the statical ordered decay, the microparameter of donor-acceptor interaction, which is equal to $C_{DA}=4,3 \cdot 10^{-40} \text{ cm}^6 \text{ sec}^{-1}$, was defined by us.

In the work [4], the theory of quenching of luminescence at the presence of excitation migration on donors is spread, kinetics of the luminescence decay in all time scale is found and the expression for the velocity of migrated quenching in the common form is obtained:

$$\Pi(t) = \int_0^t W(t') dt' \quad (2)$$

$$W(t) = 4\pi n_A \int_0^\infty W_{DA}(R) n(R,t) R^2 dR \quad (3)$$

$$n(R,t) = (1 + W_{DA}\tau)^{-1} \left\{ 1 + W_{DA}\tau \exp\left[-(\tau^{-1} + W_{DA})t\right] \right\}, \quad (4)$$

here $\Pi(t)$ -function of the nonradiation energy transfer, n_A is acceptor concentration, $W_{DA}=C_{DA}/R^S$ is probability of the couple donor-acceptor interaction, S is the multiplicity of donor-acceptor interaction, $n(R,t)$ is the instant excitation density on the donor, being on the distance R from acceptor (it is considered, that $n(R,0)=1$), τ - is the more probable time of the one excitation "jump", which is equal to the case of dipole-dipole donor-donor interaction:

$$\tau = \left(\frac{8}{27} \pi^3 C_{DD} n_D^2 \right)^{-1} \quad (5)$$

The consideration the real crystalline structure of the sample leads to the expression, obtained in [5] in limits of approach [4]:

$$W(t) = \frac{n_A}{n_D} \sum_i W_{DA} n(R_i, t), \quad (6)$$

summation on the points of donor lattice, n_D is the number of donor points in the volume unit. The calculation of total kinetics decay of the excited state on the expression [6] allows to define the microparameter of donor-donor transmission C_{DD} without use of the approximation treatment methods of experimental results, based on the asymptotic approximations, the evidence of which needs the special consideration. The definition circuit C_{DD} , offered in the work [6] is following. The decay curves in all time interval corresponding to the experimental plots at the above mentioned definite value C_{DD} are calculated. The design lattice of the curves puts on the experimental plot, which is obtained at the given concentration of donors and acceptors and from the condition of the best agreement of calculated and experimental kinetics, the microparameter C_{DD} value is defined. The best agreement of the calculated and experimental decay curves in the all time range at $C_{DD}=3 \cdot 10^{-38} \text{ cm}^6 \text{ sec}^{-1}$. Thus, the microparameters, defined by us, allow to define such characteristics of the substance, as luminescence quantum output, optimal concentrations of the active impurities and e.t.c.

2. The comparison of the generation parameters $\text{La}_2\text{O}_2\text{S-Nd}^{3+}$ and $\text{Y}_{2,97}\text{Nd}_{0,3}\text{Al}_5\text{O}_{12}$

The wave lengths of λ_p pumping, corresponding to the transfer maximums $^4I_{9/2} \rightarrow ^4F_{9/2}$ of Nd^{3+} ions, are equal to 820 nm and 808 nm for the crystals $\text{La}_2\text{O}_2\text{S-1\%Nd}^{3+}$ and $\text{Y}_{2,97}\text{Nd}_{0,3}\text{Al}_5\text{O}_{12}$, correspondingly. The crystal length ℓ was considered as optimatod one $\ell \sim \frac{1}{\alpha_p}$, where α_p is

absorption coefficient on the wave length of pumping. The life times τ of upper laser layer $^4F_{3/2}$ are equal to 100 mcsec and 230 mcsec, the value of resonance loss F_R is equal to 0,16% and 0,2%, the cross-section of the generation transfer (σ) is equal to $2,1 \cdot 10^{-18} \text{ cm}^2$ and $46 \cdot 10^{-20} \text{ cm}^2$, particle part (F)

on the Stark sublevel of upper laser level is equal to 0,52 and 0,4 for the crystals $\text{La}_2\text{O}_2\text{S-1\%Nd}^{3+}$ and $\text{Y}_{2,97}\text{Nd}_{0,3}\text{Al}_5\text{O}_{12}$, correspondingly.

Applying the expression

$$P_{\text{nopoz}} = \frac{hc(\Gamma_0 + \Gamma_R)}{2\lambda_p [1 - \exp(-\alpha_p \ell)] \cdot F \cdot \tau \cdot \sigma} \quad (7)$$

for the calculation of the generation threshold at the longitudinal excitation, the plots of dependencies P_{thres} on nonresonance loss Γ_0 for crystals $\text{La}_2\text{O}_2\text{S-1\%Nd}^{3+}$ and $\text{Y}_{2,97}\text{Nd}_{0,3}\text{Al}_5\text{O}_{12}$ have been constructed by us. From the fig.2 it is well seen, that power of generation threshold of $\text{Y}_{2,97}\text{Nd}_{0,3}\text{Al}_5\text{O}_{12}$ is higher, than $\text{La}_2\text{O}_2\text{S-1\%Nd}^{3+}$.

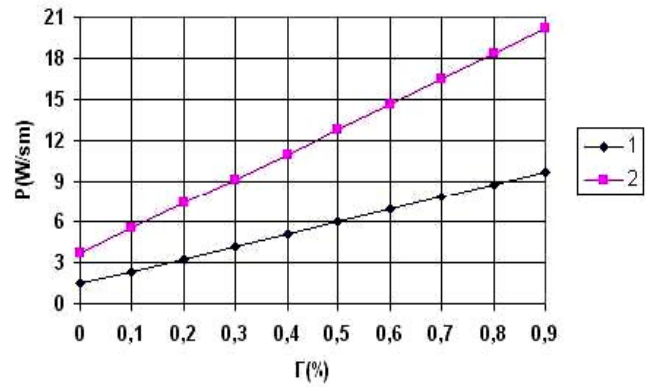


Fig.2. The dependence of the density of pumping threshold power on the nonresonance losses at the longitudinal pumping: 1- $\text{La}_2\text{O}_2\text{S-1\%Nd}^{3+}$
2 - $\text{Y}_{2,97}\text{Nd}_{0,3}\text{Al}_5\text{O}_{12}$

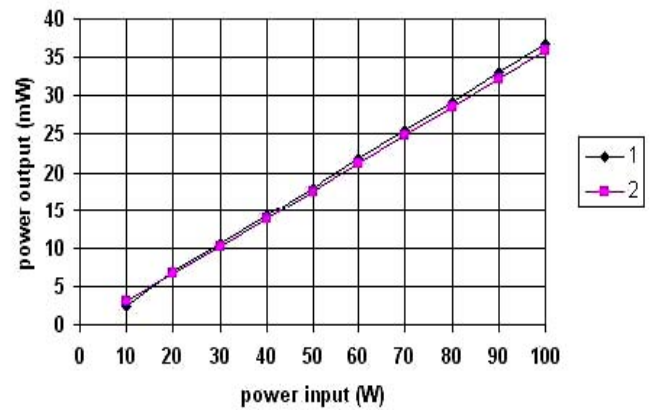


Fig.3. The dependence of output power on the input one at the longitudinal pumping in the multimode regime: 1 - $\text{La}_2\text{O}_2\text{S-1\%Nd}^{3+}$
2 - $\text{Y}_{2,97}\text{Nd}_{0,3}\text{Al}_5\text{O}_{12}$

The laser output power is defined by the following expression

$$P_{output} = f\left(\frac{\nu_L}{\nu_P}\right) \left(P_{input} - \frac{\Gamma_R}{\Gamma} P_{thres}\right) \left(1 - \frac{1}{\sqrt{\frac{P_{input} - \frac{\Gamma_R}{\Gamma} P_{thres}}{\left(1 - \frac{\Gamma_R}{\Gamma}\right) P_{thres}}}}\right)^2 \quad (8)$$

The ratio $\left(\frac{\nu_L}{\nu_P}\right)$, (where ν_L, ν_P are frequencies of generation and pumping) is equal to 0,763 for the crystals $\text{La}_2\text{O}_2\text{S}-1\%\text{Nd}^{3+}$ and $\text{Y}_{2,97}\text{Nd}_{0,3}\text{Al}_5\text{O}_{12}$. The values of nonresonance losses were accepted as 0,15%.

The calculated values of P_{thres} were equal to 0,079 mW and 0,8 mW for the crystals $\text{La}_2\text{O}_2\text{S}-1\%\text{Nd}^{3+}$ and $\text{Y}_{2,97}\text{Nd}_{0,3}\text{Al}_5\text{O}_{12}$ at the beam diameter $D=60\text{mcm}$ and $\Gamma_0=0,15\%$. The plots, describing the dependences of P_{output} on

the P_{input} are given on the fig.3. It is seen, that both plots are almost coincide. This is connected with the fact, that at $P_{input} > \frac{\Gamma_R}{\Gamma} P_{thres}$ in formula (8) the P_{input} gives the main deposit.

Thus, we conclude, that it is possible to create miniature lasers with the record characteristics on the crystal base $\text{La}_2\text{O}_2\text{S}-1\%\text{Nd}^{3+}$.

- | | |
|--|--|
| [1] R.V. Alves, R.A. Buchanan, K.A. Wickersheim and E.A.C.Yates. J.Appl. Phys 42, 3043 (1971). | [4] L.D. Zusman. JETF 73.662. (1977). |
| [2] Yu.K. Voronko, T.G. Mamedov, V.V. Osiko, A.M. Prokhorov, V.P. Sakun, I.A. Sherbakov. JETF 71.478 (1976). | [5] A.G.Avanesov, B.I.Denker, V.V.Osiko, V.G.Ostroumov, V.P. Sakun, V.A. Smirnov, I.A. Sherbakov. Kv. elektronika 9. 681 (1982). |
| [3] W.H. Zachariasen. Acta. Cryst 2.57 (1949). | [6] A.V. Krutikov, V.A. Smirnov, I.A. Sherbakov. Preprint FIAN №72, 1983. |

H.İ. Abutalıbov, A.Ə. Məmmədov

NEODİMLƏ AKTİVLƏŞDİRİLMİŞ LANTAN OKSİSULFİDİ - MİNİATYÜR LAZERLƏR ÜÇÜN PERSPEKTİVLİ KRİSTALLARDIR

$\text{La}_2\text{O}_2\text{S}$ kristallarında Nd^{3+} ionlarının $^4\text{F}_{3/2}$ səviyyəsinin kinetikasi tədqiq olunub. Generasiyanın baş vermə həddinin qeyri-rezonans itkilərdən və çox modalı rejimdə çıxış gücün giriş gücündən asılılığı hesablanıb.

Г.И. Абуталыбов, А.А. Мамедов

ОКСИСУЛЬФИДЫ ЛАНТАНА, АКТИВИРОВАННЫЕ ИОНАМИ НЕОДИМА - ПЕРСПЕКТИВНЫЕ КРИСТАЛЛЫ ДЛЯ МИНИАТЮРНЫХ ЛАЗЕРОВ

Исследована кинетика распада $^4\text{F}_{3/2}$ уровня Nd^{3+} в кристаллах $\text{La}_2\text{O}_2\text{S}$. Вычислена зависимость порога генерации от нерезонансных потерь, а также выходная мощность от входной при многомодовых режимах.

Received: 11.11.2004

EFFECT OF SPIN-VIBRATIONAL 1^+ STATES ON GROUND STATE CORRELATIONS OF NUCLEI

A.A. KULİEV^{1,2,3}, M. GÜNER⁴, E. GULİYEV^{2,3}, M. TÜTÜNÇÜ²

¹*Institut für Theoretische Physik der Universität Tübingen, Auf der Morgenstelle 14
D-72076 Tübingen, Germany*

²*Department of Physics, Faculty of Science and Art, Sakarya University, Sakarya, Turkey*

³*Institute of Physics, Azerbaijan National Academy of Science, Baku, Azerbaijan*

⁴*Department of Mathematics, Faculty of Science and Art, Sakarya University,
Sakarya, Turkey*

We have considered a number of features of the ground state correlations (GSC) in deformed nuclei connected with the effective spin-spin forces in the framework FR-QRPA, R-QRPA and QRPA. The result of calculations has indicated a significant role of the high energy 1^+ states and the importance to use a complete set of the RPA solutions for reliable predictions of the theory in GSC. It is concluded that collective excitations, which form M1 resonance give dominant contribution to GSC. The total number of quasiparticles in the ground state N_{qp} and the nuclear transition matrix elements are significantly affected due to the collective states of the M1 resonance energy region. The results are practically insensitive to the QRPA, R-QRPA and FR-QRPA methods with isovector spin-spin interactions in particle-hole (p-h) channel.

1. Introduction

Quasiparticle Random Phase Approximation (QRPA) is based on the quasiboson approach (QBA), which treats the two quasi-particle states as bosons [1]. An improvement of this approach is the Renormalized QRPA (R-QRPA), which takes into account the Pauli principle for the fermion pairs in the correlated ground state [2-4]. A further development of this approach for realization of a self-consistent condition between ground state and RPA matrix elements was presented in [5-7]. Recently the pn R-QRPA for charge-exchange processes was formulated in [8]. An extended version of this approach with proton-neutron pairing (Full Renormalized QRPA) was proposed and applied to the double beta decay [9]. The R-QRPA has been intensively used in previous studies of the double beta decay [10,11].

But R-QRPA violates the Ikeda sum rule, which is fulfilled within QRPA and must be fulfilled for an exact solution [11-13]. In the last decade different ways were used to extend R-QRPA in order to cure this drawback of R-QRPA [12-14]. But the drawback has not been cured neither in the self-consistent QRPA [14] nor in the second order QRPA [12] and self-iterative BCS+RQRPA [13]. The main disadvantage of the R-QRPA is inconsistency between the model Hamiltonians and one phonon wave functions. Modification of the phonon operators by including scattering terms is unavoidable if one wants to restore the ISR [15] or EWSR within R-QRPA [16].

Recently the Fully Renormalized QRPA (FR-RQRPA) was formulated in [17]. In this approach the phonon operator is constructed from a given quasiparticle structure of the effective interactions by means of invariance principles. By requiring that the phonon operators must have a good angular momentum J and commute with the total particle number operator a consistent description with given Hamiltonian is achieved. Because of this full consistency between the phonon structure and Hamiltonian the FR-RQRPA fulfills ISR exactly.

The calculation beyond QRPA requires the solution of the complex nonlinear system of equations of motion. It follows to take all RPA solutions for all the R-QRPA calculations

into account. Indeed in this approach the collective states are important in ground state correlations. In numerical calculations we must, in principle, take into account all the eigenstates of QRPA Hamiltonian in the GSC calculations. Many R-QRPA calculations [2,13-18] take into account only the first or some lowest QRPA solutions neglecting high energy QRPA solutions in the ground state expectation value of operator equations. Excepting [13], as a rule, the description of Double Beta Decay (DBD) [10,11] in all R-QRPA calculations have been performed without taking into account the effects of high energy state, since there are no physical grounds whatever for neglecting the effect of high energy solutions. It is impossible to guarantee the smallness of the effects associated with these approximations. Therefore, the results of numerical calculations are not fully correct because of the collective high energy admixtures. One can expect large effects of the collective high energy states of resonance energy region on the average number of quasiparticles in ground state ($N_q = 2 \sum_{i,q'} Y_{qq'}^i$) [7] if one

keep in mind that for collective states backward amplitudes are large Y_{ssr}^i than non collective states [1,19]. Therefore their influence on the results and contribution to GSC should be large.

Here we want to study the influence of high energy spin-vibrational 1^+ states and the FR-RQRPA approach in comparison with QRPA and R-QRPA on the ground state correlations in deformed nuclei. Up to now, the important aspect of high energy RPA solutions on GSC has not been examined. In connection with this, it is interesting to establish how important the role of high energy RPA solutions for the ground state correlations is and to estimate their contributions to the average quasiparticle number N_{qp} .

In order to demonstrate the order of magnitude of the effects of high energy solutions in the GSC we have calculated N_{qp} and B(M1) value of the 1^+ excitations generated by the isovector spin-spin forces for the deformed ^{154}Sm , ^{156}Gd , ^{168}Er and ^{178}Hf of the rare-earth nuclei.

2. Theory

Let us consider a system of nucleons in an axially symmetric mean field interacting via pairing forces. In this case the corresponding single-particle Hamiltonian of the system is given as

$$H_{sqp} = \sum_s E_s(\tau)(\alpha_s^+(\tau)\alpha_s(\tau) + \alpha_{\bar{s}}^+(\tau)\alpha_{\bar{s}}(\tau)) \quad (1)$$

here E_s are the single-quasiparticle energies of the nucleons and isospin index τ takes the value n(p) for neutrons (protons), $\alpha_s^+(\alpha_s)$ are the quasiparticle creation (annihilation) operator and single particle states $|\tilde{s}\rangle$ are the time-reversed of $|s\rangle$. Now supposing the isovector spin-spin interactions

generate the 1^+ states in deformed nuclei, then the model Hamiltonian of system can be written as [20]

$$H = H_{sqp} + V_{\sigma\tau} \quad (2)$$

where

$$V_{\sigma\tau} = \frac{1}{2}\chi_{\sigma\tau} \sum_{i,j} \sigma_i \sigma_j \tau_i^Z \tau_j^Z. \quad (3)$$

Here $V_{\sigma\tau}$ is charge-exchange spin-spin interaction, $\chi_{\sigma\tau}$ denote spin-isospin coupling parameter. σ and τ are Pauli matrices representing the spin and isospin, respectively. In FR-RQRPA the modified phonon operator of the collective excitations in even-even deformed nuclei can be written as

$$|\Psi_i\rangle = Q_i^+ |\Psi_0\rangle = \frac{1}{\sqrt{2}} \sum_{sst,\tau} [X_{sst}^i(\tau) \tilde{C}_{sst}^+(\tau) - Y_{sst}^i(\tau) \tilde{C}_{sst}(\tau)] |\Psi_0\rangle \quad (4)$$

$$\sum_{sst,\tau} [X_{sst}^i(\tau)^2 - Y_{sst}^i(\tau)^2] = 1 \quad (5)$$

Hereafter we use all definition of ref. [21], now, we present the expressions of the Hamiltonian (1) and σ_{+1} in FR-QRPA representation

$$V_{\sigma\tau} = \frac{1}{2}\chi_{\sigma\tau} \sum_{\mu} \sigma_{\mu}^+ \sigma_{\mu} \quad (6)$$

where

$$\sigma_{+1} = \sqrt{2} \sum_{sst} \sqrt{G_{sst}} \sigma_{sst} (u_s v_{s\tau} \tilde{C}_{sst}^+ - u_{s\tau} v_s \tilde{C}_{sst}) \quad (7)$$

Here, G_{sst} takes into account the blocking effect due to the Pauli principle (scattering terms, exact commutator etc.), $\sigma_{\mu}^+ = (-1)^{\mu} \sigma_{-\mu}$ and $\sigma_{sst} = \langle s | \sigma_{+1} | s\tau \rangle$. Employing the conventional procedure [19,20] of QRPA with the equation of motion:

$$[H_{sqp} + V_{\sigma\tau}, Q_i^+] = \omega_i Q_i^+ \quad (8)$$

one can obtain the equation for the energy ω_i of one-phonon 1^+ excitations in the form (see, e.g., refs. [21])

$$D_{\sigma} = 1 + \chi_{\sigma\tau} F_{\sigma} = 0 \quad (9)$$

where

$$F_{\sigma} = 2 \sum_{sst} \frac{G_{sst} E_{sst} L_{sst}^2 \sigma_{sst}^2}{E_{sst}^* E_{sst} - \omega_i^2} \quad (10)$$

Here, the function F_{σ} is defined as usually for the spin-vibration, $E_{ss'} = E_s + E_{s'}$ are two-quasiparticle energies, $L_{\mu} = u_s v_{s'} - u_{s'} v_s$, u_s and v_s the Bogolyubov transformation parameters and

$$E_{sst}^* = E_{sst} + \tilde{E}_{sst} \quad (11)$$

$$\tilde{E}_{sst} = (E_s - E_{s'}) \frac{u_s v_s u_{s'} v_{s'}}{G_{sst} (v_{s'}^2 - v_s^2)^2} (N_s - N_{s'}) \quad (12)$$

and

$$G_{sst} = 1 - \frac{1}{2} \frac{u_s^2 - v_s^2}{v_{s'}^2 - v_s^2} N_s + \frac{1}{2} \frac{u_{s'}^2 - v_{s'}^2}{v_{s'}^2 - v_s^2} N_{s'} \quad (13)$$

Here N_q is average quasiparticle occupation number in the ground state modified by interactions between nucleons. The calculation of the N_{qp} can be performed with help of the fermion-boson mapping [7]. In the phonon representation one gets $N_q = 2 \sum_{i,q'} Y_{qq'}^i$. We show that in FR-QRPA the two-

quasiparticle energies E_{sst}^* are naturally modified by the given interactions between nucleons. As a result the interactions between quasiparticles and the transition matrix elements are changed since it involves particles with modified properties. \tilde{E}_{sst} is responsible for the modification of the quasiparticle energies. Note that in the R-QRPA and QRPA the expression (12) is zero. The two-quasiparticle amplitudes of the one phonon wave function (4) can be written as

$$X_{\mu}^n = -\sqrt{\frac{G_{\mu}}{4\omega_i Z_{\sigma}}} \frac{\sigma_{\mu} L_{\mu}(E_{\mu} + \omega_i)}{E_{\mu}^* E_{\mu} - \omega_i^2}, \quad X_{\mu}^p = \sqrt{\frac{G_{\mu}}{4\omega_i Z_{\sigma}}} \frac{\sigma_{\mu} L_{\mu}(E_{\mu} + \omega_i)}{E_{\mu}^* E_{\mu} - \omega_i^2} \quad (14)$$

$$Y_{\mu}^n = -\sqrt{\frac{G_{\mu}}{4\omega_i Z_{\sigma}}} \frac{\sigma_{\mu} L_{\mu}(E_{\mu} - \omega_i)}{E_{\mu}^* E_{\mu} - \omega_i^2}, \quad Y_{\mu}^p = \sqrt{\frac{G_{\mu}}{4\omega_i Z_{\sigma}}} \frac{\sigma_{\mu} L_{\mu}(E_{\mu} - \omega_i)}{E_{\mu}^* E_{\mu} - \omega_i^2} \quad (15)$$

where

$$Z_{\sigma} = 2 \sum_{ss'} \frac{G_{ss'} E_{ss'} L_{ss'}^2 \sigma_{ss'}^2}{(E_{ss'}^* E_{ss'} - \omega_i^2)^2}, \quad (16)$$

3. Results and Discussion

Numerical calculations have been carried out for the deformed nuclei in the rare-earth region $150 < A < 172$. The experimental values of deformation parameters of these nuclei were taken from [22]. The single particle energies are obtained from the Warsaw deformed Woods-Saxon potential [23]. The basis contains all discrete and quasi-discrete levels in the energy region up to 3 MeV. The pairing interaction constants chosen according to Soloviev [1] are based on single particle levels corresponding to the nucleus in question. The isovector spin-spin interaction strength was chosen to be $\chi_{\sigma\sigma} = 40/A$ MeV [20].

As the R-QRPA and FR-QRPA calculations are very time consuming processes in the deformed case, it is interesting to determine which spin matrix elements are important to be taken into account while calculating the RPA solutions. We

calculate the energy weighted and non-energy weighted sum rules of M1 transition matrix elements. The calculation shows that the matrix elements $\langle s | s_{+1} | s' \rangle^2 \leq 10^{-4}$ do contribute only little to the sum rules (the effect does not exceed 2%). We perform all the numerical calculations with this restriction on the matrix elements.

The aim of the present calculations is to demonstrate the role of collective high energy RPA solutions in GSC calculations. This can be obtained by the comparison with the results calculated in different energy regions. The results of calculated N_{qp} values for ^{154}Sm and ^{178}Hf taking into account RPA solutions in different energy region are given in Table I for the various FR-QRPA, R-QRPA and QRPA methods.

Table 1
Comparison of the value of N_{qp} calculated with Hamiltonian (1) using FRQRPA approach, RQRPA and QRPA

^{154}Sm				^{178}Hf		
ω (MeV)	FR-QRPA	R-QRPA	QRPA	FR-QRPA	R-QRPA	QRPA
2-5	0.0100	0.0100	0.0100	0.0097	0.0097	0.0097
5-9	0.0108	0.0108	0.0108	0.0160	0.0160	0.0160
9-13	0.1361	0.1364	0.1364	0.1485	0.1482	0.1489
13-25	0.0077	0.0077	0.0078	0.0048	0.0048	0.0048
2-25	0.1646	0.1649	0.1650	0.1790	0.1787	0.1794

There is a fragmentation of the 1^+ states at low energy. For these 1^+ states the summed N_{qp} is order of 0.07 and contains about 8 % of the total N_{qp} . Contributions of the 1^+ states with large value N_{qp} are obtained in the energy region 9-13 MeV. The absolute value N_{qp} in this region is in the order of 0.15. The relative contribution of the high energy RPA solutions which form M1 resonance gives more than 80% of the total number of quasiparticles in the ground state of the nuclei considered. Thus we see that the models, which

take into account only low-lying states overestimate ground state correlations strongly.

Besides the N_{qp} another important quantity of the 1^+ states is $N_{qp}(\omega)$ distribution over RPA solutions. The distribution of the average number of quasiparticles in the ground state $N_{qp}(\omega)$ for the different RPA solutions ω_i gives important information about the role of the 1^+ states and their relative contributions on ground state correlations. In Fig.1 we show examples of these calculations for the nucleus ^{168}Er .

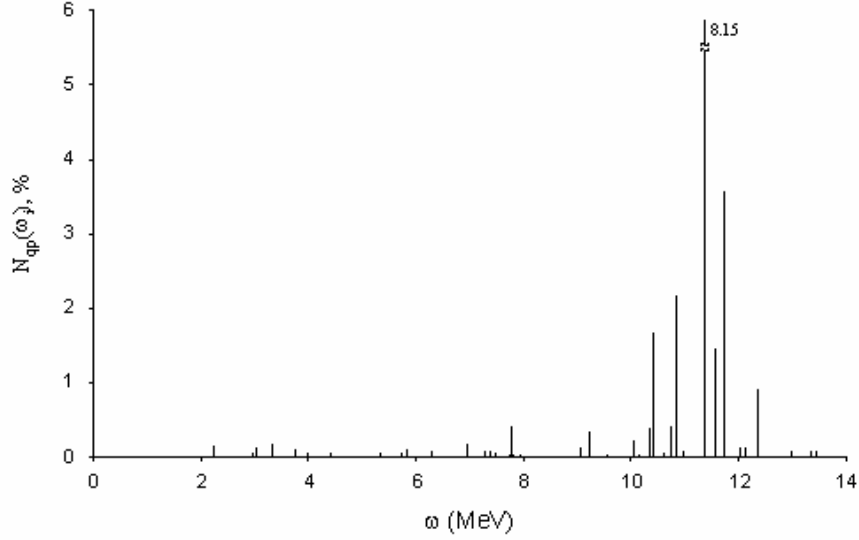


Fig.1. Distribution of the relative values of $N_{qp}(\omega)$ in relation to the total N_{qp} value for the 1^+ states in ^{154}Sm .

As seen from the figure, most contributions come from the high energy collective states which form M1 resonance. We note that the 1^+ states in the M1 resonance region take up to about 80% of the total N_{qp} . Unlike previous calculations [2,8,18] we conclude that the collective states of the

resonance region exhaust the main part of the total N_{qp} and their role is very important for GSC.

The comparison of the calculated value of N_{qp} for ^{154}Sm , ^{156}Gd , ^{168}Er and ^{178}Hf in framework QRPA, R-QRPA and FR-QRPA approaches are given in Fig.2.

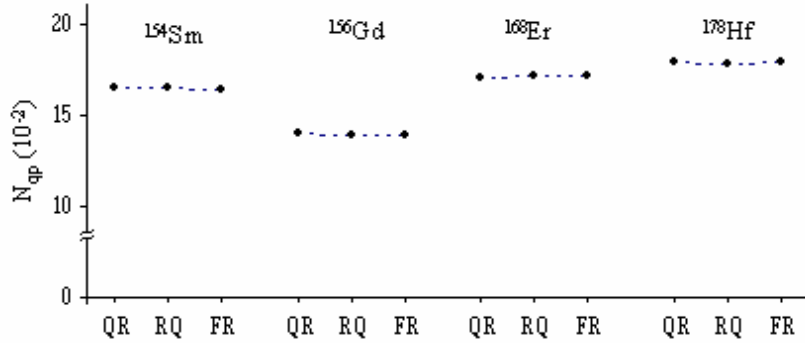


Fig.2. Comparison of the average number of quasiparticles in the ground state N_{qp} due to the vibrational 1^+ states calculated in the QRPA, R-QRPA and the FR-QRPA approaches. The three different approaches QRPA, R-QRPA and FR-QRPA are denoted below the axes as QR, RQ and FR, respectively.

It follows from Fig.2 that the total values of N_{qp} are almost the same in QRPA, R-QRPA and FR-QRPA approach (a difference is about 1-2% of the total N_{qp}). The results that we have obtained indicate a significant role of the high energy 1^+ states and the importance to use a complete set of the RPA solutions for reliable predictions of the theory in ground state correlations calculations. Besides the calculations show that the absolute values of N_{qp} are almost the same in QRPA, R-QRPA and FR-QRPA for the p-h isovector spin-spin interaction.

4. Conclusions and outlook

Thus, we have considered a number of features of the GSC in deformed nuclei connected with the effective spin-spin forces in p-h channel. It is concluded that high energy

collective excitations which form M1 resonance give dominant contribution to GSC. The total N_{qp} and renormalized nuclear transition matrix elements are significantly affected by the collective states of the M1 resonance energy region. The study of ground state correlations seems to give some evidence for the importance of taking into account a full spectrum of RPA solutions for reliable predictions of the theory.

ACKNOWLEDGEMENTS

Prof. A.A. Kuliev thanks the "Deutsche Forschungsgemeinschaft (DFG) under Contracts Fa 67/27-2 " and the Landesforschungsschwerpunkt "Low energy Neutrino Physics" of the Land Baden-Wuerttemberg for support. Dr. E. Guliyev was supported by The Scientific and Technical Research Council of Turkey (TUBITAK).

- [1] *P. Ring and P. Schuck*, "The Nuclear many Body Problem" (Springer-Verlag, Berlin), 1980; V.G. Soloviev "Theory of Complex Nuclei" Pergamon Press, New York, 1976.
- [2] *K. Hara*, Progr. Theor. Phys. 1964, 32, 88.
- [3] *K. Ikeda T. Udagava and H. Yamura*, Progr. Theor. Phys. 1965, 33, 22.
- [4] *D. J. Rowe*, Rev. Mod. Phys. 40 (1968) 153; Phys. Rev 1968, 175, 1283.
- [5] *P. Schuck and S. Ethofer*, Nucl. Phys. 1973, A 212, 269.
- [6] *J. Duckelsky and P. Schuck*, Nucl. Phys. 1990, A 512, 466; Mod. Phys, 1991, Lett. A 6, 2429. ; *D. Janse and P. Schuck*, Z. Phys. 1991, A 339, 43.
- [7] *F. Catara N. Dinh Dang and M. Sambataro*, Nucl. Phys. 1994, A 579, 1.
- [8] *J. Toivanen and J. Suhonen*, Ph. Rev. 1995, C75, 410.
- [9] *J. Schwieger, F. Simkovic and Amand Faessler*, Nucl. Phys. 1996, A 600, 179.
- [10] *A. Faessler S. Kovalenko, F. Simkovic, and J. Schwieger*, Phys. Rev. Lett. 1998, 78, 183, *Faessler S. Kovalenko, and F. Simkovic*, Phys. Rev. 1998, D 58, 115004;
- [11] *A.A. Raduta, F. Simkovic and A. Faessler*, J. Phys. 2000, G26, 793; *F. Simkovic, M. Nowak, W. A. Kaminski, A. A. Raduta and A. Faessler*, Phys. 2001, Rev C 64, 035501.
- [12] *J. Toivanen and J. Suhonen*, Phys. Rev. 1997, C 55, 2314.
- [13] *S. Stocia and H. V. Klapdor-Kleingrothaus*, Euro. Phys. J. 2000, A9, 345; Phys. Rev. 2001, C 63, 064304 (; Nucl. Phys, A 694, 269 (2001); *J. G. Hirsch, P. O. Hers and I. Civitarese*, Phys. Rev. 1996, C 54, 1976; Phys. Lett. 1997, B 390, 36 ; *I. Civitarese, P. O. Hers and J. G. Hirsch*, 1997, ibid 412, 1.
- [14] *A. Bobyk, W. A. Kaminski and P. Zareba*, Nucl. Phys. 2000, 669, 221; *P. Zareba*, Ph.Dthesis, 2000, unpublished.
- [15] *D.S. Delion, J. Duckelsky and P. Schuck*, Phys. Rev. C 1997, 55, 234010.
- [16] *A.A. Raduta, C. M. Raduta, Amand Faessler, W. A. Kaminski*, Nucl. Phys. 1998, A 634, 497.
- [17] *N. Dinh Dong and A. Arima*, Phys. 2001, Rev. C 621, 024303.
- [18] *Vadim Rodin and Amand Faessler*, Phys. 2002, Rev. C 66, 051303.
- [19] *D. Karadjov, V. V. Voronov and F. Catara*, Phys. 1993 Lett. B 306, 166.
- [20] *D.J. Thouless* Nucl. Phys. 1961, 22, 78.
- [21] *A.A. Kuliev, R. Akkaya, M. Ilhan, E. Guliev, C. Salomov and S. Selvi*, Int. Journal of Modern Physics. 2000, E, 9 249.
- [22] *A.A. Kuliev, Amand Faessler, M. Güner, Vadim Rodin*, (submitted to the Nucl. Phys G, 2004)
- [23] *S. Raman, C. W. Nestor, Jr., P. Tikkanen*, Atomic Data and Nucl. Data. Tables 2001, 78, 1.
- [24] *J. Dudek, W. Nazarewicz and A. Faessler*, Nucl. Phys. 1984, A412, 61.

Ə.Ə. Quliyev, M. Güner, Ə. Quliyev, M. Tütüncü

SPİN-VİBRASIYA 1^+ SƏVIYYƏLƏRİNİN NÜVƏLƏRİN ƏSAS HALINDAKI KORELASİONLARINA TƏSİRİ

Məqalədə deformasiyalı nüvələrin əsas hal korelasionlarının effektiv spin-spin qüvvətləri ilə əlaqədar olan bəzi xassələri FR-QRPA, R-QRPA və QRPA metodları çərçivəsində tədqiq edilmişdir. Hesablamalar əsas hal korelasionlarında etibarlı nəticələr əldə edilməsi üçün yüksək enerjili kollektiv 1^+ səviyyələrin və RPA metodunun bütün köklərinin (tam set) nəzərə alınmasının mühüm rol oynadığını göstərmişdir.

M1 rezonansı meydana gətirən kollektiv səviyyələrin əsas hal korelasionlarına əlavəsinin qalan səviyyələrdən daha böyük olduğu göstərilmişdir. Bu kollektiv səviyyələr, əsas haldakı kvazizərrəciklərin tam sayına və nüvə keçidlərinin matris elementlərinə daha çox təsir etməkdədir. Nəzəri hesablamalar spin-spin qüvvətlərini zərrəcik-deşik kanalında nəzərə alan QRPA, R-QRPA və FR-QRPA metodlarında əldə edilən nəticələrin bir-birinə yaxın olduğunu göstərmişdir.

A.A. Кулиев, М. Гунер, А. Кулиев, М. Тютюнчу

ЭФФЕКТ СПИН-ВИБРАЦИОННЫХ 1^+ УРОВНЕЙ НА КОРРЕЛЯЦИИ В ОСНОВНОМ СОСТОЯНИИ В ЯДРАХ

В статье рассмотрено несколько свойств корреляции в основных состояниях деформированных ядер, связанных с эффективными силами в рамках FR-QRPA, R-QRPA и QRPA. Результаты вычислений указывают на значительную роль высоких энергетических 1^+ состояний, важность использования полного набора RPA для надежного предсказания теории корреляции в основном состоянии. Показано, что коллективные состояния, формирующие M1 резонанс дают доминирующий вклад корреляции в основное состояние. Выше упомянутые состояния имеют значительное влияние на полное число квазичастиц в основном состоянии и матричные элементы ядерных переходов. Полученные результаты практически не чувствительны к использованию QRPA, R-QRPA и FR-QRPA методов, которые используют изовекторное спин-спиновое взаимодействие в канале частица-дырка.

Received: 09.11.2004

THE PERSPECTIVITY OF THE SEMICONDUCTOR GLASSES, AS THE ACTIVE MEDIUM FOR THE MINIATURE LASER

G.I. ABUTALIBOV, A.A. MAMEDOV

*Institute of Physics, Azerbaijan National Academy of Sciences,
Baku AZ-1143, H. Javid av.,33.*

The threshold of generation at the longitudinal and transversal methods of pumping and output power at the multimode and one mode regimes for the miniature lasers have been calculated. The probability of miniature laser creation on the base of the sulfide, oxy-sulfide and sulfide- oxygen glasses, activated by Nd^{3+} at the longitudinal and transversal excitation methods, has been created.

The high-qualitative optical fibers, used in the communication systems, have the minimal losses in the wave length region 1mcm-1.3mcm. It is followed, that miniature neodymium lasers, generating the radiations on the wave lengths $\sim 1.06\text{mcm}$, can be successfully applied in these systems, as the light source. For the clearing of the perspectivity of sulfide, oxy-sulfide and sulfide-oxygen glasses, as the miniature laser medium, it is need to compare the dependence of threshold on the nonresonance losses at the different pumping configurations and also the dependence of the output power on the input one for these glasses with the corresponding dependences for the glasses by the type ED-2 [1].

As it is known, the laser generation condition has the form:

$$r_1 r_2 e^{2l(\gamma_1 - \delta)} = 1, \quad (1)$$

where r_1 and r_2 are mirror reflection coefficients, γ_1 is the medium gain exponent, l is the medium length, δ are losses in the medium. Taking into consideration, that $\gamma_1 = \sigma \Delta N$, where ΔN is the population inversion between Stark sublevels of the generation transition, σ is the cross-section of this transition. Taking into consideration (1), we have:

$$\Delta N = \frac{I}{2\sigma} \left(2\delta + \frac{I}{l} \ln \frac{I}{r_1 r_2} \right). \quad (2)$$

If photon number, falling on the unit area of laser medium in the unit time is I_0 , then the photon number, absorbed on the unit area in the unit time will be $I_0(1 - e^{-\alpha_p l})$. Here α_p is the medium absorption coefficient.

In the continuous regime of laser work:

$$I_0(1 - e^{-\alpha_p l}) = \frac{l \Delta N}{F_\alpha \tau_f}, \quad (3)$$

where τ_f is the life time of the upper laser level, F_α is the particle part in the Stark sublevel of the upper laser level, from which the laser transition takes place:

$$F_\alpha = \frac{e^{-\frac{\Delta E}{kT}}}{1 + e^{-\frac{\Delta E}{kT}}} \quad \text{or} \quad \frac{I}{1 + e^{-\frac{\Delta E}{kT}}},$$

where ΔE is the energy gap between Stark sublevels of the upper laser level ${}^4F_{3/2}$. The first expression for F_α corresponds to the case, when laser transition takes place from the upper sublevel ${}^4F_{3/2}$ and the second expression corresponds to the case, when transition takes place from the lower sublevel.

From the formula (3), we define the I_0

$$I_0 = \frac{l \Delta N}{\tau_f (1 - e^{-\alpha_p l}) F_\alpha} \quad (4)$$

Substituting the formula (2) in the formula (4), we obtain:

$$I_0 = \frac{(2l\delta + \ln \frac{I}{r_1 r_2})}{2\sigma \tau_f (1 - e^{-\alpha_p l}) F_\alpha} \quad (5)$$

Let's write $2l\delta + \ln \frac{I}{r_1 r_2}$ in the form:

$$2l\delta + \ln \frac{I}{r_1 r_2} = \Gamma_0 + \Gamma_R,$$

where Γ_0 is the nonresonance losses, but Γ_R is the resonance ones $\Gamma_R = 2l\sigma N \beta / Z$, where N is the work ion density,

$\beta = e^{-\frac{\Delta E}{kT} \frac{{}^4I_{11/2} \cdot {}^4I_{9/2}}{Z}}$, Z is the ratio of summary population of Stark sublevels ${}^4I_{9/2}$ and sublevels ${}^4I_{11/2}$ till the lower laser sublevel to the population of the lowest Stark sublevel ${}^4I_{9/2}$. Expressing the formula (5) in the energies, we define the power density at the threshold:

$$P_{\text{threshold}} = h\nu_p I_0 = \frac{hc(\Gamma_0 + \Gamma_R)}{2\lambda_p \sigma \tau_f F_\alpha (1 - e^{-\alpha_p l})} \quad (6)$$

In the case of transversal pumping we have:

$$P_{\text{threshold}} = \frac{hc(\Gamma_0 + \Gamma_R)}{2\lambda_p \sigma \tau_f F_\alpha \alpha_p l}. \quad (7)$$

Let's consider the 4-level energy laser circuit. The time change of the stored atom energy N on the upper laser level

and the energy E_f of coherent electromagnetic field inside the resonator is described by the equations:

$$\frac{dN}{dt} = R - A_n - A(N-n) - \beta E_F(N-n) \quad , \quad (8)$$

$$\frac{dE_F}{dt} = \beta E_F(N-n) - E_F(T + \varepsilon)$$

where t is time, N is the atom quantity in the upper laser level, but n is the atom quantity in the lower laser level. The both values N and n are multiplied on the energy of laser transfer. R is the atom quantity, pumped in the upper laser level in the unit time. The parameter of the stimulated radiation $\beta = \frac{C\sigma}{SLh\nu_L}$, where $h\nu_L$ is the laser transition

energy, S is the laser medium cross-section, L is the length of the one transfer in the resonator, T is the omission of the output mirror, divided on the $\frac{2L}{C}$, ε are losses in two

transfers, in the resonator, divided on the $\frac{2L}{C}$, A is equal to the inverse life time of the upper laser level. The ε parameter is the damping coefficient of the resonator, excepting the losses, caused by the output mirror and any resonance losses. The Boltzman population of lower laser level, namely, the resonance losses (Γ_R) have been taken into consideration by us. In the formula (8) the derivations on t are equal to zero in the continuous laser regime:

$$0 = R - A_n - A(N-n) - \beta E_F(N-n) \quad (9)$$

$$0 = \beta E_F(N-n) - E_F(T + \varepsilon)$$

The output power is defined as TE_f . Calculating (9) in respect of E_F , we obtain:

$$P = T \left(\frac{R - A_n}{T + \varepsilon} - \frac{A}{\beta} \right). \quad (10)$$

From the extremum condition $\frac{dP}{dT} = 0$, we find the maximum output power in the continuous regime:

$$T_0 = \varepsilon(\sqrt{\phi} - 1) \quad , \quad (11)$$

$$P_0 = (R - An) \left(1 - \frac{1}{\sqrt{\phi}} \right)^2$$

where $\phi = \frac{\beta(R - An)}{A\varepsilon}$. Thus, ϕ parameter is defined as the

ratio of the effective pumping to the minimal effective pumping, needed for the achieving of threshold (at $T=0$). The

R parameter is equal to $P_{input} \left(\frac{\nu_L}{\nu_p} \right)$, where P_{input} is pumping

power, of absorbed laser medium ν_p is pumping center frequency. Taking into consideration, that resonance losses

$$\Gamma_R = 2l\sigma \frac{n}{h\nu_L S l} = \frac{2\sigma n}{h\nu_L S} \quad , \quad \text{and} \quad \text{total loss}$$

$\Gamma = \Gamma_0 + \Gamma_R = \frac{c}{2L}\varepsilon + \Gamma_R$, instead of the formulae (11), we obtain:

$$P_{output} = \left(\frac{\nu_L}{\nu_p} \right) \left(P_{input} - \frac{\Gamma_R}{\Gamma} P_{threshold}^I \right) \left(1 - \frac{1}{\sqrt{\phi}} \right)^2, \quad (12)$$

$$\phi = \frac{P_{input} - \frac{\Gamma_R}{\Gamma} P_{threshold}^I}{\left(1 - \frac{\Gamma_R}{\Gamma} \right) P_{threshold}^I} \quad \text{and} \quad P_{threshold}^I = P_{threshold} \cdot S \quad \text{is}$$

absorbed power at the threshold.

Multiplying the right part of the formula (12) on the f , we obtain the output in the multimode regime at the longitudinal pumping

$$P_{output} = f \left(\frac{\nu_L}{\nu_p} \right) \left(P_{input} - \frac{\Gamma_R}{\Gamma} P_{threshold}^I \right) \left(1 - \frac{1}{\sqrt{\phi}} \right)^2. \quad (13)$$

The f is defined as the ratio of the volume, engaged by the in the active medium to the pumped volume.

Instead of the step function, in limits of which, the transversal distribution of the intensity stays constant, we take Gaussian distribution function, which is character for TEM_{100} mode:

$$E_F = E_{F_c} e^{-\frac{2\rho^2}{\omega^2}}, \quad (14)$$

where E_{F_c} is light energy on the surface unit along resonator axis, ρ is the distance from the resonator axis, ω is gudgeon radius.

The density of the light energy and the density of the inversion energy are described by the equations:

$$\int \frac{dE_F}{dt} dS = \int [\beta E_F(N-n) - E_F(T + \varepsilon)] dS \quad (15)$$

$$\frac{dN}{dt} = R - A_n - A(N-n) - \beta E_F(N-n). \quad (16)$$

Here, it is proposed, that values E_F , N and R are beforehand integrated on the length of laser medium. Here N and n are atom quantities in the surface unit in the upper and lower levels correspondingly, and parameter of the stimulated radiation β is equal to $\frac{c\sigma}{Lh\nu_L}$. R is the atom quantity, pumped in the upper laser bed, on the surface unit in the time unit and is equal to $P_{input} \left(\frac{\nu_L}{\nu_p} \right) / S$. The dS is the surface element in the plane, which is perpendicular to resonator axis. In the stationary case instead of the equations (15) and (16), we obtain:

$$\int E_F dS = \frac{\beta}{T + \varepsilon} \int E_F (N - n) dS \quad (17)$$

$$R - A_n = A(N - n) + \beta E_F (N - n) \quad (18)$$

Substituting the formula (18) in the formula (17), we obtain:

$$\int E_F dS = \frac{\beta(R - An)}{T + \varepsilon} \int \frac{E_F dS}{A + \beta E_F} \quad (19)$$

Substituting the expression for E_F of formula (14) in the both parts of the equation (19), after integration, we obtain:

$$E_{Fc} = \frac{(R - An)}{T + \varepsilon} L n \left(1 + \frac{\beta E_{Fc}}{A} \right) \quad (20)$$

The laser output is defined by the following expression:

$$P_{output} = T \int E_F dS \quad (21)$$

Substituting the formula (14), we obtain:

$$P_{output} = \frac{\pi \omega^2}{2} T E_{Fc} \quad (22)$$

Substituting the E_{Fc} value, defined in the formulae (22), in the formula (20), we obtain:

$$P_{output} = \frac{\pi \omega^2 (R - An) T}{2(T + \varepsilon)} L n \left(1 + \frac{2\beta P_{output}}{\pi \omega^2 A T} \right) \quad (23)$$

At the optimal omission of mirror and the maximum output the $\frac{dP_{output}}{d\left(\frac{1}{T}\right)} = 0$ takes place. Differentiating the both

parts of the formula (23), relatively $\frac{1}{T}$ and taking into

consideration $\frac{dP_{output}}{d\left(\frac{1}{T}\right)} = 0$, we obtain:

$$P_{output}^0 = \frac{T^0(\phi - 1)}{\varepsilon \phi} (R - An) \frac{\pi \omega^2}{2}, \quad (24)$$

where $\phi = \frac{(R - An)\beta}{A}$ and upper indexes on P_{output}^0 and T^0 correspond to maximum and optimal values correspondingly. Substituting the P_{output}^0 (24) in the right part of the formula (23), we obtain:

$$P_{output} = \frac{\pi \omega^2 (R - An) T^0}{2(T^0 + \varepsilon)} L n \phi \quad (25)$$

Using the expression T^0 , found in the formula (24), we obtain:

$$P_{output} = \frac{\pi \omega^2}{2} (R - An) \left(L n \phi - \frac{\phi - 1}{\phi} \right), \quad (26)$$

Using for expressions for R , threshold and loss, we obtain:

$$P_{output}^0 = \frac{\omega^2}{2\omega_0^2} \left(P_{input} - \frac{\Gamma_R}{\Gamma} P_{threshold}^1 \right) \left(L n \phi - \frac{\phi - 1}{\phi} \right), \quad (27)$$

where ω_0 is radius of the active medium.

Using the expressions of the formulae (6), (7), (13) and the spectroscopy data (table 1), the comparisons of the generated parameters of glasses in the corresponding parameters of ED-2, in which the generation has been obtained, were carried by us.

Table 1.

Spectroscopy data of glasses

Material	λ_L , nm	λ_p , nm	α_p , cm ⁻¹	σ , Cm ²	τ , Mcc	N , cm ⁻³	F_α	β_x (10 ⁴)	$\frac{1}{z}$	Γ_R , (%)
0.112Nd ₂ S ₃ 0.888La ₂ S ₃ -3Ga ₂ S ₃	1073,2	12	22,6	4,7 · 10 ⁻²⁰	45	5 · 10 ²⁰	0,74	1,05	0,505	0,011
0.095Nd ₂ S ₃ 0.905La ₂ S ₃ -2.3Ga ₂ S ₃	1073,2	812	18,4	3,8 · 10 ⁻²⁰	62	5,3 · 10 ²⁰	0,75	1	0,444	0,0097
0.097Nd ₂ S ₃ 0.903La ₂ S ₃ 3Ga ₂ O ₃	1067,4	809	14,8	2,5 · 10 ⁻²⁰	88	6,08 · 10 ²⁰	0,76	1	0,457	0,0094
0.085Nd ₂ S ₃ 0.915La ₂ S ₃ 2.3Ga ₂ O ₃	1071,2	810	15	2,9 · 10 ⁻²⁰	82	6,2 · 10 ²⁰	0,75	1,05	0,449	0,011

				20						
$\text{La}_2\text{S}_3 \cdot 2\text{Ga}_2\text{O}_3 - 3.8\% \text{Nd}^{3+}$	1071,2	810	20,8	$2,9 \cdot 10^{-20}$	51	$7,6 \cdot 10^{-20}$	0,75	1	0,48	0,01
$0.11\text{Nd}_2\text{O}_3 \cdot 0.89\text{La}_2\text{O}_3 \cdot 3\text{Ga}_2\text{S}_3$	1071	812	16,9	$3,2 \cdot 10^{-20}$	65	$5,2 \cdot 10^{-20}$	0,73	1,1	0,442	0,009
ED-2	1060	808	1,27	$2,9 \cdot 10^{-20}$	300	$2,83 \cdot 10^{-20}$	0,64			0,064

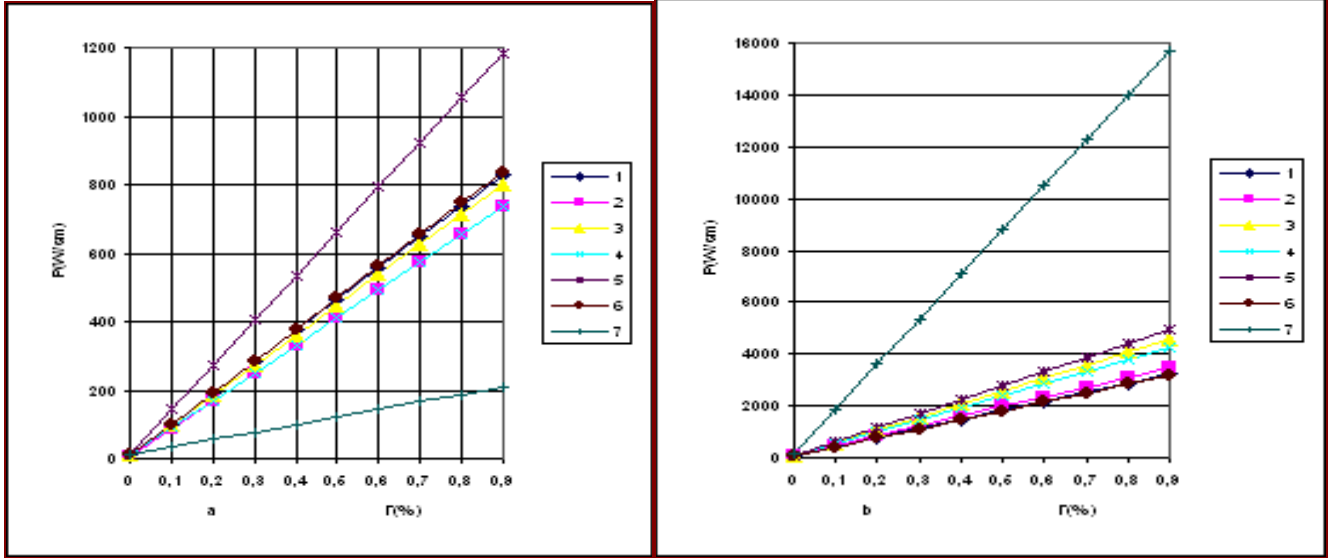


Fig.1. The dependence of the density of threshold power of pumping on the nonresonance losses at the (a) longitudinal and (b) transversal pumpings:

- 1- $0.112\text{Nd}_2\text{S}_3 \cdot 0.888\text{La}_2\text{S}_3 \cdot 3\text{Ga}_2\text{S}_3$
- 2- $0.095\text{Nd}_2\text{S}_3 \cdot 0.905\text{La}_2\text{S}_3 \cdot 2.3\text{Ga}_2\text{S}_3$
- 3- $0.097\text{Nd}_2\text{S}_3 \cdot 0.903\text{La}_2\text{S}_3 \cdot 3\text{Ga}_2\text{O}_3$
- 4- $0.085\text{Nd}_2\text{S}_3 \cdot 0.915\text{La}_2\text{S}_3 \cdot 2.3\text{Ga}_2\text{O}_3$
- 5- $\text{La}_2\text{S}_3 \cdot 2\text{Ga}_2\text{O}_3 - 3.8\% \text{Nd}^{3+}$
- 6- $0.11\text{Nd}_2\text{O}_3 \cdot 0.89\text{La}_2\text{O}_3 \cdot 3\text{Ga}_2\text{S}_3$
- 7- ED-2.

The dependence of the threshold on the nonresonance losses for every material at the transversal pumping is presented on the fig.1b. The length of every material $l=1\text{cm}$. For the calculation of Z parameter, we propose, that Stark sublevels $^4I_{9/2}$ are on the equal distances in the energy scale. According to F_a parameter, the gaps between Stark components $^4F_{3/2}$ for every glass on absorption spectrums $^4I_{9/2} \rightarrow ^4F_{3/2}$, fixed at $T=77\text{K}$, were defined by us. From the fig.1b, it is seen, that investigated by us glasses have the very low threshold in the comparison with ED-2 at the longitudinal pumping. Thus, investigated by us glasses are the perspective materials for the creation of miniature lasers at the transversal pumping. It is need to note, that formulae (13) and (26) have to be multiplied on the gathering of diode radiation coefficient ξ and the efficiency of diode η . These coefficients don't take into consideration by us for simplicity. The dependence of the threshold on the nonresonance losses for every material at the longitudinal pumping is presented on the fig.1c. The length of every material was considered as

optimized one, i.e. $\ell = \frac{l}{\alpha_p}$. It is seen, that the generation

thresholds are significantly higher, than ED-2 in the investigated glass by us. The relative small thresholds have the glasses with the compositions $0.095\text{Nd}_2\text{S}_3 \cdot 0.905\text{La}_2\text{S}_3 \cdot 2.3\text{Ga}_2\text{S}_3$ and $0.085\text{Nd}_2\text{S}_3 \cdot 0.905\text{La}_2\text{S}_3 \cdot 2.3\text{Ga}_2\text{O}_3$.

The dependence of the output power on the input one on the longitudinal pumping in the multimode is represented on the fig.2.

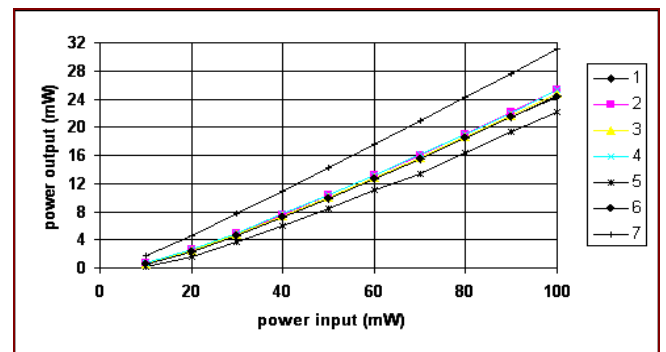


Fig.2. The dependence of the output power on the input one at the longitudinal pumping in the multimode regime:

- 1- $0.112\text{Nd}_2\text{S}_3 \cdot 0.888\text{La}_2\text{S}_3 \cdot 3\text{Ga}_2\text{S}_3$
- 2- $0.095\text{Nd}_2\text{S}_3 \cdot 0.905\text{La}_2\text{S}_3 \cdot 2.3\text{Ga}_2\text{S}_3$
- 3- $0.085\text{Nd}_2\text{S}_3 \cdot 0.915\text{La}_2\text{S}_3 \cdot 2.3\text{Ga}_2\text{O}_3$
- 4- $0.097\text{Nd}_2\text{S}_3 \cdot 0.903\text{La}_2\text{S}_3 \cdot 3\text{Ga}_2\text{O}_3$
- 5- $\text{La}_2\text{S}_3 \cdot 2\text{Ga}_2\text{O}_3 - 3.8\% \text{Nd}^{3+}$
- 6- $0.11\text{Nd}_2\text{O}_3 \cdot 0.89\text{La}_2\text{O}_3 \cdot 3\text{Ga}_2\text{S}_3$
- 7- ED-2.

For these calculations, it is proposed, that nonresonance losses are equal to 0.15%, $f=0.5$, the operating radius of the

laser element is $\sim 60\text{mcm}$ for every material and $\omega=0,5\omega_0$. It worse generation parameters, than ED-2 at the longitudinal is seen, that investigated by us glasses have the significant pumping.

[1] Yariv. Kvantovaya elektronika, M.: "Sovetskoye radio", 1980. (in Russian).

H.İ. Abutalıbov, A.Ə. Məmmədov

**YARIMKEÇİRİCİ ŞÜŞƏLƏRDƏN MİNİATÜR LAZERLƏRİN AKTİV ELEMENTLƏRİ KİMİ İSTİFADƏ
ETMƏK İMKANLARI BARƏDƏ**

Miniatur lazerlər üçün eninə və uzununa həyəcanlanma hallarında, çıxış gücü və lazer generasiyası başlayan güc bir və çox moda hallarında hesablanmışdır. Nd^{3+} aktivləşmiş sulfid, oksosulfid və sulfidoksid şüşələrinin əsasında uzununa və eninə həyəcanlanma hallarında miniatur lazerlər yaratmaq imkanları araşdırılmışdır.

Г.И. Абуталыбов, А.А. Мамедов

**О ПЕРСПЕКТИВНОСТИ ПОЛУПРОВОДНИКОВЫХ СТЕКОЛ, КАК АКТИВНОЙ СРЕДЫ
МИНИАТЮРНОГО ЛАЗЕРА**

Вычислены порог генерации при продольных и поперечных способах накачки и выходная мощность при многомодовых и при одномодовых режимах для миниатюрных лазеров. Выяснена возможность создания миниатюрных лазеров на основе сульфидных, оксосульфидных и сульфидоксидных стекол активированных Nd^{3+} при продольных и поперечных способах возбуждения.

Received: 22.09.2004

THE KINETICS OF PHASE TRANSITIONS IN AMORPHOUS FILMS TlInSe_2 , OBTAINED UNDER THE CONDITIONS OF THE ACTION OF THE EXTERNAL ELECTRIC FIELD

D.I. ISMAYLOV

*Institute of Physics of National Academy of Sciences of Azerbaijan,
AZ-1143, H. Javid av., 33*

The kinetics of crystallization of TlInSe_2 amorphous films obtained by thermal evaporation under the conditions of the action of external electric field ($E=3000 \text{ V}\cdot\text{cm}^{-1}$) is studied by kinematic electron diffraction method.

The summary activation energy of crystallization is equal to $36,04 \text{ Kkal/mol}$. Crystallization velocity of films obtained in electric field is higher than one of films obtained under ordinary conditions.

The kinematic electron diffraction method is applied for the investigations of phase transition processes. It can be applied also for the measurements of diffusion velocities in the thin films, basing mainly on the optical measurements.

For every concrete material of any substance class the stationary activation energy values showing the final of phase transitions carrying out with the creation of new phase bud and the further their growth are defined by this method. The results obtained by this method can't be achieved with the enough definiteness by the method of optical reflection and other optical methods, which are potentially not useful for the thin films of the width from the several nm till the some decades of nm, on the investigation results of X-ray spectrometry, ellipsometry.

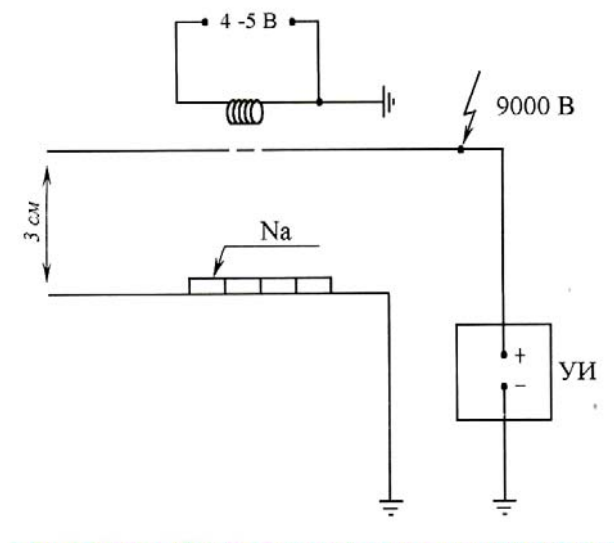


Fig1 The circuit of electric field creation.

The investigation objects (amorphous films TlInSe_2) are obtained by the way of condensation of the given compound in the vacuum 10^{-4} Pa . The amorphous films that crystallized at the different temperatures are prepared at the similar conditions. The steam condensation is carried out in the constant electric field (fig.1) of the strength $E=3000 \text{ V}\cdot\text{cm}^{-1}$. The substrates are the small fresh chips of stone salt. The films from these substrates are taken by the dissolution of NaCl in the water and put on the special furnaces, which are especially for the kinematic shooting of the diffraction figures, allowing to register the phase transformations photographically.

In the electron diffraction study the photographic registration of phase transitions is interest not only by its expressivity, but by the possibility to obtain the all picture of electron scattering immediately. From the electron diffraction pattern, it is possible to take the information about the sample microstructure: about superstructural reflections, reflexes from twins and general character of background distribution.

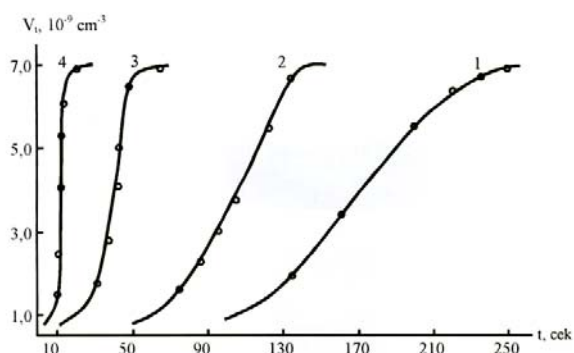


Fig. 2. Kinetic crystallization curves of amorphous TlInSe_2 . Values T_{kp} : 1 - 358 K; 2 - 368 K; 3 - 403 K; 4 - 443 K.

For the definition of kinetic parameters of phase transformations in the amorphous films TlInSe_2 of the width 25 nm obtained under the conditions of the action of electric field the isothermal kinematic electron diffraction patterns at the four different temperatures: 398, 408, 423, 443K have been obtained. The three diffusion lines corresponding to $S=4\pi\sin\theta/\lambda=0,2061$; $0,3395$; $0,5040 \text{ nm}^{-1}$; are observed on the kinematic electron diffraction pattern (fig.2), taken at 423K, on which the process of phase transformation is observed. The disappearance of diffusion lines according to amorphous phase is accompanied by the appearance of the lines of crystalline phase, the intensities of which correspond to the different moments of film annealing. The electron diffraction pattern calculation shows that amorphous film TlInSe_2 is crystallized in the tetragonal crystal system with the periods of unit cell of crystalline lattice, $a=0.8075\pm0.001$, $c=0.6847\pm0.002 \text{ nm}$, $c/a=0.8479$, SGS $I4/mcm$, the number of formulae units in the cell $z=4$ [1].

The photomicrograms have been taken with the aim of the measurement of line intensities of crystalline TlInSe_2 from the different areas of kinematic electron diffraction patterns obtained in the process of amorphous film crystallization. The intensities of lines of crystalline phase of TlInSe_2 are defined by them. The transition from the intensity values to the quantity of crystallized substance is carried out with the

help of Vainshtein formula [2], taking into consideration, that intensity of electron scattering is proportional to the volume of scattering substance.

$$I_{hkl} = I_0 \lambda \cdot \left| \frac{\Phi_{hkl}}{\Omega} \right|^2 \cdot \frac{V d_{hkl}^2 \Delta p}{4\pi \lambda l} \quad (1)$$

Here I_0 is intensity of primary beam, λ is wave length of primary beam, Φ is structure factor, Ω is the volume of unit cell, V is the irradiated volume of polycrystalline substance, d_{hkl} are interplanar distances, Δ is small area of Debye ring, p is repeatability factor, λl is device constant.

The values stay constant during the kinematic film, besides of the volume V . It is followed, that defining the line intensities change on the kinematic electron diffraction patterns, one can possible to find the change of substance quantity in the dependence on the crystallization time. During the transition from the intensity to the volume maximum value of intensity is compared with the irradiated volume $V = S \cdot h$, where S is the cross-section of electronic beam $\sim 2,8 \cdot 10^{-3} \text{ cm}^2$, h is the film width $\sim 2,5 \cdot 10^{-6} \text{ cm}$.

Defining by the given comparisons, the volume of intensity unit, the value of volume of crystallized phase in every given time moment on the base of which the plots of dependence of phase volume changing on time are constructed, are found (fig.3).

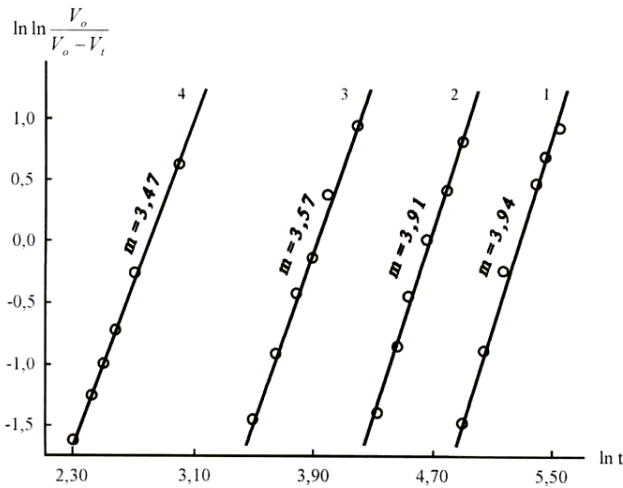


Fig. 3. Dependence $\ln \ln [V_0 / (V_0 - V_t)]$ on $\ln t$ for crystallization of amorphous TlInSe_2 . Denotes are as on Fig. 2.

The obtained isotherms are compared with the famous analytic expression of Avraami-Colmogorov for the kinetics of phase transitions carrying out with the creation of the new phase buds with the following their growth.

$$V_t = V_0 [1 - \exp(-kt^m)] \quad (2) [3-4],$$

or

$$\ln \ln \left[\frac{V_0}{V_0 - V_t} \right] = \ln k + m \ln t \quad (3)$$

where V_t is crystallized volume in time moment t , V_0 is the initial volume, K is reaction velocity constant, m is constant, characterizing the growth of size of new phase center.

From the formula (3), it is followed, the linear dependence $\ln \ln [V_0 / (V_0 - V_t)]$ on the $\ln t$. The plot of the dependence $\ln \ln [V_0 / (V_0 - V_t)]$ on the $\ln t$ for temperatures 398, 408, 423, 443K given on the fig.3 has been constructed on the base of experimental data.

The plot, given on the fig.3 shows, that this dependence is described by direct lines, on which all experimental points for given temperatures are put. From these line inclinations the values of “ m ” exponent on t have been calculated. These values were close to four. It shows, that in the case of amorphous film Tl In Se_2 crystallization obtained in the electric field the three-dimensional growth of small crystals, depending on the law established by Avraami-Colmogorov takes place and is described by the equation (2).

The values of $\ln k$, established for temperatures 398, 408, 423, 443K are equal to -15,80; -12,27; -10,57; -8,43 correspondingly. The plot of the dependence $\ln k$ on inverse temperature has been constructed on the base of these data. The linear dependence $\ln k$ on $1/T$ shows that velocities of bud creation and linear growth of small crystals need to describe by the expression of the type of Arrenius equation [5]

$$\ln k = A - \frac{(E_3 + 3E_p)}{RT}, \quad (4)$$

where A is constant independent on the temperature, R is universal gas constant, T is absolute temperature, E_3 is activation energy of bud creation, E_p is activation energy of small crystals growth.

From the direct line inclination $\ln k$ on $1/T$, the general activation energy of crystallization process, which is equal to 36,04 kkal/mol, has been estimated.

The activation energy of bud creation, calculated from the plot dependence $\ln(l, \tau)$ on $1/T$ (where τ is experimentally observed time of crystallization beginning) is equal to $E_3 = \text{tg} \alpha \cdot R = 15,3$. Here $\text{tg} \alpha$ is inclination angle of direct line from the plot $\ln(l/\tau)$ on $1/T$.

The activation energy of small crystals growth E_p defined from the ratio $E_p = (E_{\text{total}} - E_3)/3$, is equal to 10,35 kkal/mol. The values of activation energies of bud creation and their further growth, including the general activation energy of film TlInSe_2 crystallization obtained in the conditions of electric field action are smaller than corresponding values for films obtained outside the field [5].

The only one acceptable explanation of decrease of activation energy values for amorphous films in the electric field can be given in the terms of ordering process. This means, that during the process of molecular beam condensation on the surface of ion crystals NaCl , the ordered under the action of electric field, the additional centers of bud creation of crystalline phase, which can be point, line, two-dimensional defects, having electric charges or their collections, simplifying their further growth, have been created.

- | | |
|---|--|
| [1] <i>D. Muller, G. Eklenger, H. Hahn.</i> Uberternare Thalliumchalkogenide mit Thalliumselenidstruktur. Z.Anorg. Allg. Chem., 1973, 398, s.207-220. | [4] <i>M. Avrami.</i> Kinetics of Phase Change. II. Transformation–Time Relations for Random Distribution of Nuclei Journ. of Chemical Physics. 1940, v.8, N2, pp.212-224. |
| [2] <i>B.K. Vanshteyn.</i> Strukturnaya elektronografiya. M.: Izd-vo AN SSSR, 1956, 315 s.(in Russian). | [5] <i>D.I. Ismailov, F.I. Aliyev, R.M. Sultanov, R.B. Shafizade.</i> Poverkhnost'. Fizika, khimiya, mekhanika. 1991, №5, s.113-116. (in Russian). |
| [3] <i>A.N. Kolmogorov.</i> K staticheskoy teorii kristallizacii metallov. Izv. AN SSSR, ser. Matem., 1937, №3, s.355-359. (in Russian). | |

C. İ. İsmayilov

XARİCİ ELEKTRİK SAHƏSİNİN TƏSİRİ ŞƏRAİTİNDƏ ÇÖKDÜRÜLMÜŞ TlInSe₂ AMORF TƏBƏQƏLƏRİNİN KRİSTALLAŞMA KİNETİKASI

Vakuumda elektrik sahəsinin ($E=3000 \text{ V}\cdot\text{sm}^{-1}$) təsiri şəraitində çökdürülmüş TlInSe₂ amorf təbəqələrinin kristallaşma kinetikasi kinematik elektronografiya üsulu ilə tədqiq edilmişdir.

Kristallaşmanın ümumi aktivləşmə enerjisi 36,04 kkal/mol-a bərabərdir. Elektrik sahəsində alınmış təbəqələrin kristallaşma sürəti adi şəraitdə alınanlara nisbətən böyükdür.

Д.И. Исмаилов

КИНЕТИКА ФАЗОВЫХ ПЕРЕХОДОВ В АМОΡФНЫХ ПЛЕНКАХ TlInSe₂, ПОЛУЧЕННЫХ В УСЛОВИЯХ ВОЗДЕЙСТВИЯ ВНЕШНЕГО ЭЛЕКТРИЧЕСКОГО ПОЛЯ

Методом кинематической электрографии исследована кинетика кристаллизации пленок TlInSe₂, полученных термическим напылением в условиях воздействия внешнего электрического поля напряженностью $E=3000 \text{ В см}^{-1}$.

Общая энергия активации кристаллизации равна 36,04 ккал/моль. Скорость кристаллизации пленок, полученных в электрическом поле, больше, чем для пленок полученных в обычных условиях - вне электрического поля.

Received: 14.09.04

THE INVESTIGATION OF STATES OF ION Ni, Cr, Co, Bi AND K IN THE COMPOSITION OF DEHYDRATION CATALYSTS

N.A. ALIEV, R.B. JAMALOVA, S.G. FARADJEVA, S.M. GADJIZADE,
G.S. GEYDAROVA, A.A. KASIMOV

*The Institute of Petrochemical Processes of National Academy of Azerbaijan,
370025, Baku, H.Rafiev str., 30*

The states of ions Ni, Cr, Co, Bi and K, including in the composition of dehydration catalysts of paraffin hydrocarbons C₃-C₄ are considered.

The data on the ion state in the catalyst in the dependence on the preparation method are presented. For the obtaining of the imagination about ion states, the mass catalysts are used.

The catalysts are treated by drying and glowing in the atmosphere conditions and the conditions of low pressure. The conditions of catalyst syntheses influence on the valiant and coordination ion states of transition elements (Cr, Ni, Co), including in the catalyst composition, by the definite way. The catalysts, obtained in the conditions of the low pressure, have as oxidated [(Cr⁵⁺(O_h), N²⁺(O_h) and Co³⁺, Co²⁺], so the reduced Cr⁰, Ni⁰, Co⁰ forms of active components. The conduction of low pressure cause the creation the such components as K₂Cr₂O₇, NiO, Cr₂O₅, Cr₂O₃, Bi₂O₃ in the significant quantities, allowing to carry out the dehydration of paraffin hydrocarbons C₃-C₄.

The catalysts, having ions Ni, Cr, Co, Bi and K are widely used in the industrially-important processes and in a particular, in the processes of dehydration of normal low-molecular hydrocarbons [1-10]. For the optimization of the processes and improvement of exploitation properties of catalysts, it is need to study in detail the contact physico-chemical properties and in a particular, valiant and coordination ion state, including in their composition.

Below of results of spectral (electronic spectroscopy of diffuse reflection) investigation of states of ions Ni, Cr, Co, Bi and K, including in the composition of dehydration catalysts, treated in the IPChP of NAS of Azerbaijan, are given.

The technique of experiment

The electronic spectrums of diffuse reflection (ESDR) in the region 50000-100000cm⁻¹ are taken on the spectrophotometer "Specord M40", which has the ladder for taking of diffuse reflection spectrums.

The catalysts are prepared by the way of the nitrate salt borrowing of corresponding metals. The catalyst samples are treated by drying (100°-120°C) and glowing (600°-620°C) in the conditions of low atmosphere pressure.

The experiment results

The oxide system Cr (80%) – Co (20%)

In the sample spectrum, obtained in the air atmosphere, the absorption bands (a.b.), at 22000 (very weak a.b.) and in the region 12000-18000cm⁻¹ (fig.1, c.1.) are observed. According to the refs [11, 12] absorption bands can be created to the Cr³⁺ ions, stabilized in the octahedron coordination fields (transfer ⁴A_{2g} → ⁴T_{1g}). The observable absorption band at 12000-18000cm⁻¹ is structural and insist on the three components with maximums at 14000, 16100 and 17000cm⁻¹. These maximums can be related to ions Cr⁵⁺ and Co³⁺(O_h) (transfer ¹A_{2g} → ¹T_{1g}), correspondingly.

The presence of ions Co³⁺(O_h) in the system shows on the existence of phase Co₃O₄ in the system [11, 12].

Thus, the given binary system has phases Co₃O₄, Cr₂O₃, Cr₂O₅, i.e. in the given case the ions Co³⁺, Co²⁺, Cr⁵⁺ and Cr³⁺ are exist.

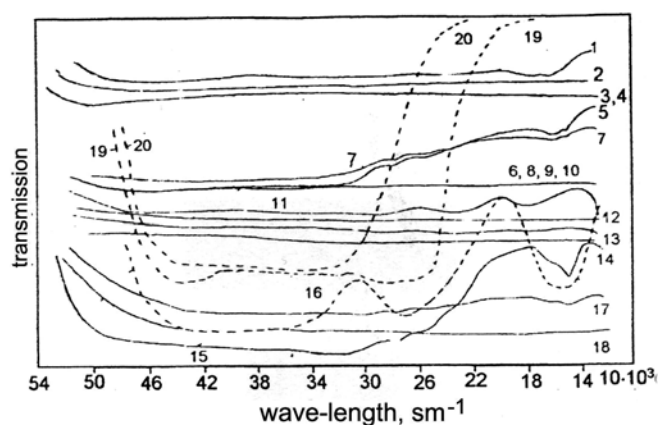


Fig.1. The spectrum of diffuse reflection of catalysts.

- 1 - Cr(80%) - Co(20%) - obtained at the atmosphere pressure
- 2 - Cr(80%) - Co(20%) - obtained in the vacuum conditions
- 3 - Ni(57%) - Co(43%) - obtained at the atmosphere pressure
- 4 - Ni(57%) - Co(43%) - obtained in the vacuum conditions
- 5 - Cr(10%) - Ni(90%) - obtained at the atmosphere pressure
- 6 - Cr(10%) - Ni(90%) - obtained in the vacuum conditions
- 7 - Cr(25%) - Ni(75%) - obtained at the atmosphere pressure
- 8 - Cr(25%) - Ni(75%) - obtained in the vacuum conditions
- 9 - Cr(25%) - Ni(75%) - obtained at the atmosphere pressure
- 10 - Cr(15%) - Ni(75%) - obtained in the vacuum conditions
- 11 - Cr(80%) - Bi(20%) - obtained at the atmosphere pressure
- 12 - Cr(80%) - Bi(20%) - obtained in the vacuum conditions
- 13 - Cr(92%) - K(8%) - obtained at the atmosphere pressure
- 14 - Cr(92%) - K(8%) - obtained in the vacuum conditions
- 15 - Ni(57%) - Bi(43%) - obtained at the atmosphere pressure
- 16 - Ni(57%) - Bi(43%) - obtained in the vacuum conditions
- 17 - Ni(80%) - K(20%) - obtained at the atmosphere pressure
- 18 - Ni(80%) - K(20%) - obtained in the vacuum conditions
- 19 - Bi(75%) - K(25%) - obtained at the atmosphere pressure
- 20 - Bi(75%) - K(25%) - obtained in the vacuum conditions

The wide unstructured absorption band, having almost all area (fig.1, c.2) is observed in the vacuum conditions in the catalyst spectrums. Moreover, the general absorption phone strongly increases. The black color of the sample shows on

this fact. Probably, in the vacuum conditions, the partial reduction process of ions Co^{3+} , Co^{2+} , Cr^{5+} and Cr^{3+} is carried out till the Co^0 , Cr^0 , correspondingly. In the given case, the sample surface has as oxidized (Co^{3+} , Co^{2+} , Cr^{5+} and Cr^{3+}), so the reduced forms of ions of cobalt and chrome (Co^0 , Cr^0).

Oxide system Ni (57%) – Co (43%)

The sample has the black color, and spectrum is characterized by the total absorption, having almost all region (fig.1., c.3). The analogical spectrum has the sample, obtained in the vacuum conditions (fig.1, c.4). Moreover, in the both cases, the general absorption phone strongly increases.

The total unstructured absorption difficults the spectrum interpretation, but taking into consideration the common positions and literature data, it can be proposed, that in the sample, obtained in the vacuum, in the result of partial reduction of ions $\text{Ni}^{2+}(\text{O}_h)$, Co^{3+} and Co^{2+} , the particles Ni^0 and Co^0 should be existed.

Oxide system Cr (10;25 and 75%) – Ni (90;75 and 25%)

The sample spectrum, having 10% Cr and 90% Ni, obtained in the air atmosphere is characterized by absorption band at 13800; 14500; 24000 and 26200 cm^{-1} (fig.1, c.5). Observable absorption bands, according to the refs [11,12], can be interpreted by the following way:

- absorption band at 14500 and 26200 cm^{-1} can be related to Cr^{5+} ions;

- the absorption in the region 24000 cm^{-1} is characterized for Cr^{3+} ions, stabilized in the octahedron coordination fields (transfer ${}^4\text{A}_{2g} \rightarrow {}^4\text{T}_{1g}$).

- the absorption band in the region 13800 cm^{-1} can be related to $\text{Ni}^{2+}(\text{O}_h)$ ions (transfer ${}^3\text{A}_{2g} \rightarrow {}^3\text{T}_{1g}$), including in the phase NiO composition.

Thus, the given catalyst is complex many phase system (Cr_2O_5 ; Cr_2O_3 and NiO).

The catalyst, obtained in the vacuum conditions, is characterized by total absorption, having almost all region (fig.1, c.6). Probably in the vacuum conditions, the ions Cr^{5+} , Cr^{3+} and Ni^{2+} partially reduce till Cr^0 and Ni^0 , correspondingly. In the given case, the oxidated Cr^{5+} , Cr^{3+} and Ni^{2+} and reduced forms of Cr^0 and Ni^0 are coexisted on the catalyst surface.

The increase of chrome quantity in the sample till 25%, insignificantly influence on the place of absorption band on ions Cr^{5+} , Cr^{3+} and Ni^{2+} (fig.1, c.7). The some increase of general phone and intensity decrease of observable absorption bands are observed.

The catalyst, obtained in the vacuum conditions, has the spectrum, identical for the previous catalyst(fig.1, c.8).

The latter increase of chrome concentration till 75%, leads to the strong change of catalyst spectrum, obtained in the air atmosphere. The total absorption, having all region (fig.1, c.9) is observed.

The identical spectrum is observed in the vacuum conditions (fig.1, c.10).

The color of the sample becomes darker at the chrome high concentrations. Probably, the general absorption phone increases and absorption bands, which are character for chrome and nickel ions, are masked. The X-ray-phase analysis of catalyst, prepared in the atmosphere conditions shows the existence of phases NiO, $\text{Ni}_2\text{Cr}_2\text{O}_4$ and in the

catalyst, treated by thermal-vacuum treatment - only phases NiO.

Oxide system Cr (80%) – Bi (20%)

In the sample spectrums, obtained in the air atmosphere, the absorption bands at 16500, 21500 and 27000 cm^{-1} are observed (fig.1, c.11). The bands in the region 16500 and 21500 cm^{-1} can be related to the absorption of ions $\text{Cr}^{3+}(\text{O}_h)$ (transitions ${}^4\text{A}_{2g} \rightarrow {}^4\text{T}_{2g}$ and ${}^4\text{A}_{2g} \rightarrow {}^4\text{T}_{1g}$ correspondingly), and at the 27000 cm^{-1} - to Cr^{5+} .

The Bi^{3+} ions have electron configurations $d^{10}s^2$ and their absorption in the ultraviolet region takes place because of the so-called Ridberg's transitions, i.e. inside the membrane of ions themselves. The Bi^{3+} ion absorption is observed in the region 28500; 32250 and 38460 cm^{-1} [11, 12]. In the given case, probably, the phone absorption masks the absorption bands from Bi^{3+} ions. The stabilization in the system of ions Cr^{5+} , Cr^{3+} and Bi^{3+} can be said.

The catalyst spectrums, obtained in the vacuum, gives the total absorption, having almost all region (fig.1, c.12). Probably, in this case, ions Cr^{5+} and Cr^{3+} , are partially reduced till Cr^0 . The Bi^{3+} ions are more stable [11, 12] and the existence of Bi_2O_3 phase and ions Cr^{5+} , Cr^{3+} and Cr^0 in the sample can be proposed.

The catalyst, prepared in the air atmosphere conditions on RFA shows the existence of phases Cr_2O_3 and Bi_2O_3 in the thermal-vacuum treatment conditions it is amorphous.

Oxide system Cr (92%) – K (8%)

The sample spectrum, obtained in the air atmosphere, is characterized by the weak absorption bands at 16500; 21500 and 27000 cm^{-1} , which can be related to the ions Cr^{5+} and Cr^{3+} (Fig.1, c.13). The absorption from K ions is masked by the phone absorption.

The catalyst, obtained in the vacuum, has the spectrum with the unstructured absorption, having almost all region (fig.1, c.14).

In the given case, as mentioned above, the oxidated (Cr^{5+} , Cr^{3+}) and reduced (Cr^0) forms of chrome ions are stabilized in the sample.

Oxide system Ni (57%) – Bi (43%)

In the sample spectrum, obtained in the air atmosphere, the absorption bands in the region 13000(arm); 13800; 15500; 21500; 24000; 26300; ~29,000 cm^{-1} (fig.1, c.15), which are character for $\text{Ni}^{2+}(\text{O}_h)$ ions, creating NiO phase, are observed [11, 12]. The grey-green sample color shows on this fact. The absorption from Bi^{3+} ions is masked by the absorption of the phase NiO.

The sample spectrum, obtained in the vacuum condition, significantly differs from the above mentioned case. Thus, the wide intensive absorption bands in the region 13000 - 16000 and ~25500 cm^{-1} (fig.1,c.16) are observed. Besides, in the given case in the difference from all previous binary systems, the disappearance of absorption bands from active component [in the given case absorption bans from $\text{Ni}^{2+}(\text{O}_h)$ in NiO], connected with the partial reduction of transition element under influence of reduction medium, which the vacuum is, doesn't observed. Probably, this effect can be explained by the alloying influence of Bi^{3+} on NiO, that leads

to the stability of nickel oxide, to the reduction processes in vacuum conditions. From this the another important conclusion takes place, i.e. Bi^{3+} ions reveal the alloying properties in the case of binary oxide systems Cr-Bi.

The catalyst, prepared in the atmospheric conditions on RFA shows the existence of phases NiO and Bi_2O_3 .

Oxide system Ni(80%) - K(20%)

The absorption bands from $\text{Ni}^{2+}(\text{O}_h)$ in the phase NiO are observed in the sample spectrum, obtained in the air atmosphere (fig.1,c.17). The dark green sample color also shows on this fact (pure NiO has grey-green color). The significant increase of general absorption phone, connected with the darkness of sample color, is observed.

Thus, the existence of phases NiO and K_2O in the catalyst composition can be said.

The sample, obtained in the vacuum, is characterized by the unstructured absorption (fig.1,c.18). Probably, the part of $\text{Ni}^{2+}(\text{O}_h)$ ions transfers to Ni^0 in the result of reduced processes. The change of sample color from dark-green to black also shows on this fact. Thus, the catalyst includes the phase NiO and Ni^0 particles. The X-ray-phase analysis shows the existence of NiO phase in the both samples, prepared as in the vacuum conditions, so in the atmosphere ones.

Oxide system Bi(75%) - K(25%)

The absorption bands from Bi^{3+} (in Bi_2O_3 phase) at 40800; 31200 and 27000 cm^{-1} are observed in the sample spectrum, obtained in the air atmosphere (fig.1,c.19). The yellow color, which is character for Bi_2O_3 also shows on this fact.

The absorption bands from Bi^{3+} ions are absent in the catalyst spectra, obtained in the vacuum conditions (fig.1,c.20). Probably, in this case part of Bi^{3+} reduce till Bi^0 .

Thus, in the given case, the catalyst includes Bi^{3+} ions (in Bi_2O_3 phase), the Bi^0 particles, K^+ ions and probably K^0 .

Oxide system Cr(63%) - Ni(21%) - Bi(16%)

The total absorption in all investigated spectral region is observed in the catalyst spectrum, obtained in the air atmosphere (fig.2,c.1). The sample has black color. Probably, in the given case, the absorption bands from ions Cr^{5+} , Cr^{3+} , Cr^{2+} and Bi^{3+} are masked by more phone absorption and don't reveal in the spectra.

In the difference from this, in the sample spectra, obtained in the vacuum conditions, the weak, but allowed absorption bands at 16000 and 23000 cm^{-1} , which are accord to Cr^{3+} ions, stabilized in the octahedron coordination fields (transfers $^4\text{A}_{2g} \rightarrow ^4\text{T}_{2g}$ and $^4\text{A}_{2g} \rightarrow ^4\text{T}_{1g}$ correspondingly), are observed. Besides, the weak-intensive absorption band at 27000 cm^{-1} from Cr^{5+} is observed. Probably, at the catalyst synthesis in the vacuum conditions, part of $\text{Cr}^{3+}(\text{O}_h)$ and ion quantity of trivalent chrome increases in the system. The dark-green color of the sample, which is character for $\text{Cr}^{3+}(\text{O}_h)$ ions shows on this fact. The given conclusion doesn't except the presence of ions Cr^{5+} , Ni^{2+} and Bi^{3+} in the system.

Besides, probably the Bi^{3+} ions or Bi^0 ions influence with the alloying influence on $\text{Cr}^{3+}(\text{O}_h)$ ions, increasing their stability to the reduction processes.

Thus, the given catalyst has the complex composition and includes the ions Cr^{5+} , $\text{Cr}^{3+}(\text{O}_h)$, $\text{Ni}^{2+}(\text{O}_h)$ and Bi^{3+} probably creating the phases Cr_2O_5 , Cr_2O_3 , NiO and Bi_2O_3 , correspondingly.

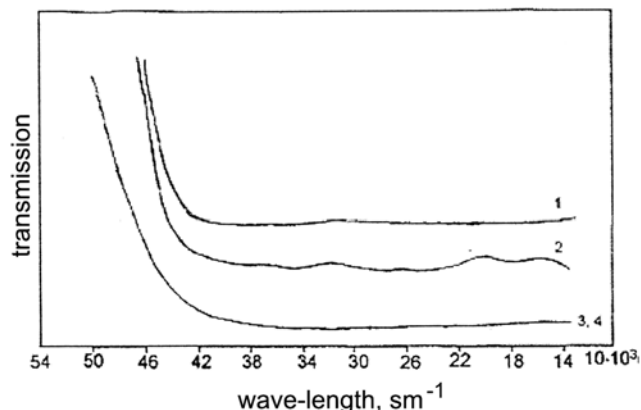


Fig.2. The spectra of diffuse reflection of catalysts.

- 1 - Cr(63%) - Ni(21%) - Bi(16%) - obtained at the atmosphere pressure
- 2 - Cr(63%) - Ni(21%) - Bi(16%) - obtained in the vacuum conditions
- 3 - Cr(63%) - Ni(21%) - Bi(16%) - obtained in the vacuum conditions

Oxide system Cr (63%) – Ni (21%) – Co (16%)

The sample has the black color and gives the total unstructured absorption, having all region (fig.2,c.3). The catalyst, obtained in the vacuum conditions, has the identical spectrum (fig.2,c.4). In the given case the interpretation of these spectra is difficulted, but it can be proposed, that oxidated-reduced processes, carrying out with the participation of ions Cr^{5+} , (Cr^{3+}), Ni^{2+} and $\text{Co}^{3+}(\text{Co}^{2+})$ realize in these samples.

Thus, on the base of spectral (ESDR) investigation of massive two- or trivalent component oxide systems, we can make the following conclusions:

-the catalyst synthesis conditions (air or vacuum atmospheres) influence on the valence and coordinate ion states of transition elements (Cr, Ni, Co), including in the catalyst composition, in the definite way;

-the catalyst, obtained in the air atmosphere, include the oxidated forms of ions of chrome, nickel and cobalt Cr^{5+} , $\text{Cr}^{3+}(\text{O}_h)$, $\text{Ni}^{2+}(\text{O}_h)$, $\text{Co}^{3+}(\text{Co}^{2+})$, including in the composition of phases Cr_2O_5 , NiO, Co_3O_4 .

-the catalysts, obtained in the vacuum conditions, have as oxidated [$(\text{Cr}^{5+}, \text{Cr}^{3+}(\text{O}_h))$ and $\text{Co}^{3+}(\text{Co}^{2+})$], so the reduced Cr^0 , Ni^0 , Co^0 forms of active components. The fact of coexistence of oxidated and reduced ion forms of transition metals as two- and trivalent oxide systems;

-in the combination with the transition elements, Bi^{3+} ions are more stable to the reduction processes and influence in the case of Ni-Bi system, the alloying influence on $\text{Ni}^{2+}(\text{O}_h)$ ions, that reveals in the stability of nickel ions to the reduction processes.

In the binary systems Bi-K, the Bi^{3+} ions are more influenced to the reduction medium

[1] V.B. Loshkina, V.V. Balashova, L.Z. Dorogochinskiy. NTIS Neftepererabotka i neftekhimiya, 1984, № 11,

s.19. (in Russian)

[2] R.A. Buyanov, N.A. Pakhomova. Kinetika i analiz,

- 2001, t.42, № 1, s.72-85. (in Russian).
- [3] V.V. Molchanov. Kinetika i kataliz. 1992, t.33, №4, s.873. (in Russian).
- [4] G.R. Kotelnikov. Reac.Kinet.Catal.Lett. 1995, v.55, N5, p.537.
- [5] P.R. Kottrell, S.T. Bakas, M.F. Bentam, J.Kh. Gregor, K.R. Khamlin. UOP Technology Conference. Moskow, 1992.
- [6] N.A. Pakhomov, R.A. Buyanov. J. Prikladnoy khimii, 1997, t.70, №7, s.1441. (in Russian).
- [7] N.A. Pakhomov, R.A. Buyanov. Advances in Catalysis Sci.-Technol. Ed. Prasado Rao. New Dehli: Wiley Ltd. 1985. p.305.
- [8] N.A. Pakhomov, R.A. Buyanov, B.P. Zolotovskiy. Stud.Surf. Sci. Catal. 1998. v.118, p.185.
- [9] N.A. Pakhomov, N.A. Zayceva, Z.M. Moroz. Kinetika i kataliz. 1992. t.33. №2. s.426. (in Russian).
- [10] S.A. Jamalova, Kh.A. Garabagli, G.S. Geydarova, N.A. Aliyev, Z.R. Ismaylova, A.A. Kasimov. AKhJ, 2003, №4. (in Russian).
- [11] S.A. Marfunin. VVedeniye v fiziku mineralov. M., Nedra, 1974, 324s. (in Russian).
- [12] D.T. Sviridov, R.K. Sviridova, Yu.F. Smirnov. Opticheskiye spektri ionov perekhodnikh metallov v kristallakh. M., Nauka, 1976, 268s. (in Russian).

**N.A. Əliyev, S.Ə. Camalova, R.B. Haqverdiyev, S.G. Fərəcova,
S.M. Hacızadə, G.S. Heydərova, A.Ə. Qasimov**

DEHİDROGENLƏŞMƏ KATALİZATORLARININ TƏRKİBİNDƏKİ Ni, Cr, Co, Bi VƏ K İONLARININ HALININ TƏDQIQI

Parafin karbohidrogenlərinin dehidrogenləşməsinə təmin edən katalizatorlarına daxil olan Ni, Cr, Co, Bi və K ionlarının halına baxılır.

Hazırlanma üsulundan asılı olaraq katalizatorlarda ionların halı haqqında məlumat təqdim olunur. İonların halının öyrənilməsi üçün massiv katalizatorlardan istifadə olunmuşdur.

Katalizatorlar atmosfer və vakuum şəraitində qurudulub və közərdilmişdir. Katalizatorların sintez şəraiti katalizator tərkibindəki Ni, Cr, Co, Bi və K ionlarının valent və koordinasiya halına təsir edir. Vakuum şəraitində hazırlanmış katalizatorun tərkibində həm oksidləşmiş $[(Cr^{5+}, Cr^{3+}(O_h), Ni^{2+}(O_h) və So^{3+}, So^{2+}]$ həm də reduksiya olunmuş (Cr^0, Ni^0, Co^0) aktiv komponentlər mövcuddur. Vakuum şəraiti $K_2Cr_2O_7$, NiO, Cr_2O_5 , Cr_2O_3 , Bi_2O_3 kimi birləşmələrin əmələ gəlməsinə şərait yaradır və onlar C_3-C_4 parafin karbohidrogenlərinin dehidrogenləşməsinə təmin edir.

**Н.А. Алиев, С.А. Джамалова, Р.Б. Ахвердиев, С.Г. Фараджева,
С.М. Гаджизаде, Г.С. Гейдарова, А.А. Касимов**

ИССЛЕДОВАНИЕ СОСТОЯНИЯ ИОНОВ Ni, Cr, Co, Bi и K В СОСТАВЕ КАТАЛИЗАТОРОВ ДЕГИДРИРОВАНИЯ

Рассматривается состояние ионов Ni, Cr, Co, Bi и K, входящих в состав катализаторов дегидрирования парафиновых углеводородов $C_3 - C_4$.

Представлены данные по состоянию ионов в катализаторе в зависимости от способа приготовления. Для получения представления о состоянии ионов использованы массивные катализаторы.

Катализаторы подвергали сушке и прокатке в атмосферных условиях и в условиях пониженного давления. Условия синтеза катализаторов определяющим образом влияют на валентное и координационное состояния ионов переходных элементов (Cr, Ni, Co), входящих в состав катализаторов. Катализаторы, полученные в условиях пониженного давления, содержат как окисленные $[(Cr^{5+}, Cr^{3+}(O_h), Ni^{2+}(O_h) и Co^{3+}, Co^{2+}]$, так и восстановленные Cr^0, Ni^0, Co^0 формы активных компонентов. Условия пониженного давления способствуют образованию в значительных количествах таких соединений как $K_2Cr_2O_7$, NiO, Cr_2O_5 , Cr_2O_3 , Bi_2O_3 , позволяющих вести дегидрирование парафиновых углеводородов $C_3 - C_4$.

Received: 29.07.04

THE PHENOMENON OF A HYSTERESIS IN AgFeTe_2 IN PHASE TRANSITION REGION

S.A. ALIEV, Z.S. GASANOV, S.O. MAMEDOVA

*Institute of Physics, Azerbaijan National Academy of Science, Baku, Azerbaijan
Ganja State University*

The electric properties are investigated and the differential thermal analysis is carried out in AgFeTe_2 . The additional PT are observed on the temperature dependence of DTA before and after SPT. The phenomenon of hysteresis is observed on the temperature dependences of electric properties in PT region in the direction of heating and cooling. The results are interpreted in the limits of DPT theory. It is shown, that the phenomenon of hysteresis is explained by the temperature dependence of the inclusion function in the second approximation of $L_2(T)$ and dL_2/dT . The diffusion region of PT and the width of hysteresis loop are defined. It is shown, that phase coexistence region is proportional to the width of hysteresis loop.

Introduction

The investigation of physical properties of bodies near and in PT region is the one of the developing directions of physics of solid body. The most actual task of the given direction is the definition of the region and diffusion degree of PT, the regularity of transition of one phase to another one, and also the thermodynamical parameter changes at PT. The double and triple argentum halcogenids, having structural PT, are the most suitable objects for the studying of these questions. In the last years the works in the given direction are carried out very intensive [1-14]. In a particular, in the refs [3-9], interpreting the expert results with DPT theory [15-16], PT parameters are calculated, defining the region and degree of diffusion, and also allowing to calculate the change of some thermodynamical parameters. For this is enough to define the temperature dependence of inclusion function $L_0(T)$ and its derivation on the temperature in the zero approximation dL_0/dT .

At the same time the phenomenon of hysteresis is observed at the investigation of electric and thermal properties of Ag_2Te near and in PT region in the direction of heating and cooling [17]. The DPT theory is applied for the explanation of phenomenon of hysteresis nature. It is proved, that the temperature dependence of inclusion function and its temperature velocity in the second approximation $L_2(T)$, dL_2/dT well enough explain the phenomenon of hysteresis.

The triple argentum halcogenid AgFeTe_2 is analog of Ag_2Te , has the structural phase transition, in it the phase transition is strongly scoured, the additional PT takes place [7]. Moreover, in the given work, with the aim of the result comparison and obtaining of new informations about phenomenon of hysteresis in argentum halcogenids, the electric properties of AgFeTe_2 in PT region in the direction of heating and cooling are investigated and differential thermal analysis (DTA) is carried out.

Experimental results

The measurement of electric properties and carrying out of differential thermal analysis are carried out on the installation, allowing to create the adiabatic and isotherm conditions [18].

The temperature dependence of DTA $T_y(T)$ in AgFeTe_2 is represented on the fig.1(a). As it is seen, the transitions (413 and 429K) with the absorption of few quantity of

heating, revealing only in the adiabatic conditions take place before and after the main structural PT (423K). The temperature units are presented on the fig.1(b) in the directions of the heating and cooling.

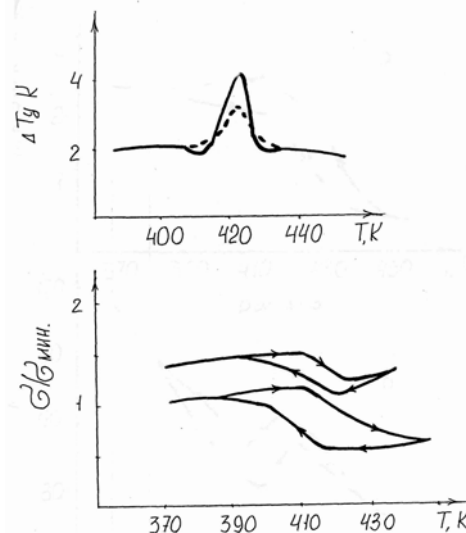


Fig.1. The temperature dependence of DTA $\Delta T_y(T)$ (a) and electroconductivity σ/σ_{min} (b) in AgFeTe_2

It is seen, that PT begin in the heating direction, for example from the initial temperature of additional PT 410K and end at 430K for the sample with the higher electron concentration (p) PT. At the cooling the $\sigma(T)$ curves goes below, than burned, than at the heating, the beginning and end of PT shift to the side of high T , the curves mix only at $T=390\text{K}$, i.e. the phenomenon of hysteresis with the big enough loop square is observed. The identical phenomenon is observed on the temperature dependencies of R (fig.2a) and therma (-----) (fig.2b). The hysteresis loop in the case of $\alpha(T)$ is more big, than in the cases of $\sigma(T)$ and $R(T)$. This is connected with the fact, that $\alpha(T)$ is measured at the presence of temperature drop in the sample deep, that leads to the additional diffusion of curves as at the heating, so at the cooling. It is need to note, that the additional transitions aren't significant on the temperature dependencies of electric properties of AgFeTe_2 in the difference from Ag_2Te [17]. Probably, this is connected with the fact, that the change of electric properties is insignificant and agrees by the direction with the change at the main PT, at the additional PT.

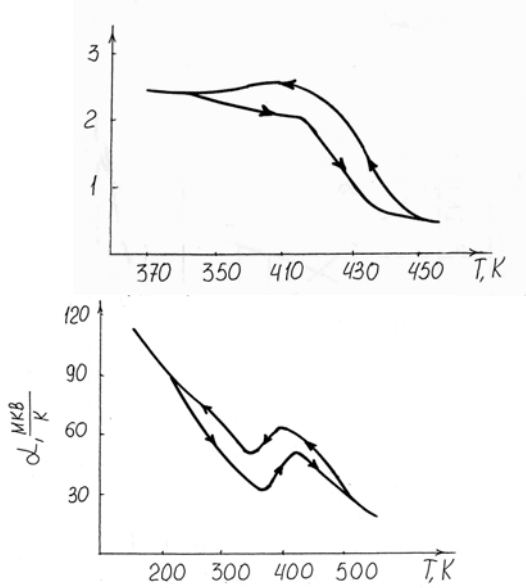


Fig.2. The temperature dependence of Hall coefficient $R(T)$ (α) and thermoe.m.f. with $\alpha(T)$ in AgFeTe_2 .

The result analysis

As it was mentioned, according to DPT theory, the temperature dependence of inclusion function in the zero approximation $L_0(T)$ allows us to understand and interpret the many PT peculiarities, in a particular, to reveal the law of mutual transition from the existing phases, to calculate PT parameters, defining the region and degree of diffusion, and also the change of some thermodynamical parameters in PT region. However, besides the general properties and regularities of PT, it is need to consider the another

decomposition members of function $F(T)$, defining $L(T)$. The different values of $F_n(T)$ are correspond to the different approximations of $L_n(T)$

$$L_n^{(r)} = \frac{I}{1 + \exp F_n(T)} \quad (1)$$

As the zero approximation results are given in the refs. [3-9], so in this ref. we are limited by the consideration of first and second approximation ($n=1$ and 2), In DPT case [15,16]

$$F_1^{(r)} = a_0(T - T_0) + a_1(T - T_0)^2 \quad (2)$$

then

$$L_1^{(r)} = \frac{I}{1 + \exp[a_0(T - T_0) + a_1(T - T_0)^2]} \quad (3)$$

$$\frac{dL_1}{dT} = -\frac{a_0}{2[I + \exp F_1(T)]} \left[1 + \frac{2a_1}{a_0}(T - T_0) \right] \quad (4)$$

In the second approximation of DPT

$$F_2^{(r)} = (T - T_0)[a_0 + a_1(T - T_0) + a_2(T - T_2)^2] \quad (5)$$

$$L_2^{(r)} = \frac{I}{1 + \exp F_2(T)} \quad (6)$$

$$\frac{dL_2}{dT} = -\frac{a_0}{2[I + \exp F_2(T)]} \left[1 + \frac{2a_1}{a_0}(T - T_0) + \frac{3a_2}{a_0}(T - T_0)^2 \right] \quad (7)$$

The PT temperature is defined from the equations $F_1(T)=0$ and $F_2(T)=0$. The roots of the equation $F_1(T)=0$, are correspond to:

$$T_{01} = T_0 ; \quad T_{02} = T_0 - \frac{a_0}{a_1} \quad (8)$$

In this case two PT take place at T_{01} and T_{02} . The one temperature is agree with T_0 , and second temperature in the dependence on the values a and a_1 is shifted to the left or to the right from T_0 . The second root of T_0 strives for the infinity at $a_1 \rightarrow 0$. The temperature difference between both points of PT is equal

$$\Delta T_0 = T_{02} - T_{01} = -\frac{a_0}{a_1} \quad (9)$$

The roots of equation $F_2(T)=0$, are correspond to

$$T_{01} = T_0 ; \quad T_{02} = T_0 - \frac{a_1}{2a_2} + \sqrt{\left(\frac{a_1}{2a_2}\right)^2 - \frac{a_0}{a_2}} \quad (10)$$

$$T_{03} = T_0 - \frac{a_1}{2a_2} - \sqrt{\left(\frac{a_1}{2a_2}\right)^2 - \frac{a_0}{a_2}} \quad (11)$$

As it is seen, $F_2(T)$ takes place at in the second approximation. In the formulae (10) and (11), the substance roots are present the interest, that gives the limit on the constant decomposition coefficients a_0 ; a_1 ; a_2 according to which the inequality $a_1^2 > 4a_0a_2$ should be carried out, taking place at, $a_0 > 0$, $a_1 > 0$, $a_2 < 0$ from which it is followed $T_{03} < T_0 < T_{02}$. The negative value of a_2 proves the main demand, which is function L . At $T \ll T_0$ $L_2 \rightarrow 0$, and at $T \gg T_0$ $L_2 \rightarrow I$.

The concrete crystal is need to define the parameter values a_0 , a_1 , a_2 and T_0 . for use of equations (3) - (7). The

values α_0 and T_0 are easily defined by the temperature dependences $\Delta T_\beta(T)$, $\sigma(T)$, $R(T)$, $\alpha(T)$ on the method, approved in the refs [3-9]. The obtained data $\alpha_0=0.17$; and $T_0=423$ are almost agree with the data of the refs [4,7,2]. The value α_1 can be calculated by the given experimental data with the use of ratio (8), and value α_2 is estimated from the condition of corporeality limit of the roots (10) and (11).

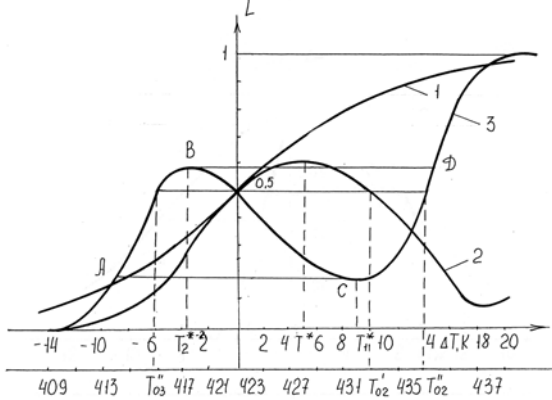


Fig.3. The temperature dependence of inclusion function in AgFeTe_2 1 - $L_0(T)$; 2 - $L_1(T)$; 3 - $L_2(T)$

The temperature dependences $L_1(T)$, $L_2(T)$ and dL_1/dT , dL_2/dT at the obtained values for AgFeTe_2 , $\alpha_0=0.17$; $\alpha_1=0.017$ and $\alpha_2=-0.002$ are given on the figures 3 and 4. The curves $L_0(T)$ and dL_0/dT at the zero approximation are given on these figures for the comparison. From the fig.3, it is seen, that $L_1(T)$ strongly differs from $L_0(T)$, especially in $T>T_0$ region. The curve $L_1(T)$ in the difference from $L_0(T)$ is asymmetrical in $T<T_0$ $L_1(T)$ region, $L_0(T)$ by the form looks like the curve $L_0(T)$, and in $T>T_0$ the extremum $\Delta T=T^*=5\text{K}$ takes place, which connects with the diffusion region of PT. The conditions of $L_1(T)$ in this region are carried out at $T>>T_0$ (curve $L_1(T)$), going through the minimum at $\Delta T=18\text{K}$, strives for $kL>>1$. The value of the observable asymmetry is defined by the value α_1 . The cross-section of horizontal line, taken from value $L_1=0.5$ (which is constant for every approximation), is equal to the temperature of second PT, $T_{02}=433\text{K}$. It is seen, that T^* is between the both temperatures $L_1(T)T_0=433\text{K}$, the ratio $T^*=T_0+\frac{\alpha_0}{2\alpha_1}=428\text{K}$ is in the agreement.

According to the refs [15, 16], the one of the physical meaning of such stroke $L_1(T)$ can be in the case of one phase existence in the definite temperature interval $(T_{02} - T_0)$ in PT region. The experimental data and temperature dependence $L_0(T)$ (fig.3) for AgFeTe_2 show on the absence of such ΔT region, which are represented on the figures 1 and 2. In this purpose says the law of α phase transition in β phase, established in the ref [7]. But informations about the existence of such regions at PT meet in the signet crystals σ [16]. This is one of the possibilities, that's why in the common case it is need to consider another approximations of inclusion function under its derivation.

The temperature dependence $L_2(T)$ for AgFeTe_2 , calculated on formulae (6) is given on the fig.3.

The look of this curve is strongly differs not only from curve $L_0(T)$, but the peaks situate on the left and right sides

from T_0 axis, moreover they are asymmetrical according to the axis. According to DPT theory [15,16] the experimental value L_2 corresponds to the temperatures

$$T_1^* = T_0 - \frac{a_1}{3a_2} + D \text{ and } T_2^* = T_0 - \frac{a_1}{3a_2} - D \quad (12)$$

where

$$D = \frac{1}{3a_1} \sqrt{a_1^2 - 3a_0a_2}$$

The ratio $T_1^* > T_0 > T_2^*$ takes place at $\alpha_0>0$, $\alpha_1>0$, the curve $L_2(T)$ is more asymmetrical and it tells on the values $T_1=9\text{K}$ and $T_2=4.4\text{K}$ correspondingly. The cross-section of horizontal line, taken from the point $L_2=0.5$ till the cross-section of the curve $L_2(T)$, corresponds to the temperatures of PT, $T_{02}=437\text{K}$, $T_{03}=417\text{K}$. The value for T_{02} , defined on $L_2(T)$ is bigger on the one degree, than on $L_1(T)$.

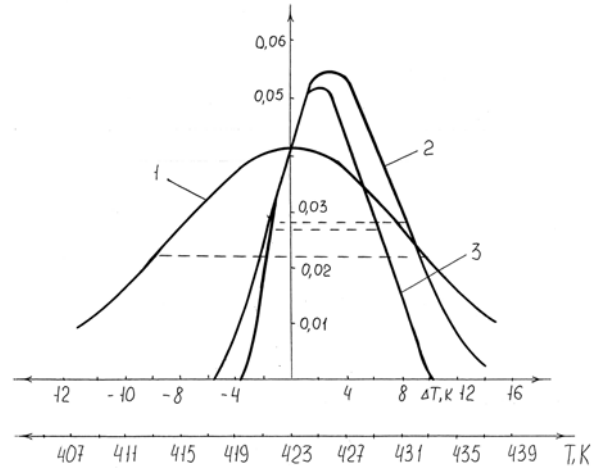


Fig. 4. Temperature dependence of PT velocity dL/dT in AgFeTe_2 1 - dL_0/dT ; 2 - dL_1/dT ; 3 - dL_2/dT

The temperature dependencies of the PT velocity in AgFeTe_2 in the zero dL_0/dT , first L_1/dT and second L_2/dT approximations of inclusion function are given on the fig.4. From these data the velocity asymmetry of transition reveals, i.e. maximums dL_1/dT and dL_2/dT aren't situated on the T_0 axis, but are shifted in the side $T>T_0$, the maximum values are significantly bigger, than dL_0/dT , moreover, the value $dL_1/dT > dL_2/dT$ is shifted to the side of big T maximums $d<1$. As it is mentioned, the asymmetry is defined by the value of dL_2/dT , in the expression of which (7) the parameter α_2 includes with the negative sign, that decreases the maximum value and shifts in the side of the more small T . According to theory, the horizontal line, taken on the half dL_0/dT , defines the diffusion region of PT. If the given method will be applied for dL_1/dT , dL_2/dT then we obtain dL_0/dT $2T^*=20\text{K}$ at dL_1/dT $2T^*=10.4\text{K}$ and at dL_2/dT $2T^*=9.5\text{K}$. As it is seen the values of diffusion region of PT at the first and second approximations are almost in two times less, than at the zero approximations. However, if we take into consideration the negative sides of dL_1/dT and

dL_2/dT , which aren't presented on the figure, then the agreement between data can be achieved.

The analysis of temperature dependence $L_2(T)$ gives in the ref [5], according to which one of the possible variants is that new phase appears in AB region (fig.3), disappears in BC region, and then it appears in CD region. The authors consider that such case is almost unreal however it is possible at the existence of several transitions, situated closely enough from each other on the temperature axis. However, the more possible is the case, which connects with the fact that BC region corresponds to some metastable system state in the definite interval.

Then, picturing BD and AC curves, we obtain the hysteresis loop ABDC.

The experimental data of electric and heat properties of double [3,6,8,9] and triple [4,7,9,11] argentum halcogenids show on the presence in them the additional PT[17]. That's why the given both mechanisms, leading to the appearance of phenomenon of hysteresis, can be applied not only to these crystals, but they even add each other.

The some information about PT diffusion and phenomenon of hysteresis can obtain from the data of hysteresis loop width. According to theory [15,16] the hysteresis loop width in the second approximation of $F_2(T)$ function is defined by the ratio

$$h_2 = T_{0_3} - T_{0_2} = 2\sqrt{\left(\frac{a_1}{2a_2}\right)^2 - \frac{a_0}{a_2}}. \quad (13)$$

From this formulae it is seen, that phenomenon of hysteresis takes place only at the inequality $\alpha_1 > 4\alpha_0\alpha_2$ carrying out and hysteresis loop width is defined by the ratio's α_1/α_2 . and α_0/α_2 . In the limit case of the loops the condition $\alpha_1 < -4\alpha_0\alpha_2$, the width $h_{m.c.}$ is defined as

$$h_{m.c} = 2\sqrt{-\frac{a_0}{a_2}\left(1 - \frac{a_1^2}{8a_0a_2}\right)} \quad (14)$$

In the case of symmetrical loops h is defined as

$$h_c = \lim_{a \rightarrow 0} \approx 2\sqrt{-\frac{a_0}{a_2}} \quad (15)$$

For crystals AgFeTe_2 , the h values, calculated on the formulas (13)-(15) are equal to $h_2=20k$, $h_{m.c}=19.4k$ and $h_c=18.4k$. In the experiment, the hysteresis width in the dependence on the investigated effect and temperature region (in PT region) changes, moreover in the several cases the hysteresis loops are strongly asymmetrical. But asymmetries $L_1^{(T)}$ and $L_2^{(T)}$ for AgFeTe_2 are bigger, than in the case of model consideration [15, 16]. In a particular, the hysteresis loop width, found from $\sigma(T)$ $h=25-30K$. It can be said, that agreement of calculated values of h and experimental ones is good, except from $\sigma(T)$. About the reason, leading to the additional PT diffusion we said above.

The one of the important questions of investigations is the definition of the region of two phase ΔT coexistence. In the case of zero approximation, the definition of region ΔT , $L_0(T)$ and dL_0/dT is more simple, than in the cases $L_1(T)$, $L_2(T)$ and dL_1/dT dL_2/dT .

For the symmetrical loops ΔT can be defined as ref. [15]:

$$\Delta T \approx 2(T_2^* - T_{0_3}) \approx 2(T_{0_2} - T_1^*) \quad (16)$$

For the loops with the small asymmetry with the exactness till the first order on α_1

$$T_{0_2} - T_1^* = \frac{1}{2}\left(1 - \frac{1}{\sqrt{3}}\right)h - \frac{a_1}{6a_2} \quad (17)$$

$$T_2^* - T_{0_3} = \frac{1}{2}\left(1 - \frac{1}{\sqrt{3}}\right)h + \frac{a_1}{6a_2} \quad (18)$$

For the total symmetrical loop $\alpha_1=1$ with the taking into consideration (13) as

$$\Delta T = \left(1 - \frac{1}{\sqrt{3}}\right)h = 0.42h. \quad (19)$$

The calculations, done on (17) and (18) with the taking into consideration of corresponding h for AgFeTe_2 , correspond to the values:

$$T_{0_2} - T^* = 5.5K, \quad T_2^* - T_{0_3} = 2.7K.$$

These data are in the agreement with the data on the fig.3. Thus, for the region of two phase coexistence we obtain: on $\Delta T = 2(T_{0_2} - T_1^*) = 11K$, on $\Delta T = 2(T_2^* - T_{0_3}) = 5.4K$ and in the case of total symmetry on $\Delta T = 0.42h_2 = 7.73K$.

These data show on the strong asymmetry of hysteresis loop in AgFeTe_2 , and also show that temperature interval ΔT of two phase coexistence is less, than hysteresis loop width. From these data, it is followed, that coexistence interval.

Thus, from the given results and discussions, it is concluded, that taking into consideration the members of temperature difference $(T-T_0)$ in the function $F(x)$, defining the inclusion function $L_2(T)$, leads to the appearance of hysteresis.

The process carries out on the ACD curve at the heating and the process carries out on DBA curve at the cooling. The stroke along parts AB (at the heating) and DC (at the cooling) isn't benefit energetically, i.e. leads to the creation of BC metastable state region. From the above mentioned, it is followed, that thermodynamic formalism of DPT gives the principal possibility to explain the hysteresis presence. At the same time as in the limits of the general thermodynamic approach for point PT, the hysteresis interpretation is impossible without input of additional supposition.

- | | |
|---|--|
| <p>[1] S.A.Aliev, F.F.Aliev. Neorg. Mater., 1989, 25, 2, 241. (in Russian).</p> <p>[2] S.A.Aliev, F.F.Aliev, G.P.Pashaev. Neorg. Mater., 1993, 29, 8, 1073. (in Russian).</p> <p>[3] S.A.Aliev, F.F.Aliev, Z.S.Gasanov. FP, 1998, 4, 9, 1693. (in Russian).</p> <p>[4] S.A.Aliyev, Z.S.Gasanov, S.M.Abdullayev. Fizika Ins. Phys. NANA VIII 3,24, 2002</p> <p>[5] Z.S.Gasanov, S.M.Abdullaev, S.A.Aliev. Az. Resp.Az. Univ. Nauch. Trudi fund. nauk., 3, 93, 2002. (in Russian).</p> <p>[6] S.A.Aliev, Z.S.Gasanov, Z.F.Agaev, R.K.Guseynov. AMEA, Izv. XXII 5, 76, 2002. (in Russian).</p> <p>[7] F.F.Aliev, E.M.Kerimova, S.A.Aliev. FTP, 2002, 36, 8, 932. (in Russian).</p> <p>[8] Prof. Dr. Habil. Sabir Aliyev, Dr. Ziraddin Gasanov. Abhandlunden dez WGB, Band 3, 98, Berlin 2003.</p> <p>[9] Prof. Dr. Habil. Sabir Aliyev, Dr. Ziraddin Gasanov, Dr. Zakir Agayev. Dipl-Phys. Rasim Guseynov Abhandlunden dez WGB, Band 3, 103, Berlin 2003</p> | <p>[10] C.A.Aliev, З.С.Гасанов, С.А.Абдуллаев, Р.К. Гусейнов. Azer. Tekn. Univ. Nauch. Trudi, Fun., 4, 103, 2002. (in Russian).</p> <p>[11] S.V.Melnikova, A.V.Kartashev, V.A.Grankin, I.N.Flerov. FP, 2003, 45, 8. (in Russian).</p> <p>[12] Z.S.Gasanov. Nauch. trudi. MPGI.sb.stat.izd.Nauka, 200, 2003. (in Russian).</p> <p>[13] Z.S.Gasanov. Nauch. trudi. MPGI.sb.stat.izd.Nauka, 205, 2003. (in Russian).</p> <p>[14] F.F.Aliev. FTT, 2003, 37, 9. (in Russian).</p> <p>[15] B.N.Rolov. Razmishiye fazoviye perekhodi, 311s, Riga 1972. (in Russian).</p> <p>[16] B.N.Rolov, V.E.Jurkevich. Fizika razmitikh fazovikh perekhodov. Izd. Rostovskogo Universiteta. 319s. 1983.</p> <p>[17] S.A.Aliev. FTP, 2004, t. 38, vip. 7, s. 830. (in Russian).</p> <p>[18] S.A.Aliev, Д. Г.Араслы, etc. Izv. AN Azerb. SSR, ser.. Fiz.-mat I tekhn. nauk 6, 87, 1982. (in Russian).</p> |
|---|--|

S.A. Əliyev, Z.S. Həsənov, S.O. Məmmədova

AgFeTe_2 KRİSTALINDA FAZA KEÇİDİ OBLASTINDA HİSTEREZİS HADİSƏSİ

AgFeTe_2 kristalında diferensial termiki analiz aparılmış və elektrik xassələri tədqiq olunmuşdur. SFK-dən əvvəl və sonra DTA asılılığında əlavə FK müşahidə olunmuşdur. FK oblastında elektrik xassələrin temperatur asılılığında qızma və soyuma zamanı histerezis müşahidə olunmuşdur. Nəticələr yayılmış faza keçidi nəzəriyyəsi əsasında təhlil olunmuşdur. Histerezis hadisəsi qoşulma funksiyasının və onun ikinci yaxınlaşmada yayılma sürətinin temperatur asılılığı ($L_2(T)$ və dL_2/dT) ilə izah olunur. FK-nın yayılma oblastı və histerezis ilgəyinin eni təyin olunmuşdur. Fazaların mövcud olduğu oblastın histerezis ilgəyinin eni ilə mütənasib olduğu göstərilmişdir.

С.А. Алиев, З.С. Гасанов, С.О. Мамедова

ЯВЛЕНИЕ ГИСТЕРЕЗИСА В AgFeTe_2 В ОБЛАСТИ ФАЗОВОГО ПЕРЕХОДА

Исследованы электрические свойства и проведен дифференциальный термический анализ в AgFeTe_2 . На температурной зависимости ДТА до и после СФП обнаружены дополнительные ФП. На температурных зависимостях электрических свойств в области ФП в направлении нагрева и охлаждения обнаружено явление гистерезиса. Результаты интерпретированы в рамках теории РФП. Показано, что явление гистерезиса объясняется температурной зависимостью функции включения во втором приближении $L_2(T)$ и dL_2/dT . Определены области размытия ФП и ширина петли гистерезиса. Показано, что область сосуществования фаз пропорциональна ширине петли гистерезиса.

Received: 01.07.04

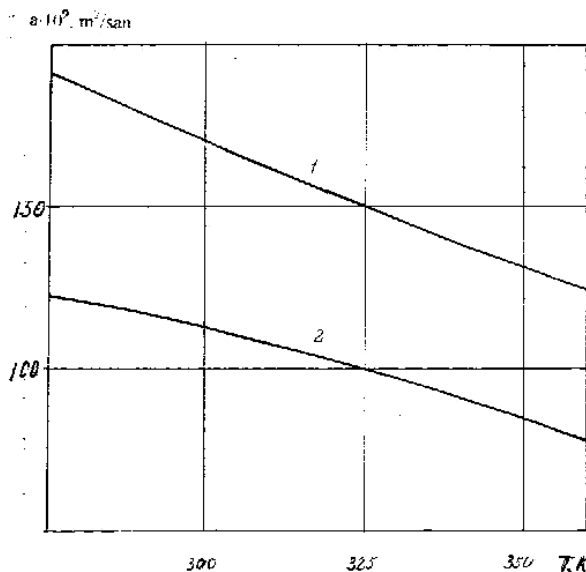
ÜZÜM MƏMULATLARININ TEMPERATURKEÇİRMƏ ƏMSALI VƏ PRANDTL ƏDƏDİ

A.D. ƏLİYEV

Azərbaycan Texnologiya Universiteti
374711, Azərbaycan, Gəncə, 28 May küç. 103.

Məqalədə istilik mübadiləsində çox vacib olan Prandtl ədədi və temperaturkeçirmə əmsalı Azərbaycanın üzüm məmulatları üçün hesablanıb. Onların temperatur asılılıqları ayrı-ayrı məmulatlardan ötrü göstərilib.

Azərbaycanda xeyli miqdarda spirtli içkilər hazırlanır. Onların istehsalını təkmilləşdirmək və keyfiyyətlərini yüksəltmək və saxlanılmasının optimal rejimini təyin etmək üçün hazırlanan və hazır olan məhsulun termodinamik və köçürmə xarakteristikalarını bilmək vacibdir [1-5], o cümlədən temperaturkeçirmə əmsalını və Prandtl ədədini. Azərbaycanın bəzi üzüm məmulatlarının sıxlığı ρ , izobar istilik tutumu C_p , istilikkeçirmə əmsalı λ və dinamik özlülük əmsalı η üzüm spirt, çaxırlar (turş və şirin) və konyaklar üçün ətraflı öyrənilib [6-11]. Bu imkan verir ki, onların temperaturkeçirmə əmsalını (a) və Prandtl ədədini (Pr) də hesablayasan. Bu kəmiyyətlərin məlum olması həm nəzəri, həm də praktiki əhəmiyyət daşıyır. Ona görə də məqalədə a və Pr kəmiyyətləri hesablanıb və nəticələr uyğun olaraq cədvəl 1 və 2-də verilib. Nümunə kimi bəzi üzüm məhsulları üçün nəticələr şəkil 1 və 2-də nümayiş etdirilib.



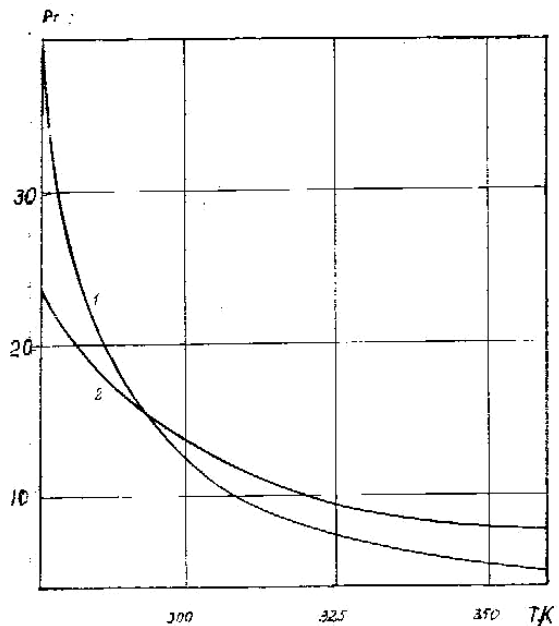
Şəkil 1. Üzüm məmulatlarının temperaturkeçirmə əmsalının temperaturdan asılılığı; 1 – Göy-göl konyakı; 2 – üzüm spirt.

Öncə ρ , C_p , λ və η üzrə alınmış məlumatlar mütləq temperaturun yuvarlaq qiymətləri üçün qrafoanalitik üsulla işlənmiş və hazırlanmışdır.

a və Pr kəmiyyətləri aşağıdakı düsturla hesablanmışdır:

$$\alpha = \frac{\lambda}{\rho C_p} \quad (1)$$

$$Pr = \frac{\eta C_p}{\lambda} \quad (2)$$



Şəkil 2. Üzüm məmulatlarının Prandtl ədədinin temperaturdan asılılığı: 1 – Göy-göl; 2 – üzüm spirt.

Cədvəl 1-dəki məlumatların təhlili göstərir ki, temperaturkeçirmə əmsalı temperatur artdıqca turş çaxırlar üçün mülayim yüksəlir (temperatur əmsalı kiçik olur), üzüm spirt, konyaklar və Alabaşlı çaxırı üçün zəif də olsa azalır. Portveyn və Ağdam çaxırlarında temperatur artdıqca a əvvəl azalır, sonra minimumu keçərək artmağa başlayır. Ağ Qarabağ çaxırında a həmişə yüksəlir. Bu hadisə spirtli içkilərin mürekkəb tərkibli olması və molekullar arasında əlaqə qüvvəsinin təbiyyətindən asılıdır. Qeyd edək ki, çaxırların tərkibində su, spirt (əsasən etil və az miqdarda metil spirt), şəkər (şirin çaxırlarda daha çox) və müxtəlif ekstraktlar var.

Pr ədədi bütün çaxır məmulatları üçün temperatur yüksəldikcə intensiv azalır. Bu əsasən özlülüyn dəyişməsilə əlaqədardır. Ona görə də alçaq temperaturalarda Prandtl ədədi yüksək olur.

Praktikada bəzən Angeleskunun [12] təxmini tənliyindən istifadə olunur:

$$\rho C_p = \text{const} \quad (3)$$

Cədvəl 1. Azərbaycan çaxırlarının temperaturkeçirməsi, $\alpha \cdot 10^{10}$, m²/san.

Çaxır	T,K								
	275	290	300	310	320	330	340	350	360
Mədrəsəli	1298	1375	1428	1482	1529	1577	1623	1669	1714
Al şərab	1239	1331	1385	1439	1484	1537	1578	1624	1664
Xindoqni	1396	1457	1496	1538	1571	1615	1659	1702	1744
Ağ Qarabağ	1501	1553	1588	1636	1704	1801	1920	2058	2184
Alabaşlı	2124	2004	1940	1884	1834	1788	1739	1694	1653
Partveyn 777	1821	1744	1702	1677	1667	1661	1673	1716	1806
Ağdam	1995	1905	1864	1841	1823	1825	1843	1865	1950
Üzüm spirti	1232	1178	1131	1081	1028	965	903	844	783
Göy-göl	1919	1781	1701	1617	1536	1455	1377	1307	1234

Cədvəl 2. Azərbaycan çaxırları üçün Prandtl ədədi

Çaxır	T,K								
	275	290	300	310	320	330	340	350	360
Mədrəsəli	17,56	10,62	8,074	6,317	5,131	4,294	3,644	3,177	2,788
Al şərab	30,38	12,59	9,247	7,143	5,670	4,529	3,760	3,196	2,626
Xindoqni	20,70	10,61	7,966	6,144	4,978	4,176	3,553	3,161	2,834
Ağ Qarabağ	29,04	14,87	10,470	7,797	6,012	4,698	3,662	2,953	2,449
Alabaşlı	26,60	13,96	10,420	8,080	6,589	5,520	4,685	4,039	3,552
Partveyn 777	26,47	14,78	10,760	8,366	6,713	5,538	4,626	3,828	3,124
Ağdam	24,36	13,38	9,637	7,503	6,043	4,957	4,073	3,415	2,776
Üzüm spirti	24,26	16,69	13,750	11,740	10,170	8,973	8,279	7,804	7,813
Göy-göl	40,03	17,51	12,230	9,640	8,049	6,846	5,980	5,2999	4,804

Bu düsturu üzüm məhsullarına tətbiq etdikdə çox böyük xəta alınır və onlar üçün temperatur artdıqca (ρC_p) daim yüksəlir. Məsələn, temperatur 275-dən 350K-ə qədər dəyişdikdə (ρC_p) 30-70% artır. Əgər (3) düsturu əvəzinə $k=(\rho C_p)_{350}/(\rho C_p)_{275}$ nisbətini götürsək görürük ki, bu nisbət turş çaxırlar üçün sabit qalacaq və təxminən $k \approx 1,32$ olacaq. Alabaşlı, Partveyn 777 və Kürdəmir çaxırları üçün $k \approx 1,64$.

Veber [13] 50 təmiz mayelər üçün apardığı təcrübələr əsasında belə bir empirik ifadə vermişdir

$$\frac{\lambda}{\rho C_p} \left(\frac{M}{\rho} \right)^{1/3} = A = const, \quad (4)$$

burada M – molekulyar kütlədir.

$(M/\rho)^{1/3}$ həddi molekulların mərkəzləri arasındakı orta məsafəyə mütənəsbidir. Veberə görə sabit $A=0,21$ (burada λ -nın ölçü vahidi $\text{kal}/(\text{sm} \cdot \text{d}^{\circ}\text{C} \cdot \text{d}^{\circ})$ -dir). Yoxlama göstərir ki, təcrübə nöqtələri (4) asılılığından çox kənara çıxır.

Sonralar Predvoditelev [14] yenidən (4) ifadəsini nəzəri yolla çıxarmış və isbat etmişdir ki, $A=f(T)$. Burada A – invariantdır. O, mayenin növündən asılı deyil. Bu asılılığı maye sinifləri üçün işlətmək əlverişlidir. Onu quruluşu və tərkibi çox müəkkəb olan üzüm məmulatlarına tətbiq etdikdə müsbət nəticə alınmır. $A(T)$ kəmiyyətinin temperatur əmsalı ayrı-ayrı çaxır məhsulları üçün kəmiyyətə və keyfiyyətə fərqlənir.

- | | |
|---|--|
| <p>[1] Г.Г. Валуйко. Справочник по виноделию. М.: Агропромиздат. 1985., 447с.</p> <p>[2] А.С. Гинзбург, М.А. Громов, Г.И. Красовская. Теплофизические характеристики пищевых продуктов. М.: Пищевая промышленность. 1980, 226.</p> <p>[3] З.Н. Килковский, А.А. Мержаниан. Технология вина. М.: Легкая и пищевая промышленность. 1984, 504с.</p> <p>[4] В.А. Субботин, С.Т. Тюрин, Г.Г. Валуйко. Физико-химические показатели вин и виноматериалов. М. Пищевая промышленность. 1972, 161с.</p> <p>[5] Н.Р. Аскеров. Теплофизические свойства виноградных изделий Азербайджана. Автор. дисс... канд. техн. наук. Баку. АзИнефтехим. 1987, 22с.</p> <p>[6] Я.М. Назиев, А.А. Абасов, А.Д. Алиев. Теплопроводность винных изделий Азербайджана. Уч. записки. АзТУ. 1994, №2, с.71.</p> <p>[7] Я.М. Назиев, А.Д. Алиев, А.А. Мирзалиев. Исследование плотности продуктов виноделия Азербайджана. Уч. зап. АзТУ. 1993, №4, с.80.</p> <p>[8] Я.М. Назиев, А.Д. Алиев, М.А. Талыбов. Исследование изобарной теплоемкости продуктов виноделия Азербайджана. Уч. зап. АзТУ. 1995, №1, с. 96.</p> | <p>[9] Я.М. Назиев, А.Д. Алиев, М.А. Талыбов, А.А. Абасов, Ш.Г. Шахмурадов, А.А. Мирзалиев. Исследование теплофизических свойств винных изделий Азербайджана. Матер. 43-ей научно-техн. и методолог. конференции. Баку. АзТУ. 1995. с.109.</p> <p>[10] Я.М. Назиев, М.А. Талыбов, А.Д. Алиев. Исследование изобарной теплоемкости некоторых виноградных изделий Азербайджана. НАН Азербайджана. Проблемы энергетики. Баку. Элм. 2002. с. 88.</p> <p>[11] В.Г. Гасанов, Дж. Я. Назиев, А.Д. Алиев. Исследование PVT – зависимости виноградного спирта при различных параметрах состояния. Научн. Труды АзТУ. Фундаментальные науки. 2003. №2, с.20.</p> <p>[12] Д. Anghelescu. Rev. CJ. Parho si politehn. Bucueresti. Ser. Stand. nature. 1953. №3. p.132.</p> <p>[13] H.F. Weber. Das Wärmeleitungsvermögen der tropfbaren Flüssigkeiten sitrungs Berichte der Kanigloch Preussichen. Akademik der Wissenschaften. Berlin. 1885. H.2, s. 809.</p> <p>[14] А.С. Предводителев. О некоторых инвариантных количествах в теории теплопроводности и вязкости жидкостей. ЖФХ. 1948. т. 22, №3, С.339.</p> |
|---|--|

A.D. Алиев

КОЭФФИЦИЕНТ ТЕМПЕРАТУРОПРОВОДНОСТИ И ЧИСЛО ПРАНДТЛЯ ВИНОГРАДНЫХ ИЗДЕЛИЙ

В статье рассмотрены экспериментальные данные по теплофизическим свойствам виноградных изделий Азербайджана и на базе их вычислены коэффициент теплопроводности и число Прандтля в зависимости от температуры.

A.D. Aliyev

THERMAL CONDUCTIVITY COEFFICIENT AND PRANDTL'S NUMBER OF GRAPE PRODUCTS

In given paper the experimental data on thermal physical properties of grape products of Azerbaijan are considered and on the basis of them thermal conductivity coefficient and Prandtl 's number in dependence on temperature are calculated.

Received: 14.09.2004

IMPROVING OF HISTOGRAM PARAMETERS OF MAGNETITE NANOPARTICLES DISTRIBUTION ON SIZE

R.A. ALI-ZADE, R.R. HUSEYNOV

*Institute of Physics Azerbaijan National Academy of Sciences,
Baku Az-1143, H. Javid str. 33*

Histogram of magnetite nanoparticles distribution on size has been constructed on the base of their vicinity to firing ground frequency. Future parameters of histogram of distribution have been improved by least square method. Constructed histogram of distribution has been applied to calculation of moments of distribution and magnetization curve of system of magnetite nanoparticles. Analysis of obtained result showed, that constructed histogram is more accurate describe disperse system of magnetite nanoparticles.

1. Introduction.

Distribution of particles of disperse systems on size is one of base physical characteristics of these systems. Distribution function is used to determination of physical parameters of disperse systems by its statistical averaging, it allows to analyze mechanism of particle growth and to describe behavior of these systems in external field and etc. Nanoparticle size distribution function has been determined by different physical methods [1-7]. Magnetic granulometry, dynamical laser light scattering, acoustics spectrometry and small X-ray scattering methods have determined size distribution function of magnetite nanoparticles on size. These all methods are based on measurement of intensity of physical parameters, related with the size distribution of nanoparticles. By this methods will obtain distribution functions of nanoparticles on magnetic, brown diameter and etc. In this case, magnetic and brown diameter of nanoparticles is necessary transfer to their geometrical diameter. For this calculations it is necessary value of thickness of nonmagnetite layer, length of stabilizer molecule and etc. [2,3,5,9-12].

At present work histogram of distribution of magnetite nanoparticles on size has been constructed. Parameters of histogram have been improved by least square method. Moments and parameters of distribution, magnetization curve of systems of magnetite nanoparticles has been obtained by experimental and calculated by frequency firing ground and histogram distributions without and with improved parameters. Results of investigation showed, that moments of distribution and magnetization of disperse systems of magnetite nanoparticles calculated by histogram with improved parameters are more near corresponding

parameters obtained by frequency firing ground and experimental.

2. Determination histogram of distribution of nanoparticles on size.

One of criterion of construction accurate histogram of some parameter distribution of disperse system may be vicinity of intensity of parameters of disperse systems calculated by statistical averaging with this histogram and frequency firing ground, respectively.

Theorem: If the constructed histogram of distribution and frequency firing ground of some parameters of disperse system are in the vicinity to each other, then characteristics of disperse system determined by this histogram and frequency firing ground will be vicinity each other too.

Proof: The vicinity of two discrete functions (histogram and frequency firing ground) will be estimated by the following formula

$$\rho(P, H) = \sum_{i=1}^n |P(r_i) - H(r_i)| \leq \delta \quad (2.1)$$

where $P(r)$ and $H(r)$ the frequency firing ground and histogram of distribution on parameters " r ", respectively.

We inequality (2.1) will transform in the following way. Both parts of inequality (2.1) multiplied to $G(r, E_j)$. $G(r, E_j)$ is the function " r ", " E " described as one of physical characteristics of disperse system. For all values of arguments " r ", " E_j " $G(r, E_j) \geq 1$. This inequality (2.1) may be generalized to all values of " E_j ". Then obtain:

$$\begin{aligned} \rho(P, H) &= \sum_{j=1}^m \sum_{i=1}^n |P(r_i) - H(r_i)| \cdot G(r_i, E_j) \leq \delta_1 \\ \rho(P, H) &= \sum_{j=1}^m \sum_{i=1}^n |P(r_i) - H(r_i)| \cdot G(r_i, E_j) = \\ &= \sum_{j=1}^m \sum_{i=1}^n \left\{ |P(r_i) \cdot G(r_i, E_j) - H(r_i) \cdot G(r_i, E_j)| \right\} = \\ &= \sum_{j=1}^m \sum_{i=1}^n |P(r_i) \cdot G(r_i, E_j)| - \sum_{j=1}^m \sum_{i=1}^n |H(r_i) \cdot G(r_i, E_j)| \end{aligned}$$

As $P(r)$, $H(r)$ and $G(r, E_j) \neq 0$ for all values of arguments “ r ”, “ E_j ” and in definition:

$$I_P(E_j) = \sum_{i=1}^n G(r_i, E_j) P(r_i)$$

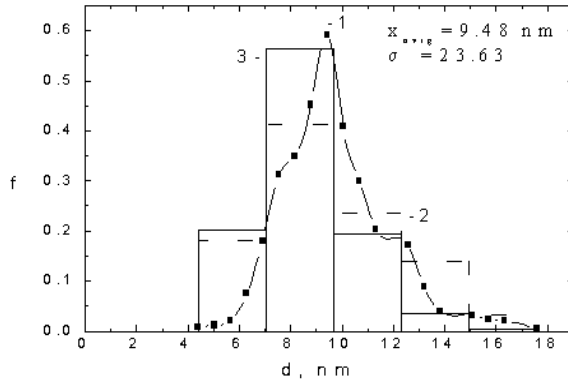
and

$$I_H(E_j) = \sum_{i=1}^n G(r_i, E_j) H(r_i)$$

These last expressions are statistical averaging of $G(r, E_j)$ on parameter “ r ” by histogram ($H(r)$) and frequency firing ground ($P(r)$), respectively. Taking into account last expressions we obtain:

$$\sum_{j=1}^m |I_P(E_j) - I_H(E_j)| \leq \delta \quad (2.2)$$

Thus the inequality (2.2) is condition of vicinity of $I_P(E_j)$ and $I_H(E_j)$, which was to be proved.



It's known, that all constructed distribution functions, histograms must have different and non-zero values at all considered values of argument [13]. Thus, numbers of histograms, which may be constructed on the base of conditions [13] and (2.1) are limited.

3. Results and discussion.

Four samples of magnetite nanoparticles have been investigated [14-16]. Improved histogram data, determined by above mentioned method are $(f; x)_I = (0.2; 0.203)$, $(0.4; 0.563)$, $(0.6; 0.194)$, $(0.8; 0.036)$, $(1.0; 0.004)$, $(f; x)_{II} = (0.25; 0.664)$, $(0.5; 0.247)$, $(0.75; 0.08)$, $(1.0; 0.009)$, $(f; x)_{III} = (0.167; 0.121)$; $(0.334; 0.403)$; $(0.54; 0.293)$; $(0.667; 0.123)$; $(0.833; 0.05)$; $(1.0; 0.01)$, $(f; x)_{IV} = (0.2, 0.304)$; $(0.4, 0.46)$; $(0.6, 0.197)$; $(0.8, 0.035)$; $(1.0, 0.004)$ for samples I-IV, respectively. In fig.1(a,b) there have been presented curve frequency firing ground (curve 1), distribution histograms magnetite nanoparticle samples I without (curve 2) and with improved data (curve 3).

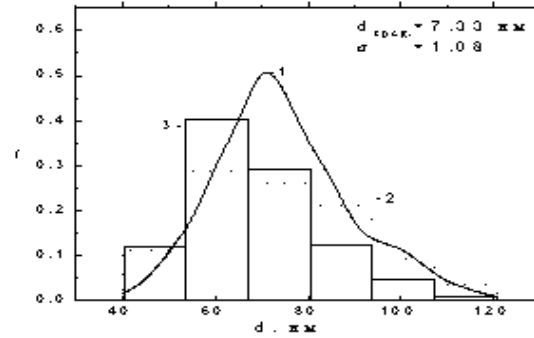


Fig.1(a,b). Curve frequency firing ground (1) [14], distribution histogram without (2) and with (3) improved parameters of magnetite nanoparticle sample –I (a). –II (b).

In table 1 there have been shown moments and parameters of distribution calculated by frequency firing ground, histogram without and with improved parameters and relative errors of calculations. As it is seen from table, moments and parameters of distribution calculated by histogram are more accurate.

In fig.2 there have been shown magnetization curves, obtained by experiment, calculated by Langevin equation using frequency firing ground, histogram, without and with improved parameters. As it is seen from fig.2 magnetization curve, calculated by histogram with improved parameters is closer to experimental magnetization curve and curves calculated by frequency firing ground.

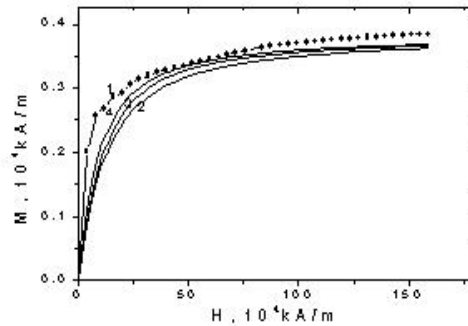
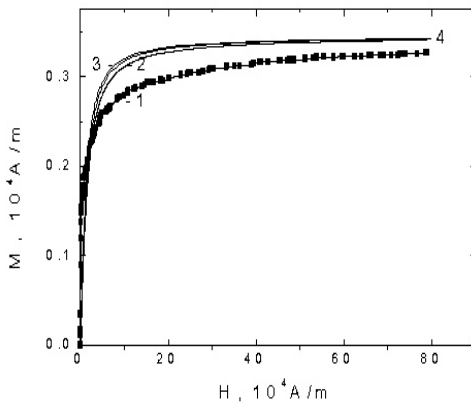


Fig.2 Magnetization curves of magnetite nanoparticle samples –I and –II obtained by experimental (1) [15,16], calculated by equation (4.1) using frequency firing ground (2), distribution histogram without (3) and with (4) improved parameters.

IMPROVING OF HISTOGRAM PARAMETERS OF MAGNETITE NANOPARTICLES DISTRIBUTION ON SIZE

Thus, analysis of carried out investigations shown, that for monodisperse systems it may be constructed one and accurate histogram describing distribution of nanoparticles on size. Physical parameters (moments, parameters of distribution, magnetization of disperse systems of magnetite

nanoparticles) of disperse systems may be calculated more accurately and rapidly by this histogram. Thus, it is established, that histogram of distribution with improved parameters more convenient and more exactly describes distribution of magnetite nanoparticles.

Table 1.
Initial moments of distribution magnetite nanoparticles samples I-IV, calculated by firing ground of frequency, histogram without and with improved parameters

N	Moments and parameters of distribution calculated by firing ground frequency (1)	Relative error of calculation of moments by histogram without (2) and with (3) improved parameters		Moments and parameters of distribution calculated by firing ground frequency (1)	Relative error of calculation of moments by histogram without (2) and with (3) improved parameters	
	1	2	3	1	2	3
I sample				II sample		
\bar{x}	.94807E+02	.1406	.0413	.77570E+02	.1706	.0375
\bar{x}^2	.95468E+04	.3035	.0625	.65486E+04	.3402	.0516
\bar{x}^3	.10200E+07	.4885	.0634	.60048E+06	.5031	.0526
\bar{x}^4	.11541E+09	.6924	.0457	.59517E+08	.6551	.0491
\bar{x}^5	.13788E+11	.9094	.0135	.6328E+10	.7949	.0461
\bar{x}^6	.173224E+13	1.1322	.0286	.715167E+12	.9239	.0453
\bar{x}^7	.227792E+15	1.3529	.0756	.851209E+14	1.0452	.0466
\bar{x}^8	.311936E+17	1.5651	.1234	.105799E+17	1.1617	.0492
\bar{x}^9	.442499E+19	1.7644	.1691	.136342E+19	1.2752	.0523
\bar{x}^{10}	.646957E+21	1.9488	.2106	.181099E+21	1.3862	.0556
III sample				IV sample		
\bar{x}	.733193E+02	.095	.024	.54401E+02	.108	.048
\bar{x}^2	.566779E+04	.190	.031	.30949E+04	.222	.077
\bar{x}^3	.461060E+06	.281	.023	.18391E+06	.344	.087
\bar{x}^4	.393497E+08	.367	.004	.11395E+08	.474	.080
\bar{x}^5	.350948E+10	.447	.023	.73457E+09	.612	.058
\bar{x}^6	.325578E+12	.518	.055	.491326E+11	.755	.024
\bar{x}^7	.312638E+14	.582	.087	.339946E+13	.901	.018
\bar{x}^8	.309242E+16	.640	.118	.242519E+15	1.047	.064
\bar{x}^9	.313672E+18	.693	.147	.177805E+17	1.190	.119
\bar{x}^{10}	.324975E+20	.742	.171	.133542E+19	1.329	.159

- [1] C.G. Granqvist, R.A. Buhrman J. Appl. Phys. 47, 1976, p. 2200-2220.
- [2] R. Kaiser, G. Miskolze, J. Applied Physics v.41, n.3, pp.1064-1072, 1970
- [3] E.E. Bibik, B.Ya. Matigullin, Yu.L. Rayxer., and et al. Magnitnaya gidrodinamika 1, 1978, p.68.
- [4] R. Anthore, C. Petipas J. de Physique, Colloque C2 supplement, v. 38, n. 7, 1977, C2-203- C2- 209
- [5] U. Neitzel, K. Barner. Physics Letters v63A, N3, 1977, p.327-329.
- [6] R.Pecora. Dynamic J. Nanoparticle Research, v. 2, n. 2, 2000, p. 123-131.
- [7] A.N. Vinogradov. J.Physial Chemistry (in Russian), 2000, v.74, n. 7, p. 1320-1323.
- [8] A.N. Tixonov, V.Ya. Arsenin. Metodi resheniya nekorrektnich zadach. M.: Hayka 1986, 288p. 3td edition.
- [9] R.A. Ali-zade. Transactions of Academy of Sciences of Azerbaiajn, 2000, v. XX, n. 2, p. 88-94.
- [10] R.A.Ali-zade. VINITI 2636-B93, 23p.

- [11] *R.A. Ali-zade*. Abstract Book of the 9th International Conference on Magnetic Fluids, Bremen, Germany, 2000.
- [12] *A.J. Gordon, R.A. Ford* The chemist's companion. A handbook of practical data, techniques and references. A Wiley-Interscience publication. New York, London, Sydney, Toronto, John Wiley & Sons, 1972.
- [13] *W. Feller*. An introduction to probability theory and its applications. Third edition, New York, Chichester, Brisbane, Toronto, John Wiley & Sons, 1970.
- [14] *A.N. Buryakov, I.A. Gritskova, V.P. Zubov, et al.*, Sposob polycheniya magnitonapolnennich polimerov. USSR Inventor's Certificate N. 1628478, Byull. Izobret., 1991, N. 6, p.194.
- [15] *S.I. Turkin, Yu.V. Lukin, E.A. Markvicheva, et al.*, Sposob polycheniye jelatinovich mikronositeley dlya kultivirovaniya kletok, USSR Inventor's Certificate N.1486515, Byull.Izobret.,1989,N. 22,p.100.
- [16] *S.I. Turkin, Yu.V. Lukin, E.A. Markvicheva, et al.*, Sposob polycheniye magnitnich mikronositeley dlya kylvitirovaniya kletok, USSR Inventor's Certificate no. 1 567 623, Byull. Izobret., 1990, n. 20, p. 105.

R.Ə. Əli-zadə, R.R.Hüseynov

NANOÖLÇÜLÜ MAQNÉTİTLƏRİN ÖLÇÜLƏRƏ GÖRƏ HİSTOQRAM PAYLANMASININ PARAMETİRLƏRİNİN TƏKMİLLƏŞDİRİLMƏSİ

Nanoölçülü maqnetitlərin ölçülərə görə histoqram paylanması onun tezliklər poliqonuna daha yaxın olması şərti əsasında təyin olunmuş və daha sonra onun parametrləri ən kiçik kvadrlar metodu ilə dəqiqləşdirilmişdir. Təyin olunmuş histoqram paylanması paylanmanın momentlərini və nanoölçülü maqnetitlər sisteminin maqnitləşmə əyrisini hesablanmasında istifadə olunmuşdur. Alınmış nəticələr bu üsulla təyin olunmuş histoqramın dispers sistemlərin paylanmasını daha düzgün xarakterizə etdiyini təsdiq etdi.

Р.А. Али-заде, Р.Р. Гусейнов

УЛУЧШЕНИЕ ПАРАМЕТРОВ ГИСТОГРАММЫ РАСПРЕДЕЛЕНИЯ НАНОЧАСТИЦ МАГНЕТИТА ПО РАЗМЕРАМ

Гистограмма распределения наночастиц магнетита по размерам была построена на основе его близости по полигону частот. Параметры гистограммы улучшены методом наименьших квадратов. Полученная гистограмма распределения использована для определения моментов распределения и намагничивания дисперсных систем наночастиц магнетита. Анализ полученных результатов доказали, что полученная таким способом гистограмма более точно описывает распределение дисперсных систем.

Received: 16. 11. 2004.

THE MEASUREMENTS OF DIELECTRIC PROPERTIES OF ACETONITRILE-BENSOLE SOLUTIONS IN THE MICROWAVE REGION

S.T. AZIZOV, M.A. SADICHOV, Ch.O. KADJAR

*Institute of Physics of National Academy of Sciences of Azerbaijan,
AZ-1143, H. Javid av., 33*

The results of the measurement of the dielectric properties of solutions, technique and definition algorithm ε' , ε'' are given in the article. The existence of the concentration spectrum in these solutions, at which the chosen nonreflecting absorption of the falling radiation appears, it is established.

Introduction

The investigations of dielectric properties of polar liquid solutions in the region of their wave dispersion allow to obtain the information about their molecular structure. Besides, as it is shown in the ref [1], these investigations give the possibility to study the revealing of nonreflecting absorption of electromagnetic radiation, which reveals in the dissolved solutions of polar molecules.

Technique of investigation

In this connection, the investigations of solution dielectric characteristics of acetonitrile-bensole in the microwave range, at $\lambda=1,5$ cm and temperature $T=20^\circ\text{C}$ have been carried out.

The measurements are carried out on the installation, working at the wave length $\lambda=1,5\text{sm}$. In the installation, the panoramic meter of stationary wave P2-66 and indicator device JA2P-67, are used. The acetonitrile-bensole solution is put in the specially constructed short-circuit measuring waveguide cell on the end the last is thermostated and includes the mechanism of smooth regulation of layer width.

The obtained experimental data about minimums of taken dependence η on l , and also η_∞ are used for the calculation of ε' , ε'' . For their finding, the method, based on the information parameter measurement of taken dependence of stationary wave coefficient η on the substance layer width, taken in the experiment has been applied. These parameters are substance layer widths l_m and value η_m in the minimal points of $\eta(l)$ function, and also the values η_∞ at the liquid widths, at which the η value reaches its limit value η_∞ . The necessity in the usage of η_∞ at the definition of ε' , ε'' of strongly absorbing polar liquids and their solutions, which ?

The algorithm and realizing its calculation program, working in the dialogue mode of the investigator with the personal computer IBM have been treated. They base on the use of data in the refs [2,3,4] of equations, establishing the functional connection between measure η_m , l_m , η_∞ and decisions ε' , ε'' parameters, which is equitable for every number N of function minimum $\eta(l)$. The following equations are used for abnormal region (6) of function $\eta(l)$,

$$\varepsilon_1 = n^2(1 - y^2); \quad \varepsilon_2 = 2n^2 y; \quad \varepsilon_1 = (\varepsilon' - p)/(1 - p); \quad \varepsilon_2 = \varepsilon''/(1 - p) \quad (1)$$

$$x = \frac{l_m}{\lambda_g} = \frac{l \cdot n}{\lambda_b}; \quad x = \frac{2N - 1}{4} + \Delta; \quad \lambda_b = \frac{\lambda}{\sqrt{1 - p}} \quad (2)$$

$$\Delta = \frac{1}{2\pi} \arctg \left[\frac{\sqrt{1 + A^2} - 1}{2A} \operatorname{th} 2\pi x y \right]; \quad A = \frac{y}{n^2(1 + y^2)^2 - (1 - y^2)} \quad (3)$$

$$y = \frac{1}{4\pi x} \ln \frac{\eta_m \eta_\infty + 1}{\eta_m \eta_\infty - 1} \quad (4)$$

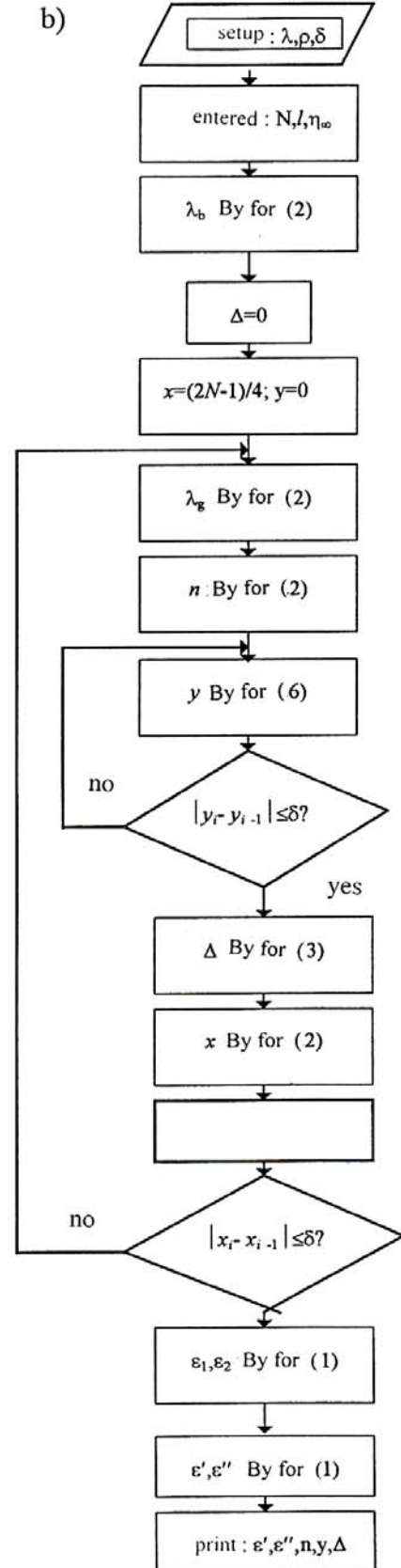
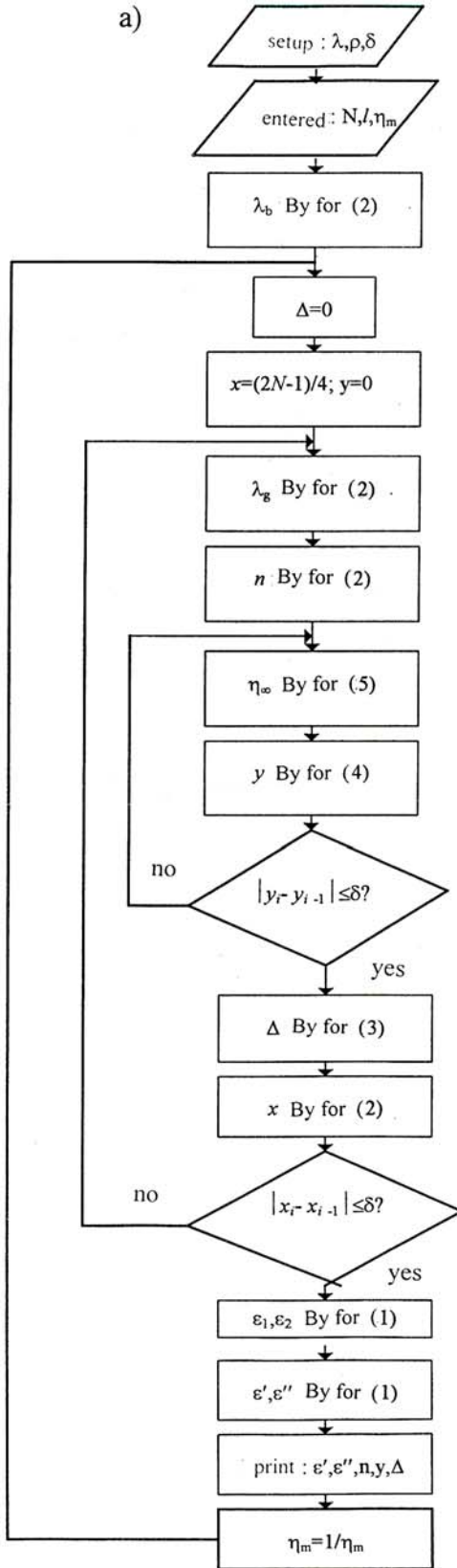
and the ratio for η_∞ , obtaining from Frenel equation, but is expressed with the use of given denotes:

$$\eta_\infty = \frac{\sqrt{1 + q} + \sqrt{1 - q}}{\sqrt{1 + q} - \sqrt{1 - q}}; \quad q = \frac{2n}{n^2(1 + y^2) + 1} \quad (5)$$

$$y = \frac{1}{n} \sqrt{n \cdot \frac{\eta_\infty^2 + 1}{\eta_\infty} - (n^2 + 1)} \quad (6)$$

$$n = \frac{1}{2(1+y^2)} \left[\frac{\eta_{\infty+1}^2}{\eta_{\infty}} + \sqrt{\left(\frac{\eta_{\infty+1}^2}{\eta_{\infty}} \right)^2 - 4(1+y^2)} \right]$$

(7)



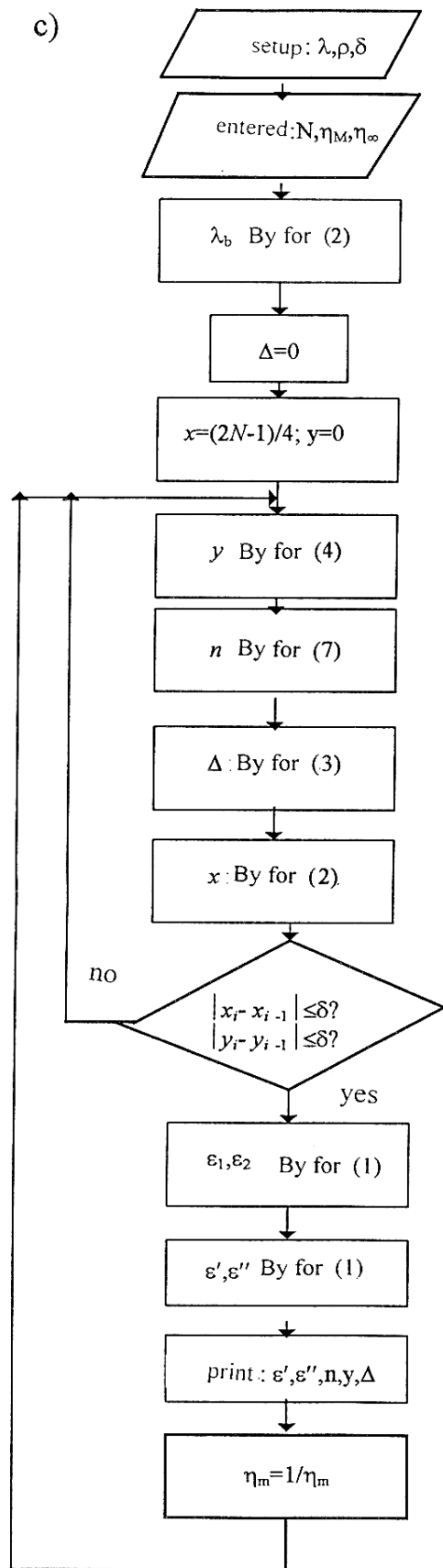


Fig.1. The block scheme of the calculation algorithms of the dielectric coefficients of polar liquids and their solutions: a) algorithm of the subprogram A, b) algorithm of the subprogram B, c) algorithm of the subprogram C.

For the improvement of exactness and reliableness of the carried out measurements and calculations on them, and also for the escape of the probable appearance of two-valued property in the calculation of ϵ' , ϵ'' , the program system includes three subprograms, the every of which is oriented on the calculation carrying out of ϵ' , ϵ'' on the one from the couple of the measured parameters l_m , η_m (subprogram A); l_m , η_∞ (subprogram B); η_∞ , η_m (subprogram C) (fig.1.). Every of these subprograms include the entering procedures of the values, including in the initial equations of the aprioristically famous parameters λ , λ_b , $p=(\lambda/\lambda_k)^2$ in the operating computer memory, depending on the type of applied experimental installation and frequency, at which the measurements are carried out. The input of the given measurements η_m , η_∞ , l_m carried out the input of the number N of the function $\eta(l)$ minimum, chosen at the measurements. The use of this or that subprogram is defined by the attenuation character of the experimental dependence η on l of the investigated objects. Thus, for the liquids with the value of the dielectric loss factor higher than 0,5 is better to use of subprogram C. At the measurements of the weak absorbing dissolved solutions of polar liquids, it is need to use the subprogram A. Independently on the subprogram choice, the search of the values ϵ' , ϵ'' is ended at the carrying out of the conditions

$$|x_i - x_{i-1}| \leq \delta; \quad |y_i - y_{i-1}| < \delta$$

where δ is the reasonable error value in the calculations of the intermediate parameters x and y ; x_i , x_{i-1} , y_i , y_{i-1} are the values of the intermediate parameters x and y on i -m and j -m repeating steps.

The discussion of results

The obtained data of the solutions ϵ' , ϵ'' are given in the table 1 and on the fig.2. The solutions of polar acetonitrile in the nonpolar bensole, the dielectric properties of which are well enough studied in the high-frequency range, have been chosen in the capacity of the objects. Earlier, in the refs [5,6], by the investigations of dielectric properties and reflection characteristics of acetone-bensole and water-dioxan solutions in the centimeter wave range, the probability of the observation of the total absorption effect of the electromagnetic radiation has been proved. It is established, that at the given frequency of falling radiation and solution temperature, the total nonreflecting wave absorption appears at the strong defined layer widths and solution compositions. Taking into consideration, that dispersion regions of acetonitrile are in the centimeter and millimeter wave ranges, the investigations are carried out at the wave length $\lambda=1,5\text{sm}$ and temperature 20°C . For the prediction of the layer width and solution composition, at which the appearance of the total absorption of the falling radiation in the chosen solutions is expected, the given measurements of their dielectric constants ϵ' and dielectric losses ϵ'' , represented in the ref [7], are used.

Found by the calculation way, with the help of the above mentioned method, the resonance values of the layer width and solution compositions are compared with the similar data, obtained from the experimental investigations of the

dependences η on l at the different concentrations of bensole in the solutions.

The obtained in the experiment values of ε' and ε'' at the different bensole concentrations are used for the construction of the dependences of the values ε' and ε'' of the corresponding solutions in the same coordinate ox.

The experimental x and calculated x_p values of resonance molar concentrations of polar component of acetonitrile solutions in the bensole at the temperature 20°C and wave length 1,5 cm. The ε_0 , $\tau \cdot 10^{12}$ s is the statistical dielectric constant and relaxation time of solution polar component; the critical wave length $\lambda_k=2,3$ cm.

Table 1

Solutions ε_0, τ Number of zero minimums N	Acetonitrile-bensole	
	36,8	3,3
	X_p	X
1	19,4	19,4
2	7,4	6,6
3	4,8	4,6
4	3,6	3,4

The coordinates of the cross-section points of the experimental and theoretical dependences fig.2 are found by the graphical way by their combination with the values of the curve family of resonance values ε' , ε'' , obtained by the calculated way, and on the last values are found the corresponding resonance values of bensole concentrations in the solutions.

The calculated by such graphical method, the values of resonance concentrations of polar component in the chosen solutions are given in the table 1. For the comparison there are also the values, but obtained from the behavior analysis of the experimentally taken concentration dependences of wave reflection coefficient module in the minimum points of the curves ρ on l .

The given in the table calculated and experimental values of resonance concentrations of solution polar component are in well agreement between each other.

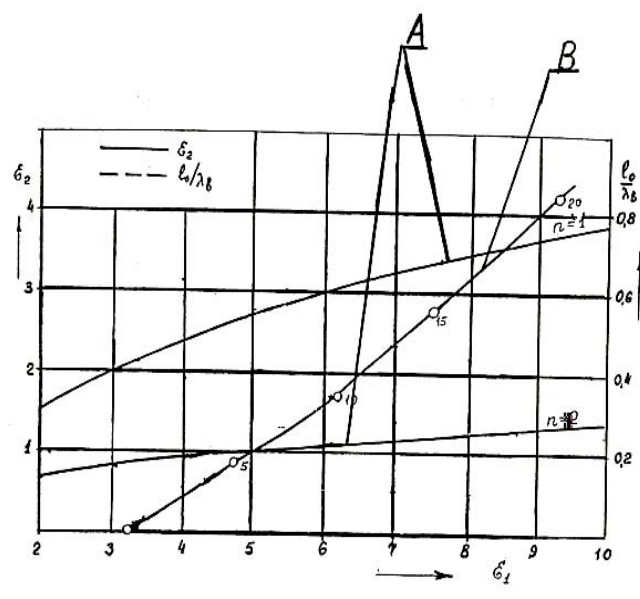


Fig.2. The experimental dependencies of ε' on ε'' of the acetonitrile solution in the bensole at the temperature $T=20^\circ\text{C}$ and the wave length $\lambda=1,5$ sm.

Conclusion

The investigated effect of the resonance nonreflecting absorption of electromagnetic waves in the solution has the general character and can be revealed in many solutions of polar dielectrics at the definite measurement frequency selection, temperature and composition of the investigated solution. The method and calculation algorithm of the dielectric properties and characteristics of polar substances and their solutions is also treated.

- [1] E.Salaev, E.Gasimov, S Azizov, Ch. Qajar. Turkish journal of Phisiks, vol. 22, №5,1998, p. 389-393.
- [2] R.M. Kasimov, Ch.O. Kadjar. Dokladi AN Azerb., 1999, №5-6.
- [3] P.I. Dvoretzkiy, S.B. Popov, I.G. Yarmakhov. Radiotekhn. i electron., 1996 т.41, №12, c. 1448-1461.
- [4] I.P. Kozlov. Radiotekhn. i electron., 1997, т. 42, №2, c. 142-146.

- [5] R.M. Kasimov, Ch.O.Kadjar, M.A.Kalafi, E.R. Kasimov, E.Yu. Salaev. JTF, t.66, №5,1996, c.167-171.
- [6] R.M. Kasimov, Ch.O. Kadjar, M.A. Sadikhov, E.R. Kasimov. Izmeritelnaya tekhnika, №5,1999, c. 45-47.
- [7] Ya.Yu. Akhadov. Dielectricheskiye svoystva binarnikh rastvorov. Moskva, Nauka,1977, 400 c.

S.T. Əzizov, M.A. Sadıxov, Ç.O. Qacar

MİKRODALĞALI DİAPAZONDA ASETONİTRİL-BENZOL MƏHLULLARININ DİELEKTRİK XASSƏLƏRİNİN ÖLÇÜLMƏSİ

Məqalədə ε' , ε'' -in təyin olunması metodu və alqoritmi, məhlulların dielektrik xassələrinin ölçülərinin nəticələri göstərilib. Bu məhlullarda konsentrasiya spektrinin mövcud olması təyin olunub və bunun əsasında düşən şüanın seçilmə əksolunmayan udulması baş verir.

С.Т. Азизов, М.А. Садыхов, Ч.О. Каджар

**ИЗМЕРЕНИЯ ДИЭЛЕКТРИЧЕСКИХ СВОЙСТВ РАСТВОРОВ АЦЕТОНИТРИЛ-БЕНЗОЛ В
ДИАПАЗОНЕ МИКРОВОЛН**

В статье приведены результаты измерения диэлектрических свойств растворов, методика и алгоритм определения ε' , ε'' . Установлено существование в этих растворах спектра концентраций, при которых возникает избирательное безотражательное поглощение падающего излучения.

Received: 15.09.2004

.

OBTAINING AND RESEARCH OF ELECTRICAL PROPERTIES OF $Y_{1-x}Cd_xBa_2Cu_3O_{7-\delta}$

S.A. ALIEV, S.S. RAGIMOV, V.M. ALIEV

*Institute of Physics Azerbaijan National Academy of Sciences**Baku - 1143, H.Javid ave., 33*

The temperature dependences of electrical conductivity, thermoelectromotive force and thermal conductivity of $Y_{1-x}Cd_xBa_2Cu_3O_{7-\delta}$ were carrying out. It was established, that the superconducting transition is not vanished up to 80 at.% of Cd. On the temperature dependences of investigated coefficients are observed the sharp changes of dependence course likely phase transition.

The obtaining new HTSC with higher critical temperature (T_c) of transition in a superconducting (SC) state from not deficient and cheap materials, easily yielding to mechanic processing still remains to one of actual questions of physics of superconductors. There is a large number of the publications, in which one were made partial replacement of atoms Y by atoms Tm, Nd and other elements observing a superconducting (SC) transition at $T_c=91-95K$.

The given work is dedicated to obtaining and research of electrical properties of $Y_{1-x}Cd_xBa_2Cu_3O_{7-\delta}$. Samples $Y_{1-x}Cd_xBa_2Cu_3O_{7-\delta}$ were obtained in two stages: the mixture of oxides CdO, BaO and CuO in the conforming ratio was mixed, was frayed and caked at 800-850°C on air during 20-25 hours. The obtained mixture for the second time was frayed, was extruded in tablets and undergo to an annealing in a flow of oxygen under pressure 1,2-1,5 at. at 900-950°C during 25-30 hours.

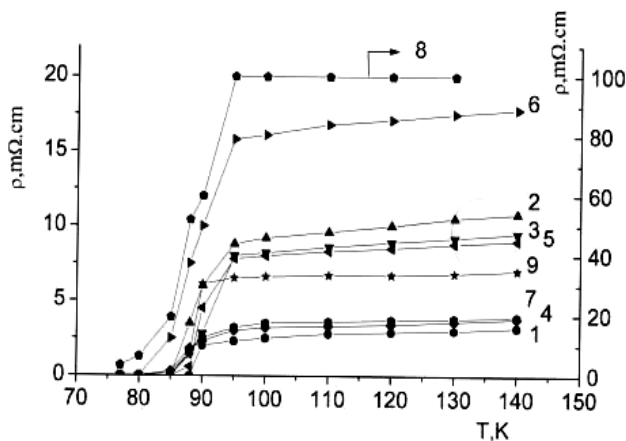


Fig.1. The temperature dependence of specific resistivity for different values X (see to text) of $Y_{1-x}Cd_xBa_2Cu_3O_{7-\delta}$

In a fig. 1 are submitted the temperature dependences of specific resistivity $\rho(T)$ of $Y_{1-x}Cd_xBa_2Cu_3O_{7-\delta}$ at different values X ($X=0-1$; 0,1-2; 0,2-3; 0,3-4; 0,4-5; 0,5-6; 0,6-7; 0,7-8; 0,8-9). As it is seen, up to 80 at.% Cd the superconductivity in them does not vanish. Let's remark, at $X=0,9$ (though the data $\rho(T)$ for specimens with $X > 80$ at. % in figure are not submitted), value ρ increases in 50 times, and course of temperature relation $\rho(T)$ becomes semi conducting. In a sample with $X=1$ the value of ρ increases for 4 order, the semi conducting course $\rho(T)$ becomes sharper, passing through a maximum at 170K, decreases in 6 times, but the SC up to 77K does not observed. From the data introduced in a fig.1, it is seen, that change of values of resistance in a normal condition, in process of increasing X , is not systematical. In particular values ρ for structures $X=0,4$ and 0,7 are close to a sample with $X=0$, or ρ for sample with

$X=0,5$ is maximal and on much more, than sample with $X=0,8$. Notably, that in samples with Cd temperature of SC transition T_0 displaces in the party low T , but also here it is difficult to observe for regularity of change T_0 from X . However, it is seen that at replacement of atoms Y by atoms Cd (up to 80at. %) the temperature of SC transition is saved, and varies within the limits 88-90K. With the purpose of improvement of the obtained results experiments were suggested with some changes. In this case the carbonate of barium - $BaCO_3$ is used in return for of barium oxide - Ba_2O and is made some changes in a temperature regime. A mixture of oxides Cd, CuO and $BaCO_3$ in accordance to a structure $CdBa_2Cu_3O_{7-\delta}$ ($X=1$) was mixed, was frayed in an agate mortar, and was heated up to 920°C within 6 hours. Temperature of heating was rise as contrasted to by previous case, with the purpose of decomposing $BaCO_3$ on Ba and CO_2 . On completion of heating from the obtained material the spacers were pressed in. The spacers were heated up to 920°C and were stand during 15-20 hours, then, with the purpose of a sintering, temperature was increased up to 1000°C, and not for long having stand up to former value 920°C was lowered. Having stand at this temperature during 2 hours, up to the room temperature slowly was cooled.

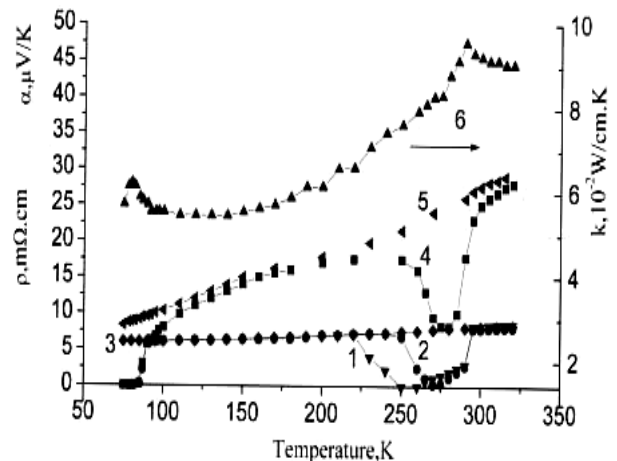


Fig.2. The temperature dependences of specific resistivity (1,2,3), thermo-e.m.f. (4,5) and thermal conductivity (6) of $CdBa_2Cu_3O_{7-\delta}$.

In a fig. 2 the temperature dependences of resistance $\rho(T)$ (1,2,3-after first, second and third measurement respectively), thermoelectromotive force $\alpha(T)$ (4,5 – after second and third measurement respectively) and thermal conductivity (k) (6,7- after second and third measurement respectively) for $CdBa_2Cu_3O_{7-\delta}$ is submitted. As is seen the value of resistance for the obtained sample is of the same order, as well as in Y-123 ceramics: has a metallic course,

the value of α and its temperature dependence also corresponds to a metallic course. The superconducting transition was observed at the temperature of $T_c=85K$.

It is necessary to mark some peculiarity on temperature dependences of investigated coefficients in area 250-290K. As it is seen, there is some sharp change of these coefficients similarly to phase transitions. Temperature dependences of thermal conductivity at room temperatures same, as at phase transitions in superconducting state, i.e. the temperature dependences of thermal conductivity passes through a maximum below T_c . Below room temperatures the behavior of all three investigated coefficients resembles phase transition in superconducting state at 90K. The specific

resistivity, decreasing up to zero, further is raised with temperature decreasing. The experiments were conducted repeatedly three times. The two times observed peculiarity on $\alpha(T)$ and $\rho(T)$ in third and fourth time were not watched. The temperature dependence course of thermal conductivity has not changed after the third measurement. Is probably, it was connected to a metastable superconducting phase at these temperatures.

Proceed from the obtained results it is possible to conclude, that at is successful a selected technological regime it is possible to receive samples $Y_{1-x}Cd_xBa_2Cu_3O_{7-\delta}$ with $X<1$ with superconducting properties to a close structure $YBa_2Cu_3O_{7-\delta}$.

[1] Zhao.Y, Sun .S, Zhang Q. J.Appl.Phys.,1998, 64, p.1999.

[2] S.A.Aliev, S.S.Ragimov, V.M.Aliev et.al. J.Rare Earths, 1991, v.3, p.1060.

[3] E.V.Vladimirskaya, M.V.Yelizarova, N.V.Ageev. FTT, 1998, v.40, №12, p.2145.

S.A. Əliyev, S.S. Rəhimov, V.M. Əliyev

$Y_{1-x}Cd_xBa_2Cu_3O_{7-\delta}$ ALINMASI VƏ ONUN ELEKTRİK XASSƏLƏRİ

$Y_{1-x}Cd_xBa_2Cu_3O_{7-\delta}$ nümunələrin elektrikkeçiriciliyi, termoelektrik h.q. və istilikkeçirməsi tədqiq edilmişdir. $Y_{1-x}Cd_xBa_2Cu_3O_{7-\delta}$ -də ifratkeçiricilik 80 at.% Cd-yə qədər yox olmur. Tədqiq edilmiş əmsalların temperatur asılılıqlarında 260-280K oblastında faza keçidlərinə oxşar kəskin dəyişmə müşahidə edilmişdir.

С.А. Алиев, С.С. Рагимов, В.М. Алиев

ПОЛУЧЕНИЕ И ИССЛЕДОВАНИЕ ЭЛЕКТРИЧЕСКИХ СВОЙСТВ $Y_{1-x}Cd_xBa_2Cu_3O_{7-\delta}$

Исследованы температурные зависимости электропроводности, термоэдс и теплопроводности образцов $Y_{1-x}Cd_xBa_2Cu_3O_{7-\delta}$. Получено, что в $Y_{1-x}Cd_xBa_2Cu_3O_{7-\delta}$ сверхпроводимость не исчезает вплоть до 80 ат.% Cd. На температурных зависимостях исследованных коэффициентов образца $CdBa_2Cu_3O_{7-\delta}$ в области 260-280K обнаруживается резкое изменение хода зависимостей, аналогично поведению при фазовых переходах.

Received: 20.10.04

ELECTROLUMINESCENCE (EL) IN GaS:Ln^{3+} (Ln-Nd, Er, Tm)

F.Sh. AYDAYEV, O.B. TAGIYEV

*Institute of Physics of Azerbaijan of Sciences
Az-1143, Baku, H. Javid ave., 33*

Excitation of EL was accomplished by the applied to a crystal, constants and variable electrical fields. Thus, the luminescence of the matrix and radiation caused by transitions of rare earth ions is observed.

Research of EL of rare earth ions in wide (-band-) gap semiconductors represents the big interest in connection with perspectives of reception of stimulated radiations with electrical rating and creations of plane solid-state display, oscillographic and television screens [1,2].

Investigation results of EL characteristics of monocrystals GaS:Ln^{3+} are presented in the given article. The samples with thickness from 70 up to 150mkm with sandwich contacts, made of In, Al, Ag etc, were used for investigation of EL.

Spectra of an electroluminescence in monocrystal GaS:Nd at 77K and 200Hz are shown on fig. 1. Narrow-band lines of radiation in an interval of wavelength on electroluminescence spectrum $0.53\div 0.55$ and $0.59\div 0.61$ mcm are caused accordingly by transitions of $^4G_{7/2} \rightarrow ^4I_{9/2}$ and $^4G_{7/2} \rightarrow ^4I_{11/2}$ of Nd^{3+} . It is known, that Nd ions have rich radiating ability in infrared area of a spectrum. In our researches intensity of radiation in infrared region is very weak. Therefore this part of a spectrum is not shown on fig. 1.

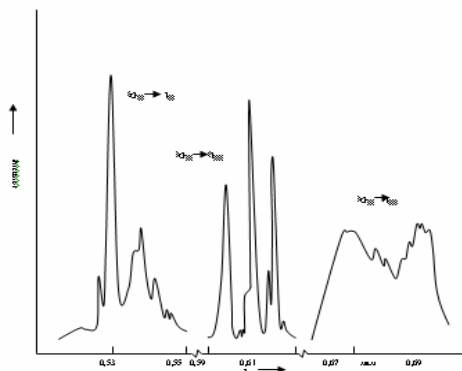


Fig.1. EL spectra of GaS:Nd ($T=77\text{K}$, $f=200\text{Hz}$).

EL spectra of monocrystal GaS:Er are shown on fig.2. From all investigated transitions the most intensive was a transition $^4S_{3/2} \rightarrow ^4I_{15/2}$.

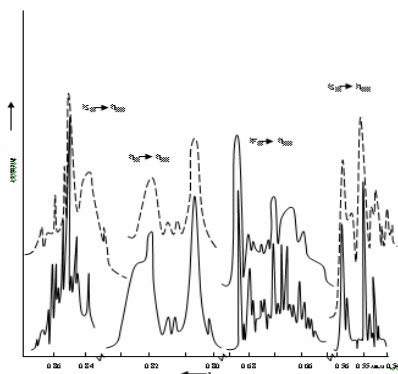


Fig. 2. Spectra of photo (continuous curves) and electro-

luminescence (dotted curves) of monocrystals

Electroluminescence spectra of monocrystal GaS:Tm are shown on fig. 3. The area $0.79\div 0.83$ mcm is caused by transition $^3F_4 \rightarrow ^3H_6$, and $0.68\div 0.72$ mcm is caused by transitions $^3F_3 \rightarrow ^3H_6$ of Tm^{3+} ion.

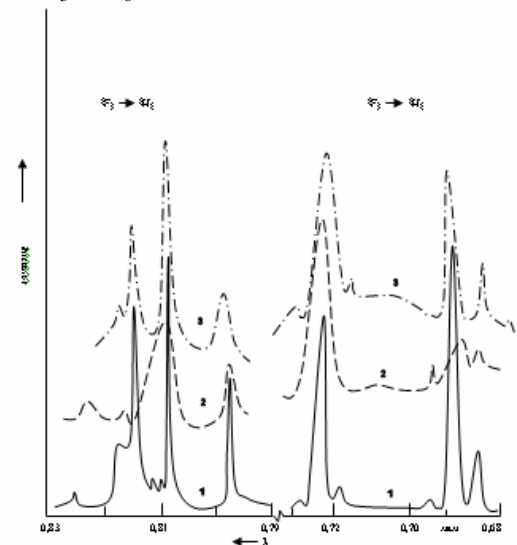


Fig. 3. Spectra of photo (curve 1 at 77K, curve 2 at 300K) and electroluminescence (curve 3 at 77K) of monocrystals GaS:Tm

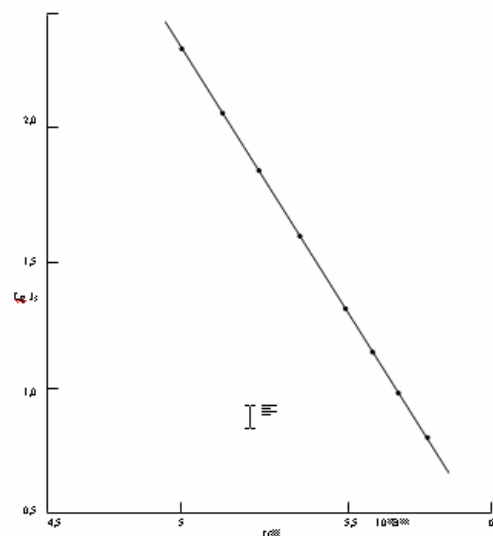


Fig. 4. Dependence of EL intensity on applied to the sample (GaS:Nd).

One of the most essential characteristics of electroluminescence, allowing to determine its mechanism, is the dependence of intensity of radiation on the applied voltage. This dependence for monocrystal GaS:Nd^{3+} is

shown on fig. 4. Obviously, dependence of intensity of an electroluminescence on voltage submits to the exponential law [3]

$$I = I_0 \exp\left(\frac{b}{\sqrt{u}}\right) \quad (1)$$

I_0 is defined by an external source of electrons, and parameter of exponent is defined by the value of area. Similar dependence for crystal GaS:Er is shown on fig. 5. Such character of dependence of EL intensity is observed also at excitation of samples by a constant electrical field.

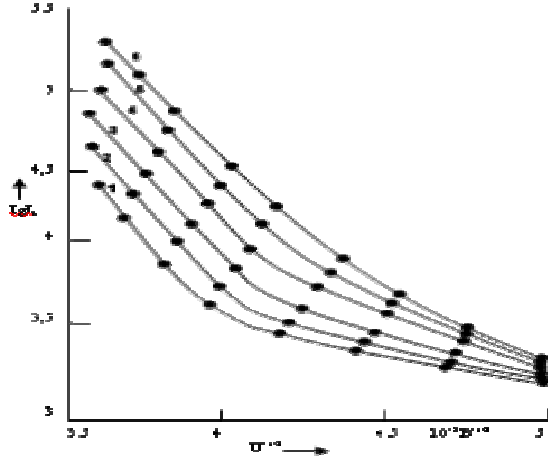


Fig. 5. Field dependences of EL intensity at different frequencies of applied variable field, at 77K ($^4S_{3/2} \rightarrow ^4I_{15/2}$ GaS:Er); 1- 200, 2-300, 3-400, 4-600, 5-800, 6-1000Hz.

Exponential growth of EL intensity from voltage specifies that EL in the area of strong fields is caused by shock ionization of impurity centers. We also establish, that the relation of intensity of luminescence I_l to dark current I_c passing through a sample, also changes on the exponential law [4].

$$I_l / I_T = A \exp\left(-\frac{c}{u}\right) \quad (2)$$

Such dependence for crystal GaS:Er is shown on fig. 6. Realization of such regularity also specifies the shock mechanism of excitation of an electroluminescence in GaS:Ln³⁺. In the area of electrical fields where the deviation from exponential dependences is found out, the cubic site and a site of sharp growth of a current comes to light on current-voltage characteristics of monocrystals GaS:Ln³⁺.

It is shown in work [5,6], that passage of a current in structures is In- GaS:Ln³⁺-In is caused by double injection. Besides the visible luminescence in monocrystals GaS:Ln³⁺, at small voltage is observed near to the cathode and with growth of voltage is distributed to the anode. Hence, it is possible to assume, that at small fields the injection electroluminescence phenomenon is observed.

It is known, that the mechanism of shock ionization is possible at presence of a strong field ($\geq 10^5$ V/cm). However, in the investigated crystals, EL is observed in an interval of electrical fields 10^3 to 10^5 V/cm. Obviously, acceleration of carriers occurs on barrier of Shottki. It is possible, that the electroluminescence at fields of $\geq 10^5$ V/cm may be connected

with microasperity of crystal, formed at doping of rare earth elements.

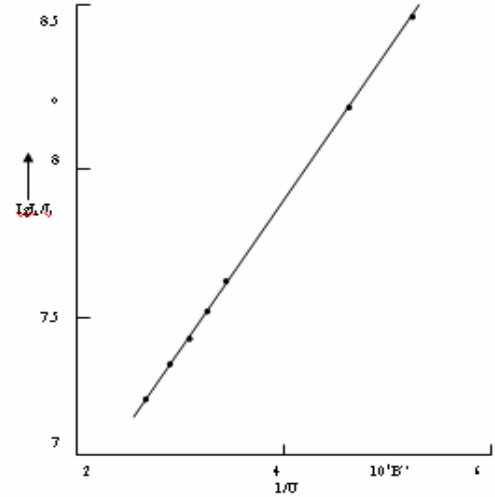


Fig. 6. Dependence of $\lg J_x/J_m$ on U^{-1} for monocrystal GaS:Er at excitation by constant field $T=77$ K, $^4S_{3/2} \rightarrow ^4I_{15/2}$ Er³⁺

The low-frequency peak is found on frequency dependences of EL intensity at 200 Hz (fig7). Intensity grows with increase of frequency from 20 up to 200Hz. With the further increase up to 10Hz intensity slowly decreases. Expression for a quantum output of radiation is received in work [7]:

$$P = \frac{\alpha N_a}{\alpha N_a + \beta N_t} \exp\left[-c_1 \frac{\beta N_t}{\alpha N_a + \beta N_t} \Delta t \exp\left(-\frac{E}{kt}\right)\right] \quad (3)$$

where N_a and N_b -concentration of activating and braising impurity, the C_1 -constant, α and β - probabilities of capture of holes from a valent zone on levels of activating and braising impurity, T -time of holes redistribution, E -depth of activator deposition, Δt -is the certain part of the period (δ): $\Delta t = \delta/f$. Apparently from the formula (3), the quantum output grows with increase of frequency of the applied variable field. The increase of brightness of a luminescence observed on experiment at low frequencies, apparently, is caused by increase of a quantum output. With the further increase of frequency the quantum output does not play an essential role anymore as the power absorbed at the big frequencies, poorly depends on the frequency. The high-frequency area of this curve is well straightened in double logarithmic scale (fig. 7). It specifies on capacitor character of recession [8].

Temperature dependence of EL intensity of broadband radiation ($\lambda_m=0,58$ mkm) contains three sites. EL intensity practically does not vary in the area of temperatures 77÷95K, that specifies the impurity character of energy absorption [9]. The inclination, which is equal to 0.70 eV is found above temperature 95K. As is known, the wide strip with a maximum at wavelength ($\lambda_m=0,58$ mcm is caused by transition of electrons from a zone of conductivity on p-type levels [10]. P-type levels grasp electrons from a valence zone with increase of temperature. Temperature dependence of EL intensity of transition $^4S_{3/2} \rightarrow ^4I_{15/2}$ of Er³⁺ electrons repeats a course of temperature dependence of broadband radiation. Apparently, transfer of energy to ions Er³⁺ is accomplished

through strips with maximum $\lambda=0.58\text{mkm}$. Similar results were received for monocrystal GaS:Tm [11].

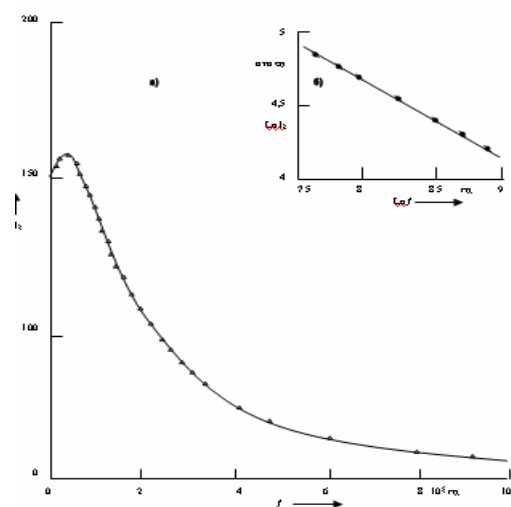


Fig. 7. Frequency dependence of EL intensity at 77K
($^4S_{3/2} \rightarrow ^4I_{15/2}$ GaS:Er)

Electroluminescence in monocrystals GaS:Ln³⁺ is found at fields where the cubic law is broken to CVC (current-voltage characteristic) and enough amount of free carriers of both types is injected in volume of the semiconductor. The similar situation is formed at excitation of a crystal $h\nu > E_g$. The only difference is in the infusing of the electrical field ($E \geq 10^4 \text{V/cm}$) applied to a crystal on capturing of carriers and in facilitating of the process of liberation of the located carriers (thermal field effect). Formed in volume of a crystal free carriers may recombine on interzoned transitions and through local conditions in the forbidden zone.

Thus, on the basis of experimental results it is possible to conclude, that found EL in monocrystals GaS:Ln³⁺ at relatively weak fields, EL mechanism is injection, and at more strong fields - shock ionization. GaS:Er at $T=77\text{K}$

- | | |
|--|--|
| <p>[1] Y.Inone, I.Tanaka, K.Tanaka, Y.Izumi, S.Okamoto, M.Kawanishi. Electroluminescent thin films.V.96, ISSUE 1, p. 69-74, 2002.</p> <p>[2] K.Yanagisawa, N.Kuroda, J.Nishina. J.Phys. Soc. Jap., 1974, 37, 4, p. 1180</p> <p>[3] I.K.Vereshagin. Electroluminescent source of light. M.1990, 168 s..</p> <p>[4] F.Yeitz. Phys.Rev, 1949, 76, p.1376-1393.</p> <p>[5] B.G.Tagiev, G.M.Niftiev, F.Sh.Aidaev. Phys.Stat.Sol (a), 1985, 89, p. 639-645.</p> <p>[6] B.G.Tagiev, F.Sh. Aidayev. FTP, 1986, t.20, v.4,s.723-726. (in Russian)</p> | <p>[7] I.K.Vereshagin. Electroluminescence of crystals. M.Science, 1974, 279c.</p> <p>[8] V.L.Rabotkin, N.D.Abrosimova V. A. Burobin, V. V. Domkov. Electroluminescence of solid states and its application. Kiev, Naukova Dumka, 1972, c.125-134.</p> <p>[9] E. I. Adirovich. Some questions of luminescence theory of the crystals. M-L, 1951, 351c.</p> <p>[10] I.M.Catalano, A.Cingolani, A.Minafra. 1977, 22, 4, p.225-226</p> <p>[11] B.G.Tagiev, G.M.Niftiev, F.Sh.Aidaev.Solid State Communs. 1985,55, 4, p.385-386.</p> |
|--|--|

F. SH. AYDAYEV, O.B.TAĞIYEV

GAS:LN³⁺ (LN – ND, ER, TM) KRISTALLARIN ELEKTROLÜMINİSENSİYASI

GaLn3(Ln – Nd , Er , Tm) kristallarında elektrolüminessensiya hadisəsi sabit və dəyişən elektrik sahələrində tədqiq olunmuşdur. Bu zaman nadir torpaq elementinə xas olan şüalanma və həmçinin zonalar arası keçidə uyğun şüalanma müşahidə olunmuşdur.

Ф.Ш. АЙДАЕВ, О.Б. ТАГИЕВ.

ЭЛЕКТРОЛЮМИНЕСЦЕНИЯ (ЭЛ) В GAS:LN³⁺ (LN – ND, ER, TM)

Возбуждение ЭЛ осуществлялось приложением к кристаллу постоянных и переменных электрических полей. При этом наблюдается свечение самой матрицы и излучение, обусловленное внутрицентровыми переходами редкоземельных ионов.

Received: 22. 09. 2004

INFLUENCE OF IR-RADIATION ON KINETIC EFFECTS IN $\text{Cd}_x\text{Hg}_{1-x}\text{Te}$

E.I. ZULFUGAROV

*Institute of Radiation Problems of Azerbaijan National Academy of Sciences
Baku-1143, H. Javid av., 31a*

The results of influence of an electron beam irradiation on galvano-tehmomagnetic properties in monocrystals $\text{Cd}_x\text{Hg}_{1-x}\text{Te}$ ($0 \leq x \leq 0,25$) in the wide range of temperatures ($4,2 \div 300\text{K}$) and magnetic fields ($60 \leq H \leq 22.000\text{ers.}$) were analyzed in given work.

It is shown, that action of irradiation on Hall effects is most essential at weak fields and low T . Comparison of results $\sigma(T)$, $R(T, H)$ with the two – zoned theory has to reveal quantitatively influence of an irradiation on concentration and mobility of carriers of a charge and to conclude, that the electron beam irradiation of CMT crystals leads to increase of electron concentration, caused by vacancies of tellurian with donor type. It is established, that $\text{Cd}_x\text{Hg}_{1-x}\text{Te}$ (with $x = 0,12 \div 0,15$) can be used as sensitive elements in termomagnetic receivers of IR irradiation. It is established, that at $T < 40\text{K}$ in $\text{Cd}_x\text{Hg}_{1-x}\text{Te}$ ($x \leq 0,15$) concentration of acceptor centers which are included in a conductivity zone, greater more that concentration of donors.

The acceptor levels plays role of traps for both – for ionizing electrons and for electrons induced by irradiation. It was set up, that electron beam irradiation with integral dose $5,6 \cdot 10^{17} \text{ elec/cm}^2$ to increase of specific sensitivity of receivers of IR radiations up to twice at $T = 300\text{K}$.

Introduction

The first studies of influence of radiation defects on physical properties of CMT appeared in the beginning of 70-ies [1,2]. In [2], the irradiation was made by electron beam at 25K. After the irradiation, samples of p-type were converted to n-type and the electroconductivity grew by 4 order. However after heating of samples, the initial properties almost were restored. In [3] irradiation was made by integrated beam $\Phi = 4 \cdot 10^{17} \text{ sm}^{-2}$ at 77K. The increase of n and reduction of photoconductivity is revealed. Short term heating at 300-320K eliminate the entered radiation infringements. It was shown, that created at low temperature irradiation defects, has a small thermal stability and anneals basically at temperatures 50-75K [2] and 150-225K [4]. It is known, that using of temperatures of the irradiation leads to formation of various types of stable defects [5].

Meanwhile, practical use of the irradiation demands knowledge of physical properties of radiation defects and their thermal stability at 300K. In this sense, the works [6, 7], in which n and p -type samples were irradiated at 300K are interesting: in n -type samples p insignificantly decreased, and conductivity remained almost constant, whereas in p -type samples was a change of type and σ passed through a minimum. Authors [6, 7] analyzing the obtained results, conclude, that the electron beam irradiation at 300K, irrespective at initial type of conductivity, leads to formation of new donor centers in CMT crystals. MOD-structure is investigated in [8]. More detailed researches were carried out in [9-15]. As seen from brief review, the study of influence of the electron beam irradiation on kinetic phenomena CMT has only incidental character up to our researches. Coefficients of electro conductivity and Hall have been considered only at 300K and in the certain value of magnetic field and irradiation dose for limited structure and concentration. Thus, the methodical shortcomings were tolerated. In particular, many authors argue on change of a sign of the conductivity, influence of the irradiation on the mobility on the dates of σ and R at one certain the magnetic field, meant at this product $R \cdot \sigma$ as mobility. As known, there is a simultaneously participation of electrons and holes in conductivity of CMT, therefore dependences of $R(H)$, $\sigma(H)$ and other factors are

complex. Change of sign of R at any value H does not mean change of conductivity type and $R \cdot \sigma$ not always is the mobility of one of carriers of charge and etc.

The features of zone structure of crystals, state of admixture levels were not considered at interpretation of the obtained results. For example, in some studies, there are such conditions: the electron beam irradiation results in growth acceptor centers, reduce or has no effect on mobility etc.

With the aim of elimination of the listed blanks of the problem, the complex researches of the influence of electron beam irradiation on electric, galvanomagnetic and thermomagnetic properties of CMT of various structures and concentration of carries of the charge at wide interval of temperature and magnetic fields has been carried out, and a role of electron RD and opportunities of practical use of electron processing has been studied.

1. Influence of an electron beam irradiation on conductivity and galvanomagnetic phenomena in $\text{Cd}_x\text{Hg}_{1-x}\text{Te}$ (CMT)

The galvanomagnetic effects are one of the sensitive phenomena to external influences. By studying the influence on them of temperature, the magnetic field and irradiation is possible to obtain exhaustive data on concentration, mobility, mechanism of dispersion, etc.

The influence of the electron irradiation on CMT with energy 3,5 Mev, an integrated beam to $\Phi = 1,46 \cdot 10^{18} \text{ cm}^{-2}$, on R for structures $x=0, 0,1, 0,12, 0,15, 0,20, 0,25$ at $T=4,2 \div 300 \text{ K}$ will be considered in this study. The characteristic curves of dependences $R(H, T, \Phi)$ for samples $x=0,12$ and $0,15$ are submitted in Fig.1.2. Apparently, the lead to significant change of factors, and irradiation is most effective at low T and weak H . As seen from curves $R(H)$, the irradiation lead to increase of R at investigated range of T . The point of inversion of sign of R is displaced to high values of H by rising of the irradiation dose. Rising of the $R(H_0)$ sign inversion at high fields H should be connected with, reduction of mobility and hole concentrations or with increase in concentration and mobility of electrons, according to expression (1).

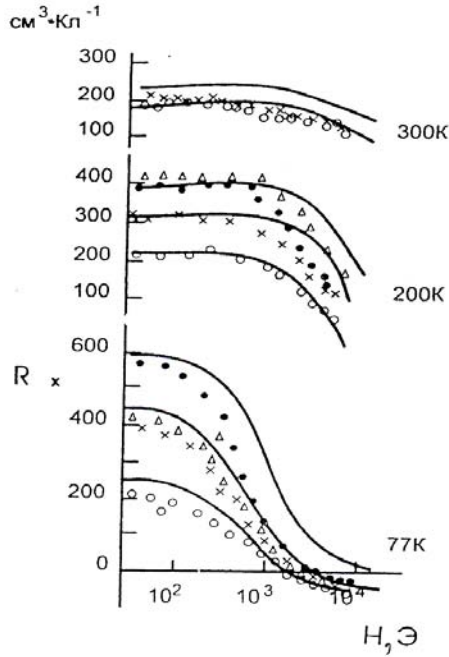


Fig. 1. Field dependences of Hall coefficient for samples of $\text{Cd}_{0.12}\text{Hg}_{0.88}\text{Te}$. Continuous line – calculation, \circ - $\Phi=0$; \bullet - $\Phi=5.6 \cdot 10^{17} \text{ cm}^{-2}$; Δ - $\Phi=1.5 \cdot 10^{18} \text{ cm}^{-2}$, \times - $D=10^{19} \text{ rad}$

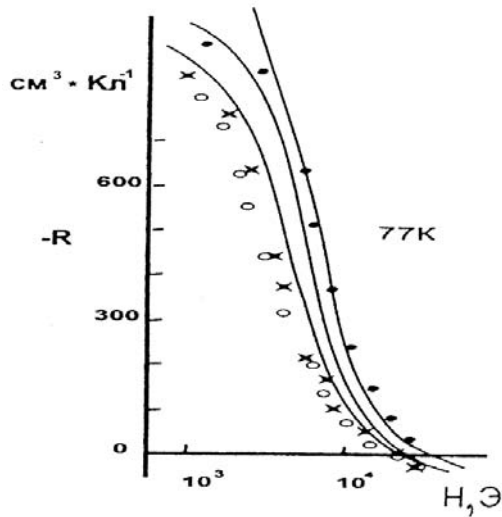


Fig. 2. Field dependences of Hall coefficient for samples of $\text{Cd}_{0.12}\text{Hg}_{0.88}\text{Te}$. Continuous line – calculation, \circ - $D=0$; \bullet - $\Phi=7.2 \cdot 10^{17} \text{ cm}^{-2}$; \times - $D=10^{19} \text{ rad}$

As in two-zone model, the influence of n on R is most essential, the growth H_0 is caused, basically by increasing of n . The $R(H)$ in any magnetic field, according to theory looks like:

$$eR(H) = \frac{\frac{p\mu_p^2}{1+\tau_p^2} - \frac{n\mu_n^2}{1+\tau_n^2}}{\left(\frac{p\mu_p}{1+\tau_p^2} + \frac{n\mu_n}{1+\tau_n^2}\right) \left(\frac{p\mu_p\tau_p}{1+\tau_p^2} - \frac{n\mu_n\tau_n}{1+\tau_p^2}\right)^2} \quad (1)$$

where $\tau_i = \mu_i H$; $i = p, n$

The strong dependence of $R(H)$ should be observed at $\mu \ll 1$ and not too great value of p/n . Analysis of temperature

dependences $R(T)$ shows, that the $R(T)$ differ both quantitatively and qualitatively at the strong and weak fields. R monotonously decrease by reduction of T at $H=8.7 \text{ kErs}$ and there is the inversion of the sign of R at $T=80\text{K}$.

The course of $R(T)$ radically changes in process of decreasing of H .

R grows with reduction of T up to 200K at $H=1.5 \text{ kErs}$ occurs through a maximum, and with further downturn of T up to 77 , the value of R decreases.

At weak fields ($H=60 \text{ Ers}$) character of curves $R(T)$ strongly differ before and after the irradiation: before of the irradiation, has a weak maximum, it disappears in process of the irradiation and monotonous growth of R by increasing of T is observed. The location of the maximum and value of R changes on depending of H . With growth of H the maximum is displaced aside high T and value of maximum decreases.

The growth of maximum in $R(T)$ is connected with competing action of electrons and holes.

At weak fields a leading role plays electrons, at high H , holes, that results in shift of position of a maximum aside of high T , which causes reduction of the value of a maximum. The shift of a maximum aside low T and growth of its value is observed at irradiation.

So, the observable effect is explained by growth of n at an irradiation.

As is known, at the mixed conductivity, irrespective of the from izoenergy surfaces and the constancy of time of a relaxation, in weak fields always $S(H)$ looks like $\Delta\rho/\rho_0 \sim H^2$ and it strongly depends on values of mobility and concentration of each of carries of a charge. In case of the mixed conductivity in approach $\tau=\text{const}$, in any H we have:

$$\frac{\Delta\rho}{\rho_0} = \frac{\sigma_1\sigma_2(\sigma_1\sigma_1 - \sigma_1R_2)^2}{\frac{\sigma_1 + \sigma_2}{H} + \sigma_1^2\sigma_2^2(R_1 + R_2)^2} \quad (2)$$

Where $\sigma_1, \sigma_2, R_1, R_2$ - factors of electro-conductivity and the Hall electrons and holes.

The characteristic data on dependence $\frac{\Delta\rho}{\rho_0}(H)$ at various T

and dozes of an irradiation are submitted on Fig. 3.

The passage $\frac{\Delta\rho}{\rho_0}(T)$ through a maximum at 200K

showed be take attention. It is connected, by that, the $\frac{\Delta\rho}{\rho_0}$

should get the maximal value at $\rho\mu_p^2 \cong n\mu_n^2$. For submitted samples CMT, such conditions, are carried out in nearly of 200K . As we seen, the electron irradiation in an interval $200-300 \text{ T}$ does not affect almost on $\frac{\Delta\rho}{\rho_0}$. At helium

temperature the $\frac{\Delta\rho}{\rho_0}$ grows, but the most essential increase of

$\frac{\Delta\rho}{\rho_0}$ occurs at $T=77 \text{ K}$. It is connected with increasing of n at the irradiation.

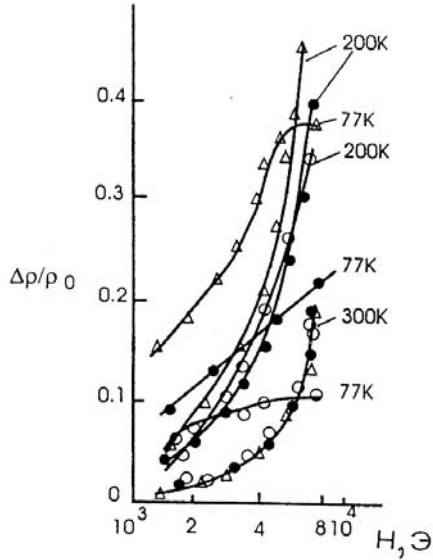


Fig. 3. Field dependences of cross magnetoresistance of $\Delta\rho/\rho_0$ of sample of $\text{Cd}_{0.12}\text{Hg}_{0.88}\text{Te}$ before and after e-irradiation; o- $\Phi=0$; •- $\Phi=5,6 \cdot 10^{17} \text{ cm}^{-2}$; Δ- $\Phi=1,5 \cdot 10^{18} \text{ cm}^{-2}$ at different temperatures.

From the submitted results follows, that it is possible to pick up such structure CMT and ratio of n and p , that the $\frac{\Delta\rho}{\rho_0}$ gets the much greater value, than in the investigated

crystals. Using of high value of $\frac{\Delta\rho}{\rho_0}$ and its increase under

action of an electron irradiation, it is possible to create various converters. In particular, having compensated a voltage in a zero field it is possible to create the high-sensitivity gauge of a magnetic field.

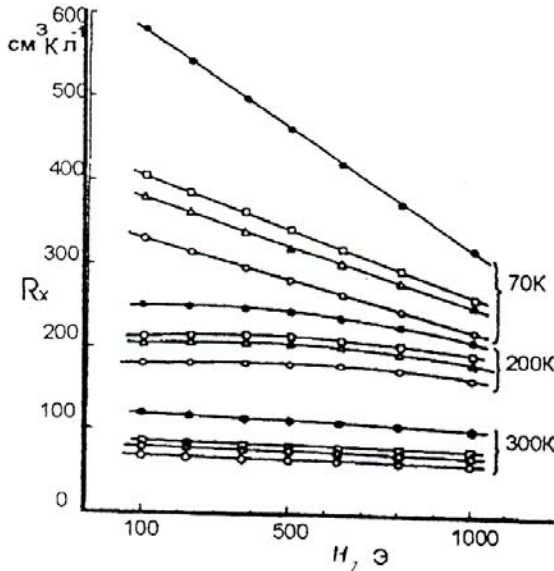


Fig. 4. Restore of R_x at thermal treatment ($t=1$ hour, $T_{\text{annealing}}=430\text{K}$) in sample of $\text{Cd}_{0.12}\text{Hg}_{0.88}\text{Te}$ after e-irradiation; o- $\Phi=0$ (before thermal treatment; Δ-after thermal treatment ($\Phi=0$); •- $\Phi=7 \cdot 10^{17} \text{ cm}^{-2}$; □-after annual.

For an establishment of temperature anneals for the defects entered by an irradiation, samples after measurements

were exposed izochronic annuals. As heat treatment in itself influences on electric properties of CMT, samples previously (up to an irradiation) were exposed to heat treatment.

On Fig. 4 characteristic curve actions of an electronic irradiation on $R(H)$, and also izochronic annuals before and after an irradiation are submitted. It is visible, that the annuals during one hour at 160°C practically liquidates RD. Similar results are received and from the analysis of other kinetic factors. We shall note, that before our researches there were no quantitative data of irradiation influences on n , p , μ_n , μ_p . This rather challenge as in conductivity simultaneously participate electrons and holes.

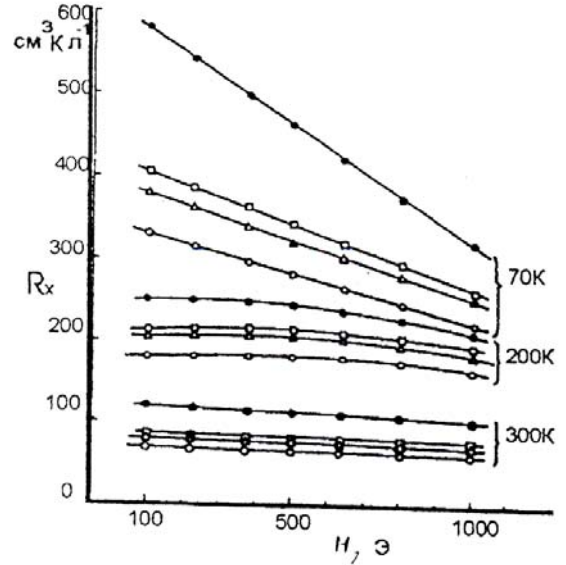


Fig. 5. Temperature dependences of parameters of charge carriers in $\text{Cd}_{0.15}\text{Hg}_{0.85}\text{Te}$; dotted- $\Phi=0$; continuous- $\Phi=7,2 \cdot 10^{17} \text{ cm}^{-2}$.

In [16,22-24] we have described the technique of the definition of parameters of charge carries in CMT. It has been applied here, for quantitative definition of n , p and μ_n and μ_p before and after an irradiation which results are presented in Fig. 5.

With the purpose of check of reliability of the received results about $R(H)$, experimental data have been compared with theoretical curves designed under the formula (1) by

attraction of the found parameters n^{μ_n} , p^{μ_p} . The characteristic dependences $R(H)$ compared with calculation curves are presented in Fig. 1 and 2.

It is seen, that the character of curves $R(H)$ before and after an irradiation does not vary, and the consent of experiment with the theory in weak and strong fields is good enough, and the deviation in intermediate fields is observed. This question was analyzed in detail in [16,17]. Same situation is observed for other irradiated samples.

Apparently, the irradiation reduce of mobility of electrons in 1.4 times and of holes in 15-20%. At this, the irradiation does not influence on mechanism of dispersion.

The most interesting fact is the temperature dependence of concentration, arisen of a result of the irradiation. This question was not discussed in literature, but it is most attractive. It seems, that if the irradiation results in increase of concentration of electrons (at $T \geq 200\text{K}$, $n \approx 10^{13} \text{ cm}^{-3}$) and with downturn of T they should not decrease as donor

impurity in CMT are ionized at the lower temperatures [18-20]. Hence, concentration of electrons at 4.2K before and after an irradiation should grow strongly.

However, the ratio of concentration of electrons remains to be constant in wide range of T . From our data follows, that this process occurs and induced by electrons (as result of before and after an irradiation).

2. Influence of the electron irradiation of thermo-emf and thermomagnetic pheno-mena

It is known, that the determining factors in thermo-emf and thermomagnetic pheno-mena are the concentration and mobility of electrons. As electron irradiation of crystals CMT results in increase in concentration of electrons and some reduction of mobility. Therefore, the study of the influences irradiation of thermoelectric and thermomagnetic phenomena can give the additional information on the nature of electroactive defects, arising during the irradiation with this purpose the study of thermo-emf, magneticthermo-emf and the cross-section thermomagnetic effect in temperatures of 4,2-300K and magnetic fields $0 \leq H \leq 22$ kErs has been carried out.

The characteristic dependences $\alpha(T)$ before and after an irradiation for a samples with $x=0.12$ and $x=0.15$ are presented in Fig. 6.

As seen, in area, where $\alpha > 0$, the irradiation reduced value of α , and in area where $\alpha < 0$ leads to increase of α . Thus, the sign of inversion of thermo-emf is displaced in area of low temperatures, and in the sample with $x=0.15$ in the same direction, the position of the maximum of dependence $\alpha(T)$ is placed also. There results and data on galvanomagnetic properties, confirm a conclusion on increase of electron concentration at irradiation.

It is necessary to know the temperature dependence of parameters of charge carries for the quantitative analysis of thermo-emf.

These parameters which have been determined, are involved for the analysis of the data $\alpha(T, \Phi)$.

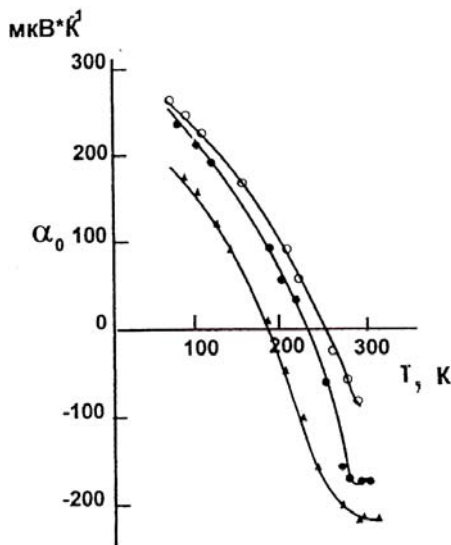


Fig. 6. Temperature dependences of thermo-emf α_0 for samples of $\text{Cd}_{0.12}\text{Hg}_{0.88}\text{Te}$; o- $\Phi=0$, •- $\Phi=5.6 \cdot 10^{17} \text{ cm}^{-2}$, Δ - $\Phi=1.5 \cdot 10^{18} \text{ cm}^{-2}$.

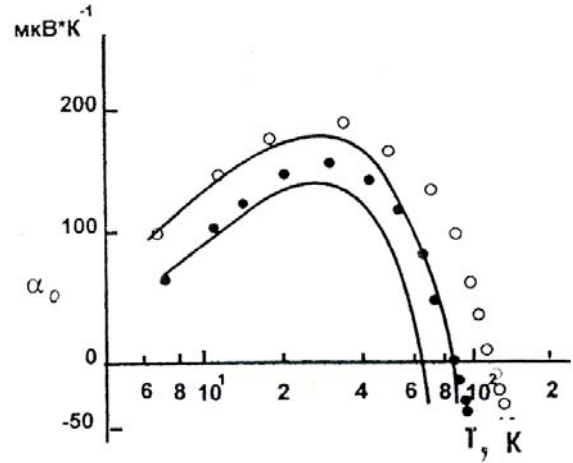


Fig. 7. Temperature dependences of thermo-emf α_0 for samples of $\text{Cd}_{0.12}\text{Hg}_{0.88}\text{Te}$; continuous lines – calculation; o- $\Phi=0$; •- $\Phi=5.6 \cdot 10^{17} \text{ cm}^{-2}$.

The continuous lines in Fig.7 present the results of calculation of $\alpha(T)$, made according two-zonal model. As seen, that the calculated curves well describes the experimental data: The reduction of α and displacement of positions of maximum and point of inversion of the sign of α . The appreciable deviation of calculated results from experiment at $T > 50\text{K}$ is connected with unsplit condition of zone structure $\text{Cd}_{0.15}\text{Hg}_{0.85}\text{Te}$, at which the nonparabolic zones of conductivity strongly amplifies ($\beta \geq 1$), that results in growth of an error of definition of zone parameters (E_g, m, η) and Fermis corresponding integrals.

As shown by calculations, up to an irradiation, at low T ($T < 25\text{K}$) in spite of the fact, that $\alpha_n > \alpha_p$, the holes dominate at thermo-emf with growth of T (since 4.2), the α_n, α_p and σ_n grow, and the growth α_p outstrips α_n . Strong growth $\alpha_p(T)$ is connected with the constancy $P(T)$. At performance of conditions, growth $\alpha_n \approx \alpha_p$ (at $T=25\text{K}$), the $\alpha(T)$ passes through a maximum the further reduction of $\alpha(T)$ (despite of $\alpha_p > \alpha_n$) is caused by strong growth of σ_n and σ_0 . It not only compensates the reduction of α_n , but also reduces α_p . The condition $\alpha_n \approx \alpha_p$ is carried out already at $T \approx 18\text{K}$, that explains shift of position of the maximum $\alpha(T)$ at low T range. Increasing of $\sigma_n(T)$ at radiation process causes also displacement of the point of inversion of the sigh of α at low T . The behavior of field dependences of magneticthermo-emf $\alpha(H)$, measured at various temperatures is interesting. The researches have shown that, the irradiation leads to increase of $\alpha(H)$ in all range of it (and $\alpha(H) < 0$) at room temperature. The $\alpha(H) > 0$ before irradiation at $T=200\text{K}$, the irradiation with doze up to $\Phi=5.6 \cdot 10^{17} \text{ cm}^{-2}$ decrease the magneticthermo-emf, and the increase of doze up to $1.46 \cdot 10^{18} \text{ cm}^{-2}$ leads to change of sign of $\alpha(H)$ at low fields ($H < 2\text{kErs}$). At ($H > 2\text{kErs}$) the $\alpha(H) > 0$, but quantity of magneticthermo-emf less than initial. Character of charge magneticthermo-emf at $T \geq 200\text{K}$ shows the increase n (hence σ_n and σ_0) at the irradiation. It is difficult to explain a course $\alpha(H)$ at the irradiation doze up to $\Phi=5.6 \cdot 10^{17} \text{ cm}^{-2}$ and $T=100\text{K}$. In week fields ($H \leq 2\text{kErs}$) magneticthermo-emf less than initial value, that corresponds to behavior $\alpha(H)$ at high T , but value $\alpha(H)$ at ($H > 1.5\text{kErs}$) exceeds the value $\alpha(H)$ up to an

irradiation. After an irradiation up to $\Phi = 1.46 \cdot 10^{18} \text{ cm}^{-2}$ the value of $\alpha(H)$ decreases in all interval of H [25].

The H - E effect is most sensitive to the mechanism of dispersion, presence of other type of charge carries, to charge

of their concentration and mobility. Dependences E_g from H and T for a sample with $x=0.15$ indicated, that the E_g grows by growing of H or passes through a maximum.

- [1] F.A.Zaitov, V.V.Aksenov Proceedings of All-Union conf. On physics and chemistry of compounds of A2B6 Kiev, 1969, p.34
- [2] J.J.Melingailis, L.R.Lean and C.H.Theodora. J.Appl.Phys.1973, №44, №6, 2647-2651
- [3] Yu.V.Lilenko, L.N.Limarenko, M.V.Kolikovsky In transactions. Semiconductors with narrow forbidden band and semimetals. Lvov 1975. p. 59-62
- [4] C.E.Mallon, J.A.Naber, J.F.Colwell. IEEE Tr .Nucl. Sci.1973, № 20. p. 214-219
- [5] A.G.Foyt, F.C.Harman, Y.P.Donelly. Type Appl.Sett.1971. v. 321-323
- [6] V.N.Brudniy, A.V.Voychekhovskiy, Qrechux, and others. FTP, 1977, v.11, №8, p.1540-1544
- [7] A.V.Voychekhovskiy, V.N.Brudniy, Yu.V.Silenko, M.A.Krivov, A.S.Petrov, Solid Sistem Commun. 1979, v.31, №2, p.105-108
- [8] F.D.Shepherd. IEEE Trans., Nucl.Sci.1074, v,21, №6, p.34-39
- [9] F.A. Zaitov. Q.Yu. Anderson, A.A. Druqova. Proceedings of All-Union conf. «Radiation effects in semoconductors and semiconductive devices» Baku, 1980, p. 87.
- [10] Q.Yu.Anderson, F.A.Zaitov Proceedings of all-Union conf. on radiation physics of semiconductors and related to them materials. Tashkent, 1984, p. 41
- [11] L.Bovina, F.A.Zaitov, O.V.Mixina, V.I.Stafecv. Neorganicheskiye materialy, 1976, v. 12, N 7, p. 1305-1306.
- [12] F.A.Zaitov, O.V.Mixina, A.Ya.Polyakova. Neorganicheskiye materialy, 1977, v. 13, N 10, p. 1922-1923.
- [13] N. Dekhtiyar, M. I. Dekhtiyar, V. V. Dyakin and others. FTP, 1984, v. 18, N 11, p. 1970-1974.
- [14] V. Voychekhovskiy, F. A. Zaitov, A. N. Kokhanenko and others. FTP, 1981, v. 15, N 8, p. 1606-1608
- [15] V. Voychekhovskiy, F. A. Zaitov, A.N.Kokhanenko and others. Proceedings of All-Union conf. on «Radiation effects in semiconductive devices»
- [16] S.A.Aliev, G. T. Gadjiev, E. I. Zulfigarov. Proceedings of all-Union conf. on radiation physics of semiconductors and related to them materials. Tashkent, 1984, p. 66
- [17] E. I. Zulfigarov, S.A.Aliev, G. T. Gadjiev. Actual problems of radiation researches. Baku, 1991, p.29.
- [18] C.T.Elliot, J.Z.Spain, Sol.State Comm.v.8,24, p.2063, 1970
- [19] C.T. Elliot, J. Melingailis, T.C. Harman, J.A. Kofalas, W.C. Vernan. Phys Rew.B.V. p. 2985, 1972
- [20] B.L.Gelmont, M. I. Dyakonov. JETR, v. 62, N 2, p. 713, 1972
- [21] B.M.Askerov. Kinetic effects in semoconductors. Nauka, L., 1970, 303 p.
- [22] A.V. Voychekhovskiy, A.N. Kokhanenko. Proceedings of International conf. «Physico-chemical processes in nonorganic materials» Kemerova, 2004, v. 2, p. 25.
- [23] C.A. Aliev, E.I. Zlfigarov, T. G. Gadjiev. Izv. vuzov SSSR «Physics », 1988, p. 11
- [24] S.A. Aliyev, E.I. Zulfigarov. Izv. Vuzov SSSR «Phisics», 1989, N5, p. 11.
- [25] E.I. Zulfigarov. Proceedings of Intern. Conf. «Phisico-chemical processes in nonorganic materials» Kemerova, 2004, v. 1, p. 35-37.

E.İ. Zülfiqarov

ELEKTRON ŞÜALANMASININ $\text{Cd}_x\text{Hg}_{1-x}\text{Te}$ KRİSTALINDA KİNETİK EFFEKTLƏRƏ TƏSİRİ

Məqalədə geniş temperatur (4,2-300K) və maqnit sahələrini ($60 \leq H \leq 22.000 \text{ E}$) diapazonunda $\text{Cd}_x\text{Hg}_{1-x}\text{Te}$ monokristalında kinetik effektlərə elektron şüalanmasının təsirinin nəticələri analiz edilmişdir.

Göstərilmişdir ki, kiçik sahələr və aşağı temperaturalarda şüalanmanın Holl effektinə təsiri daha çoxdur. $\sigma(T), R(T, H)$ asılılıqlarının nəticələrinin ikizonalı nəzəriyyə ilə müqayisəsi şüalanmanın yükdaşıyıcıların konsentrasiyası və yüklüklüyünə təsiri aydınlaşdırmağa və belə bir nəticəyə gəlməyə imkan verdi ki, KRT kristallarının elektronlarla şüalandırılması elektronların konsentrasiyasının donor tipli tellurun vakansiyaları ilə şərtlənən artımına gətirib çıxarır. Müəyyən edilmişdir ki, $\text{Cd}_x\text{Hg}_{1-x}\text{Te}$ ($x=0,12 \div 0,25$) kristalları İQ-şüalanmanın termmaqnit qəbuledijilərində əsə element kimi istifadə oluna bilər. Aşkar edilmişdir ki, $T < 40 \text{ K}$ olduqda $\text{Cd}_x\text{Hg}_{1-x}\text{Te}$ ($x \leq 0,15$) kristalında keçiricilik zonasındaki akseptor mərkəzlərinin konsentrasiyası donrların konsentrasiyasından çox-çox böyükdür. Akseptor səviyyələri həm ionlaşdırıcı elektronlar, həm də şüalanmanın yaratdığı elektronlar üçün tələ rolunu oynayırlar.

Э.И. Зульфигаров

ВЛИЯНИЕ ЭЛЕКТРОННОГО ОБЛУЧЕНИЯ НА КИНЕТИЧЕСКИЕ ЭФФЕКТЫ В $\text{Cd}_x\text{Hg}_{1-x}\text{Te}$

В работе анализированы результаты влияния электронного облучения на гальвано-термомагнитные свойства в монокристаллах $\text{Cd}_x\text{Hg}_{1-x}\text{Te}$ ($0 \leq x \leq 0,25$) в широком диапазоне температур (4,2-300K) и магнитных полей ($60 \leq H \leq 22.000 \text{ э.}$).

Показано, что действия облучения на эффект Холла наиболее существенно при слабых полях и низких T . Сопоставление результатов $\sigma(T), R(T, H)$ с двухзонной теорией позволило количественно выявить влияние облучения на концентрации и подвижность носителей заряда и заключить, что электронное облучение кристаллов КРТ приводит к возрастанию концентраций электронов, обусловленные вакансиями теллура донорного типа. Установлено, что при $T < 40\text{K}$ в $\text{Cd}_x\text{Hg}_{1-x}\text{Te}$ ($x \leq 0,15$) концентрация акцепторных центров, входящих в зону проводимости, на много больше концентрации доноров. Акцепторные уровни играют роль ловушек как для ионизирующихся электронов, так и для электронов наведенных облучением.

Received: 12.05.2004

ABOUT DIFFUSION OF PHASE TRANSITION OF AgSbTe_2

S.S. RAGIMOV, S.A. ALIEV

Institute of Physics NAS of Azerbaijan, Baku.Az - 1143, H.Javid ave, 33

It was investigated the influence of second phase on the electrical conductivity, thermo-e.m.f. and Hall coefficient of AgSbTe_2 in 200-450K temperature interval. It was shown, that the phase transition in AgSbTe_2 related by presence of p- Ag_2Te is diffuse and encompasses ~70% from all phase transition. It was established, that the $\alpha \rightarrow \beta$ phase transition has exponential character.

Introduction

In [1] was conducted the detailed research of thermoelectric properties of samples of Ag-Sb-Te system. Samples were obtained by a method of zone crystallization. The experiments have shown that from a beginning part to middle of an ingot samples are monophasic and correspond to $\text{Ag}_{19}\text{Sb}_{29}\text{Te}_{52}$. Starting from middle of an ingot on temperature dependencies of electrical conductivity $\sigma(T)$, Hall coefficients $R(T)$ and thermo-e.m.f. $\alpha(T)$ the anomalies were observed. These results were analyzed within the framework of the theory of kinetic phenomena for two-phase systems [2]. Was proposed, that in investigated samples the matrix is $\text{Ag}_{19}\text{Sb}_{29}\text{Te}_{52}$, and second phase p- Ag_2Te . Was established, that really these structures are two-phase and the contents of the second phase changes within the limits of 11-13 vol. %. In [3] is established, that in crystals of Ag_2Te the structural phase transition (SFT) has diffusion nature. Was calculated the parameters of diffusion phase transition (DFT) T_0 , a , $L_0(T)$, dL_0/dT , and is determined the area and degree of diffusion of phase transition (FT).

In this work was put the problem to consider the influencing of the second phase Ag_2Te on electrical properties of a system Ag-Sb-Te at more high temperature encompassing area of FT and to study the contents Ag_2Te on electrical properties in FT area.

Experimental results

In a fig. 1 the temperature dependencies of coefficients of electrical conductivity $\sigma(T)$, Hall $R(T)$ and thermo-e.m.f. $\alpha(T)$ of AgSbTe_2 are shown. As it is visible, since 390K the discontinuous change of all three factors takes place that unconditionally, is connected with FT Ag_2Te containing in AgSbTe_2 .

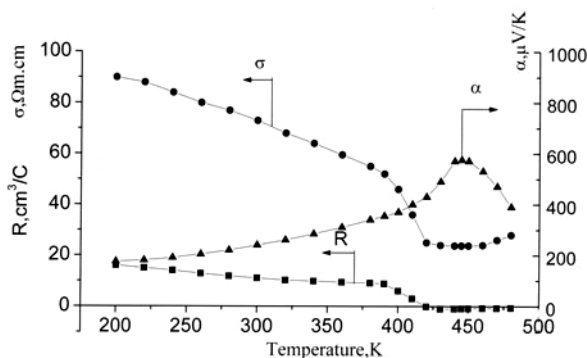


Fig.1. The temperature dependencies of electrical conductivity (σ), thermo-e.m.f. (α) and Hall coefficient (R) of AgSbTe_2 .

For a quantitative analyze of the obtained data it is necessary on basis of experimental data in FT region to find mass distribution of α and β - phases, according to the data m_α and m_β to calculate FT parameters: temperature of FT - T_0 , at which one $m_\alpha = m_\beta$; a temperature-dependent constant a of FT, function of inclusion $L_0(T)$ of a β -phase in an α -phase and temperature speed dL_0/dT of FT.

The theory and analysis of experimental results

The theory of diffusion phase transition (DFT) is particularized in [4,5]. It as well as theory of other phase transitions, is base of thermodynamic reasons. The characteristic peculiarity of DFT is the absence of sharp jumps of physical quantities, which indicates coexisting of two phases in a certain interval ΔT . It means that thermodynamic potential and other additive values of a system in DFT area contain the conforming characteristics of both phases. Thus it is possible to use general results obtained at construction of thermodynamic potential for condensate systems, according to which one:

$$\Phi(T) = \Phi_\alpha(T) + \Delta\Phi(T) \cdot L(T) \quad (1)$$

where $\Delta\Phi(T) = \Phi_\beta(T) - \Phi_\alpha(T)$, $\Phi_1(T)$ - thermodynamic potential of the first phase, $\Phi_2(T)$ of the second phase, $L(T)$ - function of inclusion. For finding $L(T)$ it is necessary to take into account, that in DFT it is necessary conditionally to distinguish three temperature interval: $T < T_1$, $T_1 < T < T_2$ and $T > T_2$. Therefore

$$\Phi(T) = \begin{cases} \Phi_1, & T < T_1 \\ \Phi_{12} = \Phi_1 + L_{12}(\Phi_2 - \Phi_1), & T_1 < T < T_2 \\ \Phi_2, & T > T_2 \end{cases} \quad (2)$$

If to designate temperature of FT beginning through T_1 , and the temperature of FT end through T_2 , then for $L(T)$ we have:

$$L(T) = \begin{cases} 0 & T < T_1 \\ 0 < L < 1 & T_1 < T < T_2 \\ 1 & T > T_2 \end{cases} \quad (3)$$

In case of diffused FT

$$L(T) = \frac{1}{1 + \exp[-a(T - T_0)]} \quad (4)$$

and

$$\frac{\partial L}{\partial T} = \frac{a}{2} \frac{1}{1 + \exp[-a(T - T_0)]} \quad (5)$$

From (4) and (5) it is seen, for their determination the parameters a_0 and T_0 are necessary found. A technique of determination a_0 and T_0 in detail are described in [3]. If to take into account, that $L(T)$ characterizes a part of phases in the region of their coexisting, it can be determined and as:

$$L(T) = \left[1 + \frac{m_\alpha(T)}{m_\beta(T)} \right]^{-1} \quad (6)$$

Values m_α and m_β it is necessary to determine directly from temperature dependences of investigated physical phenomena in FT region. From the joint solution (4) and (6) in the supposition $a=a_0$ we obtain:

$$\ln \frac{m_\alpha}{m_\beta} = a(T_0 - T) \quad (7)$$

From (7) follows, that at constant value a $\ln(m_\alpha/m_\beta=y)$ is a linear function T .

In work [3], enabling, that in FT region the abruptly change of electrical and thermal properties of Ag_2Te is related by a quantitative change α and β phases, m_α and m_β were calculated. On temperature dependences of electrical and thermal properties, the dependence $\ln y$ on T are constructed and T_0 and a are determined. For this purpose it was proposed to achieve linear change T in transition zone. Then from a beginning up to the end of FT the interval $\Delta T = T_e - T_b$ can be divided into equal intervals and corresponding values of measured coefficients to attribute to suspected phases, for example:

$$\Delta T_y = T_{y,\alpha} (1 - m_\beta/m_\alpha) + \Delta T_{y,\beta} (m_\beta/m_\alpha) \quad (8)$$

By such method distribution m_α and m_β were determined in FT region, T_0 , a , then $L(T)$, dL/dT are calculated and it is shown, that for determination of FT parameters the most sensible to FT electronic processes can be used.

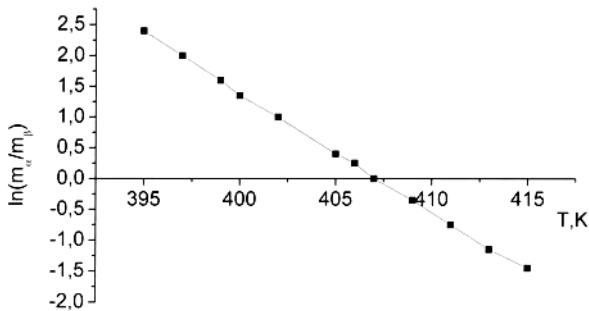


Fig.2. The temperature dependence of $\ln(m_\alpha/m_\beta)$, obtained from electrical conductivity data.

In a fig. 2 the dependence $\ln y$ on T , obtained on the data $\sigma(T)$ and $R(T)$ for AgSbTe_2 are shown. The interception of these straight lines with an axis T gives value T_0 , at which one $m_\alpha = m_\beta$, and relation $\Delta \ln y / \Delta T = a$. Under the data T_0 and a according to the formulas (4) and (5) the temperature dependence of a function of inclusion $L(T)$ and speed dL/dT of FT are calculated. The temperature dependence $L(T)$ and dL/dT are shown in a fig. 3 and 4.

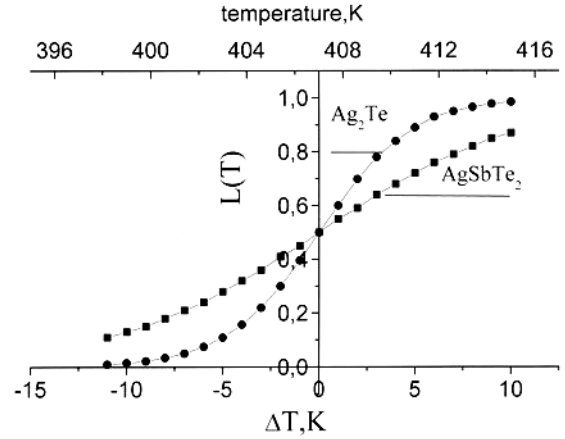


Fig.3. The temperature dependence of inclusion function L .

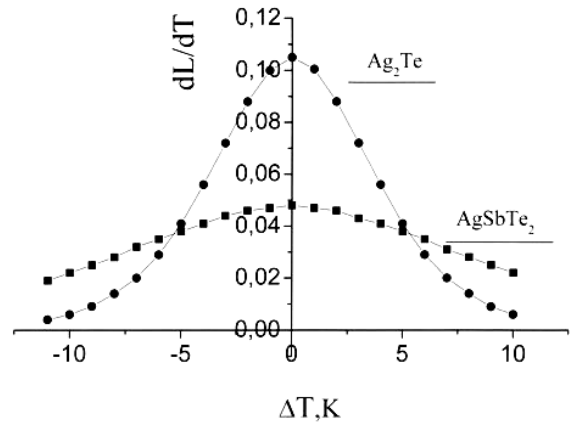


Fig.4. The temperature dependence of speed of change of inclusion function dL/dT .

In these figures for comparison, the data for Ag_2Te are presented also. These data visually demonstrate a diffuse FT in Ag_2Te and AgSbTe_2 . According to the DFT theory the region of FT diffusion ΔT is determined by interception of a straight line conducted from half of maximum value dL/dT parallel to axis ΔT , from a curve dL/dT . In a fig. 4 these straight lines are indicated by broken lines. For Ag_2Te the region of diffusion encompasses $2\Delta T = 8.5\text{K}$, and in AgSbTe_2 the diffusion encompasses $2\Delta T = 18\text{K}$. From the formula (5) follows, that maximum value dL/dT corresponds to $a/4$, i.e. degree of diffusion is the temperature-dependent constant of FT. From the obtained data also it is follows, that in the region of diffusion the transition of an α -phase in a β -phase goes on exponential law $m_\alpha/m_\beta = e^{a(T_0 - T)}$.

The calculations demonstrate, that the region of FT diffusion encompasses $\sim 70\%$ of all phase change ($\Delta T = T_e - T_b$)

The mechanism leading to diffusion of FT is fluctuations of physical states in matter. The main causes of the fluctuation

at structural FT are as follows: irregularity of distribution of temperature, owing to an allocated significant amount of heat at SFT, in particular in Ag_2Te , polycrystalline of a low temperature phase of argentums chalcogenides, distorting of crystal lattice, high impurity concentration, deviation from a stoichiometry etc. irregularity of physical states.

It is necessary to pay the special attention that diffusion of FT in AgSbTe_2 more, than twice surpass diffusion in Ag_2Te . It means that at FT Ag_2Te , arranged inside $\text{Ag}_{19}\text{Sb}_{29}\text{Te}_{52}$ as the second phase, additional source of fluctuations takes place. Certainly, it could be expected, as distribution 11-13 weights. % Ag_2Te inside a matrix should result to additional heterogeneities: temperature at FT, heterogeneities of distribution Ag_2Te on volume basis, on

borders of two phases etc. We shall note that more detailed research of two-phase systems can expand knowledge about mechanisms of FT diffusion in solids. Some results about it are obtained at research of a problem of diffusion FT in HTSC [6-9]. In these works the FT region of a lot known HTSC is considered and influence of magnetic field on a degree of FT diffusion is determined. Is shown, that the dual states (normal and superconducting), created by a magnetic field in a transition zone, hardly enhances a fluctuation, a source by which one is vortex current. However, number of vortices in SC of the second kind, though grow with increasing of a magnetic field, but they as against of phase - Ag_2Te in a matrix $\text{Ag}_{19}\text{Sb}_{29}\text{Te}_{52}$ are distributed uniformly.

-
- | | |
|--|---|
| <p>[1] S. A. Aliev, S.S. Ragimov, Izv. AN SSSR, ser. Neorganicheskie Materiali, 1992, v.28, №2, p. 329.</p> <p>[2] C. Herring, J. Appl. Phys. (1960), p.1939, v.31, №11.</p> <p>[3] S.A. Aliev, F.F. Aliev, Z.S. Gasanov. 1693 (1998). FTT, v.40, №9.</p> <p>[4] B.N. Rolov. Razmitie fazovie perexodi. (1972) 311s.</p> <p>[5] B.N. Rolov, Fizicheskie svoystva razmitix fazovix perexodov, Riga, 1974, 175s.</p> | <p>[6] S.A. Aliev, S.S. Ragimov, V.M. Aliev, Transactions NASA, ser. phys-mat-tech. scien., (2001), №2-5, 67.</p> <p>[7] S.A. Aliev. The smearing of Phase transition in HTSC, J. Fizika of NASA, 2002. v.8, №4, p.32.</p> <p>[8] Prof. Dr.habil. Sabir Aliev. Abhandlungeen der WGB, band3, Berlin, 2003.</p> <p>[9] S.A. Aliev, S.S. Ragimov, V.M. Aliev, J. Fizika NASA, 2003, v.9, № 3-4, 30.</p> |
|--|---|

S.S. Rəhimov, S.A. Əliyev

AgSbTe_2 -DƏ FAZA KEÇİDİNİN YAYILMASI

200-450K temperatur intervalında AgSbTe_2 -nin elektrikkeçiriciliyinə, termo e.h.q. və Xoll əmsalına ikinci fazanın təsiri tədqiq edilmişdir. p- Ag_2Te -un olması ilə əlaqədar olan AgSbTe_2 -nin faza keçidinin yayınıq olması və bütün faza keçidinin 70% əhatə etməsi göstərilmişdir. α -fazanın β -fazaya keçidinin eksponensial qanun ilə baş verməsi göstərilmişdir.

С.С. Рагимов, С.А. Алиев

О РАЗМЫТИИ ФАЗОВОГО ПЕРЕХОДА В AgSbTe_2

Исследовано влияния второй фазы на электропроводность, термоэдс и коэффициент Холла AgSbTe_2 в температурной области 200-450K. Показано, что фазовый переход в AgSbTe_2 , обусловленный присутствием p- Ag_2Te , является размытым и охватывает ~70% от всего фазового перехода. Установлено, что переход α -фазы в β -фазу происходит по экспоненциальному закону.

Received: 20.10.2004

INVESTIGATION OF PHOTOELECTRIC CHARACTERISTICS OF SILICON AVALANCHE MICRO-PIXEL STRUCTURES WITH SURFACE DRIFT OF CHARGE CARRIERS

R. MEHTIEVA, A. NADZHAFOV

*Institute of Radiation Problems, Azerbaijan National Academy of Sciences,
Az-1143, H. Javid ave., 31A, Baku*

M. MUSAIEV

Azerbaijan State Oil Academy, Az-1007, Baku, Azadlig ave., 20

N. MUSAIEVA, Z. SADYGOV, E. TAPTYGOV

*Institute of Physics, Azerbaijan National Academy of Sciences,
Baku Az-1143, H. Javid str., 33*

Photoelectric properties of a new high sensitive photodetector elaborated on basis of silicon avalanche micro-pixel structures being an adequate analogue of known vacuum photomultipliers are investigated. It was found that dynamic range of this device exceeds five orders at gain of photo signal of 250. The offered photodetector may be successfully used for registration of weak light pulses and gamma radiation.

During last decade the silicon avalanche micro-pixel photodiode (AMPD) is considered as one of perspective options for creation of the cheapest multichannel avalanche photodetectors [1-2]. In given article the first results on photoelectric properties of a new AMPD are presented.

Advanced properties the new AMPD is connected with a local negative feedback (LNF) effect, which significantly reduces influence of the crystal non-uniformity on the characteristics of the avalanche multiplication process. The LNF effect is achieved by forming an electric field of specific geometry in the multilayer silicon structure, which ensures localisation of avalanche processes and limits them to the micro-regions (micro-pixels) of $3-5\mu$ in diameter depending of design. This results in a unique combination of high signal amplification and uniform avalanche multiplication over sensitive area of the device.

The new AMPD is produced on basis of low-resistive silicon wafer of p-type conductivity with specific resistance of 10 Ohm-cm. A schematic cross section of this AMPD is submitted in figure 1.

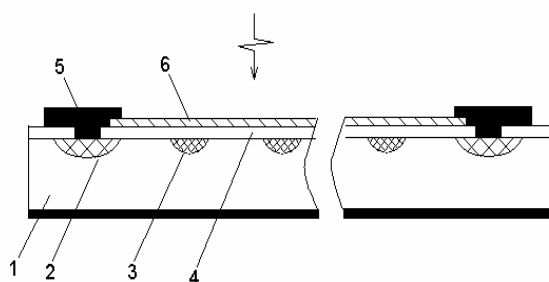


Fig. 1. Cross-section of the avalanche structure.

1-silicon substrate with p-type conductivity, 2-guard ring of n-type Si, 3-matrix of p-n-junctions, 4-silicon dioxide layer, 5-aluminium layer, 6-semitransparent titanic electrode.

A silicon dioxide layer of 1000\AA thickness was grown on silicon wafer, through which it was made ion implantation with phosphorous followed by annealing process at temperature of 1000°C . The semitransparent titanic layer surrounded with an aluminium ring was used as a field

electrode. Using this procedure and special photo masks, a matrix of small p-n-junctions with step about $8-10\mu$ was made in sensitive area of structure. About 10,000 micropixel c/mm^2 are formed over the sensitive area of the proposed avalanche photodiode.

The operation principle of the AMPD is as follows. Positive bias voltage is applied to the field electrode, large enough to cause avalanche multiplication in the array of p-n junctions. At this bias the depletion region reaches the Si-SiO₂ boundary where a very thin ($\sim 10\text{nm}$) layer of n-type conductivity with high resistance is formed. The value of the surface resistance of this layer determines efficiency of LNF effect. During the avalanche development time ($\sim 1\text{ ns}$) most of the multiplied electrons are collected in the given p-n-junction as a charge packet. Dimensions of the packet are approximately equal to diameter of p-n-junction, which is about $3-5\mu$. The packet produces local decrease of the electric field at this p-n junction, thus locally quenching the avalanche process. After the avalanche process is suppressed, the charge packet (electrons) drifts along the Si-SiO₂ boundary to the peripheral drain electrode during 100-200ns. The short signal pulse is generated by the displacement current across the dielectric (silicon dioxide) layer.

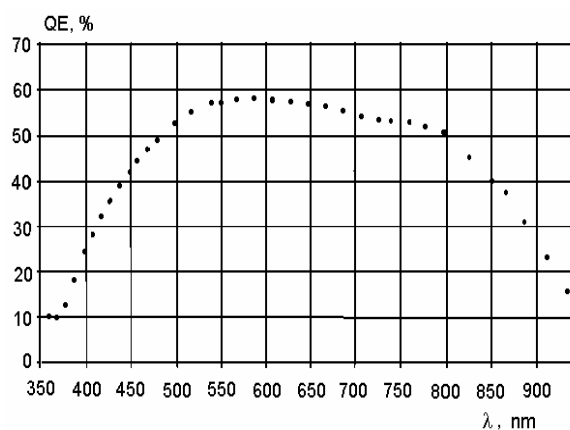


Fig. 2. Spectral dependence of quantum efficiency.

Multiplication factor (signal gain) M was determined by formula $M = \Delta J_t / \Delta i_{ph}$, where ΔJ_t - an increment of the total avalanche current at potential $U > 50V$ (in the beginning of avalanche process), Δi_{ph} - an increment of photocurrent initiating avalanche process, which is measured at $U = 20V$ (e. g. at absence of avalanche process).

Figure 2 shows quantum efficiency (QE) of the AMPD vs. light wavelength. A mercury lamp was used as a light source for this measurement. Quantum efficiency of the AMPD sample was defined concerning spectral sensitivity known p-i-n diode S1223 from Hamamatsu.

It was found that the maximal value of quantum efficiency is about 58 %, and this value is limited by transparency of the titan layer. Fall of quantum efficiency in range of short wavelength is connected with both high absorption factors for incident light and high rate of recombination process in the Si-SiO₂ boundary. Reduction of QE in the right part of this dependence is determined by lowering of absorption factor in the silicon wafers.

Dependence of photoresponse (an amplitude of photocurrent) on quantity of incident photons has been investigated at gains of $M=250$ and 4000. A light emitted diode with wavelength of 450nm was used for these measurements.

It was found that the dynamic range of photo response is determined by multiplication factor (gain) of avalanche process in semiconductor. As shown in figure 3 photoresponse increases linearly up to number of photons $N_{ph} \sim 20000$ at $M=4000$. However the AMPD may have linear photoresponse up to $N_{ph} \sim 500000$ in conditions of $M \sim 250$. This nonlinearity of photoresponse appearing at high gains may be explained by decreasing of electric field in p-n junction because the drain layer hasn't enough conductance to discharge avalanche region.

Thus, photoelectric properties of the new high sensitive

photodetector made on basis of avalanche silicon structures being adequate analogue of known vacuum photomultipliers are investigated. Dynamic range the device may exceed five orders at gain of $M \sim 250$. The AMPD offered may be successfully used for registration of very weak light pulses.

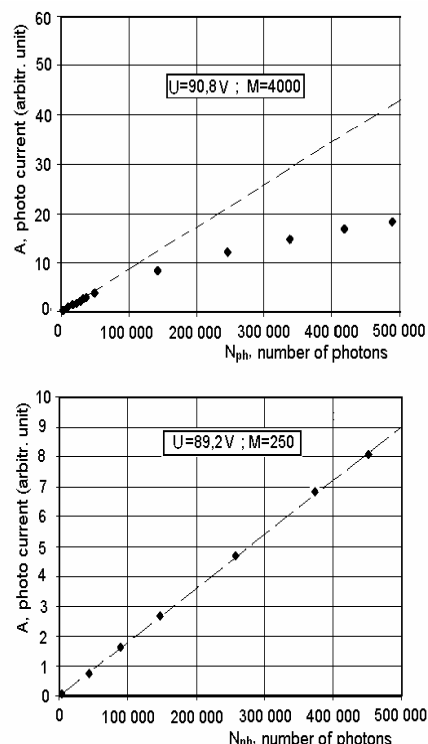


Fig.3. Dependence of photoresponse on number of falling photons in a pulse.

The work was supported in part by CRDF USA-Azerbaijan Bilateral Grant #3106.

[1] Z. Ya. Sadygov, T. M. Burbaev and V. A. Kurbatov. " An Avalanche Photodiode with Metal-Insulator-Semiconductor Properties ".-Semiconductors, v.35, N1, (2001), p.117-121.

[2] Z. Ya. Sadygov, V. N. Jejer, Yu. V. Musienko, T. V. Sereda, A. V. Stoikov, I. M. Zheleznykh. " Super-sensitive avalanche silicon photodiode with surface transfer of charge carriers ".-Nucl. Instrum. and Methods in Phys. Res., A504 (2003), 301-303.

R. Mehtiyeva, A. Nəcəfov, M. Musayev, N. Musayeva, Z. Sadıqov, E. Tapıqov

SƏTHİNDƏ YÜKDAŞIYICILAR AXAN SİLİSİUM ƏSASLI SELVARI MİKRO-PİKSEL STRUKTURLARIN FOTOELEKTRİK XASSƏLƏRİNİN TƏDQIQI

Məlum vakuum fotoelektron gücləndiricinin analoqu olan və silisium tərkibli selvari mikropiksel strukturların əsasında hazırlanmış yüksək həssaslıqlı fotodetektorun fotoelektrik xassələri tədqiqi edilmişdir. Bu qurğunun dinamik oblastının fotosiqnalın 250 dəfə böyüdülməsi zamanı 5 tərtibdən yuxarı olduğu tapılmışdır. Təklif olunan fotodetektor zəif işıq impulslarının və qama şüalanmanın qeydiyyatı zamanı uğurla istifadə oluna bilər.

Р. Мехтиева, А. Наджафов, М. Мусаев, Н. Мусаева, З. Садыгов, Е. Таптыгов

ИССЛЕДОВАНИЕ ФОТОЭЛЕКТРИЧЕСКИХ ХАРАКТЕРИСТИК КРЕМНИЕВЫХ ЛАВИННЫХ МИКРО-ПИКСЕЛЬНЫХ СТРУКТУР С ПОВЕРХНОСТНЫМ ТЕЧЕНИЕМ НОСИТЕЛЕЙ ЗАРЯДА

Исследованы фотоэлектрические свойства высокочувствительного фотодетектора, являющегося аналогом известного вакуумного ФЭУ и приготовленного на основе кремниевых лавинных микропиксельных структур. Найдено, что динамическая область этого устройства превышает пять порядков при усилении фотосигнала в 250 раз. Предложенный фотодетектор может быть успешно применен для регистрации слабых световых импульсов и гамма-излучения.

Received: 14.11.2004

THERMO-MAGNETIC EFFECTS OF HOT ELECTRONS IN NON-DEGENERATE SEMICONDUCTORS UNDER THE CONDITIONS OF STRONG MUTUAL ELECTRON-PHONON DRAG

M.M.BABAYEV

*Institute of Physics, Azerbaijan National Academy of Sciences,
AZ 1143, H. Javid av., 33, Baku*

The thermoelectromotive force and Nernst-Ettingshausen effects of non-degenerate semiconductors under the conditions of strong electron-phonon mutual drag are investigated by taking into account the electron and phonon heating in high electric field. The dependences of thermoelectromotive force and Nernst-Ettingshausen voltage on the electric field strength and lattice temperature are obtained.

Recently the theoretical and experimental interest in thermoelectric and thermo-magnetic effects in bulk and low-dimensional systems has been intensified [1-6]. There are also some theoretical investigations of thermoelectric and thermo-magnetic effects in semiconductors under high external electric and non-quantizing magnetic fields [7-12]. In addition, there are some review articles devoted to these subjects [13-14]. In this paper the thermoelectromotive force and transverse Nernst-Ettingshausen effect of non-degenerate semiconductors under the conditions of strong electron-phonon mutual drag are investigated by taking into account the electron and phonon heating in high electric (\vec{E}) field. The spectrum of electrons is assumed to be parabolic:

$$\varepsilon = \frac{p^2}{m}. \quad (1)$$

The basic equations of the problem are the coupled Boltzmann transport equations for electrons and phonons. It is assumed that the electrons and phonons are scattered mainly by each other (the conditions of strong mutual drag) via the deformation interaction. We consider the quasi-elastic scattering of electrons by acoustic phonons. In this case the distribution functions of electrons $f(\vec{p}, \vec{r})$ and phonons $N(\vec{q}, \vec{r})$ may be written as:

$$f(\vec{p}, \vec{r}) = f_0(\varepsilon, \vec{r}) + \vec{f}_1(\varepsilon, \vec{r}) \frac{\vec{p}}{p}, \quad (2)$$

$$N(\vec{q}, \vec{r}) = N_0(q, \vec{r}) + \vec{N}_1(q, \vec{r}) \frac{\vec{q}}{q}, \quad (3)$$

where f_0 (N_0) and \vec{f}_1 (\vec{N}_1) are the isotropic and anisotropic parts of the electron (phonon) distribution functions, respectively. We assume that the so called "diffusion approximation" for electrons and phonons applies.

Therefore, $|\vec{f}_1| \ll f_0$ and $|\vec{N}_1| \ll N_0$.

If the inter-electronic collision frequency ν_{ee} is much more than the collision frequency of the electrons for the energy transfer to lattice ν_e , then $f_0(\varepsilon, \vec{r})$ is the Fermi distribution function with an electron temperature T_e . Note that all temperatures are in energy units.

We assume that in the lattice there is a "thermal reservoir" of short-wavelength (SW) phonons for long-wavelength (LW) phonons interacting with electrons: $q_{max} \approx 2p \ll \frac{T}{s_0}$, where s_0 is the sound

velocity in the crystal, q_{max} is the maximum quasi-momentum of LW phonons. Under these conditions LW phonons are heated and $N_0(q, \vec{r})$ has the form [15]

$$N_0(q) = \left[\exp\left(\frac{\hbar\omega_q}{T_p}\right) - 1 \right]^{-1} \approx \frac{T_p}{\hbar\omega_q}, \quad (4)$$

where T_p is the effective temperature of the LW phonons. In accordance with Ref. [15], in the case, when the phonons are scattered mainly by electrons, the temperature of LW phonons T_p becomes equal to the temperature of electrons T_e . Therefore, under the conditions of strong mutual drag $T_p = T_e$.

The anisotropic parts of the distribution functions of electrons and phonons are obtained by solving the coupled system of Boltzmann equations:

$$\frac{p}{m} \nabla f_0 - e \vec{E}_c \frac{p}{m} \frac{\partial f_0}{\partial \varepsilon} - \Omega [\vec{h} \vec{f}_1] + \nu(\varepsilon) \vec{f}_1 + \frac{2\pi m}{(2\pi\hbar)^3 p^2} \frac{\partial f_0}{\partial \varepsilon} \int_0^{2p} \vec{N}_1(q) W(q) \hbar\omega_q q^2 dq = 0, \quad (5)$$

$$s_0 \nabla N_0(q) + \beta(q) \vec{N}_1(q) - \frac{4\pi m}{(2\pi\hbar)^3} W(q) N_0(q) \int_{q/2}^{\infty} \vec{f}_1 dp = 0. \quad (6)$$

Here e is the absolute value of the electron's charge, $\vec{E}_c = \vec{E} + \vec{E}_T$, \vec{E}_T is the thermoelectric field, m is the electron's effective mass, $\Omega = eH/mc$ is the cyclotron frequency, $\hbar = \hbar/H$, $\hbar\omega_q = s_0 Q$ is the phonon energy,

constant, $\beta(Q)$ and $\nu(\varepsilon)$ are the total phonon and electron momentum scattering frequencies, respectively:

$W(q) = \frac{\pi E_0^2}{\hbar \rho s_0} q$ is the square matrix element of the

electron-phonon interaction, E_0 is the deformation potential

$$\nu(\varepsilon) = \nu_p(\varepsilon) + \nu_i(\varepsilon), \beta(q) = \beta_e(q) + \beta_p(q) + \beta_b(q), \quad (7)$$

where the indices i, p, e and b denote the scattering by impurity ions, by phonons, by electrons and by crystal boundaries, respectively.

$$\nu_p(\varepsilon) = \frac{\sqrt{2} m^{\frac{3}{2}} T^{\frac{3}{2}} E_0^2}{\pi \hbar^4 s_0^2 \rho} \left(\frac{T_p}{T} \right) \left(\frac{\varepsilon}{T} \right)^{\frac{1}{2}}, \nu_i(\varepsilon) \cong \frac{e^4 N_i}{m^{\frac{1}{2}} T^{\frac{3}{2}} \chi_0^2} \left(\frac{\varepsilon}{T} \right)^{-\frac{3}{2}}, \quad (8)$$

$$\beta_e(q) = \left(\frac{\pi m s_0^2}{8 T_e} \right)^{\frac{1}{2}} \frac{N E_0^2}{\hbar \rho s_0 T_e} q, \beta_p(q) = \frac{T^4}{4 \pi \rho \hbar^4 s_0^4} q, \beta_b(q) = \frac{s_0}{L}, \quad (9)$$

where ρ and L are the density and the minimum size of specimen, respectively, χ_0 is the dielectric constant of the crystal, N and N_i are the concentrations of electrons and ionic impurity, respectively.

Solving the coupled equations (5) - (6) it is easy to calculate the electric current density of electrons

$$\vec{j} = - \frac{e}{3 \pi^2 \hbar^3} \int_0^\infty \vec{F}_1(\varepsilon) p^2(\varepsilon) d\varepsilon. \quad (10)$$

Let us direct external electric and magnetic fields along the y axis, and the gradient of lattice temperature (or the gradient of external electric field) along the z axis ($\vec{E} \parallel \vec{H} \parallel oy, \nabla T_e \parallel oz$). Using the equations $j_x = j_z = 0$ with (10) we obtain the following expressions for the thermoelectric field E_{Tz} and the transverse NE field E_{Tx} :

$$E_{Tz} + \frac{1}{e} \nabla_z \zeta(T_e) = \alpha_e \nabla_z T_e + \alpha_p \nabla_z T_p; \alpha_{e,p} = - \frac{\sigma_{11} \beta_{11}^{(e,p)} + \sigma_{12} \beta_{12}^{(e,p)}}{\sigma_{11}^2 + \sigma_{12}^2}, \quad (11)$$

$$E_{Tx} = -H(Q_e \nabla_z T_e + Q_p \nabla_z T_p); Q_{e,p} = \frac{1}{H} \frac{\sigma_{11} \beta_{12}^{(e,p)} - \sigma_{12} \beta_{11}^{(e,p)}}{\sigma_{11}^2 + \sigma_{12}^2}, \quad (12)$$

where $\alpha_{e,p}$ are the electron (e) and phonon (p) parts of the thermoelectromotive force and $Q_{e,p}$ are the respective parts of NE coefficient.

$$\sigma_{1i} = \int_0^\infty a(x) \left(\frac{\Omega}{\nu(x)} \right)^{i-1} [l + b_i(x)] dx, \quad x = \frac{\varepsilon}{T_e}, \quad (13)$$

$$\beta_{1i}^{(e)} = \frac{1}{e} \int_0^\infty a(x) \left(\frac{\Omega}{\nu(x)} \right)^{i-1} \left\{ x - \frac{\zeta(\vartheta_e)}{T \vartheta_e} + \left[1 - \frac{\zeta(\vartheta_e)}{T \vartheta_e} \right] b_i(x) \right\} dx \quad (14)$$

$$\beta_{1i}^{(p)} = \frac{1}{e} \int_0^\infty a(x) \left(\frac{\Omega}{\nu(x)} \right)^{i-1} [\lambda(x) + \lambda(1) b_i(x)] dx, \quad \vartheta_e = \frac{T_e}{T}. \quad (15)$$

$$\text{Here } \zeta(\vartheta_e) \text{ is the chemical potential of hot electrons} \quad (16)$$

$$a(x) = \frac{e^2}{3 \pi^2 \hbar^3} \frac{p^3(x) \nu(x)}{m [\Omega^2 + \nu^2(x)]} \times \exp \left[\frac{\zeta(\frac{\varepsilon}{T_e})}{T_e} - x \right]$$

$$b_1(x) = \frac{\gamma(x)\nu(x)}{\Omega^2 + \nu^2(I)(I - \gamma_0)^2} \left[\nu(I)(I - \gamma_0) - \frac{\Omega^2}{\nu(x)} \right], \quad (17)$$

$$b_2(x) = \frac{\gamma(x)\nu(x)}{\Omega^2 + \nu^2(I)(I - \gamma_0)^2} [\nu(I)(I - \gamma_0) + \nu(x)], \quad (18)$$

The coefficient $\lambda(x)$ characterizes the efficiency of the thermal drag, whereas coefficient $\gamma(x)$ describes the same for the mutual drag:

$$\lambda(x) = \frac{1}{4p^4} \frac{ms_0^2}{T_e} \nu_p(x) \int_0^{2p} \frac{1}{\beta(q)} q^3 dq, \quad (19)$$

$$\gamma(x) = \frac{1}{4p^4} \frac{\nu_p(x)}{\nu(x)} \int_0^{2p} \frac{\beta_e(q)}{\beta(q)} q^3 dq, \gamma_0 \equiv \gamma(x=1). \quad (20)$$

Under the conditions of strong electron-phonon mutual drag, i.e. when the electrons and phonons are scattered mainly by each other $\nu(\varepsilon) \approx \nu_p(\varepsilon)$, $\beta(q) \approx \beta_e(q)$, and as

$$\gamma(x) = 1 - \frac{\nu_i(x)}{\nu_p(x)} - \frac{1}{4p^4} \int_0^{2p} \frac{\beta_p(q)}{\beta_e(q)} q^3 dq - \frac{1}{4p^4} \int_0^{2p} \frac{\beta_b(q)}{\beta_e(q)} q^3 dq. \quad (22)$$

Using (8) and (9), from (22) we obtain:

$$\gamma(x) = 1 - \frac{e^4 \hbar^4 \rho s_0^2 N_i}{m^2 T^3 \chi_0^2 E_0^2} g_e^{-3} x^{-2} - \frac{T^{\frac{11}{2}}}{\sqrt{2m\pi}^{\frac{3}{2}} \hbar^3 s_0^4 N E_0^2} g_e^{\frac{3}{2}} - \frac{4\hbar \rho s_0 T}{3\sqrt{\pi} m L N E_0^2} g_e x^{-\frac{1}{2}}. \quad (23)$$

In the parabolic case the chemical potential of hot non-degenerate electrons with concentration N takes the form:

$$\zeta(g_e) = T g_e \ln \frac{4\pi^{\frac{3}{2}} \hbar^3 N}{(2mT)^{\frac{3}{2}}} g_e^{-\frac{3}{2}}. \quad (24)$$

Under the conditions of the strong mutual drag ($g_e = g_p, \gamma_0 \rightarrow 1$) the electron temperature is determined from the energy balance equation

$$\sigma(g_e) E^2 = W_{pp}(g_e), \quad (25)$$

where $\sigma(g_e)$ is the conductivity of semiconductor in heating electric field, and $W_{pp}(g_e)$ is the power transferred

it seen from (20) $\gamma \approx \gamma_0 \rightarrow 1$. In this case from (17) and (18) follow, that $b_1(x)$ and $b_2(x)$ grow with raising γ_0 and tend to infinity at $\Omega \rightarrow 0, \gamma_0 \rightarrow 1$. Thus to calculate γ from (20) one should take into account as well some other non-basic mechanisms of electron and phonon scatterings. In the conditions $\nu_i(\varepsilon) \ll \nu_p(\varepsilon); \beta_p(q), \beta_b(q) \ll \beta_e(q)$ the thermal drag coefficient $\lambda(x)$ and the mutual drag coefficient $\gamma(x)$ may be written in the form

$$\lambda(x) \equiv \lambda_0 = \frac{2(2mT)^{\frac{3}{2}}}{3\pi^{\frac{3}{2}} \hbar^3 N} g_e^{\frac{3}{2}}, \quad (21)$$

by the LW phonons to the thermal reservoir of the SW phonons:

$$W_{pp}(g_e) = \frac{4\pi}{(2\pi\hbar)^3} \int_0^{\sqrt{8mT_e}} \beta_p(q) \hbar \omega_q [N_{T_e}(q) - N_T(q)] q^2 dq. \quad (26)$$

We consider the case, when external electric and magnetic fields are directed along the y axis, and the gradient of lattice temperature (or the gradient of external electric field) along the z axis ($\vec{E} \parallel \vec{H} \parallel oy, \nabla T_e \parallel oz$). In these conditions

$$\sigma(g_e) = \frac{e^2}{3\pi^2 \hbar^3 m} \exp \left[\frac{\zeta(g_e)}{T g_e} \right] \int_0^\infty \frac{p^3(x) e^{-x}}{\nu(x)} \left[1 + \frac{\gamma(x)}{1 - \gamma_0} \frac{\nu(x)}{\nu(1)} \right] dx. \quad (27)$$

When $\nu_i(\varepsilon) \ll \nu_p(\varepsilon); \beta_p(q), \beta_b(q) \ll \beta_e(q)$, using (23) we obtain:

$$\sigma(\mathcal{G}_e) = \frac{e^2 N}{m} \frac{\pi \hbar^4 \rho s_0^2 \mathcal{G}_e^{-\frac{3}{2}}}{\sqrt{2} m^{\frac{3}{2}} E_0^2 T^{\frac{3}{2}}} \left[\frac{\nu_{i0}(T)}{\nu_{p0}(T)} \mathcal{G}_e^{-3} + \frac{T^{\frac{11}{2}}}{\sqrt{2} m \pi^{\frac{3}{2}} \hbar^3 s_0^4 N E_0^2} \mathcal{G}_e^{\frac{3}{2}} + \frac{4 \hbar \rho s_0 T}{3 \sqrt{\pi} m L N E_0^2} \mathcal{G}_e \right]^{-1}. \quad (28)$$

We consider the following limiting cases:

1) The relaxation channel of the electron momentum by impurities becomes wider than that of the phonon momentum scattering by the crystal boundaries or by the phonons ($\frac{\beta_p + \beta_b}{\beta_e} \ll \frac{\nu_i}{\nu_p}$). In this case the calculation of the expression $\mathcal{G}_e(E)$ from (25), (26) and (28) at $\mathcal{G}_p = \mathcal{G}_e \gg 1$

$$\text{gives } \mathcal{G}_e = \left(\frac{E}{E_1} \right)^{\frac{4}{3}}; E_1 = \frac{em^{\frac{5}{4}} T^{\frac{11}{4}}}{\hbar^{\frac{7}{2}} \chi_0 \rho^{\frac{1}{2}} s_0^2}. \quad (29)$$

2) The phonons are scattered by phonons or by crystal boundaries more intensively than electrons are scattered by impurities ($\frac{\beta_p + \beta_b}{\beta_e} \gg \frac{\nu_i}{\nu_p}$). In this case there are two

sub cases:

2a) $\beta_p \gg \beta_b$. At $\mathcal{G}_p = \mathcal{G}_e \gg 1$ using (25), (26) and (28) we obtain:

$$\mathcal{G}_e = \left(\frac{E}{E_2} \right)^{\frac{1}{3}}; E_2 = \frac{\sqrt{2} m^2 T^7}{\pi^{\frac{11}{2}} \hbar^7 e N \rho s_0^5}. \quad (30)$$

2b) $\beta_p \ll \beta_b$. In this sub case at $\mathcal{G}_p = \mathcal{G}_e \gg 1$ we obtain:

$$\mathcal{G}_e = \left(\frac{E}{E_3} \right)^{\frac{4}{11}}; E_3 = \frac{2^{\frac{7}{4}} m^{\frac{7}{4}} T^{\frac{19}{4}}}{\pi^{\frac{9}{4}} \sqrt{3} \hbar^5 e N \rho^{\frac{1}{2}} s_0^2 L^2}. \quad (31)$$

In the region of weak-heated electric field ($\mathcal{G}_e - 1 \ll 1$) the electron temperature \mathcal{G}_e may be represented as:

$$\mathcal{G}_e = 1 + \left(\frac{E}{E_i} \right)^2, \quad (32)$$

where E_i ($i=1,2,3$) are the characteristic fields in the cases 1), 2a) and 2b).

Let us study the thermoelectric power $\alpha(0)$ and Nernst-Ettingshausen effects ($\Delta\alpha(H)$ and Q) of non-degenerate semiconductors under the conditions of strong electron-phonon mutual drag in weak ($\bar{\Omega} \ll \bar{\nu}$) and strong ($\bar{\Omega} \gg \bar{\nu}$) magnetic fields. On the basis of (11) to (15) it may be shown that under these conditions the phonon part of NE coefficient (Q_p) and the variation of the phonon part of the thermoelectric power ($\Delta\alpha_p(H)$) are equal to zero, both in weak and strong magnetic fields. Under the conditions of

strong mutual drag, in the arbitrary magnetic fields we obtain from (11), (13) and (15):

$$\alpha_p = -\frac{1}{e} \frac{2(2mT)^{\frac{3}{2}}}{3\pi^{\frac{3}{2}} \hbar^3 N} \mathcal{G}_e^{\frac{3}{2}}. \quad (33)$$

The electron parts of longitudinal and transverse NE effects strongly depend on the magnetic field strength. In weak magnetic fields ($\bar{\Omega} \ll \bar{\nu}$) for the thermoelectromotive force $\alpha_e(H)$ and for the change of thermoelectromotive force

$$\Delta\alpha_e(H) = |\alpha_e(H)| - |\alpha_e(0)| \quad (34)$$

we obtain the following expressions:

$$\alpha_e(H) = -\frac{1}{e} \left[1 + \frac{3}{2} \ln \frac{2mT}{\pi \hbar^2 (4N)^{\frac{2}{3}}} \mathcal{G}_e - \left(\frac{\mu(T)H}{c} \right)^2 \mathcal{G}_e^{-3} \right] \quad (35)$$

$$\Delta\alpha_e(H) = -\frac{1}{e} \left(\frac{\mu(T)H}{c} \right)^2 \mathcal{G}_e^{-3}, \quad (36)$$

where $\mu(T_e)$ is the mobility of hot electrons in the non-degenerate semiconductors:

$$\mu(T_e) = \frac{2\sqrt{2}\pi}{3} \frac{e \hbar^4 \rho s_0^2}{m^{\frac{5}{2}} T^{\frac{3}{2}} E_0^2} \mathcal{G}_e^{\frac{3}{2}} = \mu(T) \mathcal{G}_e^{\frac{3}{2}}. \quad (37)$$

From (35)-(36) it is seen that thermoelectromotive force in weak magnetic fields decreases with increasing of the magnetic field strength. The electron part of NE coefficient in weak magnetic fields:

$$Q_e = -\frac{\mu(T)}{ec} \mathcal{G}_e^{-\frac{3}{2}} = -\frac{2\sqrt{2}\pi}{3} \frac{\hbar^4 \rho s_0^2}{cm^{\frac{5}{2}} T^{\frac{3}{2}} E_0^2} \mathcal{G}_e^{-\frac{3}{2}}. \quad (38)$$

In strong magnetic field ($\bar{\Omega} \gg \bar{\nu}$) for the thermoelectromotive force one obtains the following expressions:

$$\alpha_e(H) = -\frac{1}{e} \left[\frac{5}{2} + \frac{3}{2} \ln \frac{2mT}{\pi \hbar^2 (4N)^{\frac{2}{3}}} \mathcal{G}_e \right]. \quad (39)$$

From (39) it is seen that the thermoelectromotive force increases in strong magnetic field:

$$\Delta\alpha_e(H) = \frac{3}{2e}. \quad (40)$$

The electron part of NE coefficient in strong magnetic fields:

$$Q_e = -\frac{1}{e} \frac{64}{9\pi} \frac{c}{\mu(T)H^2} g_e^{\frac{3}{2}} = -\frac{16\sqrt{2\pi}}{3\pi^2} \frac{cm^{\frac{5}{2}}T^{\frac{3}{2}}E_0^2}{e^2\hbar^4\rho s_0^2H^2} g_e^{\frac{3}{2}} \quad (41)$$

Experimentally interesting are the total thermoelectromotive force (V) and the NE voltage (U) given by

$$V = \int_0^{L_z} (\alpha_e \nabla_z T_e + \alpha_p \nabla_z T_p) dz = V_e + V_p, \quad (42)$$

$$U = -\int_0^{L_x} (HQ_e \nabla_z T_e + HQ_p \nabla_z T_p) dx = U_e + U_p, \quad (43)$$

where L_x and L_z is the linear dimensions of the specimen in the x - and z -directions, respectively. Let us consider dependences of V and U on the heating electric field and lattice temperature under the following conditions: at one end of the specimen the electrons are in a state characterized by the lattice temperature T , whereas at the other end they are heated ($g_e > 1$) by the external electric field.

Taking into account the expressions of $g_e(E, T)$ in (33) to (43), we obtain explicit forms of V and U as functions of E and T . In the case of strongly heated ($g_e \gg 1$) electron gas in the arbitrary magnetic fields for V_e and V_p we obtain the following expressions:

$$V_e \sim E^{\frac{4}{3}} T^{\frac{11}{3}}; V_p \sim E^{\frac{10}{3}} T^{\frac{20}{3}} N^{-1} \quad \text{in the case 1),} \quad (44)$$

$$V_e \sim E^{\frac{1}{3}} T^{\frac{7}{3}} N^{\frac{1}{3}}; V_p \sim E^{\frac{5}{6}} T^{\frac{10}{3}} N^{\frac{1}{6}} \quad \text{in the case 2a),} \quad (45)$$

$$V_e \sim E^{\frac{4}{11}} T^{\frac{19}{11}} N^{\frac{4}{11}}; V_p \sim E^{\frac{10}{11}} T^{\frac{20}{11}} N^{\frac{1}{11}} \quad \text{in the case 2b).} \quad (46)$$

In weak magnetic fields ($\bar{\Omega} \ll \bar{\nu}$) for U_e one obtains the following expressions:

$$U_e \sim E^{\frac{2}{3}} T^{\frac{4}{3}} H \quad \text{in the case 1),} \quad (47)$$

$$U_e \sim E^{\frac{1}{6}} T^{\frac{2}{3}} H N^{\frac{1}{6}}; \quad \text{in the case 2a),} \quad (48)$$

$$U_e \sim E^{\frac{2}{11}} T^{\frac{4}{11}} H N^{\frac{2}{11}} \quad \text{in the case 2b).} \quad (49)$$

In strong magnetic fields ($\bar{\Omega} \gg \bar{\nu}$):

$$U_e \sim E^{\frac{10}{3}} T^{\frac{20}{3}} H^{-1} \quad \text{in the case 1),} \quad (50)$$

$$U_e \sim E^{\frac{5}{6}} T^{\frac{10}{3}} H^{-1} N^{\frac{5}{6}} \quad \text{in the case 2a),} \quad (51)$$

$$U_e \sim E^{\frac{10}{11}} T^{\frac{20}{11}} H^{-1} N^{\frac{10}{11}} \quad \text{in the case 2b)} \quad (52)$$

Note that under the conditions of strong mutual drag $|\alpha_p| \gg |\alpha_e|$, both in weak and strong magnetic fields, i.e., the total thermoelectromotive force mainly consists of the phonon part [16].

From (32), (41) and (42) it follows that in the region of weak-heated ($g_e - 1 \ll 1$) electric field the total thermoelectromotive force V and the NE voltage U are proportional E^2 .

- [1] C.W.J.Beenakker and A.A.M.Staring. Phys. Rev. B, 1992, 46, 9667.
- [2] L.D.Hicks and M.S.Dresselhaus. Phys. Rev. B, 1993, 47, 12727.
- [3] X.Zianni, P.N.Butcher and M.J.Kearney. Phys. Rev. B, 1994, 49, 7520.
- [4] I.I.Lyapilin, X.M.Bikkin. FTP, 1999, 33, 701.
- [5] X.M.Bikkin, A.T.Lonchakov, I.I. Lyapilin. FTT, 2000, 42, 202.
- [6] I.Q.Kuleev, I.Yu.Arapova. FTP, 2000, 34, 947.
- [7] X.L.Lei. J. Phys.: Condensed Matter, 1994, 6, L305.
- [8] D.Y.Xing, M.Liu, J.M.Dong and Z.D.Wang. Phys. Rev. B, 1995, 51, 2193.

- [9] E.M.Conwell and J.Zuker. J. Appl. Phys., 1995, 36, 2192.
- [10] M.W.Wu, N.J.M.Horing and H.L.Cui. Phys.Rev. B, 1996, 54, 5438.
- [11] M.M.Babaev, T.M.Gassym, M.Tas and M.Tomak. Phys.Rev. B, 2002, 65, 165324.
- [12] M.M.Babaev, T.M.Gassym, M.Tas and M.Tomak. Phys.Rev. B, 2003, 67, 115329.
- [13] Yu.G.Gurevich and O.L.Mashkevich. Physics Reports, 1989, 18, 6, 327.
- [14] R.Fletcher. Semicond. Sc. Technol., 1999, 14 R1.
- [15] L.E.Qurevich, T.M.Qasimov. FTT, 1967, 9, 105.
- [16] M.M.Babayev, T.M.Gassym. Fizika, 2001, 7, 36.

M.M.BABAYEV

GÜCLÜ ELEKTRON-FONON QARŞILIQLI SÖVQÜ ŞƏRAITINDƏ CİRLAŞMAMIŞ YARIMKEÇİRİCİLƏRDƏ QIZMAR ELEKTRONLARIN TERMOMAQNIT EFFEKTLƏRİ

Elektron və fononların elektrik sahəsində qızması nəzərə alınmaqla, güclü elektron-fonon qarşılıqlı sövqü şəraitində, cırlaşmamış yarımkeçiricilərdə qızmar elektronların termoelektrik hərəkət qüvvəsi və Nernst-Ettingshausen effektləri tədqiq edilmişdir. Termoelektrik hərəkət qüvvəsinin və Nernst-Ettingshausen gərginliyinin elektrik sahəsinin intensivliyindən və qəfəs temperaturundan asılılıqları tapılmışdır.

M.M.БАБАЕВ

ТЕРМОМАГНИТНЫЕ ЭФФЕКТЫ ГОРЯЧИХ ЭЛЕКТРОНОВ В НЕВЫРОЖДЕННЫХ ПОЛУПРОВОДНИКАХ В УСЛОВИЯХ СИЛЬНОГО ВЗАИМНОГО УВЛЕЧЕНИЯ ЭЛЕКТРОНОВ И ФОНОНОВ

Исследованы термо-эдс и эффекты Нернста - Эттингсгаузена в невырожденных полупроводниках, в условиях сильного взаимного увлечения и разогрева электронов и фононов в греющем электрическом поле. Получены зависимости термо-эдс и напряжения Нернста - Эттингсгаузена от напряженности электрического поля и температуры решетки.

Resevied:

OPTIMIZATION OF THE SIZE OF PHOTOVOLTAIC (PV) ARRAY AND BATTERY STORAGE CAPACITY FOR POWER SUPPLY SYSTEM IN REMOTE AREAS

MOHAMMAD JAVAD OKHRAWI

*Department of Electrical Engineering, Faculty of Engineering
Azarbaijan University of Tarbiat Moallem, Tabriz, Iran*

In this paper, a new model is developed for determination of the size of photovoltaic (PV) array and battery storage capacity for stand-alone power supply system. The optimum size of the PV array and battery bank is important factor for a cost effective and good performing system. Based on the energy concept, data of solar irradiance, temperature, manufactures specifications of a PV module and battery, this model enables us to optimize the number of PV modules and the size of battery bank for the best performance of the entire system.

1. Introduction

Photovoltaic energy can make a significant contribution to improving the quality of life of innumerable small communities especially in rural areas by helping to meet the basic needs such as health care, education, refrigeration, water pumping and communication [1].

The present work is to assess the economic feasibility of stand-alone PV power supply systems in sunny countries and to find hints on the most suitable plant concept [2].

Two different options were investigated in order to evaluate the most attractive photovoltaic stand-alone electricity supply concept for a remote area with an averaged daily demand of 30 kWh.

Polycrystalline (LA361K54S) was selected in both the fixed-mounted and sun-traced operational mode. This new model is developed to estimate the photovoltaic generator's area and battery storage capacity requirements. A chart recorder has recorded the annual amounts for global normal and global inclined (30°) data of irradiance. The amount of electricity produced by the photovoltaic generators (rated peak power: 50-150 kW, depending on battery capacity) was calculated the model efficiency as a function of cell temperature, irradiation intensity and air mass. The battery store (Ni-Cd) was modeled in form of linear Model [3]. These equations were all then combined to carry out real-data simulations over one year for all two cases based on hourly mean values of irradiation and temperature data [4]. Therefore, this data is used as the basis for the design and sizing of a stand-alone photovoltaic (PV) [7].

2. Investigated Options

It was intended that the power plant should consist of a PV generator (consisting of modules and panels) and battery storage only. Plant reliability should be guaranteed for 24 hours per day throughout the whole year. The following PV module (Table 1) is selected for the present investigation.

Within the simulation performed, two options were considered: Sun-traced and fix-mounted PV generators. Table 2 shows the monthly global irradiation. Two typical profiles for the summer and winter consumption resp. were created for simulation purposes. They differ remarkably.

The annually averaged daily load curve is shown in Fig.1.

Table 1

Investigated module	
Cell type	Polycrystallin
Module type	LA361K54S
Produced by	Kyocera
Efficiency (η_{PV})	11.7%
Cost US\$/Wp 1998	5.3
Lifetime	25
Maximum power	45W
Open circuit voltage	20.5 V
Short circuit cell current	$I_{ph} = 2.98$ A
Reverse saturation current	$I_O = 9.23$ nA
Voltage (max. power point)	$V_{MPP} = 16.3$ V
Current (max. power point)	$I_{MPP} = 2.76$ A
Number of cells in series	$N_s = 36$

Table 2: Monthly global irradiation (kWh/m^2) on to a sun-traced and an inclined plane 30°

Month	Sun-traced	Inclined plane 30°
Jan	225	148
Feb	234	165
Mar	275	227
Apr	264	215
May	350	234
Jun	365	228
Jul	374	230
Aug	346	247
Sep	325	246
Oct	284	225
Nov	233	175
Dec	230	170

3. Mathematical Model for the PV-Battery-Load System

The equivalent circuit of a solar cell can be best estimated by single diode in parallel with the cell [5]. The generation of current I_{ph} by light is represented by a current generator in parallel with a diode, which represents the p-n junction.

$$I = I_{ph} - I_0 \left(e^{\frac{V}{mkt/q}} - 1 \right)$$

Where k is Boltzmann's constant, T is absolute cell temperature, I_0 is the dark saturation current, m is an empirical non-ideality factor and I_{ph} is the light generated current.

The output power from a PV module is directly dependent on the irradiance level.

$$P_{out} = V_{out} \cdot I_{out}$$

$$I_{out} = I_{ph} - I_0 \left(e^{\frac{V_{out}/N_s}{mkt/q}} - 1 \right)$$

N_s is the number of cells in a series which in this study N_s equals 36.

$$P_{out} = V_{out} (I_{ph} - I_0 (e^{\frac{V_{out}/N_s}{mkt/q}} - 1))$$

$$P_{out}(i) = V_{out}(i) \cdot (I_{ph}(i) - I_0 (e^{\frac{V_{out}(i)/N_s}{mkt/q}} - 1))$$

Where i represents the i -th typical day in month.

For each typical day in a month, the necessary energy (E_{out}) to cover the energy of the load demand (E_{load}) is calculated.

While $(N_{PV} \cdot E_{out}(i) \cdot \eta_{PV} \leq E_{load}(i))$ for any typical day, is increased the number of modules N_{PV} in the PV array by one. This process continues and the final value of N_{PV} is the optimum number of PV module in the array. η_{PV} is the efficiency of a PV system due to conversion losses.

This load is to be fitted with a linear combination of two other function of time. These functions are the average power output of the PV module and the power available from battery bank. In a design of a solar-battery system, it is desirable to cover the load demand by PV module as much as possible. First step in determination of the performance of the solar-battery system is to determine the number of PV modules that meet the load for a PV system only.

$$N_{PV} = \frac{P_{load}}{P_{out} \cdot \eta_{PV}}$$

The amount of power generated by PV array can be greater than the load,

$$(N_{PV} \cdot P_{out}(i) \cdot \eta_{PV} \geq P_{load}(i))$$

or less than the load,

$$(N_{PV} \cdot P_{out}(i) \cdot \eta_{PV} \leq P_{load}(i))$$

The battery current (in-flow or flow-out) is calculated by:

$$I_{bat}(i) = \frac{N_{PV} \cdot P_{out}(i) \cdot \eta_{PV} - P_{load}(i)}{V_{bat}}$$

If $(N_{PV} \cdot P_{out}(i) \cdot \eta_{PV} \leq P_{load}(i))$, then $I_{bat}(i) \leq 0$, battery is discharging, (out-flow).

If $(N_{PV} \cdot P_{out}(i) \cdot \eta_{PV} \geq P_{load}(i))$, then $I_{bat}(i) \geq 0$, battery is charging, (in-flow).

The battery's state of charge (SOC) is computed as [6][3]:

$$SOC(i+1) = SOC(i) - SOC(i) \cdot \sigma_{SDR} \pm I_{bat}(i) \cdot \Delta t \cdot \eta_{BCE}$$

Where $SOC(t)$ is the state of charge, σ_{SDR} is the discharge rate, $\pm I_{bat}(t)$ is the battery charge (+) and discharge (-) current, Δt is time in hours, η_{BCE} is battery charging efficiency.

During discharge, η_{BCE} is assumed to be one. When charging, η_{BCE} is 0.65 to 0.85, depending on the charging current. When gassing starts at critical state of charge, η_{BCE} drops to 0.3

The demand for 100% power reliability means that the loss-of-load probability $LoLP$ [2] has to be zero during the observed period of time T :

$$LoLP = \frac{\sum_{t=1}^T k_t \cdot \Delta t}{T}$$

where

$$k_t = \begin{cases} 1 \rightarrow \text{when: } P_{load,t} > (P_{out \rightarrow load} + P_{bat \rightarrow load}) \\ 0 \rightarrow \text{else} \end{cases}$$

Battery storage lifetime is highly dependent on the number of cycles, being determined by the storage capacity and the permitted minimum state of charge SOC_{min} .

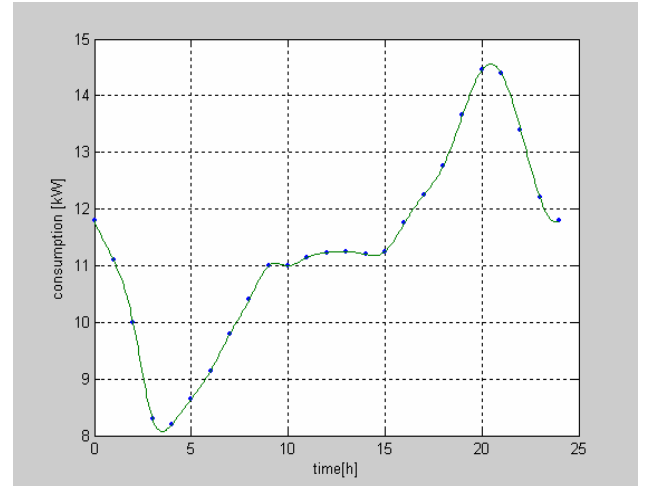


Fig. 1: Daily consumption profile of electricity

4. Simulation Model

The amount of electricity produced was calculated using correlations expressing the solar cell efficiency η_{PV} as a function of the irradiance intensity G , cell temperature U and air mass AM [7]. For the Polycrystalline modules in equation they are given bellow.

$$\eta = P1 * \left[\left(\frac{G}{G_o} \right)^{P2} + P3 * \left(\frac{G}{G_o} \right) \right] * \left[1 + P4 * \left(\frac{v}{v_o} \right) + P5 * \left(\frac{AM}{AM_o} \right) \right]$$

$$P1=0.28204 \quad P2=0.39668 \quad P3=-0.44730 \\ P4=-0.092864 \quad P5=0.016010$$

$$G_o = 1000 W / m^2 \quad v_o = 25^\circ C \quad AM_o = 1.5$$

$$50 \leq G / W m^{-2} \leq 1100$$

$$25 \leq v / ^\circ C \leq 50$$

$$1.3 \leq AM \leq 3$$

The parameters P_i in these semi-empirical correlation were found by non-linear least squares fitting techniques using hundred of tests under actual operating conditions. Measuring results and correlated values agree well in the covered ranges of independent variables [8].

The battery storage was modeled in the form of linear equation using the following recursive relationship [6][3]:

$$SOC(t+1) = SOC(t) - SOC(t) \cdot \sigma_{SDR} \pm \frac{I_{bat} \cdot \Delta t}{C_{bat}} * \eta_{BCE}$$

where SOC is the state of charge, C_{bat} is the nominal capacity of the battery store, σ_{SDR} is the discharge rate, $\pm I_{bat}$ is the battery charge (+) and discharge (-) current and η_{BCE} is battery charging efficiency.

Fig. 2 shows the simulation process. Total module or panel area A , battery capacity C_{bat} , state of charge SOC and starting time t_o are all initialized at the beginning of the simulation process. Load demand P_{load} , irradiation G and temperature v are extracted from a previously prepared data sheet. The module's efficiency η_{PV} and the air mass AM are then calculated. This information subsequently is used to determine the power P_{out} of the photovoltaic generator and the loss-of-load probability $LoLP$. Finally, a new SOC is found from the battery store model. This procedure is repeated over the time period T (one month). As long as $LoLP$ is not equal to zero at the end of this time period, either the battery storage or the generator area will have to be increased. The cost of electricity production was calculated when the generator area A and battery capacity C_{bat} satisfied the demand for 100% reliability.

5. Results

As shown in Fig. 3, the minimum permitted state of charge, SOC_{min} , has a powerful effect on the battery store capacity (at constant panel area), and therefore has a strong influence on the size of the whole battery store. High SOC_{min} values lead to very long store. As expected, small storage capacities lead to a large panel area. Conversely, large storage capacities lead to small panel area. However, the simulations also show that the panel area A must not fall below a certain minimum value. Due to the self discharge of the battery store this holds even in the case of continues no-load operation. The analysis of the electricity generation

cost shows a strong dependence on the battery store capacity and on the minimum permitted state of charge SOC_{min} (Fig. 4). In Fig. 4 the results of the most attractive case, i.e. sun-traced Polycrystalline modules is shown. Minimum cost are found at a SOC_{min} value of 0.8. From Fig. 4 it is concluded that undersizing of the battery store leads to a significant increase of the generation cost, while oversizing has less consequences.

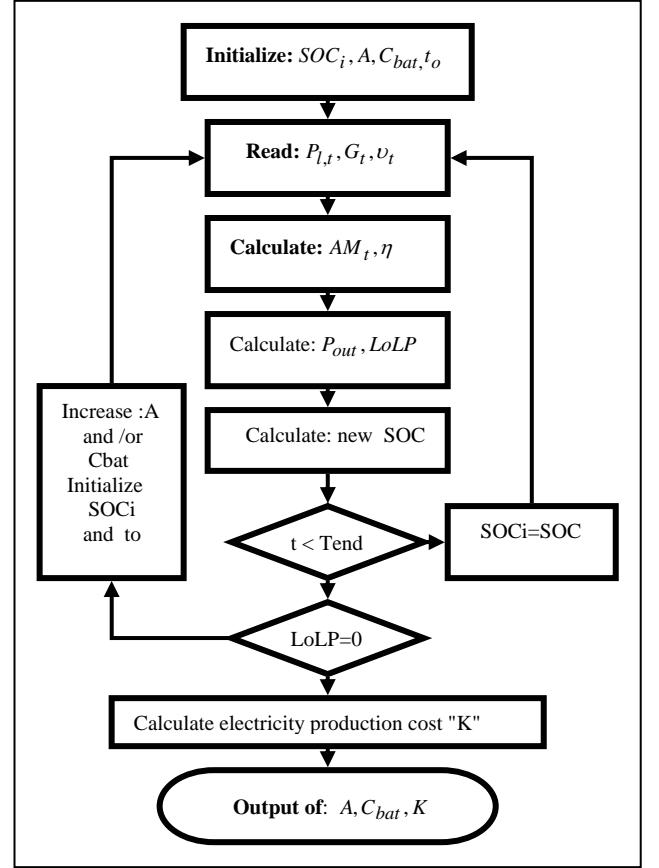


Fig. 2: Simulation process flow chart

6. Conclusions

The present investigation demonstrated that the minimum permitted state of charge SOC_{min} had a strong influence on the battery storage size and with that on the cost of the plant. Low values for SOC_{min} lead to small storage size and low storage costs, while high SOC_{min} values lead to very large and expensive battery stores. On the other hand, smaller stores have to be replaced more frequently, leading to increased electricity production cost too. In the cases examined, the optimum value of SOC_{min} was 0.8. The performed simulations show that one hour resolution for irradiation and temperature data is sufficient. Higher resolution leads to unnecessarily long computing time.

Furthermore, it has been shown for sunny countries that with stand-alone photovoltaic power plants, Polycrystalline modules in sun-traced operational mode lead to the lowest electrically production cost because of their longer lifetime

and better efficiency. In some cases, the cost of the battery store exceeds 60% of the cost of the whole plant. When planning a stand-alone PV power plant, it may be better to include a reduced battery store capacity, i.e. to replace part

of the store by the use of a fossil-fueled generator, to guarantee the reliability of the plant during periods of low irradiation. It would thus be possible to reduce the costs to about 70%.

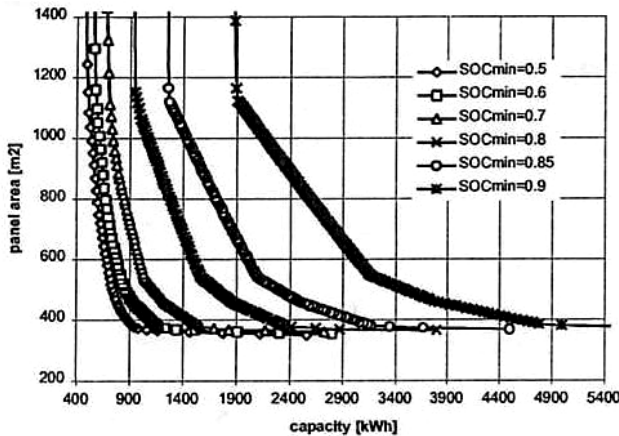


Fig. 3: Dependency of total panel area on battery store capacity

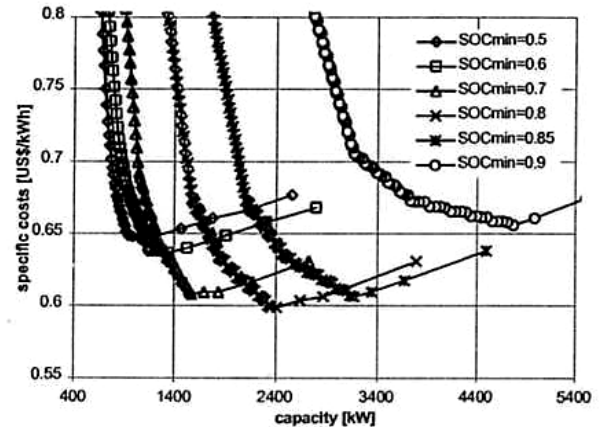


Fig. 4: Dependence of electricity cost on the battery store capacity

- [1] Häberlin: "Photovoltaic", AT Verlag, Aarau/Schweiz, 1991.
- [2] J. Badran: "A Sizing Methodology for Stand-Alone Photovoltaic Power Systems", Dissertation, Technische Universität Wien, 1995.
- [3] Y.H. Kim, H.D. Ha, "Design of Interface Circuit with Electrical Battery Models", IEEE Trans. on Industrial Electronics, Vol. 44, No. 1, Feb 1997, pp. 81-86.
- [4] J.A. Gow, and C.D. Manning, "Development of a Photovoltaic Array Model for use in Power Electronic Simulation Studies", IEEE Proceedings of electric Power Applications, 146(2), March 1999, pp. 193-200, ISSN: 13502352.
- [5] F. Nakanishe, T. Ikegami, K. Ebihara; "Modeling and operating of a 10 kW Photovoltaic Power Generator using Equivalent circuit Method", 28th IEEE PVSC, Kumamoto university, September 2000.
- [6] Z.M. Salameh, M.A. Casacca and W.A. Lynch, "A Mathematical Model for Lead-Acid Battery", IEEE Trans. on Energy Conversion, Vol. 7, No. 1, March 1992, pp. 93-97
- [7] W. Durisch et al.: "Characterization of Photovoltaic Generators. Appl. Energy" 65(2000), pp. 273-284
- [8] W. Durisch: "Internal Technical Report", Arge Solar 91, Waltenburg, Nov.1997

THE WEINBERG ANGLE IN A MAGNETIC FIELD AND THE RESTRICTION FOR A NEUTRINO MASS

V. A. GUSEINOV ^{a,b}, R. E. GASIMOVA ^a, E. Z. SAFAROVA ^a

a) Department of General and Theoretical Physics, Nakhchivan State University, AZ 7012, Nakhchivan, Azerbaijan;

b) Laboratory of Physical Research, Nakhchivan Division of Azerbaijan National Academy of Sciences, AZ 7000, Nakhchivan, Azerbaijan

The work is devoted to the calculation of the parameter $\sin^2 \theta_w$ in an external magnetic field in the framework of the Weinberg-Salam-Glashow model. The new formula for $\sin^2 \theta_w$ obtained from the ratio of the cross sections of the neutrino-electron and antineutrino-electron scattering reactions in a weak magnetic field shows that $\sin^2 \theta_w$ is a function of the kinematic and dynamic parameters. The restriction for the neutrino (antineutrino) mass is found.

The existence of weak neutral currents was confirmed by the initial observation of $\bar{\nu}_\mu + e^- \rightarrow \bar{\nu}_\mu + e^-$ reaction at CERN [1]. The relation between the weak coupling constant g and the electric charge e is established with the Weinberg angle θ_w , which characterizes the contribution of an electromagnetic current to a neutral current [2]

$$e = g \sin \theta_w \quad (1)$$

where $g = 2^{1/2} G_F^{1/2} m_w$, G_F is the Fermi constant, m_w is the mass of the W boson.

On the basis of the experimental data on the neutral currents it was found that $\sin^2 \theta_w \approx 0.23 \pm 0.01$ [3]. This value of $\sin^2 \theta_w$ belongs to $q^2 \approx m_z^2 (m_w^2)$, where q^2 is the momentum transfer squared

$$\sin^2 \theta_w = \frac{e^2}{g^2} \quad (2)$$

is not constant and it is a function of the momentum transfer squared. One of the possibilities to determine $\sin^2 \theta_w$ is measuring the ratio of the cross sections of the reactions [4-9]

$$\nu_l + e^- \rightarrow \nu_l + e^-, \quad (3)$$

$$\bar{\nu}_l + e^- \rightarrow \bar{\nu}_l + e^-, \quad (4)$$

where $\nu_l = \nu_\mu, \nu_\tau$ and $\bar{\nu}_l = \bar{\nu}_\mu, \bar{\nu}_\tau$.

Systematic uncertainties in the neutrino flux and spectrum create some difficulties in precise measurements of the cross sections of the considered processes. The primary uncertainty in the neutrino flux is connected with the uncertainty in the acceptance of the detector [8]. The questions concerning the limitation on the systematic uncertainties in the neutrino flux and spectrum is discussed in [3,7,8].

From the ratio of the cross sections of these reactions

$$Q \equiv \frac{\sigma(\bar{\nu}_\mu e \rightarrow \bar{\nu}_\mu e)}{\sigma(\nu_\mu e \rightarrow \nu_\mu e)} \quad (5)$$

it has been found that $\sin^2 \theta_w = 0.209 \pm 0.032$ [5]. The CERN group reported the result $\sin^2 \theta_w = 0.211 \pm 0.037$ [6]. The agreement of these experimental results with the

value of $\sin^2 \theta_w$ predicted by the electroweak theory is one of the best confirmations of the Standard Model.

The reactions (3) and (4) in an external magnetic field can be used for testing the theory of electroweak interactions in a strong magnetic field. Measurement of the parameter $\sin^2 \theta_w$ in an external magnetic field allows testing the Standard Model. This work is devoted to the calculation of $\sin^2 \theta_w$ in an external magnetic field in the framework of the Weinberg-Salam-Glashow model. In this paper we also try to find the restriction for a neutrino mass.

Generally, electroweak radiative corrections are important for precise measurements of the cross sections of the considered processes. These corrections to neutrino-electron scattering in the Standard Model were computed by Sarantakos, Sirlin and Marciano [10]. Radiative corrections connected with leptonic interactions were also discussed in the review [11]. We perform our calculations in the tree level approximation. In this approximation and in the conditions of relatively low energies and weak magnetic fields the electroweak radiative corrections can be neglected. Of course, the consideration of these corrections can improve an agreement of the results of our calculations with the experimental data.

In our calculations we neglect neutrino masses and mixing. For generality, we take into account the propagator effects (Z boson contribution). But in the low-energy region we will use the low-energy approximation of the Standard Model.

In calculations of the cross sections of the neutrino (antineutrino)-electron scattering reactions we apply the method of the exact solution of the relativistic wave equation (the Dirac equation) in an external magnetic field. This method is one of the most effective methods of theoretical investigations and it allows to go out beyond the perturbation theory and foretell some theoretical predictions.

The cross section of the reaction (3) in a crossed electromagnetic field was found in [12]. It is well known that a constant crossed electromagnetic field simulates an arbitrary constant electromagnetic field of the strength

$$F \ll H_0 = \frac{m_e^2}{e} = 4.41 \times 10^{13} \text{ G} \quad (6)$$

if ultra relativistic particles take part in the process. Here H_0 is the Schwinger field strength, e is the elementary charge and F can be the strength of a magnetic field or the strength of an electric field.

Let us suppose that the electrons are ultra relativistic ($\varepsilon, \varepsilon' \gg m_e$ where ε and ε' are the energies of the initial and final electrons and m_e is the electron mass) and the strength of a constant external electromagnetic field is $F \ll H_0$.

In this work we use the system of units where $\hbar = c = 1$. The signature of the metric is $(+ - - -)$. As this is a constant external field we can consider the constant magnetic field. If we take into account that the vector of intensity of the constant magnetic field H is directed along the axis Oz , the longitudinal momentum of the initial electron is zero and the vector of momentum of the initial neutrino (antineutrino) k is directed along H , we can write the following formulae for the invariant spectral variable u and the invariant parameters χ and κ :

$$u = \frac{\chi}{\chi'} - 1 = \frac{\varepsilon}{\varepsilon'} - 1, \quad (7)$$

$$\chi = \frac{e}{m_e^3} \left[- (F_{\alpha\beta} p^\beta)^2 \right]^{\frac{1}{2}} = \frac{\varepsilon}{m_e} \frac{H}{H_0}, \quad (8)$$

$$\kappa = \frac{2(kp)}{m_e^2} = \frac{2k_0 \varepsilon}{m_e^2} \quad (9)$$

where $F_{\alpha\beta}$ is the tensor of the constant external field, $\chi' = \chi(p \rightarrow p')$, p and p' are the 4-momenta of the initial and final electrons, k is the 4-momentum of the initial neutrino (antineutrino), k_0 is the energy of the initial neutrino (antineutrino), H is the strength of an external magnetic field. Here χ is the dynamic parameter and κ is the kinematic parameter. In spite of the fact $(H/H_0) \ll 1$ due to the condition $\varepsilon \gg m_e$ the field parameter χ can reach the value $\chi \geq 1$. In this case, the contribution of the field to the cross sections of the considered processes is significant.

In the framework of the Weinberg-Salam-Glashow model the cross sections of the processes (3) and (4) in a constant external magnetic field are

$$\sigma_{\pm} = \frac{G_F^2 m_e^2}{\pi^{\frac{3}{2}}} \int_0^{\infty} \frac{u du}{(1+u)^4} \left\{ \left[\frac{\kappa}{u} f_{\pm} - 2g_L g_R (1+u) \right] \Phi_1(t) - 2 \left[\frac{\chi}{u} \right]^{\frac{2}{3}} f_{\pm} \Phi'(t) \right\} \left[1 + \kappa \left(\frac{m_e}{m_z} \right)^2 \frac{u}{1+u} \right]^{-2} \quad (10)$$

where m_z is the mass of a Z boson, σ_+ and $f_+ = g_L^2(1+u)^2 + g_R^2$ are for the reaction (3), σ_- and $f_- = g_R^2(1+u)^2 + g_L^2$ are for the reaction (4), $g_L = -\frac{1}{2} + \sin^2 \theta_w$, $g_R = \sin^2 \theta_w$. Here the functions

$$\Phi'(t) = \frac{d\Phi(t)}{dt} \quad (11)$$

And

$$\Phi_I(t) = \int_t^{\infty} \Phi(\rho) d\rho \quad (12)$$

are determined with the Airy function

$$\Phi(t) = (1/2\sqrt{\pi}) \int_{-\infty}^{\infty} du \exp \left[i \left(ty + \frac{1}{3} y^3 \right) \right]. \quad (13)$$

All these functions depend on a new variable

$$t = \left(\frac{u}{\chi} \right)^{\frac{2}{3}} \left(1 - \frac{\kappa}{u} \right). \quad (14)$$

To determine $\sin^2 \theta_w$ in an external magnetic field we find the ratio $R = \sigma_+ / \sigma_-$:

$$R = \frac{(A_1 - B_1)g_L^2 + (A_2 - B_2)g_R^2 - 2g_L g_R C}{(A_1 - B_1)g_R^2 + (A_2 - B_2)g_L^2 - 2g_L g_R C} \quad (15)$$

Where

$$\alpha_1 = A_1 - B_1, \alpha_2 = A_2 - B_2, \quad (16)$$

$$A_1 = \kappa \int_0^{\infty} \frac{1}{(1+u)^2} \Phi_1 N du, \quad (17)$$

$$A_2 = \kappa \int_0^{\infty} \frac{1}{(1+u)^4} \Phi_1 N du, \quad (18)$$

$$B_1 = 2\chi^{\frac{2}{3}} \int_0^{\infty} \frac{u^{\frac{1}{3}}}{(1+u)^2} \Phi' N du, \quad (19)$$

$$B_2 = 2\chi^{\frac{2}{3}} \int_0^{\infty} \frac{u^{\frac{1}{3}}}{(1+u)^4} \Phi' N du, \quad (20)$$

$$C = \int_0^{\infty} \frac{u}{(1+u)^3} \Phi_1 N du. \quad (21)$$

If we take into account $g_L = -\frac{1}{2} + \sin^2 \theta_w$,

$g_R = \sin^2 \theta_w$, we obtain

$$R = \frac{A_1 - B_1 - 4(A_1 - B_1 - C)\sin^2 \theta_w + 4(A_1 - B_1 + A_2 - B_2 - 2C)\sin^4 \theta_w}{A_2 - B_2 - 4(A_2 - B_2 - C)\sin^2 \theta_w + 4(A_1 - B_1 + A_2 - B_2 - 2C)\sin^4 \theta_w}. \quad (22)$$

According to the general theory developed in [13] the influence of the external magnetic field on the processes (3) and (4) is determined by the parameter

$$\eta = \frac{\chi}{\kappa}. \quad (23)$$

Let us consider the asymptotic behaviour of the ratio R in the limiting case $\eta \ll 1$ (weak field). For $\eta \ll 1$, we use the weak asymptotic expansions of the Airy functions (see, for example, [14])

$$\Phi'(Ax) = \sqrt{\pi} A^{-2} \delta'(x) + O(A^{-5}), \quad (24)$$

$$\Phi_I(Ax) = \sqrt{\pi} \left[\theta(-x) + \frac{1}{3} A^{-3} \delta''(x) + O(A^{-6}) \right] \quad (25)$$

where $\delta(x) = d\theta(x)/dx$ is the Dirac delta function, $A = \eta^{-2/3}$ is the parameter ($A \gg 1$), $\theta(x)$ is the Heaviside function. Supposing in the expression (10) $\kappa(m_e/m_z)^2 \ll 1$, we find the following expression for R :

$$R = \frac{ag_L^2 + bg_R^2 - cg_L g_R + \frac{2}{s^3} \eta^2 (dg_L^2 + fg_R^2 - hg_L g_R)}{ag_R^2 + bg_L^2 - cg_L g_R + \frac{2}{s^3} \eta^2 (dg_R^2 + fg_L^2 - hg_L g_R)} \quad (26)$$

or

$$R = \frac{A_0 \sin^4 \theta_w - (A_0 - B_0) \sin^2 \theta_w + H_0 + \frac{2}{s^3} \eta^2 [D_0 \sin^4 \theta_w - (D_0 - E_0) \sin^2 \theta_w + I_0]}{A_0 \sin^4 \theta_w - B_0 \sin^2 \theta_w + C_0 + \frac{2}{s^3} \eta^2 (D_0 \sin^4 \theta_w - E_0 \sin^2 \theta_w + G_0)} \quad (27)$$

where

$$A_0 = a + b - c = 4s^2 - 2s + 1, \quad (28)$$

$$B_0 = b - \frac{1}{2}c = s^2 - \frac{1}{2}s + 1, \quad (29)$$

$$C_0 = \frac{1}{4}b = \frac{1}{4}(s^2 + s + 1), \quad (30)$$

$$D_0 = d + f - h = -2(s^4 - 6s^2 + 8s - 5), \quad (31)$$

$$E_0 = f - \frac{1}{2}h = -s^3 + 3s^2 - 10s + 10, \quad (32)$$

$$G_0 = \frac{1}{4}f = \frac{1}{4}(-3s^2 - 4s + 10), \quad (33)$$

$$H_0 = \frac{1}{4}a = \frac{3}{4}s^2, \quad (34)$$

$$I_0 = \frac{1}{4}d = \frac{1}{4}s^2(-2s^2 + 2s + 3) \quad (35)$$

and

$$a = 3s^2, \quad (36)$$

$$b = s^2 + s + 1, \quad (37)$$

$$c = 3s, \quad (38)$$

$$d = s^2(-2s^2 + 2s + 3), \quad (39)$$

$$f = -3s^2 - 4s + 10, \quad (40)$$

$$h = 2s(s^2 - 6s + 6). \quad (41)$$

In the expressions (26-41) $s = \kappa + 1 = (q + p)^2 / m_e^2$ is the normalized Mandelstam variable. The terms in (26) proportional to c and h correspond to the interference terms. In the expression (26) we retain the interference terms for low energy applications.

When the energy of the initial neutrino (antineutrino) is of order $\sim MeV$ ($k_0 = 0.5 MeV$) and the energy of the electron is $\varepsilon = 0.5 GeV$, for the kinematic parameter κ we have $\kappa = 2 \times 10^3 \gg 1$ and $s = \kappa + 1 \gg 1$. In the weak magnetic field limiting case from (27) we find the following formula for $\sin^2 \theta_w$:

$$\sin^2 \theta_w = \frac{R - 3 + 4 \frac{\eta^2}{s} \pm \sqrt{-3R^2 + 10R - 3 + 4 \frac{\eta^2}{s} (R^2 - 6R + 1)}}{8(R - 1)(1 - \frac{\eta^2}{s})}. \quad (42)$$

From the last expression we see that the contribution of an external magnetic field to $\sin^2 \theta_w$ is determined by the

terms proportional to η^2/s . If we take into account the

definition of η and formula for χ and κ , we have

$$\frac{\eta^2}{s} = \frac{1}{8} \left(\frac{H}{H_0} \right)^2 \frac{m_e^4}{k_0^3 \varepsilon}. \quad (43)$$

The contribution η^2/s is determined by three variables k_0 , H and ε . This contribution is especially significant when we have dealings with relatively strong magnetic field and low-energy neutrinos (antineutrinos). In this case not very high ε is desirable. If we set $H = 10^{-2} H_0$, $k_0 = 0.5 \text{ MeV}$ and $\varepsilon = 0.5 \text{ GeV}$, the estimations give $\eta^2/s = 0.625 \times 10^{-8}$ that is very small.

According to the formula (43) the upper limit of η^2/s is determined by the maximal possible value of H and the minimal possible values of k_0 and ε . The order of the maximal value of η^2/s can not be greater than $\sin^2 \theta_w = 0.23 \sim 10^{-1}$. The maximal possible value for H can be $H \sim H_0$ and the minimal possible value for the electron energy can be $\varepsilon \sim m_e$. In this case the value $\sin^2 \theta_w \sim 10^{-1}$ can be achieved due to the multiplier k_0^{-3} .

However, there is definite restriction for the lowest value k_{0min} of the neutrino (antineutrino) energy k_0 . The neutrino (antineutrino) energy k_0 can not be smaller than the value k_{0min} . Otherwise, the order of the parameter $\sin^2 \theta_w$ would be greater than $\sin^2 \theta_w \sim 0.1$. But η^2/s can not be greater than $\sim 10^{-1}$. It means that the lowest energy of a neutrino (antineutrino) is k_{0min} . If a neutrino (antineutrino) is a massive particle, the lowest limit of k_0 corresponds to neutrino (antineutrino) mass. So, the muon neutrino (antineutrino) mass m_{ν_l} can not be greater than k_{0min} :

$$m_{\nu_l} \leq k_{0min} = \frac{1}{2} \left[\frac{\left(\frac{H}{H_0} \right)^2 \frac{m_e^4}{\varepsilon}}{\frac{\eta^2}{s}} \right]^{1/3} \approx \frac{1}{2} m_e$$

or $m_{\nu_l} \leq 0.255 \text{ MeV}$. (44)

This estimation is right for ν_μ , $\bar{\nu}_\mu$, ν_τ and $\bar{\nu}_\tau$.

-
- [1] *Hasert.F et al* (Gargamelle Collaboration) 1973 Phys. Lett. **B 46** 121
 - [2] *Okun.L B* 1985 *Leptons and Quarks* (Amsterdam: North-Holland)
 - [3] *See Panman J* 1995 *Precision Tests of the Standard Electroweak Model* edP. Langacker (Singapore: World Scientific) p 504 and references therein
 - [4] *Steinberger J* 1990 Uspekhi Fizicheskikh Nauk **160** 136
 - [5] *Ahrens L A et al* 1990 Phys. Rev. D **41** 3297
 - [6] *Dorenbasch J et al* 1989 Z. Phys. C **41** 567
 - [7] *Marciano W J and Parsa Z* 2003 J. Phys. G **29** 2629
 - [8] *Imlay R and VanDalen G J* 2003 J. Phys. G **29** 2647
 - [9] *Vilain P et al* 1994 Phys. Lett. **B 335** 246

- [10] *Sarantakos S, Sirlin A and Marciano W J* Nucl. Phys. **B 217** 84
- [11] *Borisov A V, Vshivtsev A S, Zhukovskii V Ch and Eminov P A* 1997 Uspekhi Fizicheskikh Nauk **167** 241
- [12] *Borisov A V, Nanaa M K and Ternov I M* 1993 Vestnik Mosk. Univ. Ser. 3 Fizika. Astronomiia **2** 15
- [13] *Ritus V I and Nikishov A I* 1979 Trudy FIAN SSSR **111**(Moscow: Nauka)
- [14] *Borisov A V, Guseinov V A and Zamorin N B* 2000 Phys. At. Nuclei **63** 1949
- [15] *Borisov A V, Guseinov V A and Zamorin N B* 2000 Yad. Fiz. **63** 2041

V. A. ГУСЕЙНОВ, Р. Э. ГАСЫМОВА, Э. З. САФАРОВА

УГОЛ ВАЙНБЕРГА В МАГНИТНОМ ПОЛЕ И ОГРАНИЧЕНИЕ НА МАССУ НЕЙТРИНО

Работа посвящена вычислению параметра $\sin^2 \theta_w$ в рамках модели Вайнберга-Салама-Глешоу во внешнем магнитном поле. Новая формула для $\sin^2 \theta_w$, полученная из соотношения сечений реакций нейтрино-электронной и антинейтрино-электронной рассеяний в слабом магнитном поле, показывает, что $\sin^2 \theta_w$ является функцией кинематического и динамического параметров. Найдено ограничение на массу нейтрино (антинейтрино).

V. A. HÜSEYNOV, R. E. QASIMOVA, E. Z. SƏFƏROVA

MAQNİT SAHƏSİNDƏ VAYNBERQ BUCAĞI VƏ NEYTRİNO KÜTLƏSİ ÜÇÜN MƏHDUDİYYƏT

İş xarici maqnit sahəsində Vaynberq-Salam-Qleşou modeli çərçivəsində $\sin^2 \theta_w$ parametrinin hesablanmasına həsr olunmuşdur. Zəif maqnit sahəsində neytrino-elektron və antineytrino-elektron səpilmə reaksiyalarının en kəsiklərinin nisbətindən $\sin^2 \theta_w$ üçün alınmış yeni ifadə göstərir ki, $\sin^2 \theta_w$ kinematik və dinamik parametrlərin funksiyasıdır. İşdə neytrino (antineytrino) kütləsi üçün məhdudiyyət tapılmışdır.

INFLUENCE THE HEAT TREATMENT ON THE MECHANICAL CHARACTERISTICS OF SILICON PLATES

A.M. HASHIMOV, Sh.M. HASANLI

Institute of Physics, Azerbaijan National Academy of Sciences

H. Javid av.,33, Baku, Az-1143

The paper is devoted to research of influence the heat treatment of silicon plates on their mechanical characteristics. Silicon plates n- and p-type conductivity having diameter of 100 mm are investigated. Plates had surface orientations of (111).

1. Introduction

During the fabrication of integrated circuits and other semiconductor devices, silicon wafers are exposed to various mechanical and thermal processes. As a result, there is a big danger of dislocation generation in these wafers and deterioration of semiconductor devices characteristics. Therefore, the questions connected with the problem of dislocation generation in semiconductor materials in a wide temperature interval, still remain topical and need to be further investigated.

There are many articles that are devoted to dislocation generation under the action of various external factors

[1-3]. According to our and other articles [1,4], dislocation movement under loading has a spasmodic character.

By using the investigation methods of microhardness and fracture toughness, much valuable information can be obtained about the mechanical proprieties of semiconductor materials in a wide range of temperatures.

2. Experimental methods

Investigations were carried out on both n- and p-type silicon wafers having diameters of 76 and 100mm with (111)-1 and (100)-2 surface orientations. Microhardness H , fracture toughness K and the imprint length d were used as the characteristic parameters (Fig.1,2,3).

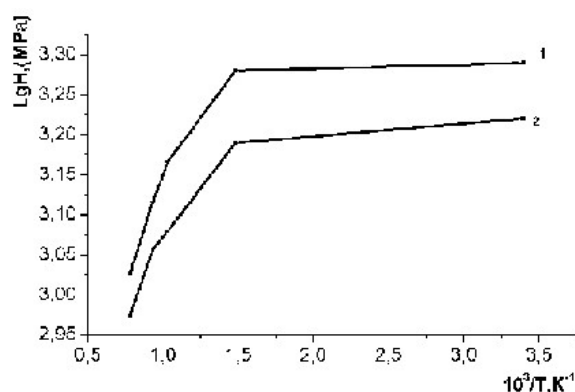


Fig.1

At least 20 tests for each sample were carried out for determination of the microhardness. The microhardness measurements were accomplished by a PMT-3 type device. The fracture toughness was determined on the same imprints as used for microhardness. The investigated samples were heat treated in the atmosphere. For heating each wafer

uniformly and avoiding it from direct heat radiation, it was covered with another wafer. The loads applied on the Vickers pyramid were varied in the range 0.3-1.2 N.

The calculations of the microhardness and the fracture toughness values were done using [5].

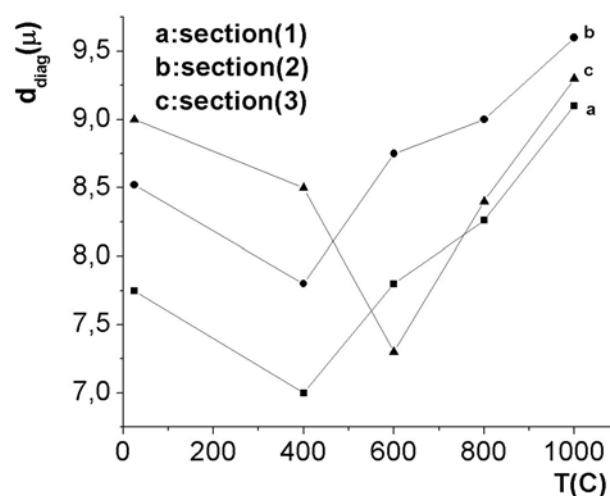


Fig.2.

The experiments were carried out at room temperature.

Microhardness and diagonal length of the replica channel have been used as characteristic parameters. Microhardness has been determined by results of not less than 20 tests for each sample by means of device PMT-3.

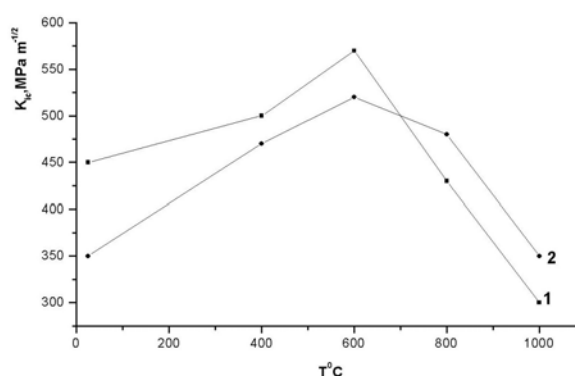


Fig.3

The Vickers pyramid has been used as indenter. Heat treatment of the investigated samples has been carried out in an air atmosphere. Loading on pyramids (at indenting) is varied from 0.3 up to 1.2 N.

The following experimental results are obtained.

1. Dependence of microhardness on annealing temperature has the exponential character, namely, with reduction of

annealing temperature the microhardness value sharply grows and further reaches the monotonous growth (Fig.1).

2. With growth of annealing temperature up to $T \sim 450^{\circ}\text{C}$ diagonal length of the replica channel decreases, at the further growth of annealing temperature it sharply increases. Moreover, at $T=250^{\circ}\text{C}$ and $T=1000^{\circ}\text{C}$ diagonal length of the replica channel at the edges of plates is more than in the middle of plates (Fig.2).

3. The non-uniform distribution of fracture toughness on the surface of wafers depends on the loading. On the edges of wafers K value is less than that on the middle of wafers. At the increasing of the annealing temperature (at constant F values) the value of K increases reaching the maximum value

and it sharply decreases at temperatures above 800°C .

3. Conclusions

1. The occurrence of dislocations at low temperatures area (where the thermal activation is practically absent) means that during the local indentation of the sample surface, stresses larger than the Pairel's stress can be created.

2. The temperature dependences of the microhardness and dislocations and sliding strips running from the imprint after annealing process confirm again the relaxation possibilities of elastic stress at the room temperatures.

-
- [1] *Gerasimov A.B., Chiradze G.D., Kutivadze H.G., Bibilashvili A.P.* FTP, 2000, v.42, No.4, pp.683-687 (in Russian).
[2] *Petukhov B.V.* FTP, 2001, v.43, No.5, pp. 813-817. (in Russian).
[3] *Mezhennyj M.V., Milvidskij M.G., Reznik V.J.* .FTT, 2001, v.43. No.1, pp.47-50. (in Russian).

- [4] *Bidadi H. Sobhanian S., Hasanli Sh.M.* Microelectronics Journal, 2003, N5, p.514-519
[5] *Anstis G.R., Lawn B.R.* J.of the American Ceramic society, 1981, v. 4, No.9, pp.533-545.

A.M.Həşimov, Ş.M. Həsənli

TERMOİŞLƏMƏLƏRİN SILİSIUM LÖVHƏLƏRİNİN MEXANİKİ XÜSUSİYYƏTLƏRİNƏ TƏSİRİ

İş, diametri 100 mm olan, n və p tip keçiriciliyə malik, (111) orientasiyalı silisium lövhələrinin mikromöhkəmlik, çat əmələgəlməyə dözümlülük və s. mexaniki xüsusiyyətlərinə termoişləmələrin təsirinin tədqiqinə həsr olunmuşdur. Göstərilmişdir ki, termoişləmələr zamanı mexaniki xassələrin dəyişməsinə səbəb dislokasiyaların hərəkəti və mexaniki gərginliklərin relaksasiyalarıdır.

A.M.Гашимов, Ш.М.Гасанли

ВЛИЯНИЕ ТЕРМИЧЕСКОЙ ОБРАБОТКИ НА МЕХАНИЧЕСКИЕ ХАРАКТЕРИСТИКИ КРЕМНИЕВЫХ ПЛАСТИН

Работа посвящена исследованию влияния термической обработки кремниевых пластин n- и p- типа проводимости диаметром 100 мм и с ориентацией (111) на механические характеристики: микротвердость, трещиностойкость и др. Показано, что изменения механических характеристик при термической обработке обусловлены движением дислокаций и релаксацией механических напряжений.

Received: 12.10.2004

THE TRANSIENT RADIATION OF THE MAGNETIC MOMENT IN THE NON-STATIONARY MEDIUM

I.M. ABUTALIBOV, M.B. ASADOVA, I.G. JAFAROV

The Azerbaijan State Pedagogic University

370000, Baku, Uz. Hajibekov str., 34

The process of transient radiation of magnetic moment at the strong change of dielectric constant in time is considered. The formulae for eigen field and radiation field are obtained. It is established, that with the increase of energy the contribute of magnetic transient radiation with comparison of charge one increases essentially. In the case of magnetic medium at the strong change of physical properties isotropic radiation appears.

The transient radiation, appearing at the intersection of the boundary section of two mediums by the charge, firstly was considered by Ginzburg and Frank [1]. In our previous works the transient radiation of the magnetic moment on the strong boundary section of two mediums [2], and also the transient radiation of the magnetic moment on the scoured boundary of section of mediums, in a particular, the transient radiation in the plane-layered medium [3-6] were investigated.

One of the reason of the appearance of the transient radiation at the constant velocity of the source is the change of the physical properties of the medium in time. In the given task the transient radiation, appearing in the medium, physical properties of which strong change in time, is considered. The sharpness criterion of medium properties change is defined by the condition, when the time length of the change is much less, than time of the radiation forming. It is considered, that in the time moment $t=0$, the dielectric and magnetic constants change by the jump from the values ε_1 and μ_1 till the values ε_2 and μ_2 correspondingly.

On the base of Maxwell equations the differential equations for field vectors have been obtained:

$$\left(\nabla^2 - \frac{\varepsilon \mu}{c^2} \frac{\partial^2}{\partial t^2} \right) \vec{B} = - \frac{4\pi\mu}{c} [\vec{\nabla} \vec{j}], \quad (1)$$

$$\left(\nabla^2 - \frac{\varepsilon \mu}{c^2} \frac{\partial^2}{\partial t^2} \right) \vec{E} = \frac{4\pi}{\varepsilon} \left[\text{grad } \rho + \frac{\varepsilon \mu}{c^2} \frac{\partial \vec{j}}{\partial t} \right]. \quad (2).$$

Here the current density and charge density, created constantly by the moving magnetic moment are defined by the formulae

$$\vec{j} = c \text{rot} \vec{M} + \frac{\partial \vec{P}}{\partial t}, \quad (3)$$

$$\rho = -\text{div} \vec{P}, \quad (4)$$

where $\vec{M}(\vec{r}, t) = \vec{m} \delta(\vec{r} - \vec{v} t)$ and $\vec{P}(\vec{r}, t) = [\vec{\beta} \vec{m}] \delta(\vec{r} - \vec{v} t)$ are vectors of electric and magnetic polarization.

The considered task is completely homogeneous by the space that is why all values need to decomposition in Fourier integral on the space components. Moreover, we have Fourier-images of equations (1) and (2):

$$\left(k^2 + \frac{\varepsilon \mu}{c^2} \frac{\partial^2}{\partial t^2} \right) \vec{B}_k(t) = \frac{4\pi i \mu}{c} [\vec{k} \vec{j}_k(t)], \quad (5)$$

$$\left(k^2 + \frac{\varepsilon \mu}{c^2} \frac{\partial^2}{\partial t^2} \right) \vec{E}_k(t) = - \frac{4\pi}{\varepsilon} \left[i \vec{k} \rho_k(t) + \frac{\varepsilon \mu}{c} \vec{\beta} \frac{\partial \rho_k}{\partial t} \right]. \quad (6)$$

In the equations (5) and (6) the Fourier-images of current density and charge density are correspondingly equal to:

$$\vec{j}_k(t) = - \frac{ic}{(2\pi)^3} [\vec{m} \vec{K}] \exp(-i \vec{k} \vec{v} t), \quad (7)$$

$$\rho_k(t) = - \frac{i(\vec{k} [\vec{\beta} \vec{m}])}{(2\pi)^3} \exp(-i \vec{k} \vec{v} t), \quad (8)$$

where $\vec{K} = \vec{k} - \vec{\beta}(\vec{k} \vec{\beta})$ and $\vec{\beta} = \vec{v} / c$.

The equations (5) and (6) are nonhomogeneous common differential equations, the common solutions of which are presented in the sum form of the private solution of nonhomogeneous equation (eigen field) and common solution of homogeneous equation (radiation field):

$$B_k^s(t) = \frac{4\pi [\vec{k} [\vec{m} \vec{K}]] \mu \exp(-i \vec{k} \vec{v} t)}{(2\pi)^3 [k^2 - \varepsilon \mu (\vec{k} \vec{\beta})^2]}, \quad (9)$$

$$\vec{E}_k^s(t) = \frac{4\pi}{(2\pi)^3 \varepsilon} \frac{\varepsilon \mu (\vec{k} \vec{\beta}) [\vec{m} \vec{K}] - \vec{k} (\vec{k} [\vec{\beta} \vec{m}]) \exp(-i \vec{k} \vec{v} t)}{k^2 - \varepsilon \mu (\vec{k} \vec{\beta})^2}. \quad (10)$$

$$\bar{B}_k^r(t) = \frac{4\pi [\vec{k} [\vec{m} \vec{K}]]}{(2\pi)^3 k^2} \left[b_+ e^{-i(kc/\sqrt{\varepsilon\mu})t} + b_- e^{i(kc/\sqrt{\varepsilon\mu})t} \right], \quad (11)$$

$$\bar{E}_k^r(t) = -\frac{4\pi}{(2\pi)^3 k^3 \sqrt{\varepsilon\mu}} [\vec{k} [\vec{k} [\vec{m} \vec{K}]]] \left[b_+ e^{-i(kc/\sqrt{\varepsilon\mu})t} - b_- e^{i(kc/\sqrt{\varepsilon\mu})t} \right], \quad (12)$$

In these formulae the s index corresponds to the eigen field, and r index corresponds to radiation field. In the formulae (11), (12) the complex coefficients b_+ and b_- describe the amplitudes of two waves, propagating in the opposite directions - on \vec{k} and against \vec{k} correspondingly.

At $t < 0$, the radiation field is absent and at $t > 0$ the two waves appear immediately. The amplitudes of the radiation field are defined from the condition of the linking of the solutions:

$$\bar{B}_k^{s(1)}(0) = \bar{B}_k^{s(2)}(0) + \bar{B}_k^{r(2)}(0), \quad (13)$$

$$\varepsilon_1 \bar{E}_k^{s(1)}(0) = \varepsilon_2 [\bar{E}_k^{s(2)}(0) + \bar{E}_k^{r(2)}(0)] \quad (14)$$

from which we obtain:

$$b_{\pm}(\vec{k}, \vec{\beta}) = \frac{k^2}{2} \left[\frac{\mu_1}{k^2 - \varepsilon_1 \mu_1 (\vec{k} \vec{\beta})^2} - \frac{\mu_2}{k^2 - \varepsilon_2 \mu_2 (\vec{k} \vec{\beta})^2} \pm k(\vec{k} \vec{\beta}) \sqrt{\mu_2 / \varepsilon_2} \frac{\varepsilon_1 \mu_1 - \varepsilon_2 \mu_2}{(k^2 - \varepsilon_1 \mu_1 (\vec{k} \vec{\beta})^2)(k^2 - \varepsilon_2 \mu_2 (\vec{k} \vec{\beta})^2)} \right] \quad (15)$$

From the condition of the field corporeality we have:

$$b_{\pm}^*(\vec{k}, \vec{\beta}) = b_{\mp}(\vec{k}, \vec{\beta}). \quad (16)$$

Moreover, the formulae (15) it is followed, that

$$b_{\pm}(-\vec{k}, -\vec{\beta}) = b_{\pm}(\vec{k}, \vec{\beta}). \quad (17)$$

From the formulae (15) it is followed, that module is $|b_+| > |b_-|$ at any source velocity, and in the ultrarelativistic case it is $|b_+| \gg |b_-|$. It is need to note specially, that in the rest state of the magnetic moment at the strong change of the physical properties of magnetic medium

$$b_{\pm}(\vec{k}, 0) = \frac{\mu_1 - \mu_2}{2} \neq 0,$$

that proves about the fact, that radiation takes place that can't be said about rest charge, amplitudes of radiation field of which is such case $\bar{a}_{\pm}(\vec{k}, 0) = 0$, i.e. the radiation doesn't take place. This effect is interest by the fact that the rest particle is the nonstationary medium, having magnetic moment, then because of the magnetic moment the transient radiation will be exactly, that has the real value for fixation of particles. For the nonmagnetic medium ($\mu_1 = \mu_2 = 1$) the amplitudes of transient radiation, charge and magnetic moment are proportional to the jump of the dielectric constant, $|\varepsilon_1 - \varepsilon_2|$, i.e. the more bigger the jump of the dielectric constant, the more stronger the radiation is. For the nonmagnetic medium the ratio of module quadrate is equal to:

$$\frac{|b_+|^2}{|b_-|^2} = \frac{|1 + \beta \sqrt{\varepsilon_2} \cos \theta|^2}{|1 - \beta \sqrt{\varepsilon_2} \cos \theta|^2}.$$

The dependence of the ratio (18) on the energy at the fixed angle θ is given on the fig.1. As it is seen from the plots, the ratio $|b_+|^2 / |b_-|^2$ strongly increase with the increase of energy, that shows, that the main part of the radiation energy is on the radiation part forward.

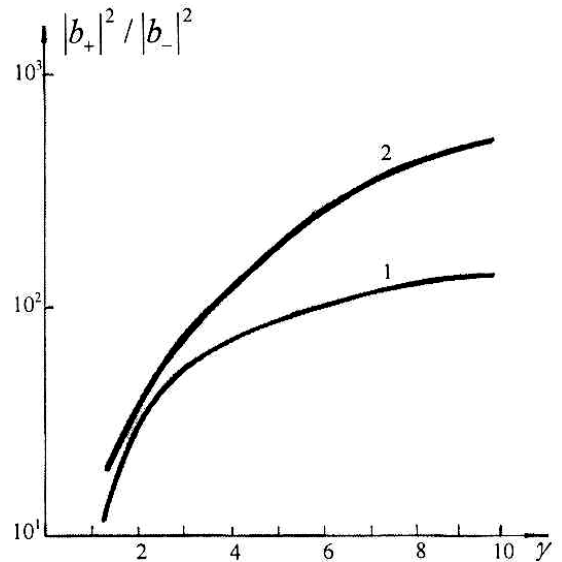


Fig.1. The energy distribution of the ratio of quadrate module amplitudes. Here curve 1 corresponds to the value $\theta = 15^\circ$, but curve 2 corresponds to the value $\theta = 5^\circ$.

The plot of the dependence of the ratio (18) on the angle θ at the fixed energy value is given on the fig.2. From the fig.2 it is seen, that in the region of small angles the forward radiation becomes stronger, i.e. the radiation is along the source velocity.

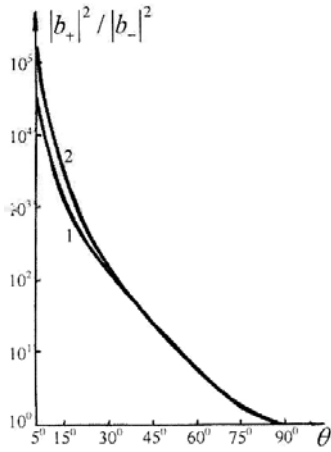


Fig.2. The angular distribution of the ratio of quadrate module amplitudes. Here curve 1 corresponds to the value $\gamma=10$, but curve 2 corresponds to the value $\gamma=25$.

In the work the influence of the electron magnetic moment on its transient radiation is also considered. The expression for the ratio of the intensity module quadrate of the transient forward radiation of the magnetic moment and charge:

$$\Delta = \frac{|\vec{E}_{\vec{k},m}^{r1}|^2}{|\vec{E}_{\vec{k},q}^{r1}|^2} = \frac{I}{4} \left(\frac{\varepsilon_\gamma}{Mc^2} \right)^2 f(\beta, \theta), \quad (19)$$

where

$$f(\beta, \theta) = \frac{1}{\beta^2} (2 - \beta^2 - 3\beta^2 \cos^2 \theta + \beta^4 (\cos^2 \theta + \cos^4 \theta)) , \quad (20)$$

and m_0 is the electron magnetic moment in the eigen reference system.

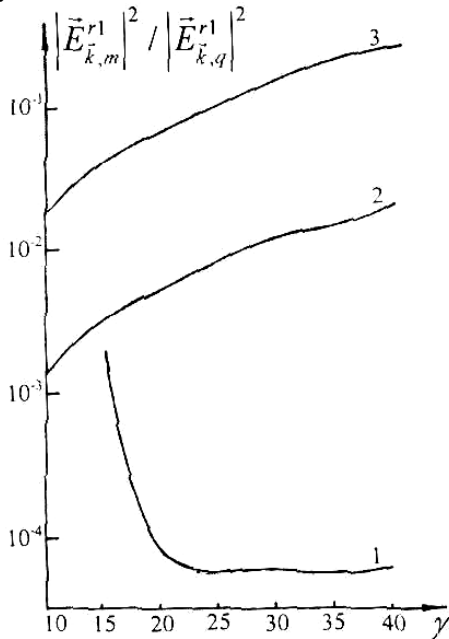


Fig.3. The energy dependence of the ratio of quadrate of module intensities of transient radiation of magnetic moment and charge. Here curve 1 corresponds to the value $\theta=5^\circ$, but curve 2 corresponds to the value $\theta=15^\circ$, curve 3 corresponds to the value $\theta=30^\circ$.

The plot of the dependence of the ratio (19) on the γ energy at the fixed values of angle θ is given on the fig.3. From the figure it is seen, that at small angles and velocity increase, this ratio strongly decreases. This is connected with the fact, that charge transient radiation with the velocity increase more increases, than transient radiation of the magnetic moment. At the transition to the big angles ($\theta=15^\circ$, 30°) with γ energy increase, to ratio (19) increases, i.e. deposit of the magnetic transient radiation becomes more significant, than charge one.

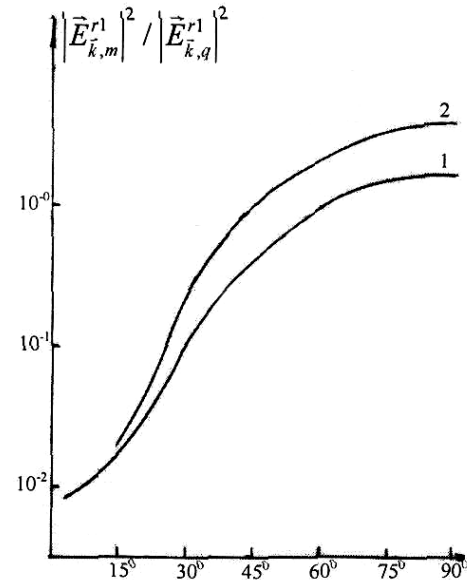


Fig.4. The angular dependence of quadrate of the module of intensities of transient radiation of magnetic moment and charge. Here curve 1 corresponds to the value $\gamma=25$, but curve 2 corresponds to the value $\gamma=40$.

The angular distribution of the ratio (19) at the fixed values of γ energy is represented on the fig.4. As it is seen from the plots, the deposit of the magnetic transient radiation significantly increases with the angle increase, so for example at the angle $\theta=45^\circ$ ($\gamma=40$) and $\theta=60^\circ$ ($\gamma=25$) the charge and magnetic transient radiation become almost equal. The energy of the radiated transient photon is chosen by $\varepsilon_\gamma = 0,1\gamma Mc^2$, where $Mc^2=0.51MeV$ is electron rest energy at the construction of the curves on the figures 3 and 4.

These results can be applied in the one of the important tasks of the modern physics of high energies.

- [1] V.L. Ginzburg, I.M. Frank. JETP, 1946, t. 16, s. 15. (in Russian). [4] I.G. Jafarov, I.M. Abutalibov, M.B. Asadova. «Хябярляр», АМЕА, Физ.– Рий.– вя Техника елм. сер., № 5(1), с. XXIII, Бақы, 2003, с. 104.
- [2] I.M. Abutalibov, M.B. Asadova, I.G. Jafarov. «Билэи» дярэиси, Физ.– Рий.– Йер елм. сер. №1, 2000, s. 19. [5] I.M. Abutalibov, M.B. Asadova, I.G. Jafarov. «Fizika», с. 9, Бақы, 2003, s. 34.
- [3] I.M. Abutalibov, M.B. Asadova, I.G. Jafarov. «Билэи» дярэиси, Физ.– Рий.– Йер елм. сер. №1, 2001, s. 4. [6] I.M. Abutalibov, M.B. Asadova, I.G. Jafarov. «Fizika», с. 10, Бақы, 2004, s. 10.

İ.M. Abutalıbov, M.B. Əsadova, İ.H. Cəfərov

MAQNİT MOMENTİNİN QEYRİ-STASİONAR MÜHİTDƏ KEÇİD ŞÜALANMASI

Dielektrik nüfuzluğun zamana görə kəskin dəyişməsində maqnit momentinin keçid şüalanmasına baxılmışdır. Məxsusi və şüalanma sahələri üçün ifadələr alınmışdır. Müəyyən edilmişdir ki, enerjinin artması ilə maqnit keçid şüalanmasının payı yük şüalanmasına nisbətən kifayət qədər artır. Maqnit mühitlər üçün fiziki xassələrin kəskin dəyişməsində izotrop şüalanma baş verir.

И.М. Абуталыбов, М.Б. Асадова, И.Г. Джафаров

ПЕРЕХОДНОЕ ИЗЛУЧЕНИЕ МАГНИТНОГО МОМЕНТА В НЕСТАЦИОНАРНОЙ СРЕДЕ

Рассмотрен процесс переходного излучения магнитного момента при резком изменении диэлектрической проницаемости во времени. Получены формулы для собственного поля и поля излучения. Установлено, что с ростом энергии вклад магнитного переходного излучения относительно зарядового значительно увеличивается. В случае магнитной среды при резком изменении физических свойств возникает изотропное излучение.

THE GROWTH PROCESS AND SOME OPTICAL PROPERTIES OF NANOPARTICLES GaSe, FORMED IN THE VOLUME OF GLASS MATRIX

M.B. MURADOV, Y.M. YOLCHIEV, N.G. DARVISHOV, G.M. EYVAZOVA

*Baku State University,
Az-1073, Baku, Z.Khalilov str.,23*

The nanoparticles of gallium selenide in the volume of glass matrix are obtained with the help of the crystallization method in the matrix. The X-ray diffraction investigations show, that the nanoparticles of gallium selenide with structure δ -GaSe form in the glass matrix. In the obtained structures, the photoluminescence radiation spectra (at the excitation wave length 510nm) have half-widths of lines $\sim 0,23\text{eV}$ with the radiation maximum 710nm.

Introduction

Last years, the big attention has been paid for the technology working of the obtaining and studying of nanoparticle physical properties of layered gallium selenide semiconductor [1-5]. The limit of particle sizes leads to very interest physical phenomena. With the decrease of the particle sizes, the material physical properties change significantly. The decrease of the particle sizes increases the ratio of surface area (S) to the particle volume (V) and increases the contribution of the surface atoms to the physical and thermodynamical properties of nanoparticles. For example, the decrease of nanoparticle sizes CdSe from 10 nm to 1nm increases the past of surface atoms practically from 20% till 100% [6]. The increase of the ratio (S/V) at the decrease of the particle sizes increases the contribution of surface energy to the free energy. As result, the materials, which are unstable in the volume state, can be stable in the nanoparticle form [7]. The semiconductor nanoparticles are perspective materials in the computers, medicine and instrument making [6]. The one of the important problem of the computers is the increase of system speed, which can be solved with the help of nanomaterials, having the high nonlinear-optical properties [6]. Such materials can allow to create the computing systems, working in the terahertz regions. That's why the working of new technologies and materials for the high-speed computers present the big interest. The composite materials on the base of nanoparticles of layered semiconductor GaSe, which has the high nonlinear optical properties can become the one of such materials. As it is known with the decrease of nanoparticle sizes the forbidden band width of material increases because of quant-size effect [8-9]. However, the situations are possible at witch with the decrease of the particle sizes, the forbidden band width of nanomaterials decreases. Such situation described in the work [10] is realized for nanotubes of GaSe. It is shown, that such systems are stable. The possibilities of the change of forbidden band width of GaSe in the wide interval make this material one of the interest object of scientific researches.

The technology of obtaining and nanoparticle structure of GaSe

The meaning of the technology is that nanoparticle and matrix materials (or its components) are taken into quartz ampoule or corundum crucible. The matrix melting point should be lower, than nanoparticle material melting point.

The mixture is heated up to the homogeneous mass formation at the temperature higher than melting point of nanoparticle material. Moreover, components (anions and cations) of nanoparticle dissolve in the melt of matrix material and form the homogeneous mixture. Further the mixture is cooled by the definite program. At the mixture cooling, the supersaturation on semiconductor components forms in the system. At the same time, the creation of buds and nanoparticle formation begins. The process of nanoparticle formation in the matrix melt volume accompanies with the creation of buds of different sizes and carrying out of crystallization process. Moreover, the absorption of small particles by the big ones is benefit on energy expenditure.

As result, the nanoparticle crystallization centers form. The formation of these centers in the matrix melts volume decreases of supersaturation factor around the nanocrystal. In this connection, the probability of new bud creation around nanoparticles decreases. The sizes of the created microcrystals depend on the mixture duration time at such temperature. After that the mixture is cooled till the room temperature by the definite program.

The GaSe nanoparticles in the volume of glass matrix are formed by us by the following method. The glass and components of nanoparticle (Ga and Se) are taken in the quartz ampoule. Metallic Ga and Se in the stoichiometric weight ratio are mixed with the well ground glass and are taken in the quartz ampoule. The nanomaterial components are 5% in the weight ratio with matrix. The quartz ampoule is pumped, with the help of forvacuum pump and made unbrazing. After that the ampoule is taken in the muffle stove and is heated till the temperature 1200°C . The heating time was near 90 minutes. Moreover, the homogeneous mixture creates. The Ga and Se components interreact in the volume and totally dissolve in the glass melt. After that the homogeneous melt is cooled by the special program. The melt is kept at the temperature 850°C during 60 minutes, later the melt is cooled till the room temperature. The obtained composite material is porous one. The planes, prepared from this material, are treated by the thermal annealing at the temperature 570°C during hours. In the result of this process, the nonhomogeneous of composite material removed.

The GaSe nanoparticle structure is defined with the help of X-ray diffraction analysis (DRON 2.0). The glass, in the volume of which the gallium selenide nanoparticles are formed, is ground in the mortar. After that the powder X-ray-grams are obtained (fig.1).

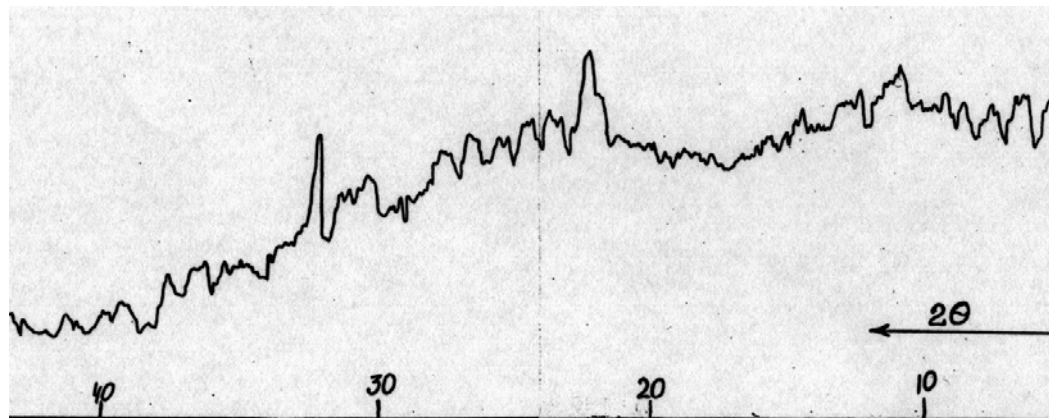


Fig1. X-ray diffraction from powder GaSe:glass

The analysis results are shown in the table 1. As it is seen from the table, the observable values of spacing of lattice planes significantly don't differ from standard values.

Table 1.

№	Observable value d in Å ⁰	Standard value d in Å ⁰	I	hkl
1	7,993	7,988	40	004
2	3,998	3,994	100	008
3	3,234	3,232	36	101
4	2,899	2,90	42	105
5	2,776	2,779	94	106
6	2,5226	2,527	12	108
7	2,3989	2,392	30	109
8	1,874	1,8697	15	1014

The value of interplanar distances corresponds to phase δ-GaSe. The nanoparticle sizes δ -GaSe are founded from the ratio [11].

$$d = \frac{0,9\lambda}{\beta \cos \theta} , \quad (1)$$

where β- is intensity half-width of diffraction line, measured in radians, $\lambda=1,5406\text{Å}^0$ is wavelength CuKα, θ- is diffraction angle. The average value of particle sizes GaSe, calculated from the equation (1), is equal 15,6nm. Such small value for nanoparticle sizes of gallium selenide is explained by the fact, that duration time for crystallization process is chosen very small. In the result of this, the process of nanoparticle enlargement (coalescence) was difficulties. Besides, probably, the high temperature (850⁰C) harms to the increase of the particles in the direction Van der Waals forces evidently.

The photoluminescence in nanoparticles of GaSe

The optical properties of gallium selenide nanoparticles, formed in the metanol volume are investigated in detail in the ref.[1]. The particle sizes in these experiments change from 2nm till 6nm. The average particle size is 4,0nm. The half-width of radiation line depended on wavelength and changed in interval (0,16-0,7)eV. After chromatographic particle division on sizes the average size is equal ~ 2,5 nm. In this case the half-width of radiation line decreases in 1,5 times in the comparison with the previous samples.

The radiation spectra (fig.2a) and excitation spectra (fig.2b) in the GaSe nanoparticles: glass at the temperature 90K, are investigated by us. At the excitation by photos with the energy $\lambda=510$ nm, the not wide band with half-width, which is equal to 0,23 eV and radiation maximum at 710nm (1,75eV) are observed. The nanoparticle excitation spectra have very wide band with half-width $E=0,42$ eV, and maximum is in the region 2,42 eV.

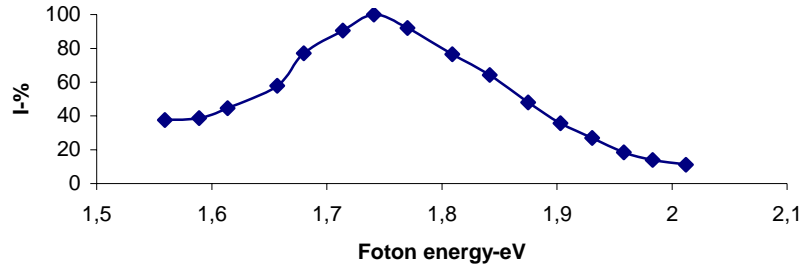


Fig. 2a. Radiation spectra of GaSe nanoparticles.

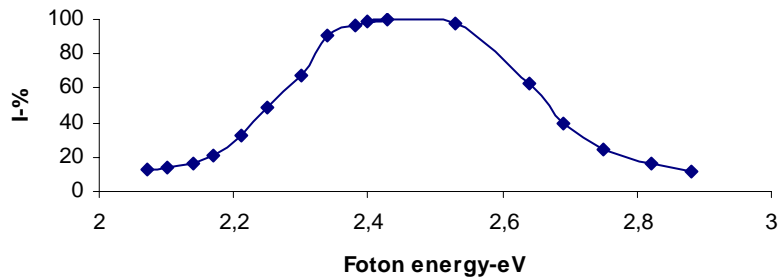


Fig. 2b. Excitation spectra of GaSe nanoparticles.

The observable by us wide excitation spectrum testifies about the wide interval of particle distribution on the sizes. In the result of which, the width of the prohibited band in the dependence on the sizes, changes in the wide range, according to the ref [8].

$$\Delta E = \frac{\pi^2 \hbar^2}{2m^* d^2} \quad , \quad (2)$$

where \hbar is Plank's constant, d is particle size, m^* is effective reduced mass of electrons and holes, $\pi=3,14$ constant. In the result of which, the of fundamental absorption edge in the nanoparticles spreads.

The temperature dependence of photoluminescence of Ga Se nanoparticles, formed in the glass matrix is investigated also by us. The dependence of radiation intensity maximum (λ 710nm) on the sample heating temperature in the temperature interval 80-270K is investigated (fig.3).

As it is seen from the figure 3, in the temperature interval (80-120)K, the radiation intensity increases~15%, and in the temperature interval (120-200)K, the intensity change doesn't significant (less, than 2%). The temperature increase leads to the insignificant intensity increase of photoluminescence (~7%). Such form of temperature dependence is explained by the fact, that nonradiative transfers are near radiative transition. At the temperature increase, the carrier transition from the nonradiative transitions into the radiative one takes place, in the result of which the radiation intensity increases. The last heating leads to the radiation level saturation. In the temperature interval (200-270)K the decrease of the carrier concentration in the radiated level takes place and radiation intensity decreases.

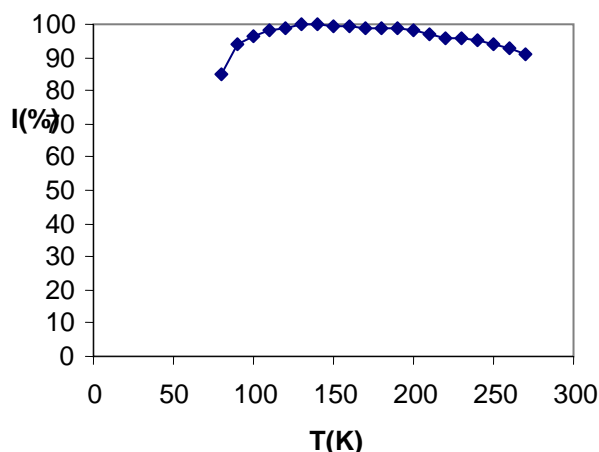


Fig.3. Temperature dependence of photoluminescence of GaSe nanoparticles.

Conclusion

Thus, for the first time the gallium selenide nanoparticles in the volume of glass matrix are formed by the crystallization method. By X-ray diffraction analysis, it is shown, that the nanoparticles with the structure δ -GaSe form in the glass matrix. The wide value of excitation spectrum half-width is explained by the distribution of particle sizes in the big range. It is shown, that maximum radiation intensity of photoluminescence weakly depends on the temperature.

- [1] V.Chikan, D.F.Kelly. Nano letters, v.2, №2, 2002, pp.141-145
- [2] V.Chikan, D.F.Kelly J. Chemical Physics, v.117, №19, 2002, pp.8944-8952
- [3] V.Chikan, D.F.Kelly. Nano letters, v2, №9, 2002, pp.1015-1020
- [4] H.Tu, S.Vang, V.Chikan, D.F.Kelly. J. Phys.Chem. B, v.108, 2004, pp.4701-4710
- [5] K.Allakhverdiev, J.Hagen, Z.Salaeva. Z.Phys. Status Solidi, v.163, 1997, pp.121-127
- [6] X.Chen, Y.Lou, C.Burda. Int.J.of Nanotechnology, v.1, №1/2,2004, pp.105-118
- [7] H.Nabika, M.Mizuhata, A.Kajinami, S.Deki, K.Akamatsu. J. Electroanalytical Chemistry v.559, 2003, pp.99-102
- [8] M.B.Muradov, A.A.Agasiyev. Pisma v Zhurnal Tekhnicheskoy Fiziki, v.17, is.13, 1991, p.54
- [9] M.B.Muradov. Optical waveguide on the basis of dielectric matrix and semiconductive microcrystallites, Proc. Of 2-nd International Conf. On lasers and their application. Tehran 1993, p. 179-184.
- [10] M.Cote, M.L.Cohen, D.J.Chadi. Phys. Rev. B, v.58, №8, 1998, pp.4277-4280
- [11] H.M. Pathan, J.D. Desai, C.D. Lokhande. Appl. Surf. Science, v.202, 2002, pp.47-56

M.B. Muradov, Y.M. Yolçiyev, N.Q. Dərvişov, G.M. Eyvazova

ŞÜŞƏ MATRİSDƏ FORMALAŞDIRILMIŞ GASE NANOHISSƏCİKLƏRİNİN BƏZİ FİZİKİ XASSƏLƏRİ

Matrisdə kristallaşma metodu ilə şüşə matrisdə GaSe nanohissəcikləri alınmışdır. Rentgen struktur analizi vasitəsilə müəyyən edilmişdir ki, şüşə matrisdə δ -GaSe strukturlu nanohissəciklər formalaşır. Alınmış nümunələrdə fotolumenensensiya spektrinin yarım eni (510nm dalğa uzunluğu ilə həyəcanlandırıldıqda) $\sim 0,23$ eV, şüalanma spektrinin maksimumu isə 710nm diapazonundadır.

М.Б. Мурадов, Я.М. Елчиев, Н.Г. Дарвишов, Г.М. Эйвазова

ПРОЦЕСС РОСТА И НЕКОТОРЫЕ ОПТИЧЕСКИЕ СВОЙСТВА НАНОЧАСТИЦ GaSe, СФОРМИРОВАННЫХ В ОБЪЕМЕ СТЕКЛЯННОЙ МАТРИЦЫ

С помощью метода кристаллизации в матрице были получены наночастицы селенида галлия в объеме стеклянной матрицы. Рентгеноструктурными исследованиями было показано, что в стеклянной матрице формируются наночастицы селенида галлия со структурой δ -GaSe. В полученных структурах спектры излучения фотолюминесценции (при длине волны возбуждения 510nm) имеют полуширины линий $\sim 0,23$ eV с максимумом излучения 710nm.

ФОТОЭЛЕКТРИЧЕСКИЕ СВОЙСТВА БАРЬЕРА ШОТТКИ НА ОСНОВЕ ГИДРОГЕНИЗИРОВАННОГО АМОРФНОГО КРЕМНИЯ (α -Si:H)

А.Г.МАМЕДОВА, Ш.С.АСЛАНОВ, С.В.ГАМИДОВ, С.Т.ГАХРАМАНОВА, А.И.БАЙРАМОВ

Институт Физики НАН Азербайджана

В работе приведены результаты получения пленок гидрогенизированного аморфного кремния (α -Si:H) методом магнетронного распыления и исследования их электрических, фотоэлектрических и оптических свойств. На основе полученных пленок созданы солнечные элементы с барьером Шоттки с высокими фотоэлектрическими параметрами.

Последние годы все большее внимание уделяется исследованию свойств тонких пленок неупорядоченных полупроводников. Среди них особенно выделяется гидрогенизированный аморфный кремний (α -Si:H). Интерес к этому материалу обусловлен, главным образом, возможностью создания на его основе эффективных и дешевых фотоэлектрических преобразователей солнечной энергии[1].

В ряде исследований было установлено, что в процессе разложение силана в плазме при приложении магнитного поля улучшаются фотоэлектрические свойства пленок [2, 3]. Поэтому в данной работе для получения пленок α -Si:H применяется метод магнетронного распыления на постоянном токе из монокристаллической кремниевой мишени. Метод магнетронного распыления на постоянном токе обладает рядом преимуществ; эффективный контроль содержания водорода в камере и в пленке, а также температуры подложки в широком интервале, использование для распыления мишени сложного состава, высокая скорость осаждения, относительно низкое напряжение осаждения (менее 400В), что ограничивает отрицательное воздействие энергии ионов на структуры и водородной связи в пленках, применимость в массовом производстве и др.

Целью данной работы является получение α -Si:H с использованием метода магнетронного распыления на постоянном токе, исследование их электрических и фотоэлектрических свойств в зависимости от состава, а также изготовление на их основе барьеров Шоттки с высокими фотоэлектрическими параметрами.

Нами разработано и изготовлено магнетронное распылительное устройство в вакууме, позволяющее использовать мишень в виде плоского диска с диаметром 100мм. При получении пленок α -Si:H использовалась кремниевая мишень чистоты 99,99. Для осуществления эффективного процесса гидрогенизации с пониженной плотностью дефектов в запрещенной зоне, нами оптимизировались параметры осаждения - парциальное давление водорода P_H , давление аргона P_{Ar} , температура подложки T_s , входная мощность P и смещение на подложке V_B . Наилучшие пленки были получены при параметрах приведенных в таблице 1.

Таблица1. Технологические условия получения пленок α -Si:H.

T (°C)	P _H (%)	P _{Ar} (%)	P _{total} (mtorr)	V _B (V)
250	50	50	10	-100

Результаты комплексного исследования характеристик пленок приведены в таблице 2.

Таблица 2. Характеристики полученных пленок α -Si:H

Содержание водорода по отношению к Si (%)	содержание кислорода по отношению к Si (%)	Оптическая ширина запрещенной зоны (eV)	Плотность состояний ($\text{cm}^{-3} \cdot \text{eV}^{-1}$)	Диэлектр. постоянная	Отношение световой и темновой проводимостей
1	2	3	4	5	6
19	1	1.92	$8 \cdot 10^{16}$	8.5	10^5

Нами были изготовлены солнечные элементы с барьером Шоттки на основе гидрогенизированного аморфного кремния α -Si:H на стеклянной подложке. Площадь изготовленных элементов составляли $2 \times 2 \text{ cm}^2$, в качестве металлического контакта использованы аморфные слои Al+Ni, а для создания барьера Шоттки использованы монокристаллические пленки силицида платины PtSi. Термообработка для получения моно-PtSi и стабилизация параметров α -Si:H были совмещены и проведены в вакууме и в среде форминг газа ($\text{N}_2 + \text{H}_2$).

Структура металлической пленки определена методами рентгенодифрактометрии и электронографии. Результаты представлены на рис.1

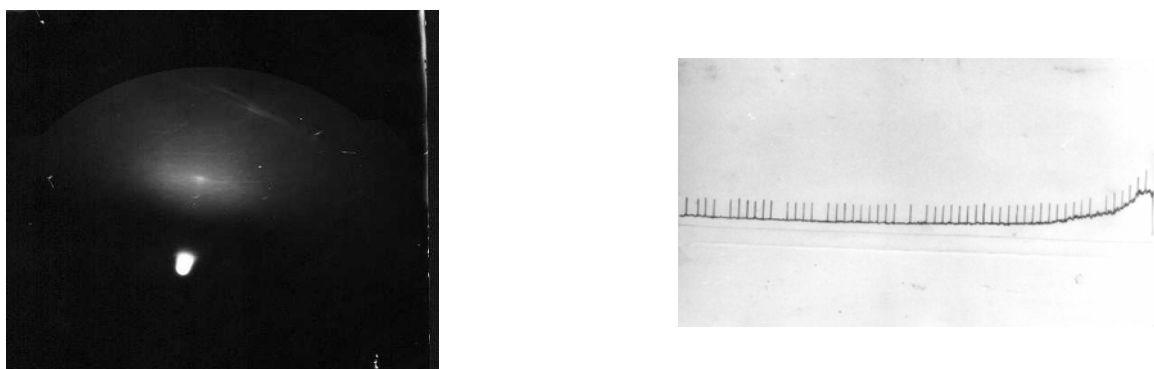


Рис 1. *a* –рентген дифракционная картина монокристаллической пленки PtSi и *b*-электронографическая картина аморфной пленки Al+Ni.

Следует отметить, что применение аморфных и монокристаллических металлических пленок обеспечивает долговечность и надежность элементов, так как в этих пленках отсутствуют диффузионные процессы по границам зерен. Конструкция изготовленных солнечных элементов представлена на рис 2:

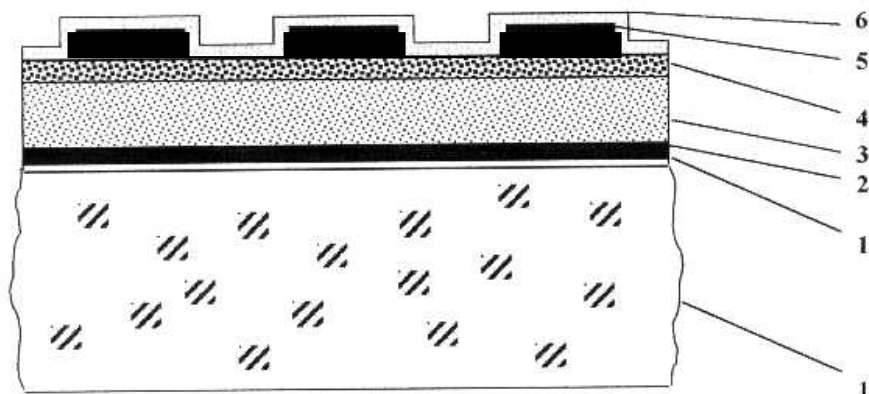


Рис.2

1 – стеклянная подложка, 2 – n^+ - α -Si:H, 3 – n - α -Si:H ,
1' - α -Al+Ni, 4 – моно-PtSi, 5-Ti+W метал. контакты, 6- просветляющее покрытие

В процессе распыления с целью получения n^+ типа проводимости использован фосфин PH_3 .

Для улучшения адгезии к стеклянной подложке металлических контактов нанесен очень тонкий слой SiO_x толщиной 0,01мкм.

Параметры изготовленных элементов определены на специальном стенде с регулируемой освещенностью. При освещенности 100 mW/cm^2 , AM1 напряжение холостого хода, $U_{OC}=0,88 \text{ mV}$ (open circuits voltage) , ток короткого (short circuits current) $I_{sc}=15.3 \text{ mA/cm}^2$,

Литература

1. С. А. Ендриховский, А. С. Нестеров, С. А. Неустроев, Е. В. Соколов, Ш. Г. Хурошвили. Получение, свойства и применение гидрогенизированного аморфного кремния. Обзоры по электронной технике, серия 6, выпуск 1986
2. Abdulrida M. C. , Allison J. . Thin film field effect transistors incorporating hydrogenated amorphous silicon prodused by magnetron sputtering, Thin Solid Films, 1983, v. 102, p. L43-L46
3. Moafok C., Abdulrida M.C., Allison J., Influence of hydrogen on the performance of magnetron-sputtered amorphous hydrogenated silicon field-effect transistor, Appl.Phys.Lett., 1983, v.43, №8, p.768.

A.H. Məmmədova, Ş.S.Aslanov, S.V.Həmidov, S.T.Qəhrəmanova, A.H.Bayramov

**HİDROGENLƏŞDİRİLMİŞ AMORF SİLİSİUM (α -Si:H) ƏSASLI ŞOTTKİ BARYERİNİN
FOTOELEKTRİK XASSƏLƏRİ**

İşdə maqnetron tozlandırma metodu ilə hidrogenləşdirilmiş amorf silisium incə təbəqələrinin alınması və onların elektrik, fotoelektrik və optik xassələrinin tədqiqi nəticələri verilmişdir. Alınmış təbəqələrin əsasında yüksək fotoelektrik parametrlərə malik Şottki baryerli günəş elementləri yaradılmışdır.

A.G. Mamedova, Sh.S.Aslanov, S.V.Gamidov, S.T.Kakhramanova, A.I.Bayramov

**PHOTOELECTRICAL PROPERTIES OF SCHOTTKY BARRIERS ON THE BASIS OF
HYDROGENIZED AMORPHOUS SILICON (α -Si:H)**

In this work the results of preparing of hydrogenized amorphous silicon thin films by the magnetron sputtering method and studies of their electrical, photoelectrical and optical properties are given. On the basis of obtained films high efficient solar cells with Schottky barriers are created.

ON THE MIXED PHASE OF STRONGLY INTERACTING MATTER

M.K. SULEYMANOV, O.B. ABDINOV

Institute of Physics of ANAS, Baku

B.Z. BELASHEV, A.S. VODOPIANOV

Joint Institute for Nuclear Research, Dubna

YA.G. GUSEYNALIYEV

Aerocomic Agency of ANAS, Baku

1. Introduction.

The studying of the behavior of some characteristics of hadron-nuclear and nuclear-nuclear interactions as a function of the collision centrality Q is an important experimental method to get information about the changes of nuclear matter phase, because the increasing of the centrality could lead to the growth of the nuclear matter baryon density. In other words, the regime change in the behavior of some centrality depending characteristics of events is expected by the varying the Q . It would be the signal about the phase transition. This method is considered as the best tool reaching the quark-gluon plasma phase of strongly interacting matter.

Some experimental results demonstrate already the existence of the regime changes in the event characteristics behavior as a function of collision centrality.

Let us look over some of them¹.

First results of hadron -nuclear reactions.

In paper [1] the results are presented from BNL experiment E910 on pion production and stopping in proton-Be, Cu, and Au collisions as a function of centrality at a beam momentum of 18 GeV/c. The centrality of the collisions is characterized using the measured number of «grey» tracks, N_{grey} , and a derived quantity, ν , the number of inelastic nucleon-nucleon scatterings suffered by the projectile during the collision. The values of average multiplicity for π^- mesons ($\langle\pi^- \text{ Multiplicity}\rangle$) as a function of N_{grey} and ν for the three different targets are plotted in Fig. 1.

We see that the $\langle\pi^- \text{ Multiplicity}\rangle$ increases approximately proportionally to N_{grey} and ν for all three targets at small values of N_{grey} or ν and saturates with increasing of N_{grey} and ν in the region of more high values of N_{grey} and ν . It is also shown with a solid line in Figure the expectations for the $\langle\pi^- \text{ Multiplicity}\rangle$ (ν) based on the wounded - nucleon (WN) model and with dashed line, does a much better job of describing p-Be yields than the WN model. So the results demonstrate definitely the regime changes of the behavior for these distributions. BNL E910 has measured the Λ production as a function of collision centrality for 17.5 GeV/c p-Au collisions [2]. Collision centrality is defined by ν . The Λ yield versus ν is plotted in Fig.2(5). The open symbols are the integrated gamma function yields. The black symbols are the fiducial yields. The various curves represent different functional scalings. We see that the measured Λ yield increases for $\nu \leq 3$ and then it saturates with increasing ν . Similar results for K^+ , K_s^0 - mesons and Ξ^- multiplicity in p+Au collision at 17.5 GeV/c have also been obtained by the BNL E910.

The results on the nuclear-nuclear reactions.

In paper [3] the experimental results of particle multiplicity distributions in silicon-emulsion collisions at 4.5A GeV/c are reported. The correlations between the multiplicities of target fragments are given. The saturation effect of target black fragment multiplicity in the collisions is observed. It is demonstrated in Fig. 3 where the dependence of $\langle N_b \rangle$ on N_g for silicon-emulsion collisions at 4.5A GeV/c (closed circles) is presented. The corresponding results for oxygen-emulsion collisions at 3.7A GeV (open circles) and 200A GeV (open squares) are given in the figure, too. One can see that the value of $\langle N_b \rangle$ increases with the increasing N_g in the region of $N_g < 8$, and the saturation effect appears in the region of $N_g > 8$. The saturation effect was previously observed in proton-emulsion collisions at high energy [4]. Recently, in oxygen-emulsion collisions at the Dubna and SPS energies, the saturation effect was also observed [5].

¹ It is necessary to note that the number of identified protons (N_p), fragments (N_F), slow particles (N_{slow}), of h - and g - particles (N_h and N_g accordingly in emulsion experiments) have been used to obtain information on the Q and correspondingly on the impact parameter of the collision. The measured energy flow of the particles at an emission angles $\theta=0^\circ$ and $\theta=90^\circ$ have also been used to define the Q . Apparently, it is not simple to compare quantitatively the results on Q -dependencies of event characteristics taken from different papers.

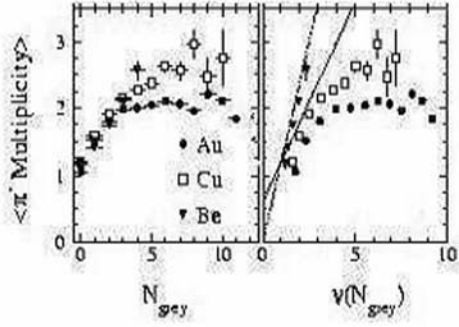


Fig.1. The values of average multiplicity for π^- - mesons ($\langle \pi^- \text{ Multiplicity} \rangle$) as a function of N_{grey} and v for the three different targets. Solid line in figure is expectations for the $\langle \pi^- \text{ Multiplicity} \rangle$ (v) based on the wounded-nucleon (WN) model and the dashed line, does a much better job of describing p-Be yields than the WN model.

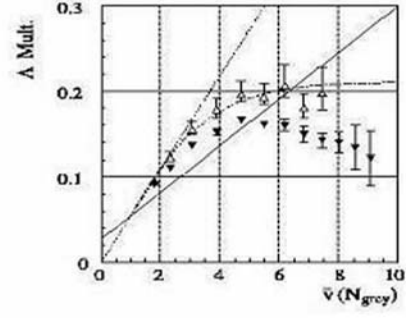


Fig.2 Λ production as a function of collision centrality for 17.5 GeV/c p-Au collisions. The open symbols are the integrated gamma function yields. The black symbols are the fiducial yields. The various curves represent different functional scalings.

In paper [6] the results are presented on dimuon production in proton-tungsten and sulphur-tungsten interactions at 200 GeV/c/nucleon were measured using the HELIOS/3 dimuon spectrometer at the CERN SPS. It was made a direct experimental comparison between the S-W and p-W results for the ratio $\mu\mu/\text{charged particles}$ and found there was a clear excess in $\mu\mu$ production relative to charged particle production in S-W interactions compared to p-W interactions as a function of mass. The excess is defined as the difference between S-W and p-W spectra. The values of inverse slope parameter of the transverse mass distribution for low mass excess versus of the charged multiplicity is shown in next Fig. 4. We can also see the regime change in the behavior of this distribution.

The ratio of the J/ψ to Drell-Yan cross-sections has been measured by the CERN NA50 as a function of the centrality in Pb-Pb collision at 158 GeV/nucleon [7]. It is shown in this Fig.5. E_T fixes the centrality, which was a transverse energy flow. The result for light nuclei collisions is also demonstrated with solid line in the figure. The regime change is observed for the behavior of these dependencies.

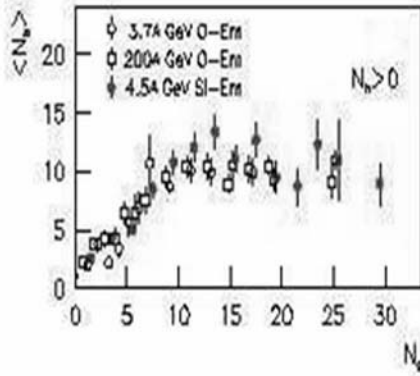


Fig. 3 The dependence of $\langle Nb \rangle$ on N_g for silicon-emulsion collisions at 4.5A GeV/c (closed circles). The corresponding results for oxygen-emulsion collisions at 3.7A GeV (open circles) and 200A GeV (open squares) are given in the figure, too.

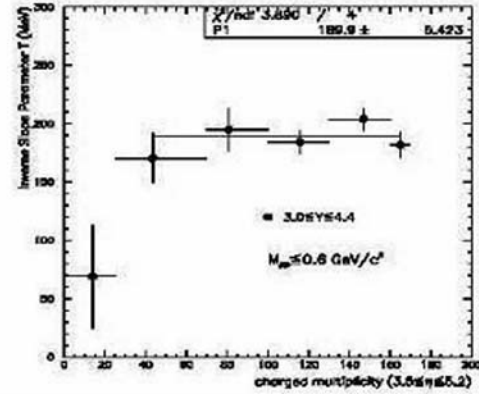


Fig. 4 The values of inverse slope parameter of the transverse mass distribution for low mass excess versus of the charged multiplicity production in proton-tungsten and sulphur-tungsten interactions at 200 GeV/c/nucleon.

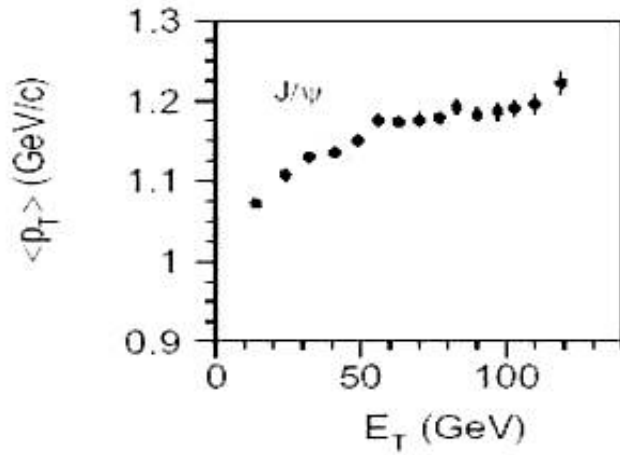


Fig.5 The ratio of the J/ψ to Drell-Yan cross-sections as a function of the centrality in Pb-Pb collision at 158 GeV/nucleon.

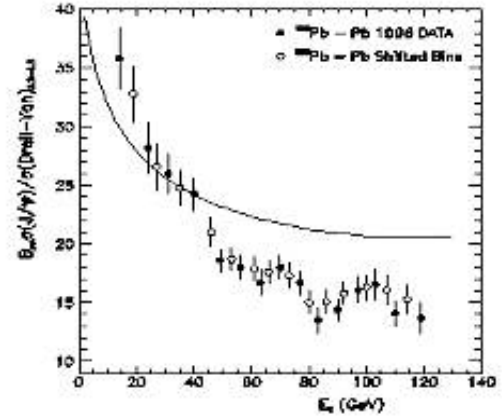


Fig. 6 $\langle P_T \rangle$ as a function of the transverse energy for J/ψ mass intervals. The error bars are only statistical.

In paper [8] the muon pairs produced in Pb-Pb interactions at 158 GeV/c per nucleon are used to study the transverse momentum distributions of the J/ψ, Ψ' and dimuons in the mass continuum. In particular, the dependence of these distributions on the centrality of the Pb-Pb collision is investigated in detail.

The $\langle P_T \rangle$ values obtained for the J/ψ are plotted in Fig. 6 as a function of E_T . It is seen for the J/ψ, the values of $\langle P_T \rangle$ first increase and then tend to flatten when the centrality of the collision increases.

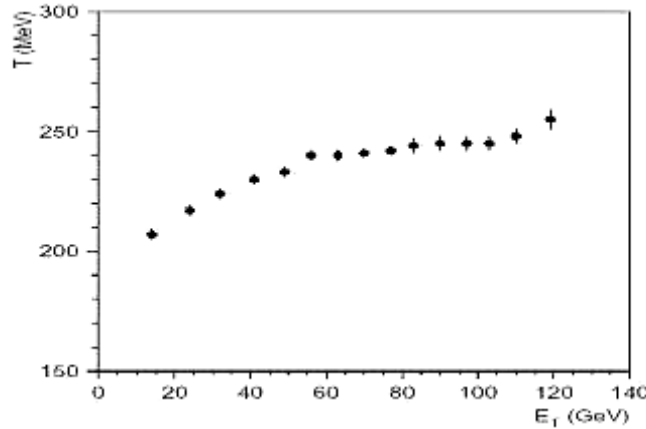


Fig. 7 Inverse slope parameter, T, of the J/ψ transverse mass distributions, plotted as a function of the transverse energy.

The transverse mass distributions of the produced muon pairs have also been studied in order to allow a comparison with thermal models. The inverse slope T of J/ψ transverse mass distributions is also plotted in Fig. 7 as a function of the E_T . First it increases with E_T and then seem to flatten at high E_T , as the $\langle P_T \rangle$ values.

So the main obtained result is the existence of the regime changes. The regularity is observed for hadron-nuclear and nuclear-nuclear interactions as well for the interaction of light and heavy nuclei; at high and at low temperature; and for the π-mesons, nucleons, fragments (F), strange particles (S) and J/ψ, that is the regularity is also observed at small densities and temperatures. Therefore it could not be connected with the existing of the predicted QCD point for hadronic matter quarks-gluons phase transition.

2. The Mixed Phase

Therefore it was suggested to consider the appearance of the strongly interacting matter mixed phase (MP) for a qualitative understanding of the regularity. MP is considered as a phase of compressed nucleons. These phase are predicted by QCD for the temperatures around the critical temperature T_c . It could be formed in the result of nucleon percolation in density nuclear matter. It is well known the statistical and percolation theories can describe the critical phenomena best of all. But how we have seen the regime changes have also been observed for small density and temperature for which the conditions of applying of statistical theories are practically absent. So the percolation approach could be the only approach for the description of the results. Therefore we consider the percolation mechanisms as one of the mean mechanisms for MP formation. It would lead to the formation of the percolation cluster.

In paper [9] was discussed that percolation clusters much larger than hadrons, within which color is not confined; deconfinement is thus related to percolation cluster formation. This is the central topic of percolation theory, and hence a connection between percolation and deconfinement seems very likely [10-12]. So percolation cluster can be color object.

Therefore MP could be considered as a system of color and color-neutral objects and experimental information on the particular conditions of the MP formation is important for the fix the onset stage of deconfinement.

2.1. Experimental signals on Mixed Phase

To experimental confirmation the MP formation it is necessary to extract the signals on the accompany effects of MP. We can say that the effects of cluster formation, the appearance of critical nuclear transparency and the π -meson condensate could be the accompany ones.

3.1 Effect of percolation cluster formation.

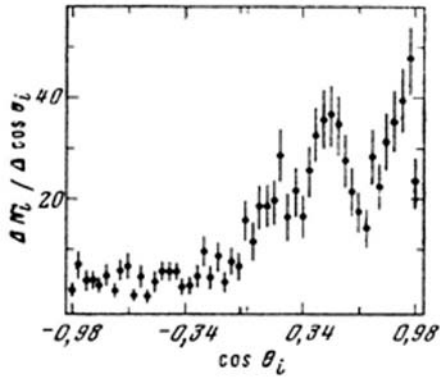


Fig. 8 Angular distributions of protons emitted in $\pi^{12}\text{C}$ -interactions at momentum 40 GeV/c

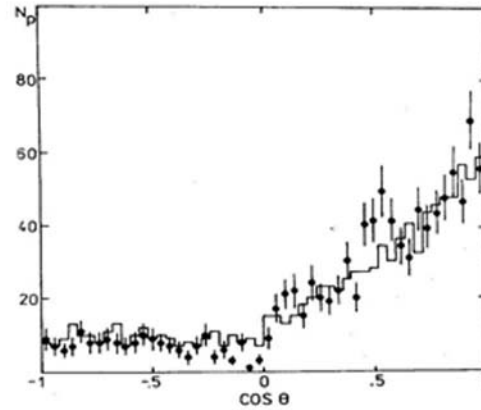


Fig. 9 Angular distributions of protons emitted in $\pi^{12}\text{C}$ -interactions at the momentum 5 GeV/c.

The cluster could be form in the result of percolation of nucleons in high-density baryon system. There are many papers in which the processes of nuclear fragmentation [13] and the processes of central collisions [14] are considered as critical phenomena and it is suggested that the percolation approach to be used to explain these phenomena. We suppose that the cluster had formed at some critical values of Q in hadron-nucleus and nucleus-nucleus collisions and then with increase of Q it would decay on fragments and free nucleons.

The existence of the percolation cluster could explain the experimental results on the angular distributions of emitted protons in $\pi^{12}\text{C}$ -interactions at the momentum 40 GeV/c [15]. In these experiments the angular distributions of protons (with the momentum less than 1.0 GeV/c) were studied in the events with total disintegration of nuclei (or central collisions). This distribution is shown in Fig.8. The anomalous peak in this distribution is seen. The results on the angular distributions of protons emitted in $\pi^{12}\text{C}$ -interactions at momentum 5 GeV/c [16] confirm the existence of the anomalous peak (Fig.9). We believe that it could be connected with formation and decay of the percolation cluster. The anomalous peak in angular distribution of emitted protons and fragments could be considered as the signal of the percolation cluster and MP formation (signal I).

3.2 Effect of critical nuclear transparency

When the MP appears the conduction of nuclear matter could sharply increase and the matter could become a superconductor [9] because the nucleons must be bound in the result of percolation in high-density baryon system. It could lead to critical change of the angular correlation of particle production and might be another signal on MP formation (signal II).

3.3 Effect of π -meson condensation

The meson condensate appearance effect might be the other accompanying effect for the processes of MP formation. The idea of a meson condensate formation was predicted [17] many years ago. But up to now there are no experimental results definitely confirming this idea. When we analyzed the results from the TAPS setup [18] we found some results, which could be interesting for the experimental search of the meson condensate. In these papers the temperature of the slow π^0 -mesons defined as slopes of the invariant transverse mass (m_t) spectrum, which are shown in Fig.10 - 11. The result at low m_t is to be very interesting as the behavior of the m_t -spectrums differ from the exponential law (in Fig. 10). We believe that some part of these deviations could be connected with the appearance of meson condensate. It depends on the centrality (Fig.11). The last is the main argument confirming that the observed deviation could be connected with the meson condensate. The centrality dependence of this deviation could be considered as one more signal on MP formation (signal III).

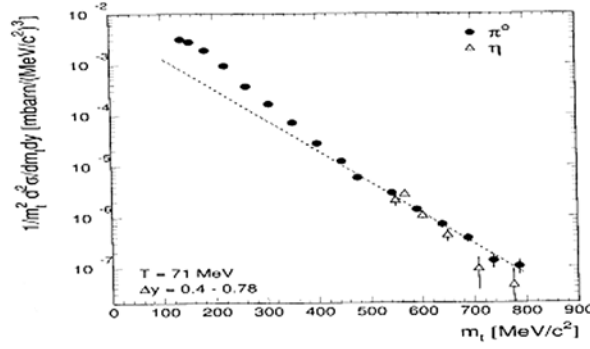


Fig.10 Transverse-mass spectra of π^0 and η -mesons for Au+Au interactions at 0.8 A MeV.

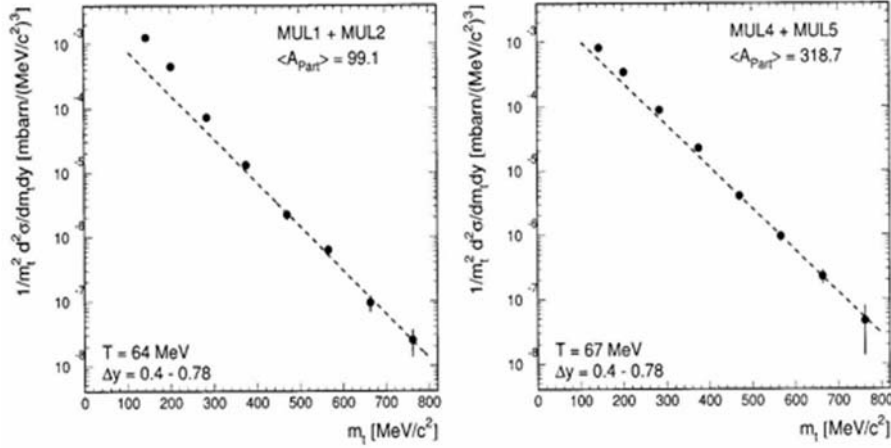


Fig.11. Transverse-mass spectra of π^0 and η -mesons for Au+Au interactions at 0.8 A MeV in:
a) noncentral collisions; b) in central collisions.

4. Conclusion

So we think that the simultaneous observation of signals I-III could all low to get an important information for answer of the question on MP formation. Therefore we are going to investigate the behavior of angular distributions of protons; a behavior of π^0 - or $\pi^+\pi^-$ -mesons pair invariant spectrum as a function of the m_t ; the particles yield at different emission angle as a function of the centrality.

We expect to see a simultaneous appearance of the signals I-III.

- [1] Chemakin et al. The BNL E910 Collaboration, E-print:nucl-ex/9902009 v1, 19, Feb 1999, 3
- [2] Ron Soltz for the E910 Collaboration. J. Phys. G: Nucl. Part. Phys. 27 (2001) 319–326
- [3] Fu-Hu Liu et al. Phys. Rev. C 67, 047603(2003)
- [4] Abduzhamilov et al., Z. Phys. C 40, 223 (1988)
- [5] F.H. Liu, Chin. J. Phys. (Taipei) 40, 159 (2002)
- [6] A.L.S. Angelis et al. Eur. Phys. J. C 13, 433–452 (2000) The HELIOS/3 Collaboration.
- [7] M.C. Abreu et al. Phys.Let. B450,1999,456; M.C. Abreu et al. Phys.Let.B410,1997,337; M.C. Abreu et al. Phys.Let. B410,1997,327
- [8] M.C. Abreu et al. By NA50 Collaboration : Phys.Lett.B499:85-96,2001
- [9] H.Satz. E-print:hep-ph/0007069 v1 7 Jul 2000
- [10] H.Satz, Nucl. Phys. A 642 (1998) 130c.
- [11] G. Baym, Physica 96 A (1979) 131.
- [12] T. Celik, F. Karsch and H. Satz, Phys. Lett. 97 B (1980) 128. J. Desbois, Nucl. Phys. A466 (1987) 724 ; J. Nemeth et al. Z.Phys.A 325 (1986) 347;
- [13] S. Leray et al. Nucl. Phys.A511(1990)414; A.J. Santiago and K.C. Chung J. Phys. G:Nucl.Part. Phys. 16 (1990)1483; G.Musulmanbekov, A.Al-Haidary.Russian J.Nuc.Phys.,v.66 (2003) 1.
- [14] X.Campi, J. Desbois Proc. 23 Int. Winter Meeting on Nucl. Phys. Bormio,1985; Bauer W. et al. Nucl. Phys. 452(1986) 699; A.S. Botvina, L.V.Lanin. Sov. J. Nucl. Phys. 55 (1992) 381.
- [15] A.I.Anoshin et al.Yad.Fiz.33:164(1981)
- [16] O.B.Abdinov et al. Preprint JINR,1-80-859,Dubna (1980)
- [17] A.B.Migdal, Zh ETF (USSR) 61(1971),2210 JETP (Sov.Phys) 34 (1972) 1184; Zh ETF (USSR) 63(1972),1933 JETP (Sov.Phys) 36 (1973),1052; R.F. Sawyer, Phys.Rev.Lett.29 (1972),382 ;D.J. Scalapino, Phys.Rev.Lett. (1972),386; R.F. Sawyer And D.J. Scalapino, Phys.Rev.D7(1972),953.
- [18] R. Averbek et al. Z.Phys.A359:65-73,1997 ; A. Marin et al. Phys.Lett.B409:77-82,1997 ; A.R. Wolf et al. Phys.Rev.Lett. Vol.80,N 24,P.5281; A. R. Wolf, Doktorarbeit, Gieben 1997

PHOTO-ELECTRONIC PROPERTIES OF CU-DOPED CDS THIN FILMS

T.D.DZHAFAROV^{1,4}, V.D.NOVRUZOV^{2,4}, S.AYDIN¹, M.ALTUNBAS³, D.OREN¹,
M.TOMAKIN²

¹*Department of Physics, Yildiz Technical University, 34210 Istanbul, Turkey*

²*Faculty of Science and Arts, Karadeniz Technical University, Rize, Turkey*

³*Department of Physics, Karadeniz Technical University, 61080 Istanbul, Turkey*

⁴*Institute of Physics, Azerbaijan National Academy of Sciences, AZ1143 Baku, Azerbaijan*

The effect of copper diffusion and electrodiffusion on structural, electrical, optical and photosensitivity characteristics of thin film Cu/CdS structures was investigated. The thermal diffusion of copper at 300-400°C is accompanied by conversion of conductivity type of the films from n- to p-type, decrease of resistivity and origin the long-wave photosensitivity at $\lambda \geq 540$ nm.

XRD patterns of Cu/CdS structures exposed to thermal diffusion showed presence of Cu-S compounds. Diffusion under direct electrical field (electrodiffusion) of copper in Cu/CdS structures at room temperature results in increase or decrease the photosensitivity in depending on polarity of applied electric field.

1. Introduction

CdS thin films have been widely studied in the past 10 years due to their potential applications as windows in solar cells manufacturing. On the other hand, the Cu-CdS bilayer system is used for the preparation of metal-coated semiconductor nanocrystals which are of great interest for the fabrication of optical and electroluminescent devices [1]. As a rule, the as-grown CdS films has n-type conductivity, the high dark resistivity (about 10^5 - 10^8 Ω cm) and exhibit a high photoconductivity (10^4 - 10^6). Donor centers which formed in CdS during growth, were attributed to the strong self-compensation effect due to the native point defects (vacancies of the sulfur sublattice, the interstitial cadmium atoms etc) caused by deviation of CdS composition from the stoichiometry. To make the as-grown CdS films useful in optoelectronic applications, the dark resistivity must be reduced from 10^5 - 10^8 Ω cm to almost 10 Ω cm. Moreover, on this view preparation of p-type CdS thin films is need. Growth of the p-type CdS by doping or conversion of n-type CdS into p-type and by thermal impurity diffusion is a hardly realized process [2,3]. Copper is substitutional acceptor impurity in CdS. Copper are reported to be incorporated also as interstitial donors, and mobility of interstitial Cu atoms is known to be very high [4]. Cu-diffusion doping was used for preparation of p-type CdS [5].

Here, we report the results of investigations of the effect of copper diffusion and electrodiffusion on structural, electrical, optical and photosensitivity properties of CdS thin films.

2. Experimental Procedure

The n-type CdS thin films with a thickness of 2-4 μ m were fabricated on glass and SnO₂-coated glass substrates by spray-pyrolysis technique. The temperature of the substrates was 250°C. The resistivity of as-grown n-type CdS films was about of ... Ω cm. The Cu films (about of 20 - 30 nm) were deposited onto the upper surface of the CdS films by vacuum evaporation. Then, Cu diffusion in n-type CdS thin films was performed by annealing of Cu/nCdS structures at 300°C for 10 min in vacuum. Moreover, the doping of CdS films was also carried out by electrodiffusion of Cu in CdS at room temperature under applying the accelerating or retarding electric field. Current-voltage characteristics of Cu-CdS structures were measured at room temperature in darkness and under an illumination of about 100 mW cm⁻² from a solar simulator. The spectral distributions of photosensitivity were measured in the wavelength range 400-1100 nm at room temperature. Optical transmission spectra of films grown on glass substrates were measured in the range 400 - 1100 nm by using a "Lambda 2" Perkin-Elmer spectrometer.

The crystalline structure and composition of the undoped and Cu-doped films were analysed by the X-ray diffraction (XRD) technique using a Rigaku D/Max 111C diffractometer with CuK α radiation. The surface morphology of films was studied using a JEOL JSM-6400 scanning electron microscope (SEM).

3. Results and discussion

The electrical measurement showed that resistivity of as-grown n-type CdS films was about of 10^9 Ω cm.

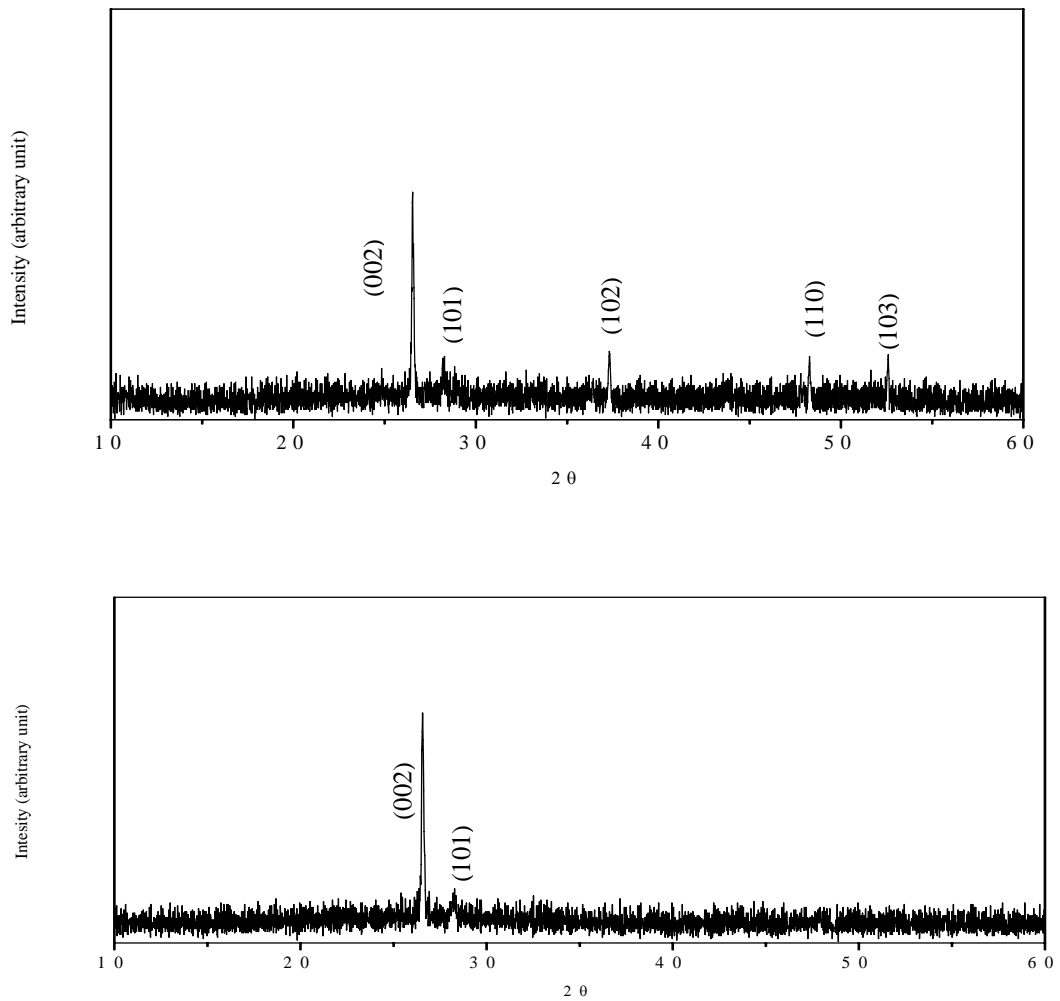


Fig 1. XRD patterns for (a) CdS film and (b) Cu/CdS structure (300°C, 10 min).

Figure.1 illustrate the XRD patterns of as-grown CdS film and Cu/CdS structure exposed to annealing at 300°C for 10 min. The strong XRD peak at $2\theta = 26.6^\circ$ corresponds to diffraction angles of the (002) plane of hexagonal CdS [6]. Therefore, the CdS films deposited on a glass substrate by spray-pyrolysis were of a hexagonal structure and the c-axis of crystallites was mostly oriented perpendicular to the substrate. (102), (110) and (103) peaks Cu-S compounds (Cu_2S) in XRD patterns were additionally observed for the Cu/CdS structure exposed to copper diffusion at 300°C. The morphology studies of CdS and Cu-doped CdS films reveal the existence of polycrystalline structure with crystallite dimension of and ... μm (Figure 2).

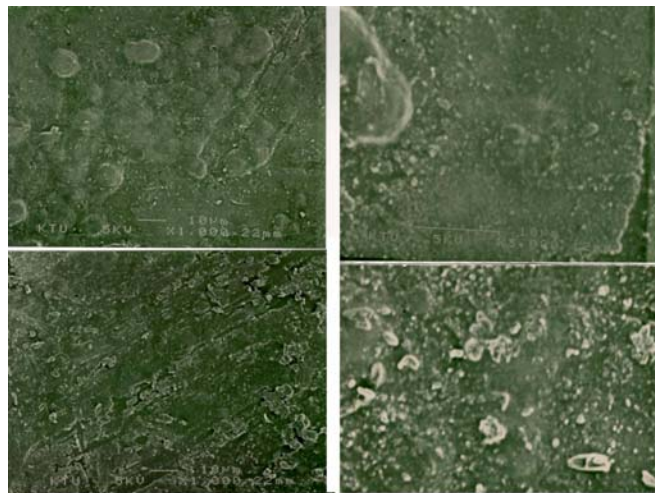


Fig 2. SEM micrographs for (a) CdS and (b) Cu-doped CdS films.

The conversion of conductivity type of CdS film from the n-type to the p-type, as result of Cu diffusion into CdS film at 300-400°C is measured by thermoprobe. Herewith the resistivity of p-type film decreases from 10^9 up to $2 \times 10^7 \Omega \text{ cm}$. Optical absorption coefficient spectra, depending on the duration of copper diffusion in bilayer Cu/CdS structure at 400°C are presented in Figure 3.

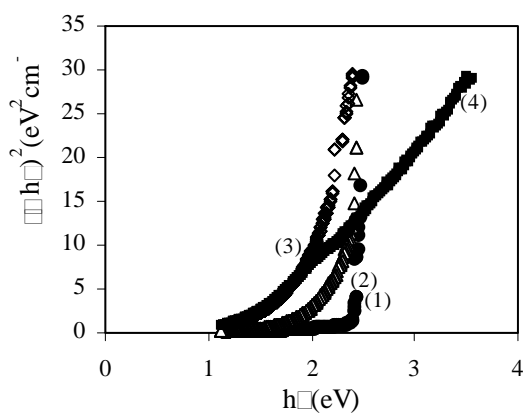


Fig 3. Optical absorption coefficient spectra of Cu/CdS structure (1) before and after annealing at 400°C for (2) 15, (3) 30 and (4) 45 min.

Data on the absorption edge of films determined from $(\alpha h\nu)^2 - h\nu$ plots are presented in Figure 4.

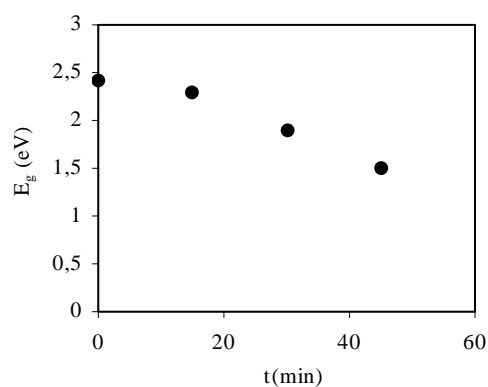


Fig 4. The energy band gap of Cu-doped CdS film in dependency on duration of annealing at 400°C.

It is seen that the band gap of films decreases from 2.42 eV (CdS) to 1.5 eV ($\text{Cu}_{1.96}\text{S}$) as result of Cu diffusion in CdS film. These results can be explained by diffusion of Cu in CdS accompanied with formation a new Cu-S phases in CdS films.

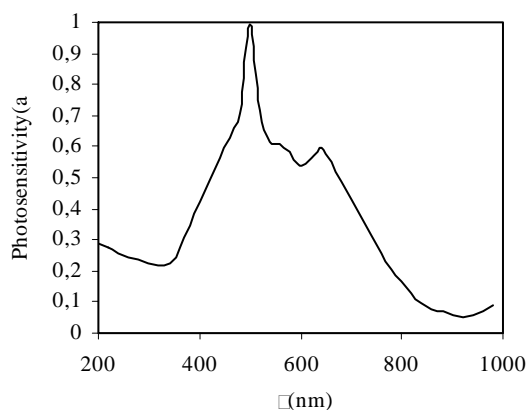


Fig 5. The spectral distribution of photosensitivity of Cu/CdS structure after annealing at 400°C for 30 min.

Figure 5 shows the spectral distribution of photocurrent for Cu/CdS structure exposed to annealing at 400°C. It can be seen that the edge of photosensitivity begins at about 800 nm (1.55 eV) and a peak of photosensitivity settles down at 510 nm (2.43 eV) corresponding to the band gap of CdS.

Thus the thermal diffusion of copper in Cu/nCdS structures at 300-400°C results in the conversion of conductivity type of the film from n-type to the p-type, decreases the resistivity from 10^9 to $2 \times 10^7 \Omega \text{ cm}$ and the band gap from 2.4 eV to 1.5 eV, and origins the long-wave photosensitivity at $\lambda \leq 800 \text{ nm}$.

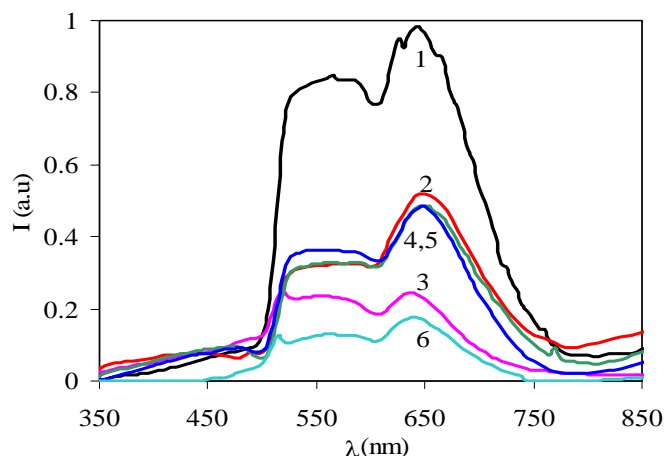


Fig 6. The spectral distribution of photosensitivity of Cu/CdS structure (1) before and after electrodiffusion for (2) 5, (3) 7, (4) 10, (5) 15 and (6) 20 min at 25°C (“+” on Cu).

Figure 6 shows normalized spectra of photocurrent of Cu/CdS structure in depending on duration of electrodiffusion at room temperature (+10V on Cu-side). Region of spectral photosensitivity for all spectra spreads from 500 to 780 nm and photosensitivity decreases with increase duration of electrodiffusion. In contrast, applying the negative polarity (-10V) on Cu-side of Cu/CdS structure results in increase of photosensitivity of Cu/CdS structure as a function of duration of electrodiffusion (Figure 7).

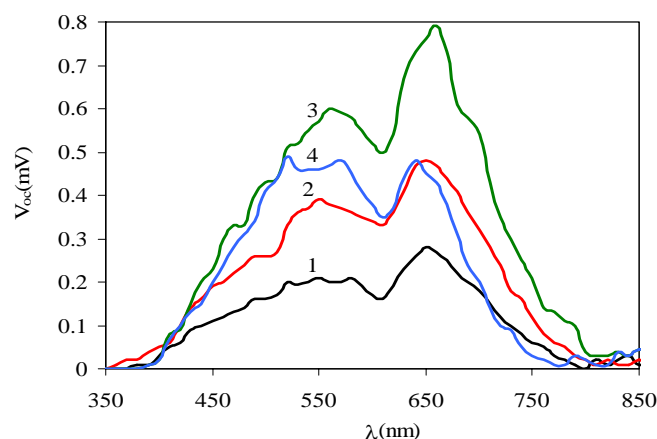


Fig 7. The spectral distribution of photosensitivity of Cu/CdS structure (1) before and after electrodiffusion for (2) 2, (3) 4 and (4) 6 min at 25°C (“-” on Cu).

Decrease of photosensitivity of Cu/CdS structure on accelerating action (for positive Cu ions) of applied electric field can be explained by the fast penetration of Cu^+ ions into CdS film accompanied by decrease of copper concentration at Cu/CdS interface. Applying the retarding electric field to Cu/CdS structure, on the one hand, prevents to penetration of Cu^+ ions inside of CdS film and the others hand, assists the out-electrodiffusion of S^{2-} ions to interface, accompanied by formation of Cu-S phases.

- [1] B.A.Smith, D.M.Water, A.E. Foulhaber, M.A. Kreger, T.W.Roberti, J.Z. Zhang, J. Sol-Gel. Sci. Technol. 9 (1997)125.
- [2] S. Keitoku, H. Izumu, H. Osono, M. Ohto, Japan J. Appl. Phys.34 (1995) L138.
- [3] B. Ulrich, H. Ezumi, S. Keitoku, T. Kobayashi, Mater.Sci.37(1995) 117.
- [4] H. Wolf, F. Wagner, T. Wichert, Physica B, 340-342 (2003) 275.
- [5] T.D.Dzhafarov, M. Altunbas, A.I.Kopya, V. Novruzov, E. Bacaksiz, J. Phys.D: Appl.Phys. 32 (1999)L125.
- [6] Y. Kashiwaba, T. Komatsu, M. Nishikawa, Y. Ishikawa, K. Segawa, Y. Hayasi, Thin Sol. Films, 408 (2002) 43.

RAMAN SPECTRA AND PHOTOLUMINESCENCE OF POLYCRYSTALLINE $\text{CaGa}_2\text{S}_4\text{:Tb}^{3+}$ COMPOUND

E.F.GAMBAROV

Institute of Physics Azerbaijan Academy of Sciences,

H. Javid av. 33, Baku, 370143, Azerbaijan

Raman and photoluminescence studies of CaGa_2S_4 compound was performed. The orthorhombic thiogallate $\text{CaGa}_2\text{S}_4\text{:Tb}^{3+}$ exhibits phonon energies: 280 cm^{-1} ($\sim 35\text{ meV}$) and 360 cm^{-1} ($\sim 45\text{ meV}$) for the most intense vibration modes. Factor group model predicts that the total number of Raman-active phonons is 84 for this structure.

It is shown that the excitation spectra contains wide intense band (max $\sim 320\text{ nm}$) and emission process of $\text{CaGa}_2\text{S}_4\text{:Tb}^{3+}$ connected with radiative ($^5\text{D}_4 \rightarrow ^7\text{F}_6$, $^5\text{D}_4 \rightarrow ^7\text{F}_5$, $^5\text{D}_4 \rightarrow ^7\text{F}_4$, $^5\text{D}_4 \rightarrow ^7\text{F}_3$) energy transitions of Tb^{3+} ions.

Decay characterisation of intensive maximum (545 nm) shows that the lifetime of Tb^{3+} ions is 2.7 ns (fast decay) and $615\text{ }\mu\text{s}$ (long decay).

1. Introduction

Ternary compounds of general formula $\text{M}^{\text{II}}\text{M}^{\text{III}}_2(\text{S,Se})_4$ (where M^{II} and M^{III} are respectively divalent and trivalent cations) form an extensive class of semiconductors and present luminescent properties when doped with rare earth elements. Photoluminescence and cathodoluminescence properties of thiogallate compounds doped with rare earth activators have been studied since the seventies [1-5]. The Eu^{2+} - and Ce^{3+} doped CaGa_2S_4 and SrGa_2S_4 compounds are well known respectively as efficient green and blue phosphors with excellent colour coordinates [1]. They have been claimed as promising candidates for full-colour Thin Film Electroluminescence (TFEL) displays [6] and Field Emission Display (FED) applications [7]. The aim of this work is to clarify the origins of the vibration modes in the chalcogallate based phosphors in order to increase the knowledge about the lattice dynamical properties that influence the luminescence efficiency. Indeed, among the non-radiative transition mechanisms leading to a thermal relaxation of the luminescent centre, a multiphonon process is often observed between 4f excited levels of rare-earth ions. It involves mainly the high-energy optical phonons. The non-radiative multiphonon transition probability is increasing with the frequency increase of the high-energy phonons of the lattice. In the case of ElectroLuminescent (EL) materials, the most frequent scattering event under high electric field is the emission of optical phonons and the cooling of "hot electrons" is dominated by the coupling to the high-frequency modes. The scattering rate is lower for EL phosphors presenting low phonon energies. For CathodoLuminescent (CL) materials the rate of phonon energy loss is controlled by the phonons with highest energy and the CL efficiency of the phosphors decreases with increasing phonon energy [8]. This work is also an opportunity to collect spectra of powders $\text{CaGa}_2\text{S}_4\text{:Tb}^{3+}$ that will be used as references to study by Raman spectroscopy and photoluminescence the quality of thin films prepared for device applications.

2. Samples and experimental details

CaGa_2S_4 compound was obtained from an intimate mixture of CaS and Ga_2S_3 in a single zone furnace in quartz ampoules at 1200°C . The good crystalline properties of the powders were showed by XRD measurements. Activation by Tb (2 atom %) was realised using TbF_3 doping during the synthesis process.

The samples were excited by a pulsed nitrogen laser (Laser Photonics LN 1000, 1.4 mJ energy per pulse, pulse width 0.6 ns). The emitted light from the sample, collected by an optical fiber located at 10 mm perpendicular to the surface, was analysed with a Jobin-Yvon spectrometer HR460 and detector for visible range.

The decay curve was analyzed with a Jobin-Yvon HR360 monochromator coupled with: - a PM Hamamatsu R5600U and a scope Tektronix TDS 784A with a time constant of the order of 2 ns for the fast decay time; - a PM Hamamatsu R928 and a scope Nicolet 400 with a time constant of the order of 10 ns for the longer decay time. Stokes and anti-Stokes spectra were recorded between -500 cm^{-1} and $+500\text{ cm}^{-1}$. Line positions are determined by calculating the arithmetic average of both Stokes and anti-Stokes values. Raman scattering spectra of CaGa_2S_4 were measured by a Jobin-Yvon U1000 spectrometer with a Kr Spectrophysics laser and a photomultiplier counter at room temperature in back scattering configuration, with a laser excitation wavelength of $\lambda = 676.4\text{ nm}$ and a laser power of 140 mW .

3. Results and discussion

3.1. Normal vibration modes

Stokes spectrum of the polycrystalline CaGa_2S_4 is given from 20 cm^{-1} to 500 cm^{-1} in fig.2. Each line in the Stokes part of the spectrum can be associated to an anti-stokes line positioned symmetrically with respect to the laser line frequency.

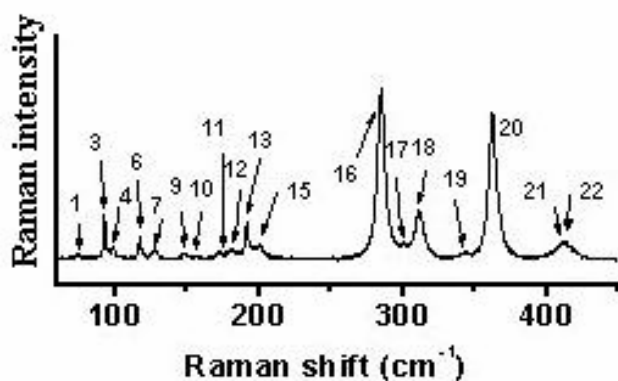


Fig.1. Raman spectra of polycrystalline CaGa_2S_4

The Stokes spectrum consists of 18 vibration lines positioned between $\omega=74.4 \text{ cm}^{-1}$ and $\omega=413 \text{ cm}^{-1}$ listed in table. In spectra the Raman vibration lines are divided into two groups separated by a domain without Raman frequencies between 200 and 275 cm^{-1} . Two intense vibration lines dominate the (Fig.1.) Raman spectra of polycrystalline CaGa_2S_4 $284.8\text{-}361.8 \text{ cm}^{-1}$.

Table.

X-Ray Diffraction data and Raman frequencies of polycrystalline $\text{CaGa}_2\text{S}_4\text{:Tb}^{3+}$

h	K	L	D(Å)	Raman frequencies(cm^{-1})
0	4	0	5.083	74.7
4	0	0		92.3
				98.3
2	2	2	4.624	117.2
				127.2
4	2	2	3.635	148.6
				156.5
0	6	2	2.934	171.8
				180.8
2	6	2	2.825	191.7
6	2	2		199.8
				284.8
0	8	0	2.533	300.8
8	0	0		311.4
2	4	4		342.5
				361.8
4	4	4	2.300	408.0
				413.0
4	8	0	2.251	
8	4	0		
5	7	5	1.682	
7	5	5		
3	9	5	1.593	
9	3	5		
12	2	2		

The CaGa_2S_4 compounds of the type $\text{M}^{\text{II}}\text{Ga}_2\text{S}_4$ (where $\text{M}^{\text{II}} = \text{Sr, Eu, Pb, Ca, Yb}$) belong to the orthorhombic crystal class with the space group $\text{D}_{2h}^{24} (\text{F}_{dd})$. There are 32 formula-mass units per unit cell ($z=32$) and therefore 56 atoms in a primitive cell: 8 M^{II} , 16 Ga, 32 S. According to our XRD data and [1,9] the M^{II} atoms occupy square anti-prismatic sites formed by eight sulphur atoms (fig.2) (symmetry group: D_{4d}).

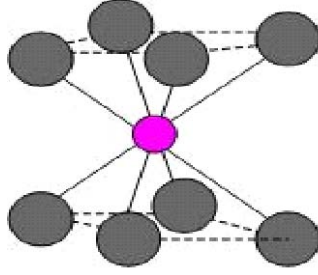


Fig.2. Schematic illustration of the local environment around one of the Ca ions in CaGa_2S_4 phosphors. The Ca ion occupies square antiprismatic sites (eightfold coordinated surrounded by S^{2-} ions).

Gallium atoms are tetrahedrally coordinated to four sulphur or atoms forming GaS_4 units (symmetry group: T_d) and the sulphur atoms are at the centre of deformed $\text{M}^{\text{II}}_2\text{Ga}_2$ tetrahedrons forming $\text{SM}^{\text{II}}_2\text{Ga}_2$ units.

The factor-group analysis [10] shows that vibration modes can be classified as $\Gamma_v = 19 A_g + 21 B_{1g} + 22 B_{2g} + 22 B_{3g} + 19 A_u + 20 B_{1u} + 21 B_{2u} + 21 B_{3u}$. According to the symmetry rules, the A_g , B_{1g} , B_{2g} and B_{3g} modes are Raman active. Thus the factor group method predicts that the total number of Raman-active phonons is 84 for this structure. We observe the vibrations between Ga and S atoms but also those concerning the S neighbours of Ca or Ga atoms that move together along the anion-cation direction. The vibrations of S around Ca can be described in the CaS_8 molecular model: the Raman-active modes have the A_1 , E_2 and E_3 symmetry in the D_{4d} group and their frequencies are independent of the Ca mass [11]. The vibrations of Ga-S bindings can be described in the GaS_4 molecular model in the T_d symmetry.

The fact that the Ca mass has very slight influence on the Raman spectrum excludes the possibility of the SGa_2Ca_2 vibrating units. The interpretation of the spectrum in terms of vibrations of isolated groups seems to provide an adequate first approximation because the binding energy of the Ga-S bonds is significantly higher than that of the Ca-S bonds in CaGa_2S_4 compound. Thus the GaS_4 model seems to be more adequate than the CaS_8 model to interpret the CaGa_2S_4 Raman spectra. So we can formally consider the structure as consisting of isolated ions Ca and isolated GaS_4 . The model of isolated vibrating GaS_4 and isolated Ca subunits is in good agreement with the fact that no mass effect of Ca atoms is observed.

We propose to investigate the Raman vibrations of Ga-S bindings in respect with Ga_2S_3 Raman spectrum because the vibrations of Ga_2S_3 have been also described in the GaS_4 molecular model in the T_d symmetry [12]. By analogy with the assignment of Ga_2S_3 vibrations, vibration lines of CaGa_2S_4 compound above 270 cm^{-1} are assigned to internal vibration modes due to stretching vibrations of S-S and Ga-S in the tetrahedral GaS_4 units. Among those located at frequencies lower than 200 cm^{-1} some may be due to bending vibrations of the GaS_4 tetrahedral units and others may correspond to external vibration modes issued from translation vibrations of molecular subunits (lattice modes)[13,14].

3.2 Luminescent properties

Fig. 3a and 3b show the excitation and emission spectra of the Tb^{3+} ion incorporated in CaGa_2S_4 . In addition to the band below 290 nm which corresponds to an excitation via the host lattice, excitation specter contains an intense band.

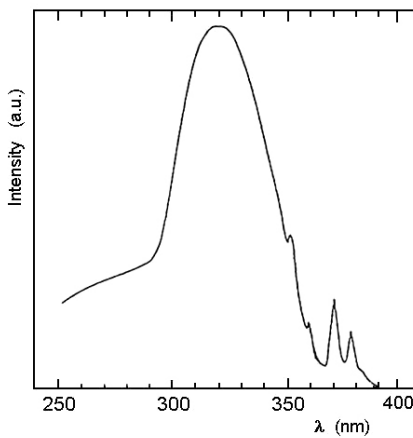


Fig.3a. Excitation spectra of $\text{CaGa}_2\text{S}_4:\text{Tb}^{3+}$ at 300 K.(Excitation of the $^5\text{D}_4 \rightarrow ^7\text{F}_5$ emission lines.)

For excitation into this band $\text{CaGa}_2\text{S}_4:\text{Tb}^{3+}$ shows an intense visible emission at 300K. The probability of non-radiative transitions between $4f^n$ levels is dropped owing to the low phonon energies. Because of the large energy gap between the $^5\text{D}_4$ and $^7\text{F}_0$

(see fig.4) levels of Tb^{3+} , multiphonon de-excitation processes from the 5D_4 level are negligible. The most intense radiative transition originating this level, $^5D_4 \rightarrow ^7F_5$, lies in the green, but because of the transitions to the other components ($^5D_4 \rightarrow ^7F_6$, $^5D_4 \rightarrow ^7F_4$, $^5D_4 \rightarrow ^7F_3$) of the 7F_J multiplet, the color purity ($x=0.372$, $y=0.524$, fig.7) is unsatisfactory.

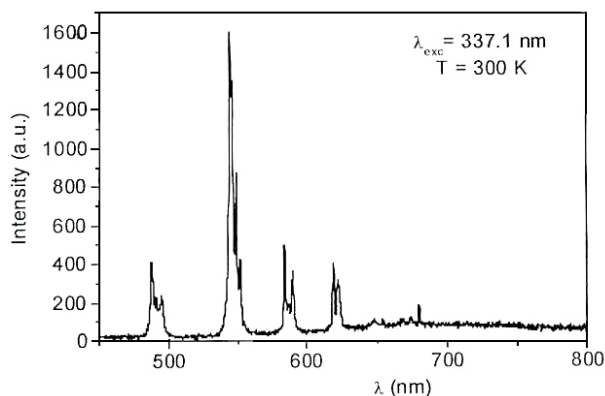


Fig.3b. Emission spectrum of the $CaGa_2S_4:Tb^{3+}$ at 300 K. (Excitation in the f→d band; $\lambda_{exc}=337.1$ nm.)

However the lowest-energy f-d transitions of the latter are spin forbidden, so the first intense bands Tb^{3+} ion lie at close wavelengths. The charge transfer and f-d bands lie at energies higher than that of the absorption edge of the host lattices. Among the non-radiative transition mechanisms leading to a thermal relaxation of the luminescent center a multiphonon process is often observed between 4f excited levels of rare-earth ions.

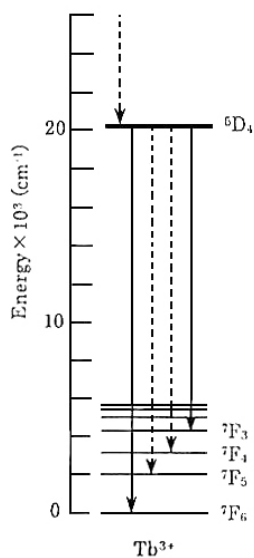


Fig.4. Diagram of energy transfer Tb^{3+} ion.

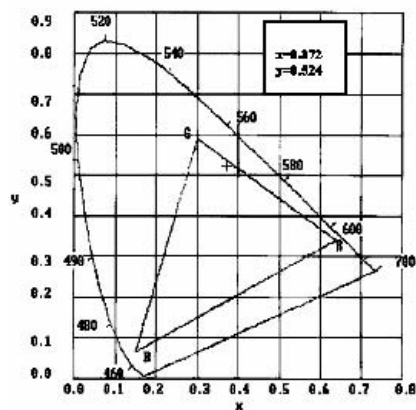


Fig.5. Color coordinates for $CaGa_2S_4:Tb^{3+}$ crystal. (R, G, B: CRT coordinates).

The non-radiative multiphonon transition probability is dependent on the energy difference between the electronic states ΔE and n , the number of phonons necessary to fill the energy gap, i.e. $\Delta E = n \hbar \omega$.

3.3. Decays

As all the main transitions observed come from the same $^5\text{D}_4$ excited level, we analyzed only the decay for the most intense transition ($^5\text{D}_4 \rightarrow ^7\text{F}_5$) at 545 nm.

The fig.6a represents the fast decay at $\lambda_{\text{anal}} = 545$ nm. This fast decay must come from the broad band observed on the emission spectrum under $\lambda_{\text{exc}} = 337.1$ nm (Fig.3b).

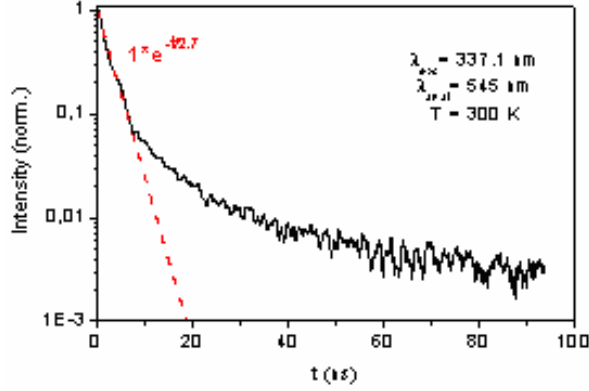


Fig 6a. Decay curve under $\lambda_{\text{exc}} = 337.1$ nm. The dashed line represents the decay time of 2.7 ns

The fig.6b represents the long decay at $\lambda_{\text{anal}} = 545$ nm. We made a fitting of the exponential part of this decay with a lifetime of 615 μs (fig.6b). This exponential part of 615 μs corresponds to the intrinsic lifetime of Tb^{3+} . At short time, the decay presents a non exponential part due to an energy transfer mechanism with nonradiative transitions and a loss of energy.

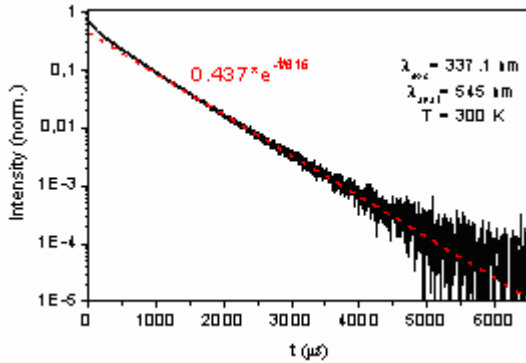


Fig.6b. Decay curve under $\lambda_{\text{exc}} = 337.1$ nm. The dashed curve represents the simulation of two exponential decays of 615 μs and 271 μs .

4. Conclusion

The Raman study of polycrystalline $\text{CaGa}_2\text{S}_4:\text{Tb}^{3+}$ compounds was performed to clarify the origins of the Raman vibrations. We observe that no vibration involving directly the divalent cation Ca is present in the Raman spectra since the mass of the Ca has very little influence on the vibration frequencies. The Raman vibrations depend essentially on the M^{II} cation size. Since the effect of the M^{II} cation on the $\text{M}^{\text{II}}\text{Ga}_2\text{S}_4$ Raman spectra is very slight we conclude that the orthorhombic thiogallates present nearly the same phonon energies whatever the M^{II} cation..

The non-radiative multiphonon transition probability is given by:

$$W_{NR}(\Delta E) = W_{NR}(0) \exp(-\alpha \Delta E / \hbar \omega).$$

The non-radiative multiphonon transition probability is increasing with the frequency increase of the high-energy phonons of the lattice [15]. In the case of EL materials, the energy exchange between electron and phonon is described by the electron-phonon interaction Hamiltonian. Under high electric field the most frequent scattering event is the emission of optical phonons and the energy relaxation of electrons is dominated by the coupling to the high-frequency modes. Scattering rate is lower for EL phosphor lattice presenting low high-frequency phonons [15]. For CL materials the rate of phonon energy loss is controlled by the highest energy phonons and the CL efficiency of the phosphors decreases with increasing phonon energy [16]. Several conclusions can be drawn from Raman vibration spectra of CaGa_2S_4 compound. The optical high-frequency phonons of crystal we have to consider correspond to the vibration modes dominating the high-frequency domain, i.e. at about 35 and 45 meV.

References

- [1] T.E.Peters and J.A.Baglio, J. Electrochem. Soc., 119, p. 230 (1972).
 - [2] P.C.Donohue and J.E.Hanlon, J.Electrochem.Soc., 121, p.137 (1974).
 - [3] W.A.Barrow, R.C.Coovert, E.Dickey, C.N.King, C.Laakso, S.S.Sun, R.T.Tuenge, R.Wentross, J. Kane, SID , p.761 (1993).
 - [4] A.N. Georgobiani, B.G.Tagiev, O.B.Tagiev, B.M. Izzatov, R.B. Jabbarov, Cryst. Res.Technol., 31, S 849-852 (1996).
 - [5] S.Iida, T.Matsumoto, N.Mamedov, G. An, Y. Maruyama, A. Bairamov, B. Tagiev, O.Tagiev, R. Jabbarov, Jpn.J.Appl.Phys. Vol.36, pp.L857-L859 (1997).
 - [6] Benalloul P., Barthou C. and Benoit J., J. of Alloys and Compounds, 275-277, p.709 (1998).
 - [7] I.Ronot-Limousin, A.Garcia, C.Foussier, C.Barthou, P.Benalloul and J.Benoit, J.Electrochem. Soc., 144, p.687 (1997)
 - [8] Robbins D J 1980 *J. Electrochem. Soc.* **127** 2694
 - [9] B.Eisenmann, M.Jakowski, W.Klee, H.Schafer, Revue de Chimie Minerale 20, 255 (1983).
 - [10] R.S.Halford, Journal of Chemical Physics, 14 (1), p.8 (1946).
 - [11] H.L.Schlafer and H.F.Wasgesstian, Theoret. Chim.Acta 1 369 (1963).
 - [12] G. Lucazeau and J.Leroy, Spectrochimica acta, 34A, p.29 (1978).
 - [13] N.N.Syrbu, V.E.L'vin, I.B.Zadnpru, V.M.Golovei, Sov.Phys.Semicond., 25(10), p.255 (1983).
 - [14] S.Barnier, M.Guittard and J.Flahaut, Mat. Res. Bull., 15, p.689 (1980).
 - [15] Phosphor Handbook, CRC press (1999).
 - [16] D.J.Robbins , J. Electrochem. Soc., 127, p.2694 (1980).
-

Simplex presentation of the real world in the quantum mechanics

Isaeva E.A.

Institute of Physics of Azerbaijan National Academy of Sciences, 33H.Javid av.,
Baku, Az-1143, e-mail: elmira @physics.ab.az

It is known that superposition of states of states taking place in the quantum world can occur in the macroworld too due to the mechanism of intensification. "Schrodinger cat" is a fact of such intensification. It is known that in an open system the "Schrodinger cat" paradox is explained by the decoherence phenomenon but in a close system it is explained by the many-world interpretation of quantum mechanics Everett-Wheeler. The quantum real world is presented as a certain complex multi-spatial geometric figure and what we call the "classical" world is one of face of this figure. In the paper it has shown that the this complex figure constitutes the simplex notion in the functional analysis. It has been shown that such an interpretation of mechanics enables one to obtain the non-uniform wave equation, and Schrodinger equation is the uniform equation of this equation.

1. Simplex.

From the functional analysis [1] it is known that the sequence of points $\{x_{n+1}\}$ are in general provisions when these points are not in $(n-1)$ -dimensional space. If these points are connected with each other, they form n -dimensional simplex. For example, one point – zero-dimensional simplex, the piece – one-dimensional one, the triangle – two-dimensional one, the tetrahedral – three-dimensional simplex, etc. (Table 1).

Table 1

THE SIMPLEX					
0-dimensional	1-dimensional	2-dimensional	3-dimensional	4-dimensional	etc.
Point	Piece	Triangle	Tetrahedral	It isn't possible to imagine	
THE NUMBER OF FACES OF SIMPLEX $C_n^K = \frac{n!}{K!(n-K)!}$					
1	2	6	14	30	

It is known that if x_1, x_2, \dots, x_n points are in the general provisions, any $(k+1)$ points of them, where $k < n$, are also in the general provisions and form k -dimensional simplex named k -dimensional face of the given simplex. For example, the three-dimensional simplex – the tetrahedral – has 4 two-dimensional faces (triangles), 6 one-dimensional faces (pieces) and 4 zero-dimensional faces (points). In total the sum of the faces equals 14. Let's note that a cube are not the simplex because for creation of the simplex from the 8 points it is necessary all these points are in the 6-dimensional space. Let's consider the 4-dimensional simplex. Here the number of the points are 5. All of them should not be located in the three-dimensional space. It is impossible to imagine such a figure. This 4-dimensional simplex has 30 faces: 5 three-dimensional faces (tetrahedron), 10 two-dimensional faces (triangles), 10 one-dimensional faces (pieces) and 5 zero-dimensional faces (points). Thus the formed from more than four points simplex cannot be presented in our three-dimensional space. It is the complex volumetric figure.

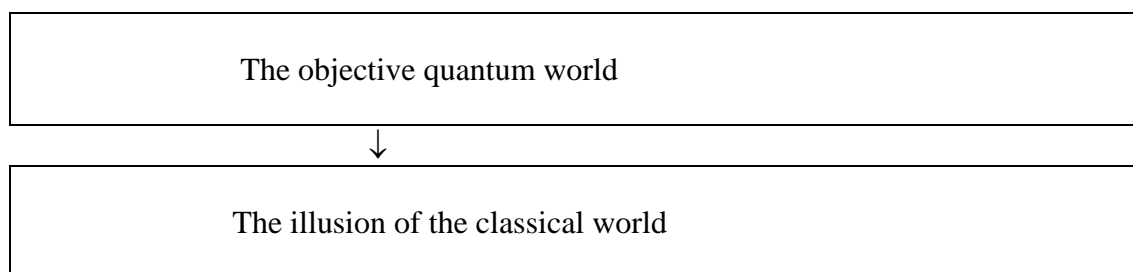
The simplex in n -dimensional space is the minimal convex set, i.e. all points of a kind $\sum a_n x_n$, where $\sum a_n = 1$ belong to this simplex. From the theory of probabilities [2] it is known that the probability of event is closely connected to random and average value. The belonging to a simplex points are the set of all average value if we count that the tops of the simplex $\{x_n\}$ are the random value and a_n are probabilities of x_n . In this point of view the consideration of a simplex is expedient. Also from the point of view of

A.Einstein who wrote [4]: "... We should refuse from the description of the nuclear phenomena as phenomena in the space and the time. We should go away from old mechanical review. The quantum physics formulates the laws which manager sets but not individuals. It is described the probabilities and not the properties. It is formed the laws opening the future of systems but not the laws managing the changes of probabilities in the time and concerning to large sets of individuals."

2. Superposition in quantum mechanics.

It is known that by using imagination experiment "shrodinger cat" [5] it is proved that the superposition of two microstate (atom decayed and atom didn't decay) transform in the superposition of two macrostate (cat is alive and cat is dead). If in the open system this paradox is solved by the "decoherence" [12] than in the close system that is solved by the theory in which the consciousness is included. One of such theory is many- word interpretation of quantum mechanics of Evverett-Willer [9,10].

The author of paper Menskii M.B. [6] the quantum world symbolically represented as some complex volumetric figure and what we name "a classical reality" is only one of projections of this figure. He presents the following interesting scheme.



In this scheme the quantum world is objective because it does not depend on consciousness of the observer. In this case the system is close, i.e. our consciousness inside volumetric figure. The objective real world exists in the form of the parallel worlds, each of which is not realer than the rest. In scheme the classical world is illusion because it depend on consciousness of the observer. In this case the system is open, i.e. our consciousness outside volumetric figure. Being outside the volumetric figure our consciousness is interacting with the surrounding world and in consequence the decoherence take place. Picture of the world seen by us is the result of the coupling of wave functions of our consciousness and surrounding world [13]. We always see only one of the parallel worlds, but other worlds do not cease to exist. Therefore the classical world is only one of many variants and it arises in our consciousness. From the beginning of existence of the quantum mechanics the famous scientists Pauli [11], Wigner[12], Shredinger [5] said about the necessity of inclusion of the observer's consciousness in the quantum theory of measurements. Wigner paper contains more stronger statement: the consciousness not only should be included in the theory of measurements but the consciousness may influence on the reality. As M. Plank wrote:

"... We are compelled to recognise that behind the sensual world there is a second, real world, which exists independently from the man, the world which we cannot directly study but which we comprehend through the sensual world, known signs which inform us just as if we could consider the subject interesting for us through glasses, optical properties of which are completely unknown for us."

3. Construction of the simplex

Apparently the above mentioned complex volumetric figure is the simplex. Let's imagine that on two-co-ordinate plane xoy, on an axis x the number of dead "Schrodinger cats" and on an axis y the number of alive cats are marked. Let's suppose in experiment with 100 "Schrodinger cats" 80 cats are alive and 20 cats are dead. It is may be different numbers alive and dead cats from the total number all cats. But we consider numbers 100, 80, 20. In this case the probabilities are approximately equal 0,8

(alive cat) and 0,2(dead cat). The points 20 and 80 are two tops of the simplex. In the other case or at other moment of time with 100 "Schrodinger cats " there are 60 alive cats and 40 dead cats. These points we put in other system of coordinates x^1oy^1 in 3 dimensional space. If we connect given 4 points we receive three-dimensional simplex - tetrahedral. (Fig.1)

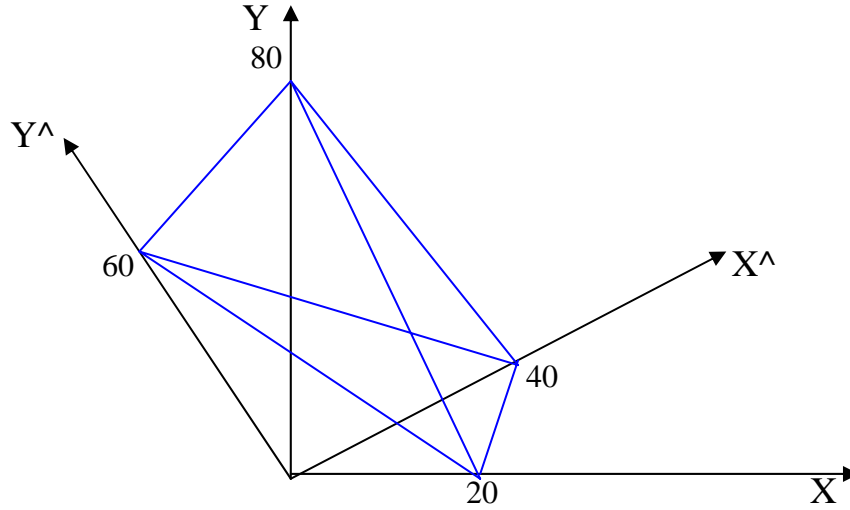


Fig.1

If we would consider a lot of points we shall receive the complex volumetric figure – n-dimensional simplex. Tetrahedral is the final simplex that we can represent in our three-dimensional space. The simplex of higher order have faces taken from these tetrahedron. The ribs of the tetrahedral indicate to various probabilities. For example, the rib linking the points 80 alive cats and 40 dead cats point out at $80/120=2/3$ of probability of case in that cat is alive. In the case 60 alive and 20 dead cats the rib of the simplex shows the probability that is equal $60/80=3/4$ and etc. The rib linking the points 20 dead and 40 dead cat and the rib linking the points 80 alive and 60 alive cats point out to probability of 1. Let's consider the faces of the simplex. In the case of alive cat on one of them the probability changes from $2/3$ to 0,8 ; on another face – from $3/4$ to 0,6; on third - from $2/3$ up to 0,6; on fourth – from $3/4$ to 0,8 etc.

4.The directing cosines and the probabilities.

From the quantum mechanics [7] it is known the following: Let's assume that e is the energy eigenvalue operator \hat{E} .

$$e = \sum C_k e_k$$

where e_k are eigenvectors (the basis),

C_k are coefficients and $\sum C_k e_k = 1$.

$$(e_k, e) = |e_k| * |e| * \cos \alpha$$

where $\cos^2 \alpha$ is the corresponding to e_k part of e .

From the physical point of view this means that if we measure the energy of the identical systems that are in the e state then the part of the number of E_k energy measurements equals $\cos\alpha$ (more exactly it equals $|\cos\alpha|$). Therefore $|\cos\alpha|$ is called directing cosine and it is the probability that the system have E_k energy in the state e .

It is known that for many operators $\cos\alpha$ is the complex number

$$\cos\alpha = x+iy = Ae^{i\beta}$$

where $A=\text{const}$ is the length of the vector $\cos\alpha$.

Then $\cos^2\alpha = x^2 + y^2$.

Using the mentioned simplex, the above can be imagined and presented as the following.

Let's assume that e_1 and e_2 are eigenvectors.

E_1 and E_2 are the eigenvalue energy E (E_1 is energy of decayed atom, E_2 is energy of normal atom).

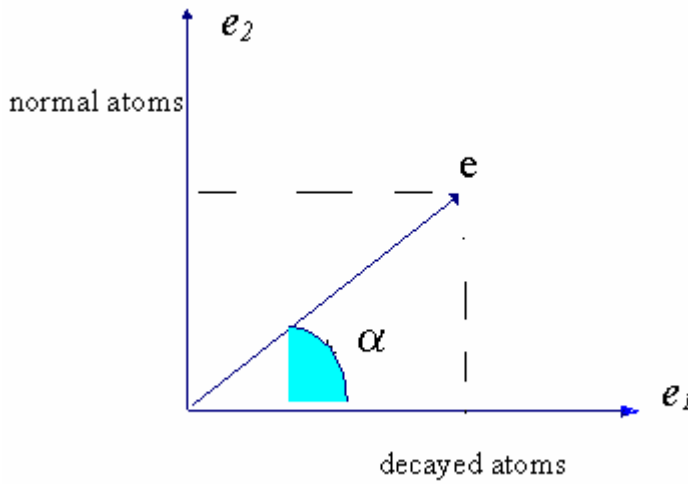


Fig.2

The information about an amounts of atoms with energy E_1 and E_2 are given us on the axis e_1 , e_2 , respectively.

The exact information about the amounts of normal or decayed atoms are presented on the e_1 and e_2 axes. The statement of physical system and uncertainty of information are presented by vector e and angle α that is formed by rotation of e on the plane e_1oe_2 , respectively (fig.2). Note that in [14] paper the statements of physical system are pictured by unit rays. The rotation of unit vector was considered by Orlov [8] and called by him “the intention” of the quantum system. Thus angle α is the uncertainty measure.

The vector e is non-eigenvector and one may be written in the form superposition of e_1 and e_2 .

$$e = C_1e_1 + C_2e_2$$

The projections of e on e_1 and e_2 axes are the number of decayed and normal atoms, respectively and $\cos\alpha$ is the part of decayed atoms and $\sin\alpha$ ($\sin\alpha=\cos(90-\alpha)$) is part of normal of total number of all atoms. Let's assume that e_1 is a real axis and e_2 is a imaginary one of a complex number. When constricting the simplex let's consider the case which we used at constricting the simplex: from 100 “schrodinger cats” ($c=a+b=100$) 80 cats are alive ($a=80$) and 20 cats are dead ($b=20$) (fig.3). It is clear that probabilities are equal to:

$$p_1 = \frac{a}{a+b} \quad (\text{cat is alive}), \quad p_2 = \frac{b}{a+b} \quad (\text{cat is dead}).$$

It is the main point that $p_1 + p_2 = 1$.

But it is possible take also other measure p^* for which the equality $\sum p^* = 1$ will be held true.

It is known that $\sin^2 \alpha + \cos^2 \alpha = 1$.

Assume $\cos^2 \alpha = p_1^*$ and $\sin^2 \alpha = p_2^*$.

Here p_1^* and p_2^* are other measures which we will call "the new probabilities". From fig.3 it is clear that

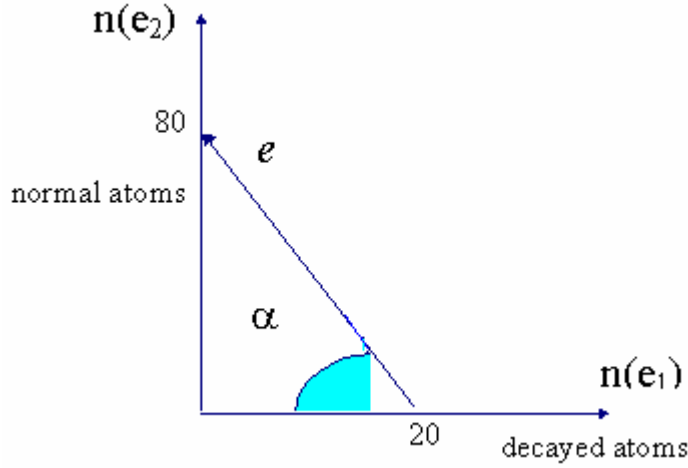


Fig.2

$$p_1^* = \frac{a^2}{a^2 + b^2} = \frac{a}{a+ib} \times \frac{a}{a-ib} \quad (\text{cat is alive})$$

$$p_2^* = \frac{b^2}{a^2 + b^2} = \frac{ib}{a+ib} \times \frac{-ib}{a-ib} \quad (\text{cat is dead}).$$

In quantum mechanics the wave function ψ is interpreted as the following. The square of wave function amplitude $|\psi|^2$ is the probability p that the particle is in state E . We suppose that in our consideration $|\psi|^2$ isn't the probability p , but that is "the new probability p^* ". Thus:

$$|\psi|_1^2 = \frac{a}{a+ib} \times \frac{a}{a-ib}. \text{ Then } \psi_1 = \frac{a}{a+ib} = \cos \alpha e^{-i\alpha} \text{ and } \psi_1^* = \frac{a}{a-ib} = \cos \alpha e^{i\alpha}$$

$$|\psi|_2^2 = \frac{bi}{a+bi} \times \frac{-bi}{a-bi}. \text{ Then } \psi_2 = \frac{bi}{a+bi} = \sin \alpha e^{-i\alpha} \text{ and } \psi_2^* = \frac{-bi}{a-bi} = -\sin \alpha e^{i\alpha}$$

So we suppose that in quantum mechanics the directional cosines can be presented not in the form $\cos \alpha = \frac{a}{a+ib}$, but as $\cos \alpha = \frac{a}{a+ib}$. Taking $\cos \alpha = \frac{a}{a+ib}$ and $\cos^2 \alpha = \frac{a^2}{a^2 + b^2}$, we can't see that $\cos^2 \alpha$ is

the part of the total amount, on the contrary taking $\cos \alpha = \frac{a}{a+ib}$ it can be seen that $\cos^2 \alpha$ ($\cos^2 \alpha =$

$\frac{a^2}{a^2 + b^2}$) is the part of the total amount. So the rubs of our simplex accordingly point on the different statement of physical system and probabilities.

5. The Schrodinger's equation and new wave equation.

It is known that Schrodinger equation

$$\frac{h^2}{2m} \Delta \psi - E \psi = 0 \quad (1)$$

(the solution of which is $\psi = A e^{-\frac{i}{h}(Et - px)}$) cannot be derived and it was obtained intuitively in order to explain strange properties of the microscopic world. In this paper it has been shown that Schrodinger equation has been derived by using the above mentioned geometrical interpretation of quantum mechanics.

As it was shown in section 3,

$$\psi = \cos \alpha e^{-i\alpha} \quad (2)$$

Then it is easy to derive the following equation: $\Delta' \psi + 4\psi = 2$. Here $\Delta' = \frac{\partial^2}{\partial^2 \alpha}$. However comparing

$\psi = A e^{-\frac{i}{h}(Et - px)}$ with $\psi = \cos \alpha e^{-i\alpha}$ we can write

$$\alpha = \frac{Et - px}{h} \quad (3).$$

In the stationary case $\alpha = \alpha(x)$. Then $\Delta = \frac{\partial^2}{\partial \alpha^2} = \frac{h^2}{p^2} \frac{\partial^2}{\partial x^2}$. But $p^2 = m^2 v^2 = 2m \frac{mv^2}{2} = 2mE$. Therefore

$$\Delta = \frac{\partial^2}{\partial \alpha^2} = \frac{h^2}{2mE} \frac{\partial^2}{\partial x^2}. \text{ Thus } \frac{h^2}{2mE} \frac{\partial^2}{\partial x^2} \psi + 4\psi = 2 \text{ or}$$

$$\frac{h^2}{2m} \Delta \psi + 4 E \psi = 2 \quad (4)$$

In order to solve this non-uniform differential equation we should solve the corresponding uniform equation

$$\frac{h^2}{2m} \Delta \psi + 4 E \psi = 0 \quad (5)$$

which is Schrodinger equation (Eq.1), if 4 factor substitutes for -1. From the theory of differential equations it is known that the general solution of Eq.4 is equal to the solution of Eq.5 plus one partial solution of Eq.4 which, taking into account the expression (3), is in given case

$$\cos \alpha e^{-i\alpha} = \cos \frac{Et - px}{h} \exp(-i \frac{Et - px}{h}). \text{ Thus the general solution of Eq.4 has the form of } \psi = A \exp(-i \frac{Et - px}{h}) + \cos \frac{Et - px}{h} \exp(-i \frac{Et - px}{h}).$$

Reference.

1. Kolmogorov A.N., Fomin S.V. Elements of the theory of functions and functional analysis. Moscow: "Nauka", 1968, 375 p.
2. Tutubalin V.N. The theory of probabilities. Moscow: "Moscow State University", 1972, 230 p.
3. Maks Plank. The picture of the world in modern physics, "Uspekhi Fizicheskikh nauk", 1929, volume 9, N. 4, page 407-436.
4. A. Einstein and L. Infeld. Evolution of Physics, Moscow- Leningrad, 1948, 289p.
5. Шредингер Э. Избранные труды по квантовой механике. М.: Наука, 1977, 356 с.
6. Menskii M.B. The Quantum mechanics, the new experiments, new appendices and old questions. "Uspekhi Fizicheskikh nauk" (UFN-УФН), 170, 6, 2000
7. David Bom. Quantum mechanics. Moscow press. 1965, 320p. (in russian)
8. Orlov Y. F. The wave logic of Consciousness: A Hypothesis, International journal of theoretical Physics, vol.21, №1, 1982, p.37-53
9. Everett H. Quantum Theory and Measurements (Eds. J.A. Wheeler, W.H. Zurek) (Princeton University Press, 1983) 168 p.
10. De Witt B.S., Graham N. The Many-Worlds Interpretation of Quantum mechanics (Princeton, N.J., Princeton University Press, 1973)
11. Laurikainen K.V. Beyond the Atom: the philosophical Thought of Wolfgang Pauli (Berlin: Springer-Verlag, 1988)
11. Wigner E.P. Quantum Theory and Measurements (Eds. J.A. Wheeler, W.H. Zurek) (Princeton University Press, 1983) 168 p.
12. Menskii M.B. The phenomena of decoherence and the theory of quantum measurements. Uspekhi fizicheskikh Nauk, 1988, v.168, p.1017-1035
13. Kadomtsev B.B. Dynamics and information. (Published by Uspekhi fizicheskikh Nauk, Moscow, 1999, 400p.
14. Streater R.F., Wightman A.S. PCT, spin and statistic and all that. (Mathematical and physical series, W.A. Benjamin, INC, New York – Amsterdam, 1964, 250 p.

ROENTGENDOSIMETRIC CHARACTERISTICS OF DETECTORS ON THE BASE OF $\text{TiGaS}_2<\text{Yb}>$ SINGLE CRYSTALS

S.N. Mustafaeva, E.M. Kerimova, P.G. Ismailova, M.M. Asadov

Institute of Physics, Azerbaijan National Academy of Sciences

Baku, AZ-1143, G. Javid av. 33

There have been studied the influence of partial substitution of Ga on Yb in TiGaS_2 single crystals, on roentgendosimetric characteristics of grown single crystals. Analysis of obtained experimental data showed that roentgenconductivity coefficient (K_σ) in all crystals under investigation is regularly decreased as with the rise of irradiation dose (E) as increasing the value of accelerating voltage (V_a) on X-ray tube. As a result of partial substitution $\text{Ga} \rightarrow \text{Yb}$ in TiGaS_2 single crystals K_σ is increased, and roentgen-ampere characteristics ($\Delta I_{E,0} \sim E^\alpha$) tend to linearity ($\alpha=1$) in the range of low intensities of soft (low V_a) roentgen radiation. In the range of comparatively high intensities of harder (high V_a) roentgen radiation $\alpha \rightarrow 0.5$ as for TiGaS_2 , as for $\text{TiGaS}_2<\text{Yb}>$.

TiGaS_2 single crystals are representatives of laminated semiconductors. These crystals are wide-band and high resistive. Dc- and ac- conductivities of TiGaS_2 single crystals were investigated in [1, 2]. In [3], the results of study of γ -radiation influence on ac-conductivity of TiGaS_2 single crystals were described. Of some interest is the study of influence of Ga partial substitution in TiGaS_2 for rare earth elements on their physical properties.

The aim of the present paper is the study of influence of partial substitution of Ga on Yb in TiGaS_2 single crystals, on roentgenconductivity and roentgendosimetric characteristics of these crystals.

Samples of $\text{TiGaS}_2<0.1 \text{ mol.\% Yb}>$ composition have been synthesized by melting of initial high-purity (no less 99.99) components in vacuumed quartz ampoules up to 10^{-3} Pa, and their single crystals have been grown by Bridgeman-Stockbarger method. X-ray analysis showed that $\text{TiGa}_{0.999}\text{Yb}_{0.001}\text{S}_2$ is crystallized in monoclinic structure with elementary cell parameters: $a = 10.776$; $b = 10.776$; $c = 15.646 \text{ \AA}$; $\beta = 100.06^\circ$; $z = 16$; roentgen density $\rho_x = 5.022 \text{ g/cm}^3$. Samples from TiGaS_2 and $\text{TiGaS}_2<\text{Yb}>$ for measurements are obtained by spalling along the C-axis of the natural spall from massive single crystals and have a thickness by $50 \div 100 \text{ }\mu\text{m}$ order. Ohmic contacts of samples are made by In melting. Samples have produced in planar structure so that constant electric field applies along the layers of single crystals, and X-rays were directed along the C-axis of crystals. Distance between the indium contacts was equal to $0.10 \div 0.15 \text{ cm}$ for different samples. Electric conductivity (σ) of obtained samples has been measured at 300 K. Intensity of applied constant electric field is corresponding to ohmic

and quadratic section on volt-ampere characteristics (VAC). For measurements the samples have been placed in screened cell. The ratio of dark resistivities after and prior to Yb-doping amounts to ~ 70 .

Roentgenconductivity and roentgendosimetric characteristic measurements are carried out in low load resistance regime at 300 K. The source of roentgen radiation is the installation of X-ray diffraction analysis (URS-55a) with the tube BSV-2 (Cu). Intensity of roentgen radiation (E) is regulated by measurement with current variation in tube at each given value of accelerating potential (V_a) on it. Absolute values of roentgen radiation dose $E(\text{R/min})$ are measured by crystal dosimeter (DRGZ-02).

Roentgenconductivity coefficients K_σ characterizing roentgensensitivity of investigated crystals are determined as the relative change of conductivity under roentgen radiation a per dose:

$$K_\sigma = \frac{\sigma_E - \sigma_0}{\sigma_0 \cdot E} = \frac{\Delta\sigma_{E,0}}{\sigma_0 \cdot E}, \quad (1)$$

where, σ_0 is conductivity in the absence of roentgen radiation (dark conductivity), σ_E is conductivity under the effect of radiation with the dose intensity $E(\text{R/min})$.

There have been determined values of characteristic coefficients of roentgenconductivity as of the initial single crystal TiGaS_2 as of $\text{TiGaS}_2\text{<0.1 mol.\% Yb>}$ at different values of accelerating voltage (V_a) on the tube and corresponding doses of roentgen radiation.

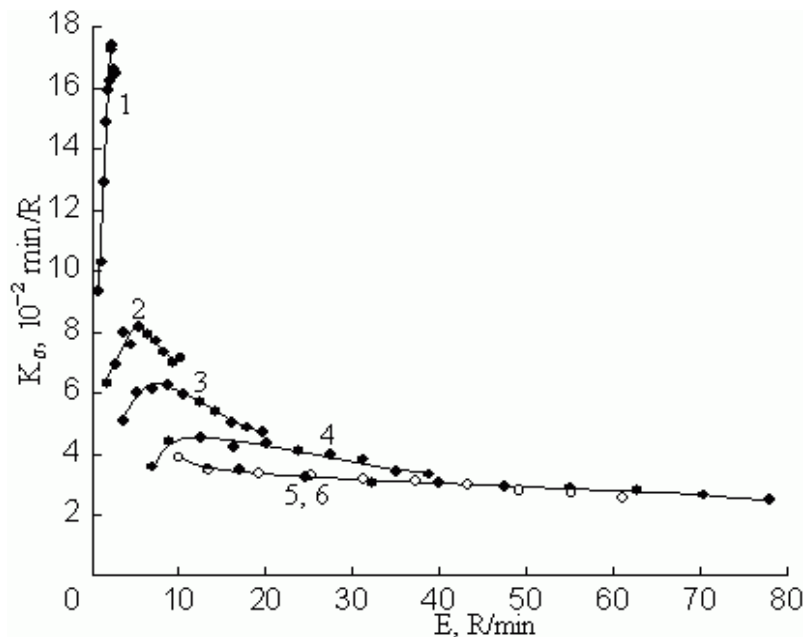


Fig. 1 Dependences of characteristic coefficients of roentgenconductivity on dose intensity for TiGaS_2 single crystal ($F = 80 \text{ V/cm}$) at various values of accelerating voltages: 1 – 25; 2 – 30; 3 – 35; 4 – 40; 5 – 45; 6 – 50 keV and 300 K.

In Fig. 1 there have been presented dependence of K_σ on dose intensity for TiGaS_2 single crystal at 300 K and electric field $F = 80 \text{ V/cm}$ (ohmic section of VAC). Curves 1-6 correspond to various values of accelerating voltage V_a from 25 to 50 keV (effective hardness).

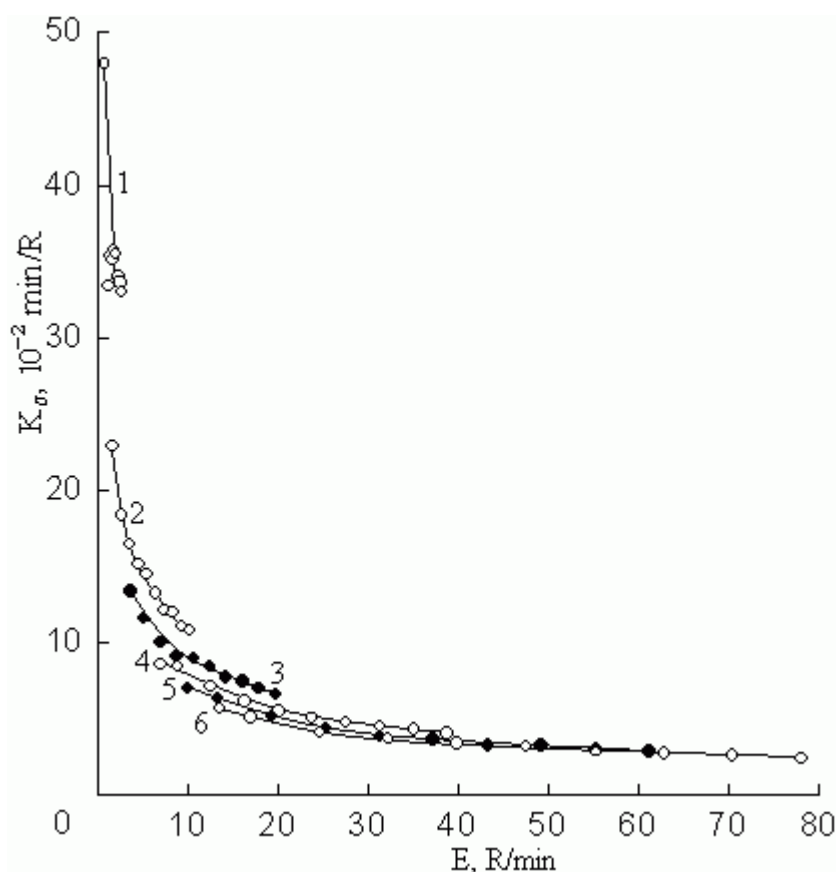


Fig. 2 $K_{\sigma}(E)$ – dependences for $\text{TiGaS}_2\langle\text{Yb}\rangle$ single crystal ($F=70$ V/cm) at various values of V_a : 1 – 25; 2 – 30; 3 – 35; 4 – 40; 5 – 45; 6 – 50 keV ($T = 300$ K)

Fig. 2 shows same dependence $K_{\sigma}(E)$ for $\text{TiGaS}_2\langle\text{Yb}\rangle$ single crystal at $F = 70$ V/cm. It is seen from these figures that roentgensensitivity of TiGaS_2 single crystal changes in interval $0.025 \div 0.174$ min/R, but in $\text{TiGaS}_2\langle\text{Yb}\rangle$ $K_{\sigma} = 0.024 \div 0.480$ min/R, i.e. roengenconductivity coefficient of $\text{TiGaS}_2\langle\text{Yb}\rangle$ crystal is increased comparing with K_{σ} of TiGaS_2 crystal. Analysis of obtained data showed that roengenconductivity coefficient of $\text{TiGaS}_2\langle\text{Yb}\rangle$ crystals are regularly decreased as with the rise of dose as with the increase of values of accelerating voltage V_a on roentgen tube. At $V_a > 30 \div 35$ keV and $E > 10 \div 15$ R/min change of $K_{\sigma}(E, V_a)$ is slight in studied crystals TiGaS_2 and $\text{TiGaS}_2\langle\text{Yb}\rangle$. One of the possible reason of observed regularities is that roengenconductivity in investigated crystals, especially at comparatively low accelerating voltages is predominantly due to radiation absorption in thin layer of crystal. In this case with the rise of radiation intensity there have been started to prevail the mechanism of surface quadratic recombination which leads to observed decrease of roengenconductivity. With the rise of accelerating potential effective hardness is increased owing to penetration depth into crystal is increased, as a result of which there have been taken place predominantly absorption-generation of free roentgen carriers in volume and fraction of incident radiation passing through crystal is increased.

Dependence of K_{σ} on dose intensity was measured also at high electric fields (from quadratic section of VAC). $K_{\sigma}(E)$ -dependence for $\text{TiGaS}_2\langle\text{Yb}\rangle$ single crystal at $F=1.5 \cdot 10^3$ V/cm has been shown in Fig. 3.

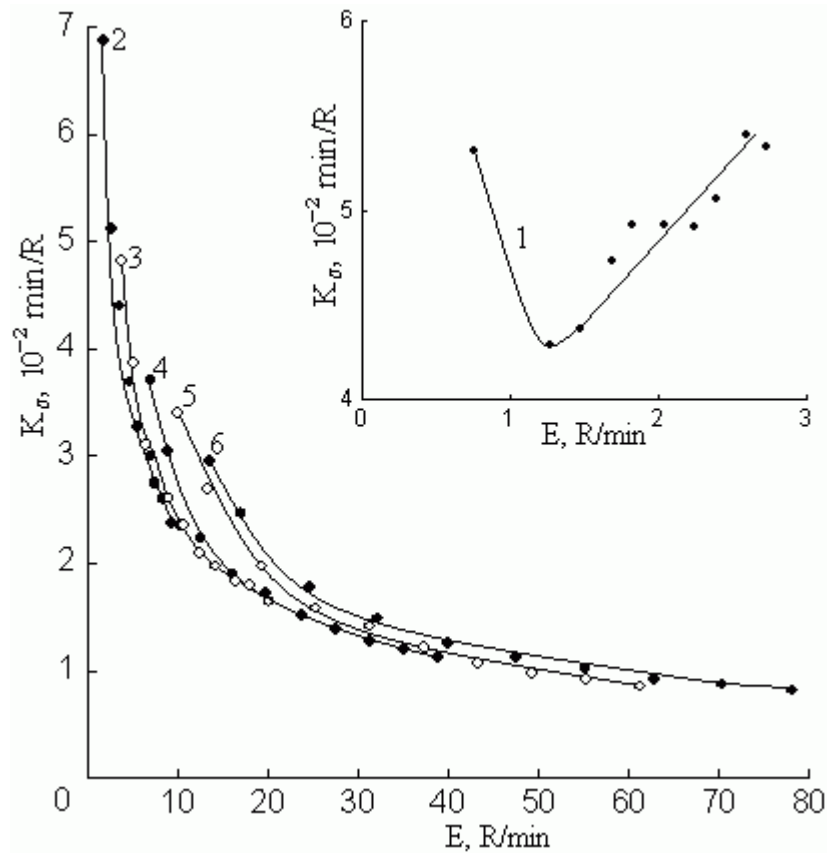


Fig. 3 Dependences of K_σ vs E for $\text{TiGaS}_2\text{<Yb>}$ at $F=1.5 \cdot 10^3$ V/cm and $V_a = 25; 30; 35; 40; 45; 50$ keV for curves 1–6.

Table 1 shows the experimental results of $K_\sigma(E)$ -study obtained for TiGaS_2 single crystal at $F = 300$ V/cm. It is seen from Fig. 3 and Table 1 that the values of K_σ at voltages from quadratic region of VAC are less comparing with K_σ measured at ohmic voltages as for TiGaS_2 as for $\text{TiGaS}_2\text{<Yb>}$ single crystals. This experimental result is evidence of fact that at high electric fields concentration of injected from contact charge carriers is more than concentration of roentgen carriers. In other words in formula (1) dark conductivity σ_0 increased due to injection and as result, K_σ decreased.

We also study roentgen-ampere characteristics of TiGaS_2 and $\text{TiGaS}_2\text{<Yb>}$ single crystals (Fig. 4 and 5), from which it follows that dependence of stationary roentgencurrent on roentgen radiation dose has a ratio character:

$$\Delta I_{E,0} = I_E - I_0 \sim E^\alpha \quad (2)$$

Table 1

Roentgenconductivity coefficients of TiGaS_2 single crystal at supply voltage (working voltage) equal to 40V ($F = 300$ V/cm) and $T = 300$ K.

V_a , keV	E , R/min	K_σ , min/R	V_a , keV	E , R/min	K_σ , min/R
25	0.75	0.067	40	7.00	0.036
	1.26	0.064		8.89	0.033

	1.47	0.068		12.60	0.030
	1.68	0.066		16.38	0.029
	1.82	0.082		20.09	0.029
	2.03	0.089		23.80	0.033
	2.24	0.085		27.58	0.031
	2.38	0.088		31.29	0.031
	2.59	0.093		35.07	0.030
	2.73	0.099		38.78	0.029
30	1.75	0.080	45	10.00	0.025
	2.73	0.073		13.37	0.025
	3.64	0.060		19.32	0.024
	4.62	0.058		25.34	0.027
	5.53	0.052		31.29	0.027
	6.44	0.053		37.24	0.028
	7.42	0.047		43.26	0.028
	8.33	0.047		49.21	0.027
	9.31	0.045		55.23	0.027
	10.22	0.047		61.18	0.026
35	3.75	0.053	50	13.50	0.024
	5.18	0.048		17.01	0.025
	7.00	0.046		24.64	0.025
	8.82	0.042		32.27	0.028
	10.64	0.041		39.90	0.029
	12.46	0.042		47.53	0.030
	14.28	0.043		55.16	0.030
	16.10	0.042		62.79	0.029
	17.92	0.039		70.42	0.029
	19.74	0.038		78.05	0.028

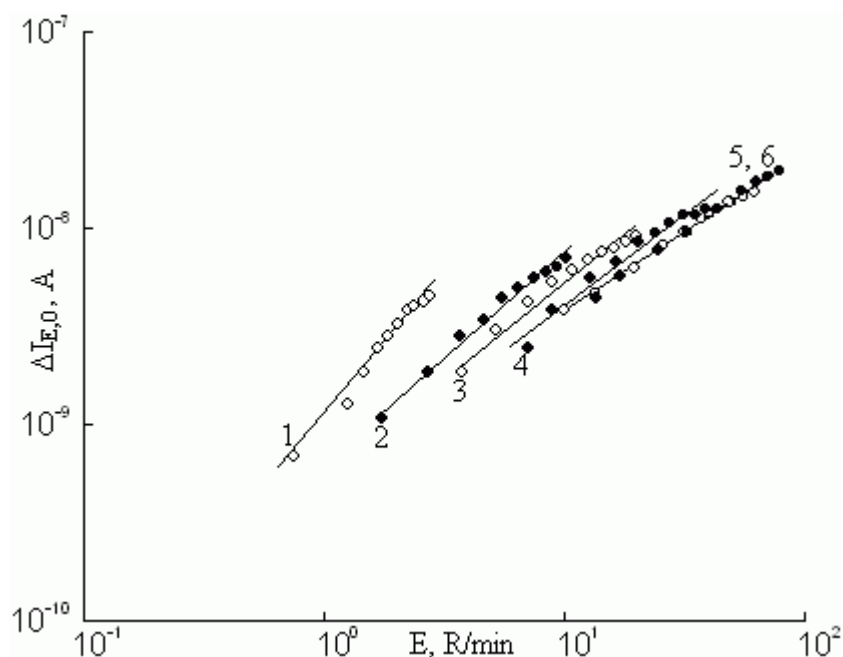


Fig. 4 Roentgen-ampere characteristics of TiGaS_2 single crystal at various effective hardnesses: 1 – 25; 2 – 30; 3 – 35; 4 – 40; 5 – 45; 6 – 50 keV ($T = 300 \text{ K}$)

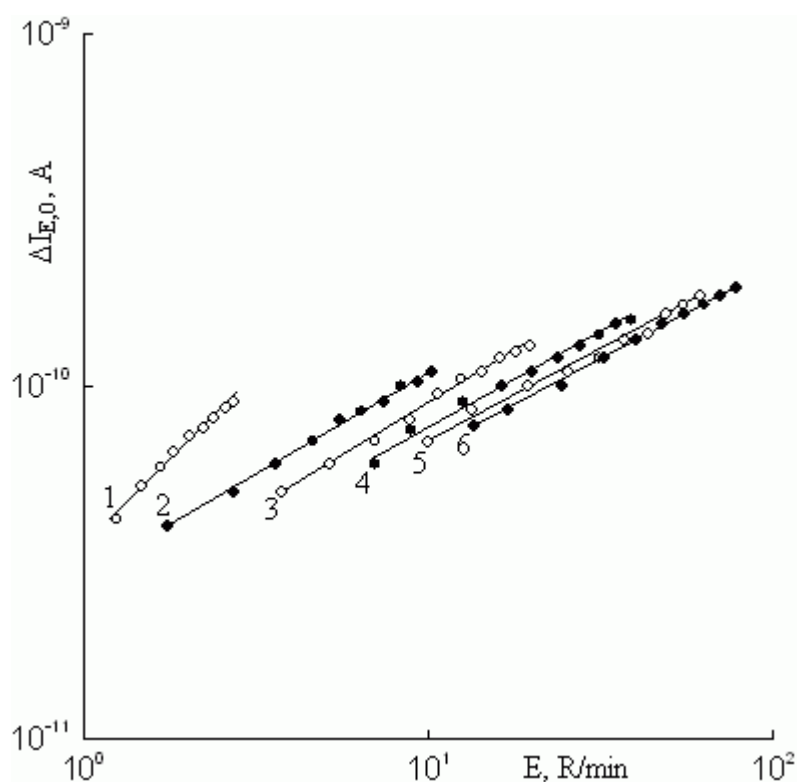


Fig. 5 Dependences of $\Delta I_{E,0}$ vs E for $\text{TiGaS}_2\text{<Yb>}$ at $V_a = 25 \div 50$ for curves 1–6.

Ratio of given dependence α is determined graphically from roentgen-ampere characteristics as the tangent of angle of slope of dependence $\lg \Delta I_{E,0}$ vs $\lg E$. α – values for investigated crystals vs effective hardness V_a are shown in Fig. 6. As it is seen from Fig. 6 with partial $\text{Ga} \rightarrow \text{Yb}$ substitution in TiGaS_2 single crystals, roentgen-ampere characteristics tend to linearity ($\alpha=1$) in the range of low intensities of

soft (low V_a) roentgen radiation. In the range of comparatively high intensities of harder (high V_a) roentgen radiation $\alpha \rightarrow 0.5$ as for initial as for doped by Yb TiGaS_2 single crystals.

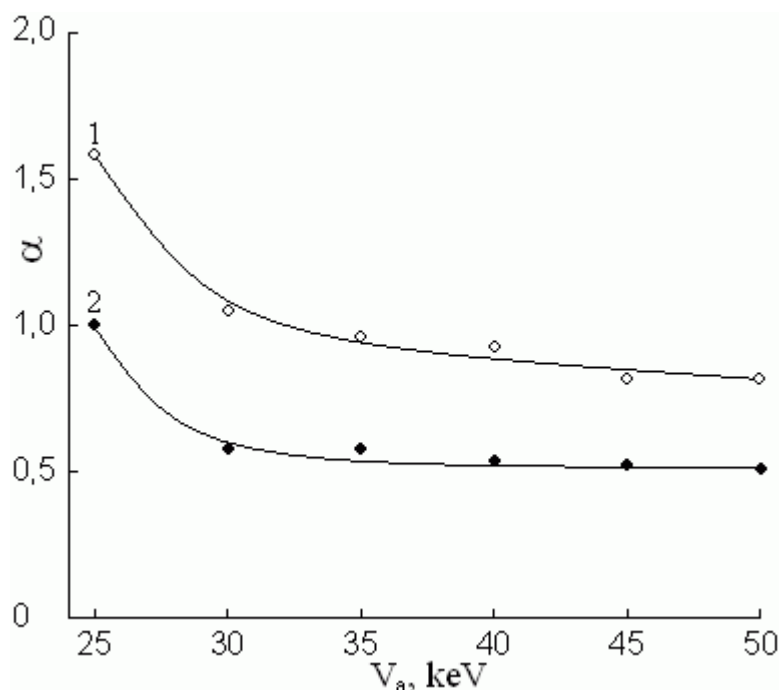


Fig. 6 $\alpha(V_a)$ – dependences for TiGaS_2 (curve 1) and $\text{TiGaS}_2<\text{Yb}>$ (curve 2) single crystals

Obtained results show that $\text{TiGaS}_2<\text{Yb}>$ single crystals have high roengensensitivity and can be used for the creation of roentgendetectors.

References

1. S.N. Mustafaeva, V.A. Aliev, M.M.Asadov, Fiz. Tverd. Tela (St. Petersburg) 40(4), 612 (1998) [Phys. Solid State 40, 561 (1998)]
2. A.U. Sheleg, K.V. Iodkovskaya, N.F. Kurilovich, Fiz. Tverd. Tela (St. Petersburg) 45(1), 68 (2003) [Phys. Solid State 45, 69 (2003)]
3. S.N. Mustafaeva Fiz. Tverd. Tela (St. Petersburg) 46(6), 979 (2004) [Phys. Solid State 46 (6), 1008 (2004)]

РЕНТГЕНОДОЗИМЕТРИЧЕСКИЕ ХАРАКТЕРИСТИКИ ДЕТЕКТОРОВ НА ОСНОВЕ МОНОКРИСТАЛЛОВ $\text{TiGaS}_2<\text{Yb}>$

С.Н. Мустафаева, Э.М. Керимова, П.Г. Исмаилова, М.М. Асадов

Изучено влияние частичного замещения Ga на Yb в монокристаллах $\text{TiGaS}_2<\text{Yb}>$ на рентгенодозиметрические характеристики выращенных монокристаллов. Анализ полученных экспериментальных результатов показал, что коэффициент рентгенопроводимости (K_σ) исследованных кристаллов закономерно уменьшается с ростом дозы (E) и энергии (V_a) рентгеновского излучения. В результате частичного замещения $\text{Ga} \rightarrow \text{Yb}$ в TiGaS_2 K_σ увеличивается, а рентген-амперные характеристики ($\Delta I_{E,0} \sim E^\alpha$) стремятся к линейности ($\alpha=1$) в области малых интенсивностей мягкого (низкие V_a) рентгеновского излучения. В области сравнительно высоких интенсивностей жесткого (высокие V_a) рентгеновского излучения $\alpha \rightarrow 0.5$ как для TiGaS_2 , так и для $\text{TiGaS}_2<\text{Yb}>$.

**$\text{TlGaS}_2<\text{Yb}>$ MONOKRİSTALI ƏSASINDA HAZIRLANMIŞ RENTGEN
DETEKTORLARININ RENTGEN DOZİMETRIK XARAKTERİSTİKALARI**

S.N. Mustafayeva, E.M. Kərimova, P.H. İsmayılova, M.M. Asadov

Yetiştirilmiş kristallarda $\text{Ga} \rightarrow \text{Yb}$ qismən əvəz olunmasının rentgen dozimetrik xarakteristikalarına təsiri öyrənilmişdir. Alınmış eksperimental nəticələr göstərdi ki, tədqiq olunan kristallarda rentgen keçiricilik əmsalı (K_σ) dozanın (E) və rentgen şüasının enerjisinin (V_a) artması ilə qanuna uyğun olaraq azalır. TlGaS_2 -də $\text{Ga} \rightarrow \text{Yb}$ qismən əvəz olunması nəticəsində K_σ yüksəlir, rentgen-ampere xarakteristikalar isə ($\Delta I_{E,0} \sim E^\alpha$) yumşaq rentgen şüasının (kiçik V_a) aşağı intensivli oblastında xəttləşir ($\alpha=1$). Sərt (yüksək V_a) rentgen şüasının yüksək intensivlikli oblastında TlGaS_2 -də olduğu kimi $\text{TlGaS}_2<\text{Yb}>$ -də $\alpha \rightarrow 0.5$ olur.

UNIFICATION OF ELECTROMAGNETISM AND GRAVITATION IN THE FRAMEWORK OF GENERAL GEOMETRY¹

Shervgi S. Shahverdiyev*

Institute of Physics, Azerbaijan National Academy of Sciences, Baku, Azerbaijan

Abstract

General geometry including Riemannian geometry as a special case is constructed. It is proven that the most simplest special case of General Geometry is geometry underlying Electromagnetism. Action for electromagnetic field and Maxwell equations are derived from curvature function of geometry underlying Electromagnetism. And it is shown that equation of motion for a particle interacting with electromagnetic field coincides exactly with equation for geodesics of geometry underlying Electromagnetism. It is also shown that Electromagnetism can not be geometrized in the framework of Riemannian geometry. Using General Geometry we propose a unified model of electromagnetism and gravitation which reproduces Electromagnetism and Gravitation and predicts that electromagnetic field is a source for gravitational field. This theory is formulated in four dimensional space-time and does not contain additional fields.

*<http://www.geocities.com/shervgis>
e-mail:shervgis@yahoo.com

¹This talk is based on papers [1] and [2].

Contents

1	Introduction	3
2	General Geometry	4
3	Geometry of Electromagnetism	5
4	Unification of electromagnetism and gravitation	7
5	Discussion	9

1 Introduction

As we know equation for geodesics of Riemannian geometry

$$\frac{d^2 x^\lambda}{du^2} = -\Gamma_{\lambda\nu}^{\sigma}(x) x_u^\nu x^\lambda,$$

$$2\Gamma'_{\lambda,\mu\nu} = \frac{\partial g_{\lambda\nu}}{\partial x^\mu} + \frac{\partial g_{\lambda\mu}}{\partial x^\nu} - \frac{\partial g_{\mu\nu}}{\partial x^\lambda}.$$

coincides with the equation of motion for a particle interacting with gravitational field $g_{\mu\nu}$. And equation for gravitational field is related to curvature characteristics of Riemannian geometry

$$\mathfrak{g}S = \int dx \sqrt{-g} R'$$

$$R' = g^{\mu\nu} R'_{\mu\nu}, \quad R'_{\lambda\nu} = \partial_\nu \Gamma^\mu_{\lambda\mu} - \partial_\mu \Gamma^\mu_{\lambda\nu} + \Gamma^\mu_{\rho\nu} \Gamma^\rho_{\lambda\mu} - \Gamma^\mu_{\rho\mu} \Gamma^\rho_{\lambda\nu}, \quad g = \det g_{\mu\nu},$$

where $R'_{\lambda\nu}$ is the curvature tensor of Riemannian geometry.

This can be generalized to a definition of underlying geometry for any theory. So, we understand geometrization of a theory as follows: 1. Equation of motion for particle interacting with a given field must coincide with equation for geodesics of the corresponding geometry. 2. Equation of motion for the given field must be related to curvature characteristics of the corresponding geometry.

Because, Riemannian geometry and theory of gravitation satisfy these two requirements, Riemannian geometry is considered as an underlying geometry for gravitation.

As it is known equation or action function for gravitation could not be found using tools of field theory because in order to get conserved energy momentum for gravitational field it was required to add to the action infinite number of terms. Only geometrization principle made it possible to find a proper action for gravitation [3].

After this was realized [4]–[5] at the beginning of XX century, many physicists and mathematicians tried to geometrize electromagnetism and unify it with gravitation using geometrization principle [6]–[16]. All these approaches considered this problem in the framework of Riemannian geometry and failed to satisfy the above mentioned requirements completely or to reproduce Electromagnetism and Gravitation exactly. I will mention drawbacks of two well known theories, only. They are Weyl and Kaluza-Klein theories.

A Drawback of Weyl theory is that some of its predictions contradict experiment [17].

Drawbacks of Kaluza-Klein theory are that it has charge/mass problem and additional dilaton field. As it is noted by its originator, T. Kaluza, this theory is not applicable even to electrons because of the charge/mass problem [7].

At the end of this talk I will show that Electromagnetism can not be geometrized in the framework of Riemannian geometry.

To solve these problems, instead of increasing dimensionality of spacetime or choosing different metrics in Riemannian geometry, we construct a new geometry, called General geometry. We show that it includes Riemannian geometry as a special case, its the most simplest special case is the geometry underlying Electromagnetism. Using its another special case we propose a unified model of electromagnetism and gravitation

which reproduces electromagnetism and gravitation exactly and predicts that electromagnetic field is a source for gravitational field. It is formulated in four dimensional spacetime and does not contain any additional fields.

Geometry underlying the proposed model is created by interacting particles and sources for electromagnetic and gravitational fields unlike geometry underlying gravitation, Riemannian geometry, which is created by sources for gravitational field only.

2 General Geometry

In this section we construct a new geometry. This geometry includes Riemannian geometry, geometry underlying Electromagnetism (see next section), geometry underlying a unified model of Electromagnetism and Gravitation, and infinite number of geometries, physical interpretation of which is not known at the present time, as special cases. Because of this we call it General Geometry. Besides mathematical applications, this new geometry has important physical applications. We demonstrate it in the next section.

Let M be a manifold with coordinates $x^\lambda, \lambda = 1, \dots, n$. Consider a curve on this manifold $x^\lambda(u)$. Vector field

$$V = \xi^\lambda \frac{\partial}{\partial x^\lambda}$$

has coordinates ξ^λ . In Riemannian geometry it is accepted that

$$\frac{d\xi^\lambda}{du} = -\Gamma'_{\lambda\nu}(x)x_u^\nu \xi^\lambda, \quad (1)$$

where $\Gamma'_{\lambda\nu}(x)$ are functions of x only.

To construct General Geometry we assume that

$$\frac{d\xi^\sigma}{du} = -\Gamma_\lambda^\sigma(x, x_u)\xi^\lambda. \quad (2)$$

$\Gamma_\lambda^\sigma(x, x_u)$ are general functions of x and x_u . The next step is to consider x as a function of two parameters u, v and find $\lim_{\substack{\Delta v \rightarrow 0 \\ \Delta u \rightarrow 0}} \Delta\xi^\sigma / \Delta u \Delta v$. In order to do that we need

$$\frac{d\xi^\sigma}{du} = -\Gamma_\lambda^\sigma \xi^\lambda, \quad \frac{d\xi^\sigma}{dv} = -\tilde{\Gamma}_\lambda^\sigma \xi^\lambda,$$

$$\Gamma_\lambda^\sigma = \Gamma_\lambda^\sigma(x, x_u, x_v), \quad \tilde{\Gamma}_\lambda^\sigma = \tilde{\Gamma}_\lambda^\sigma(x, x_u, x_v).$$

After simply calculations we arrive at

$$\lim_{\substack{\Delta v \rightarrow 0 \\ \Delta u \rightarrow 0}} \frac{\Delta\xi^\sigma}{\Delta u \Delta v} = R_\lambda^\sigma \xi^\lambda,$$

where

$$R_\lambda^\sigma = \frac{d}{dv} \Gamma_\lambda^\sigma - \frac{d}{du} \tilde{\Gamma}_\lambda^\sigma + \tilde{\Gamma}_\rho^\sigma \Gamma_\lambda^\rho - \Gamma_\rho^\sigma \tilde{\Gamma}_\lambda^\rho.$$

We call R_λ^σ curvature function.

Representing $\Gamma_\lambda^\sigma(x, x_u)$ as

$$\Gamma_\lambda^\sigma(x, x_u) = F_\lambda^\sigma(x) + \Gamma_{\lambda\nu}^\sigma(x)x_u^\nu + \Gamma_{\lambda\nu\mu}^\sigma(x)x_u^\nu x_u^\mu + \dots$$

and considering each order in x_u or their combinations separately we define a set of new geometries. Only the first order in x_u is already known Riemannian geometry. Let us show how curvature function is related to curvature tensor in the case of Riemannian geometry. Let

$$\Gamma_\lambda^\sigma(x, x_u, x_v) = \Gamma_{\lambda\nu}^\sigma(x)x_u^\nu, \quad \tilde{\Gamma}_\lambda^\sigma(x, x_u, x_v) = \Gamma_{\lambda\nu}^\sigma(x)x_v^\nu.$$

Curvature function for this case is

$$R_\lambda^\sigma = R_{\lambda\mu\nu}^\sigma(x_u^\nu x_v^\mu - x_v^\nu x_u^\mu),$$

where

$$R_{\lambda\mu\nu}^\sigma = \partial_\mu \Gamma_{\lambda\nu}^\sigma - \partial_\nu \Gamma_{\lambda\mu}^\sigma + \Gamma_{\rho\mu}^\sigma \Gamma_{\lambda\nu}^\rho - \Gamma_{\rho\nu}^\sigma \Gamma_{\lambda\mu}^\rho$$

is the curvature tensor of Riemannian geometry.

3 Geometry of Electromagnetism

In the case of Electromagnetism we do know equation for the field and particles interacting with it but we do not know geometry underlying it. This is the reversed case for gravitation. We need to know geometry underlying electromagnetism because in that case we can construct geometry underlying unified model of Electromagnetism and gravitation and as in the case of gravitation, derive equation for the unified model.

For geometry of Electromagnetism, we consider the most simplest case of General Geometry

$$\Gamma_\lambda^\sigma(x, x_u, x_v) = F_\lambda^\sigma(x(u, v)), \quad \tilde{\Gamma}_\lambda^\sigma(x, x_u, x_v) = F_\lambda^\sigma(x(u, v)),$$

when $\Gamma_\lambda^\sigma(x, x_u)$ does not depend on x_u and show that it is an underlying geometry for electromagnetism. In order to prove, that geometry defined by

$$\frac{d\xi^\sigma}{du} = -F_\lambda^\sigma(x)\xi^\lambda \quad (3)$$

with the length of a curve

$$ds = \sqrt{\eta_{\mu\nu} dx^\mu dx^\nu} + \frac{q}{cm} A_\mu dx^\mu$$

is an underlying geometry for electromagnetism we must show that equation of motion for a particle interacting with electromagnetic field coincides with equation of geodesics in this geometry, and Maxwell equations and Lagrangian for electromagnetic field are related to its curvature characteristics.

Geometry defined by (3) has different properties than Riemannian geometry defined by (1). We do not get into details here. We simply mention that in this geometry the

notion of parallel transport is not defined. As we show in the sequel this makes it be underlying geometry for Electromagnetism.

To obtain equations for geodesics we substitute ξ^λ in (3) by x_u^λ and arrive at

$$\frac{d^2 x_\sigma}{du^2} = -F_{\sigma\lambda}(x)x_u^\lambda.$$

This is exactly equation of motion for a charged particle moving in electromagnetic field A_μ , if we choose

$$F_{\sigma\lambda} = \frac{q}{cm}(\partial_\sigma A_\lambda - \partial_\lambda A_\sigma).$$

So, the first requirement is satisfied with this choice of function $F_{\sigma\lambda}$. In [18], we have proved this relation between $F_{\sigma\lambda}$ and A_μ .

It remains to show that Maxwell equations and Lagrangian for electromagnetic field is related to curvature characteristics of geometry (3). To this end let us find curvature function for (3)

$$R_\lambda^\sigma = R_{\mu\lambda}^\sigma(x_v^\mu - x_u^\mu),$$

where

$$R_{\mu\lambda}^\sigma = \partial_\mu F_\lambda^\sigma.$$

This tensor is an analog of curvature tensor of Riemannian geometry. After summing by two of the three indices we obtain

$$R_\lambda = R_{\mu\lambda}^\mu = \partial_\mu F_\lambda^\mu.$$

Vector R_λ is an analog of Ricci tensor. Equations $R_\lambda = 0$ coincide with the Maxwell equations. In order to construct a Lagrangian we need a scalar function. In our case we have two quantities R_λ and A^λ . A^λ originates from the length of a curve (metric) as $g_{\mu\nu}$ originates from the length of a curve in Riemannian geometry. We can construct from R_λ and A^λ a Lagrangian

$$R = A^\lambda R_\lambda = \partial_\mu(A^\lambda F_\lambda^\mu) - \frac{1}{2}F_{\mu\lambda}F^{\mu\lambda}.$$

This coincides with the Lagrangian of electromagnetic field up to total derivative.

We see that as in the case of Riemannian geometry and gravitation we can find equations and action functional for electromagnetic field from geometric characteristics of geometry underlying Electromagnetism. And equation for geodesics coincides with the equation of motion for a particle interacting with electromagnetic field.

From the geometrical point of view a charged particle interacting with electromagnetic field can be considered as a free particle in the spacetime with the length of a curve $ds = \sqrt{\eta_{\mu\nu}dx^\mu dx^\nu} + \frac{q}{cm}A_\mu dx^\mu$ and equation for geodesic

$$\frac{d^2 x_\sigma}{du^2} = \frac{q}{cm}(\partial_\lambda A_\sigma - \partial_\sigma A_\lambda)x_u^\lambda,$$

where A_μ is a solution to equation $R_\lambda = 0$.

This theory does not has any drawbacks like in the theories constructed before. It reproduces electromagnetism exactly is free from additional fields and extra dimensions.

4 Unification of electromagnetism and gravitation

Now, we consider a different special case of General Geometry. For geometry underlying our unified model we choose functions Γ and $\tilde{\Gamma}$ as

$$\Gamma^\sigma_\lambda(x, x_u, x_v) = F^\sigma_\lambda(x(u, v)) + \Gamma^\sigma_{\lambda\nu}(x)x^\nu_u, \quad \tilde{\Gamma}^\sigma_\lambda(x, x_u, x_v) = F^\sigma_\lambda(x(u, v)) + \Gamma^\sigma_{\lambda\nu}(x)x^\nu_v.$$

And the length of a curve as

$$ds = \sqrt{g_{\mu\nu}(x)dx^\mu dx^\nu} + \frac{q}{cm}A_\mu(x)dx^\mu.$$

For our choice of Γ^σ_λ , (2) becomes

$$\frac{d\xi^\sigma}{du} = -(F^\sigma_\lambda(x) + \Gamma^\sigma_{\lambda\nu}(x)x^\nu_u)\xi^\lambda, \quad (4)$$

We substitute ξ^σ in (4) by x^σ_u and obtain equation for geodesics

$$\frac{d^2x^\sigma}{du^2} = -F^\sigma_\lambda(x)x^\lambda_u - \Gamma^\sigma_{\mu\nu}(x)x^\mu_u x^\nu_u.$$

It coincides exactly with equation of motion for a particle with charge q and mass m interacting with electromagnetic and gravitational fields if we choose

$$F_{\mu\nu} = \frac{q}{cm}(\partial_\mu A_\nu - \partial_\nu A_\mu), \quad 2\Gamma_{\lambda,\mu\nu} = \frac{\partial g_{\lambda\nu}}{\partial x^\mu} + \frac{\partial g_{\lambda\mu}}{\partial x^\nu} - \frac{\partial g_{\mu\nu}}{\partial x^\lambda}. \quad (5)$$

In this paper we assume these relations and declare A_μ as electromagnetic field and $g_{\mu\nu}$ as gravitational field. These relations between F and A , and Γ and $g_{\mu\nu}$ are proven in [18] and it is shown that A_μ can be identified with electromagnetic field, q with charge, m with mass of a particle interacting with A_μ , c with the velocity of the light, and $g_{\mu\nu}$ with gravitational field.

The corresponding curvature function is

$$\begin{aligned} R^\sigma_\lambda &= (\partial_\mu F^\sigma_\lambda - \Gamma^\rho_{\lambda\mu}F^\sigma_\rho + \Gamma^\sigma_{\rho\mu}F^\rho_\lambda)(x^\mu_v - x^\mu_u) + \\ &\frac{1}{2}(\partial_\nu \Gamma^\sigma_{\lambda\mu} - \partial_\mu \Gamma^\sigma_{\lambda\nu} + \Gamma^\sigma_{\rho\nu}\Gamma^\rho_{\lambda\mu} - \Gamma^\sigma_{\rho\mu}\Gamma^\rho_{\lambda\nu})(x^\nu_v x^\mu_u - x^\nu_u x^\mu_v). \end{aligned} \quad (6)$$

From (6), we see that gravitational field is coupled to F^σ_λ through covariant derivative

$$\Delta_\mu F^\sigma_\lambda = \partial_\mu F^\sigma_\lambda - \Gamma^\rho_{\lambda\mu}F^\sigma_\rho + \Gamma^\sigma_{\rho\mu}F^\rho_\lambda.$$

We have $g_{\mu\nu}$, A_μ and curvature function to use to find an action for the unified model. First, we construct a tensor from (6)²

$$R^\sigma_{\lambda\mu\nu} = \frac{cm}{4q}(\Delta_\nu F^\sigma_\lambda A_\mu - \Delta_\mu F^\sigma_\lambda A_\nu) + \frac{1}{16\pi G}(\partial_\nu \Gamma^\sigma_{\lambda\mu} - \partial_\mu \Gamma^\sigma_{\lambda\nu} + \Gamma^\sigma_{\rho\nu}\Gamma^\rho_{\lambda\mu} - \Gamma^\sigma_{\rho\mu}\Gamma^\rho_{\lambda\nu}),$$

where G is gravitational constant. Finally we have a scalar

$$R = g^{\lambda\nu}R^\mu_{\lambda\mu\nu}$$

²One may construct different tensors from (6).

and action

$$\begin{aligned} {}^e\mathfrak{S} &= \int dx \sqrt{-g} R = \frac{c^2 m^2}{4q^2} \int dx \sqrt{-g} F^{\mu\nu} F_{\mu\nu} + \frac{1}{16\pi G} \int dx \sqrt{-g} \mathfrak{S}R, \\ \mathfrak{S}R &= g^{\mu\nu} \mathfrak{S}R_{\mu\nu}, \quad \mathfrak{S}R_{\lambda\nu} = \partial_\nu \Gamma^\mu_{\lambda\mu} - \partial_\mu \Gamma^\mu_{\lambda\nu} + \Gamma^\mu_{\rho\nu} \Gamma^\rho_{\lambda\mu} - \Gamma^\mu_{\rho\mu} \Gamma^\rho_{\lambda\nu}, \quad g = \det g_{\mu\nu}, \end{aligned}$$

where use has been made of

$$\Delta_\nu F^{\mu\nu} = \frac{1}{\sqrt{-g}} \partial_\nu (\sqrt{-g} F^{\mu\nu}), \quad \Delta_\nu g_{\mu\lambda} = 0.$$

Note, that the action is invariant under gauge transformations of fields and general transformations of coordinates. Covariant derivative appears naturally in this formalism. Hence, geometrization principle leads to an action which is invariant under gauge transformations of fields and general transformations of coordinates. We conclude that geometrization principle is more general than gauge principle.

Equation of motion for gravitational field is

$$\frac{c^2 m^2}{4q^2} \left(\frac{1}{2} F^{\rho\sigma} F_{\rho\sigma} g^{\mu\nu} - 2 F^{\nu\sigma} F^\mu_{\sigma} \right) + \frac{1}{16\pi G} (-\mathfrak{S}R^{\mu\nu} + \frac{1}{2} \mathfrak{S}R g^{\mu\nu}) = 0. \quad (7)$$

From (7) it follows that $\mathfrak{S}R = 0$ for $n = 4$ (in the rest of the paper we restrict ourselves to four dimensional spacetime) and (7) becomes

$$\frac{c^2 m^2}{4q^2} \left(\frac{1}{2} g^{\rho m} g^{\sigma m} F_{nm} F_{\rho\sigma} g_{\mu\nu} - 2 g^{\sigma m} F_{\nu m} F_{\mu\sigma} \right) - \frac{1}{16\pi G} \mathfrak{S}R_{\mu\nu} = 0. \quad (8)$$

We see that electromagnetic field is a source for gravitational field. In the weak gravitational and strong electromagnetic field approximation $g^{\mu\nu} \sim \eta^{\mu\nu} = \text{diag}(1, -1, -1, -1)$ and

$$\mathfrak{S}R_{00} \sim -\partial_\mu \Gamma^\mu_{00} = -\frac{1}{2} \Delta g_{00}, \quad \Delta = \frac{\partial}{\partial x^i} \frac{\partial}{\partial x^i}, \quad i = 1, 2, 3.$$

The 00 component of equation (8) gives

$$\Delta \Phi = 4\pi c^2 G (E_i E_i + H_i H_i) + O(hF), \quad g_{00} = 1 - 2 \frac{\Phi}{c^2}, \quad (9)$$

where Φ is the Newtonian potential, $E_i = \partial_0 A_i - \partial_i A_0$ and $H_i = \frac{1}{2} \epsilon_{ijk} (\partial_j A_k - \partial_k A_j)$ are electric and magnetic fields respectively and ϵ_{ijk} is antisymmetric tensor. Accordingly, total energy of electromagnetic field produces gravitational field.

Because geometrization principle gave true equation for gravitational field, we can be sure that this equation is also true. The proposed theory gives exactly Gravitation when electromagnetic field is equal to zero and Electromagnetism when gravitational field is equal to zero. It predicts that electromagnetic field is a source for gravitational field. This theory is formulated in four dimensional spacetime and does not contain any additional fields.

5 Discussion

For Riemannian geometry

$$\frac{d\xi^\lambda}{du} = -\Gamma_{\lambda\nu}^{\prime\sigma}(x)x_u^\nu\xi^\lambda,$$

it is possible to make a change of coordinates so that its right hand side will be equal to zero, because of its right hand side structure. In new coordinates x' , equation for geodesics becomes

$$\frac{d^2x'^\sigma}{du^2} = 0.$$

From physical point of view this corresponds to finding a reference frame where trajectory of particles is strait line, because this equation must coincide with the equation of motion. For gravitational interaction we can find a reference frame where gravitational interaction is absent. Accordingly, Riemannian geometry is suitable for gravitational interaction only. For electromagnetic interactions it is not possible to find a reference frame where it is absent. Therefore, all attempts to geometrize electromagnetism or unify it with gravitation in the framework of Riemannian geometry must fail.

On the other hand for geometry

$$\frac{d\xi^\sigma}{du} = -(F^\sigma{}_\lambda(x) + \Gamma^\sigma{}_{\lambda\nu}(x)x_u^\nu)\xi^\lambda$$

it is not possible to eliminate its right hand side by changing coordinates because of $F^\sigma{}_\lambda$ term. And this property makes it to be underlying geometry for the proposed unified model.

In general relativity, geometry underlying gravitation and metric are independent of properties of interacting particles. This is a consequence of equivalence principle. Geometry and metric depends on the characteristics of sources for gravitational field $g_{\mu\nu}$ only. For electromagnetic interactions there is no equivalence principle, so geometry and metric underling electromagnetism and unified model of electromagnetism and gravitation must depend on characteristics of interacting particles, because particles of different charges move in electromagnetic field differently.

For our model we have

$$\frac{d\xi^\sigma}{du} = -(\frac{q}{cm}(\partial_\mu A_\nu - \partial_\nu A_\mu) + \Gamma^\sigma{}_{\lambda\nu}(x)x_u^\nu)\xi^\lambda.$$

Accordingly, geometry underlying unified model of electromagnetism and gravitation depends not only on the characteristics of sources for A_μ and $g_{\mu\nu}$ but also on the characteristics of interacting particles q and m . This means that geometry and the length of a curve (metric) $ds = \sqrt{g_{\mu\nu}(x)dx^\mu dx^\nu} + \frac{q}{cm}A_\mu(x)dx^\mu$ are created by interacting particles too, together with sources unlike gravitational interaction. This gives us a new understanding of problem of geometry and matter.

Next, we note that in General Relativity, if we consider sources for gravitational field we must add the so called source term $g_{\mu\nu}T^{\mu\nu}$ to the action

$$\mathfrak{S} = \int dx(\sqrt{-g}R' + g_{\mu\nu}T^{\mu\nu}).$$

$T^{\mu\nu}$ is the energy– momentum tensor of sources for gravitational field. We can not simply replace it with energy- momentum tensor of any field, if it is not a source for $g_{\mu\nu}$. Some people say that General Relativity also predicts that electromagnetic field is a source for gravitational field through inclusion of it to $T^{\mu\nu}$. I would like to stress that in General Relativity there is no natural place for electromagnetic field because inclusion of electromagnetic field in $T^{\mu\nu}$ declares it as a source for gravitational field which is the assumption but not prediction.

Resuming, we can say that we have eliminated the need for extra dimensions and additional fields for formulating unified model of electromagnetism and gravitation by formulating a new geometry. This approach can be useful for formulating a unified electroweak model without Higgs fields and for unifying strong interactions with the other ones.

References

- [1] S. S. Shahverdiyev, “General Geometry and Geometry of Electromagnetism”, Focus on Mathematical Physics Research P.169-176 (2004), Nova Science Publishing, MPS: Pure mathematics/0309022, hep-th/0205224
- [2] S. S. Shahverdiyev, “Unification of Electromagnetism and Gravitation in the framework of General Geometry”, MPS: Pure mathematics/0308016, CERN/EXT-2002-050
- [3] R. Feynman, Lectures on Gravitation
- [4] A. Einstein, Ann. d. Phys. 49 (1916) 769
- [5] D. Hilbert, Grundliden der Physik, 1 Mitt; Got; Nachr; math. nat. Kl-1915.- S.395
- [6] H. Weyl, Sitzungsber. d. Preuss. Akad. d. Wiss (1918) 465; Ann. d. Phys. 59 (1919) 101:Space, Time, Matter, Dover publications Inc. New York.
- [7] T. Kaluza, Sitzungsber. d. Preuss. Akad. d. Wiss (1921) 966
- [8] A. S. Eddington, Proc. Roy. Soc. A99 (1921)104
- [9] O. Klein, Z. Phys. 37 (1926) 903
- [10] A. Einstein and Mayer, Berl. Ber. (1931) 541 and (1932) 130.
- [11] A. Einstein and P. Bergmann, Ann. Math. 39 (1938) 683
- [12] A. Einstein, V. Bargmann and P. Bergmann, Theodore von Karman Anniversary Volume, Pasadena (1941) 212
- [13] A. Einstein, Ann. d. Phys. 102(1930) 685
- [14] E. Schrodinger, “Space-Time Structure”, Cambridge University Press, 1960.
- [15] H. Akbar-Zadeh, J. Geom. Phys. 17 (1995) 342

- [16] B. G. Sidharth, Chaos Solitons Fractals 12, 2143 (2001)
- [17] W. Pauli, Theory of Relativity, Pergamon press 1958.
- [18] S. S. Shahverdiyev, “On Special Cases of General Geometry”, MPS: Pure mathematics/0308003, CERN/EXT-2002-051

A NEW LOW-NOISE AVALANCHE PHOTODIODE WITH MICRO-PIXEL STRUCTURE

O. ALEKPEROV, E. JAFAROV, Z. SADYGOV, N. SAFAROV, M. SULEIMANOV

Institute of Physics, Azerbaijan National Academy of Sciences

R. MADATOV

Azerbaijan State Oil Academy

M. MUSAIEV

Institute of Radiation Problems, Azerbaijan National Academy of Sciences

A new design of the avalanche photodiodes with an array of micro-pixel p-n-junctions was developed on base of metal-oxide-silicon structure. The thermal oxide layer of 1000Å thickness contains tunnel oxide regions with about 25Å thickness. The device exhibits a noise factor ~ 4 at a high multiplication factor ($M \sim 10000$). A high space uniformity of sensitivity was found for gain of $M \sim 1000$.

INTRODUCTION

The use of the metal-insulator-silicon (MIS) structure as an avalanche photodiode was first proposed in [1, 2]. The traditional MIS-structures exhibited very high gains in comparison with ordinary avalanche photodiodes (APD). However, the mentioned avalanche MIS-structures need pulsed bias for operation because of a thick oxide layer. This disadvantage was avoided by using wide-gap resistive layers instead of the insulator (see [3–6]). In this case, carriers accumulated during avalanche process at interface silicon-resistive layer flow out through the high-resistive layer. A major disadvantage of such structures is the poor reproducibility of wide-gap layer.

In this study, we examine the characteristics of an avalanche photosensitive MIS structure, where carriers flow out from the avalanche regions to upper electrodes through specially created pixels with tunnel oxide layer of ~ 25 Å thickness.

DEVICE DESIGN AND OPERATION

The device is intermediate between conventional avalanche photodiodes and photosensitive MIS structures intended for avalanche mode operation. This planar photodiode was made on p-Si wafer with a specific resistance about $1\Omega\cdot\text{cm}$. The photosensitive area is covered with a silicon oxide (SiO_2) layer of ~ 1000 Å and a semitransparent titanium coating connected to a collector electrode of thick aluminium ring (Fig.1.).

The silicon oxide layer separates metal electrodes from a substrate. On a surface of silicon substrate a matrix of p-n-junctions was manufactured. Above the p-n-junctions a thin oxide of ~ 25 Å was made. The sizes of p-n-junctions were $2\mu\text{m} \times 2\mu\text{m}$, and interval between them – $6\mu\text{m}$. The amplification of photocurrent is yielded only in these p-n-junctions. Then the avalanche current flows out to contacts by tunnelling process through thin oxide layer. This enables the MIS structure to operate in the avalanche mode at a continuous bias mode.

EXPERIMENTAL DATA

We studied photodiode noise properties using a conventional technique for low-signal radio engineering; i.e., a dc signal was measured after square-law detection of noise, which made it possible to restrict our measurements to a relatively narrow frequency range (3 MHz in the considered case).

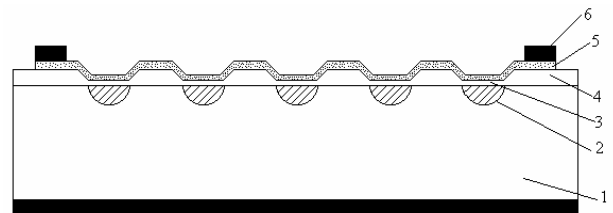


Fig. 1. Cross section of the avalanche MIS- photodiode; 1 - p-Si substrate, 2 - p-n-junction, 3 - thin oxide layer, 4- thick oxide layer, 5- semitransparent Ti layer, 6- thick Al layer.

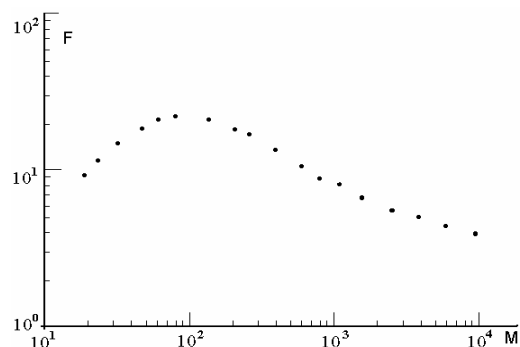


Fig. 2. Excess noise factor F versus the signal gain M .

Figure 2 displays the measured noise factor for the tested diode. The noise factor was measured using light emitting diode with $\lambda \sim 0.55\mu\text{m}$, which is absorbed mostly in near-surface region. In this case, holes are injected into the diode active region, which is extremely adverse to the signal-to-noise ratio, as is evident from the data acquired at relatively low M . The avalanche MIS photodiode exhibited substantially better noise characteristics because of local negative feedback effect. It is necessary to note, that the noise factor measured at the highest M are lower than those calculated according to the McIntyre theory [7] for electron injection and for very small $k = 0.005$.

GAIN DISTRIBUTION OVER THE PHOTOSENSITIVE AREA

One of disadvantages of APD's with traditional design is its non-uniform photosensitivity over the working area, which becomes more pronounced with increasing multiplication factor. A negative feedback mechanism in MIS avalanche photodiodes substantially levels off this problem.

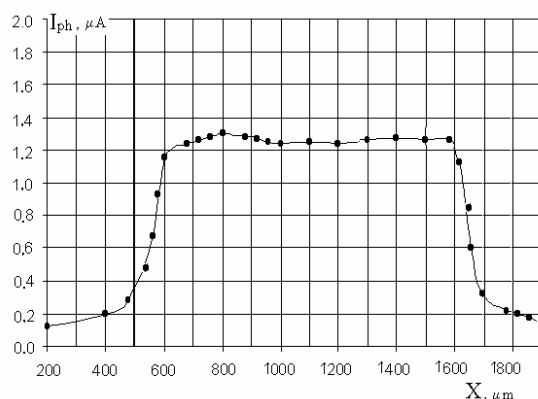


Fig.3. Coordinate dependence of photosensitivity at M~1000.

Figure 3 displays the measured coordinate dependence of photosensitivity at M~1000. The measurements were carried out using an optical probe with a diameter of 30μ. The non-

uniformity found in the sensitivity over the area does not exceed 20%. The appreciable photo- sensitivity beyond the receiving area edge is caused by scattered radiation in the optical system.

CONCLUSION

A new type of avalanche photodiode high gain was developed on base of MIS technology. The micro-pixel avalanche photodiode demonstrates very low noise factor at signal gains more than 10^2 . Further studies will be focused on increasing of signal gain up to 10^6 .

This work was supported in part by CRDF US-Azerbaijan Bilateral Grant #3106.

- [1] N. I. Gol'braikh, A. F. Plotnikov, and V.E. Shubin, Kvantovaya Elektron. (Russia) 1975,2, 2624
- [2] S. V. Bogdanov, A. B. Kravchenko, A. F. Plotnikov, and V. E. Shubin, Phys. Status Solidi 1986,A 93, 361
- [3] G. Gasanov, V. M. Golovin, Z. Ya. Sadygov, and N. Yu. Yusipov. Sov. Tech. Phys. Lett. 1988,14, 313
- [4] Z. Ya. Sadygov, Russian Patent # 2086047 (1996).
- [5] Z. Ya. Sadygov, M. K. Suleimanov, and T. Yu. Bokova. Pis'ma Zh. Tekh. Fiz. 2000,26 (7), 75 or Tech. Phys. Lett. 2000,26, 305
- [6] Z. Ya. Sadygov, V. N. Jejer, Yu. V. Musienko, T. V. Sereda, A. V. Stoikov, I. M. Zheleznykh. Nucl. Instrum. and Methods in Phys. Res., 2003,A504 , 301-303.
- [7] R. McIntyre IEEE Trans. Electron Devices ED-13 (1), 164 (1966).

O. Ələkbərov, E. Cəfərov, R. Mədətov, M. Musayev, Z. Sadıqov, N. Səfərov, M. Süleymanov

YENİ MİKRO-PİKSEL STRUKTURA MALİK AŞAĞI KÜYLÜ SELVARI FOTODİODLAR

Metal-Oksid-Silisium strukturu əsasında mikro-piksel p-n-keçidlər massivinə malik selvari fotodioların yeni forması işlənib hazırlanmışdır. 1000 Å qalınlığındakı oksid layı təqribən 25 Å qalınlığında tunel oksid bölmələrini özündə saxlayır. Yüksək gücləndirmə faktoru altında (M~10000) qurğunun küy faktoru təqribən 4-ə bərabərdir. M~1000 güclənməsi zamanı isə həssaslığın ən yüksək fəza bircinsliyinə malik olması aşkarlanmışdır.

О. Алекперов, Е. Джафаров, Р. Мадатов, М. Мусаев, З. Садыгов, Н. Сафаров, М. Сулейманов

НОВЫЙ НИЗКОШУМНЫЙ ФОТОДИОД С МИКРО-ПИКСЕЛЬНОЙ СТРУКТУРОЙ

Новый шаблон лавинных фотодиодов с массивом микро-пиксельных p-n-переходов был разработан на основе Металл-Оксид-Кремний структуры. Термальный оксидный слой толщины 1000Å содержит туннельные оксидные регионы толщины около 25Å. Устройство демонстрирует фактор шума ~4 при факторе высокого умножения (M~10000). При увеличении фактора M~1000 найдено высокое пространственное однообразие чувствительности.